Christof Hübner
Udo Kaatze

Electromagnetic Moisture Measurement

Principles and Applications

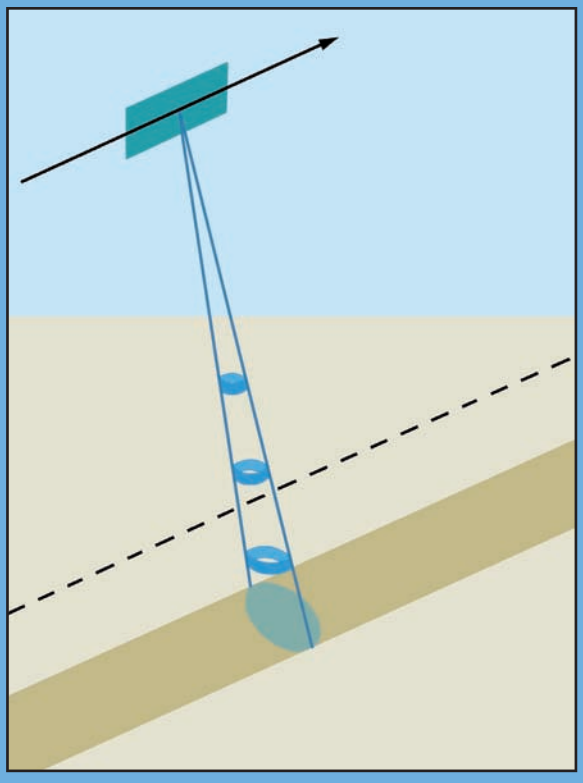

Universitätsverlag Göttingen

Christof Hübner, Udo Kaatze

Electromagnetic Moisture Measurement

Published by Universitätsverlag Göttingen 2016

Christof Hübner, Udo Kaatze

Electromagnetic Moisture Measurement

Principles and Applications

Universitätsverlag Göttingen
2016

Bibliographic information published by the Deutsche Nationalbibliothek

The Deutsche Nationalbibliothek lists this publication in the Deutsche Nationalbibliografie; detailed bibliographic data are available on the Internet at http://dnb.dnb.de

Addresses of the authors

Christof Hübner
Department of Electrical Engineering
University of Applied Sciences
Paul-Wittsack-Straße 10
68163 Mannheim
Germany
c.huebner@hs-mannheim.de

Udo Kaatze
Drittes Physikalisches Institut
Georg-August-Universität Göttingen
Friedrich-Hund-Platz 1
37077 Göttingen
Germany
Udo.Kaatze@phys.uni-goettingen.de

Set and layout: Christof Hübner, Udo Kaatze
Cover design: Jutta Pabst
Cover image: Schematic of soil moisture mapping utilizing an airborne radar platform. The image has been adapted from Figure 1 of reference [703].

http://univerlag.uni-goettingen.de
ISBN: 978-3-86395-260-0

Contents

Preface

In the recent past demands of providing the precise water content of materials have increased continuously. The reasons for this trend are multifaceted and include provisions for development related to global climate change as well as refinements of many production processes in agricultural, industrial, and civil engineering domains. Electromagnetic techniques have proven a favorable tool for moisture determination. Essentially these techniques rely on the clear difference between the dielectric properties of water and those of other materials. In many cases electromagnetic techniques can be non-invasively employed and remotely operated in automatic modes. They apply to a tremendous range of observations areas. Regions of vast sizes may be covered by airborne radar platforms or global navigation satellite systems for soil moisture or snow cover mapping. As another extreme, moisture determination of biochemically or pharmaceutically relevant samples at microliter to nanoliter levels is likewise feasible. Electromagnetic techniques of water content measurement enable fast operation and are also adapted to long-term observation for continuous moisture monitoring.

Due to their beneficial features electromagnetic techniques for moisture determination have been developed for various fields of application, comprising, for example, avalanche forecast as well as precision farming, quality assessment of building materials as well as moisture adjustment in paper production cycles. Electromagnetic moisture measurement, often referred to as electromagnetic aquametry, has thus become a highly interdisciplinary field. Design and development of adequate moisture sensors and suitable measurement procedures evidently needs expertise in the relevant fields of application but also in dielectric measurement methods, microwave and radio frequency engineering, and information technology. Last but not least, a certain understanding of the correlation between the structure and molecular dynamics of the moist materials under consideration and their dielectric properties is also essential. In order to facilitate the cooperation in different fields of science and development, we present this book as an introduction into various aspects of electromagnetic aquametry.

The book is intended to be illustrative rather than exhaustive. It depicts some basic features in the dielectric behavior of materials and relates these features to the interactions between the materials and electromagnetic fields. It also reviews general issues of dielectric measurement methods

which we believe to be useful when considering the design of special sensors and appropriate measurement techniques for moisture determination. A chapter dealing with the dielectric properties of water in its different states of interaction is also included. It is intended to provide information concerning the adequate modelling of data derived from the electromagnetic signals when affected by moist materials. Selected applications are discussed in order to introduce some proven examples of electromagnetic moisture sensors and related measurement methods. Finally, a collection of dielectric data for liquids is presented which may serve as reference in calibration procedures. Preferably data obtained from calibration-free methods is given. Additionally, most of it has been measured at different laboratories and the different series of data agree within the limits of experimental uncertainty. A detailed bibliography is provided in order to assist with further reading.

We are indebted to Alexander Brandelik, Karlsruhe, who spent much time to critically read the manuscript before publication. We thank Alexander Schaub, Mannheim, for valuable help with editing the book, including proofreading and formatting.

Mannheim, Göttingen, Spring 2016

Christof Hübner
Udo Kaatze

1 Introduction

1.1 Water, the omnipresent chemical in nature

Water is the most abundant and presumably most eccentric chemical on our planet. Except bromine and mercury it is the only inorganic liquid which appears at standard conditions for temperature and pressure. It is, in addition, the sole substance that naturally exists in all three states of matter, solid, liquid, and gas. The dynamic equilibrium between these states is one reason for the universal importance of water. The steady hydrologic cycle, in which water is circulated by evaporation and transpiration from the hydrosphere and precipitated back from the atmosphere, exposes geological structures as well as man-made constructions to continuous attacks by rainfall and rivers. This is true even though about 70% of the rainfall immediately evaporates and though the air encloses only less than 0.001% of the total water as vapor, clouds, and precipitation. But as the water in the atmosphere is turned over 37 times per year the enormous annual precipitation of $2.2 \cdot 10^{14}$ m^3 = $2.2 \cdot 10^5$ km^3 results [1, 2].

The dominating influence of the hydrologic cycle on weather and climate is undoubted. However, climate is not just controlled by the humidity of the air and the moisture content of the soil, but also by the distribution of water over oceans, seas, rivers, glaciers, ice caps, and plants. It is interesting in this context that more than 70% of earth's surface is covered by water. Of this water is 96.5% contained in seas and oceans, nearly 1.7% in ice caps and likewise about 1.7% in groundwater. We are aware that, albeit ice caps hold only a minor part of the total water, changes in their size may have dramatic effects on climate. Actually, variations of smaller reservoirs, such as the shrinking of the Aral Sea to 10% of its 10^3 km^3 water volume in 1955, have a disastrous effect on ecology and economic activity, including multiple health and social problems [3].

The exceeding role of water in the biosphere is already demonstrated by the chemical composition of living organisms. Their water content ranges from somewhat less than 50% with bacterial spores to about 96% with some marine invertebrates. The water content of adult humans amounts to 65–70% as mean, with substantial differences between tissues. In order to maintain life processes, organisms need a minimum water uptake. Unfortunately, fresh water, which is imperatively necessary for the survival of all ecosystems, is unevenly distributed on earth. Although it is estimated to account for 2.6 to 3.5 % of the total water, most of the fresh water is contained in ice sheets, ice caps, glaciers, and icebergs. If ade-

quately distributed, the remaining immediately available amount of fresh water from rivers, streams, ponds, lakes, and ground water would be sufficient to account for the needs in all regions of our planet. But as these sources are again unequally spread, many regions on earth suffer from a lack of potable water.

Human activity often intensifies apparent decrease in fresh water supply. Changes in landscape for the use of agriculture, for instance, may strongly affect fresh water flow and cycle. Another example is intensive irrigation that creates a risk of salinization [4]. For several reasons the unimaginably large area of $1.2 \cdot 10^5$ km^2 is subject to desertification every year, implying severe ecological damage but again also considerable social problems.

In addition to these global features, water is unavoidably necessary for the functions of life processes on molecular and cellular scales. In biological systems, molecular activity proceeds almost exclusively in aqueous reaction media. The relatively high specific heat and large latent heat of evaporation of water is utilized to maintain constant temperature and thus to sustain such activities as, for example, enzymatically catalyzed chemical reactions. In doing so, water does not just serve as reaction medium and as buffer material for temperature stabilization. Due to its ability to discriminate hydrophilic and hydrophobic entities, it also promotes biological structure [5]. A prominent example is the formation of cell membranes from phospholipid molecules, tending to prevent their non-polar hydrocarbon chains from contact with water [6, 7]. Other famous examples in which interactions of bio-molecules with neighboring water are of prime importance is the double helix structure of DNA [8] and the structure and stability of proteins [9].

Water is also a major component in cellular recognition and signaling procedures which are mediated by ubiquitous and diverse binding processes in biological systems [10]. Furthermore, because of the above mentioned ability to discriminate between hydrophilic and hydrophobic solutes, water constitutes an excellent reaction medium for ionic and dipolar species but a poor solvent for non-polar non-associating molecules. Another distinctive property of water in biological systems is its autoionization by separation of a proton from one water molecule and combination of that proton with another water molecule. This ampholytic nature allows water to accept protons from an acid as well as to donate protons to a base and to thus control the pH value of the reaction medium. In addition to these multiple functions, involvement in the metabolism is another demonstration of the active participation of water as an integral part in life processes.

1.2 Needs for water content determination

Increasing world population, changes in farming, advanced and often sophisticated production methods, as well as the common use of novel materials have greatly raised the demands in the correct knowledge of the water content of substances. Modern manufacturing processes often include carefully adjusted and precisely controlled dosing of the water content by drying and moistening [11]. For these reasons, methods for moisture determination of materials are presently used in broad ranges of specific applications. Nevertheless, considerable efforts are to be made to improve these methods with a view to their practicability, durability, measurement accuracy, as well as operating expense. Such efforts involve development of new concepts, addressing, for instance, moisture measurement in harsh or difficult-to-access environments or sensor integration into complex production lines. Some applications will be briefly specified below in order to illustrate the manifold requirements in the techniques for water content determination.

1.2.1 Snow, climate

The knowledge of the distribution and wetness of snow is an essential precondition for understanding climate dynamics, for water resource management, as well as for avalanche forecasting and flooding prognoses. In recent decades, much attention has been directed towards the substantial changes in the climate and hydrological cycle of the Arctic and the circumpolar boreal forest. Because of interactions between climate, land cover characteristics and plant phenology, warming of the region, correlated with reduced snow and sea ice covers as well as river discharge, has important influences on the global carbon, energy, and water balances. These balances, in turn, likely induce feedbacks and thus further influence global climate [12-16].

Apparently, moisture measurements combined with sensing of the freeze-thaw state of water in the Arctic and boreal forest zone are vital for modelling climate dynamics. This application of water content determination demonstrates an extreme in the required region of observation. Even the boreal forest covers an area of $1.2 \cdot 10^7$ km^2 which is already about 8% of the planet's land surface. In addition to the huge expanse of the observation area, the denseness of potential ground-based stations suffers from the extreme climate and thus calls for remote monitoring.

1.2.2 Soil, agriculture

Spatial distributions and temporal trends of soil moisture profiles affect natural processes on a major scale. Soil water content has a crucial effect on the quantities of water that become available as surface water and as water vapor in the atmosphere. As a consequence, the mean soil water content in more extended ecosystems influences climate and weather, including drought development. However, soil moisture is naturally also a significant parameter for local agriculture, agroforestry and water supply. Soil water content and status are essential for the activity of organisms in the soil. Among the soil properties promoting plant growth an adequate water content is the most important [17]. Soils that are either too dry or too wet are the prevailing reasons for reduced or even lost productivity. Hence balanced soil-plant-water relations are crucial for the whole civilization, notably for adequate food production at a growing population, for a minimum soil loss and contamination as well as a maximum utilization of water resources.

Efficient plant production requires the detailed measurement and control of soil moisture. This requirement becomes especially evident in precision farming, a modern site-specific crop management concept responding to inter- and intra-acreage variability. Applying such concept, not just the amount of delivered water but also the inputs of seeds, fertilizers, and pesticides are precisely matched in order to reduce costs, increase productivity and quality and minimize water consumption as well as soil pollution and environmental stress [18].

1.2.3 Civil engineering, building materials

Aspects of moisture in civil engineering are as complex as the used materials and as diverse as the demands in the variety of specific constructions. In addition to structural damage, moistness of outer wall materials is a major factor in the effective thermal resistance of a building and is thus of prime importance for a healthy indoor climate and for the fuel consumption. Too much moisture promotes mold formation, entailing the risk of infections, allergic reactions, and toxic influences on occupants. Wall wetness may have various reasons, such as insufficient protection against rain and splash water, capillary water and layer water pressing from below, as well as condensation water. Adequate measures of drying do not just consider the cause of wetness and the properties of the construction materials. They also need to relate to the spatial distribution of moisture and its

diurnal and seasonal variations which thus have to be known as precisely as possible.

Precise knowledge of temporal moisture variations often plays a key role in the restoration of historic buildings. Originally such buildings have been modestly heated only. Hence over the course of the year the indoor climate largely followed the outdoor variations. Present-day standards of an almost constant indoor temperature may result in adverse wall moisture content if no appropriate preventive actions are taken. Furthermore, adsorption and desorption of humidity from the air leads to variations of moisture in the near-surface layers of structural elements which, due to the different expansibility of materials (stone, mortar, plaster), may cause deterioration.

Because moisture poses a crucial danger for the durability of outer walls, there has always been a latent requirement for precise and manageable moisture content determinations of construction materials. Up to 90% of damage of outer brick masonry walls, for example, is assumed to be due to moisture penetration [19]. Integration of modern materials, such as insulation, enhances the demands for the correct knowledge of water uptake and storage properties of wall materials. Increasing evidence of deterioration suggests that the use of reinforced concrete as a comparatively novel construction material continues to be a widespread concern. In many of the deterioration processes the presence of moisture is a critical factor [20]. Detailed studies of the effect of quantity and form of moisture on concrete integrity and durability at different ambient conditions are therefore imperatively necessary to better understand the behavior of this popular material. The large-scale implementation of moisture sensors in a bridge, spanning a main road in Karlsruhe, Germany, is a promising approach of long-term monitoring water uptake on in-situ conditions, including exposure to brine from de-icing [21].

In the following some special constructions which need to be continuously inspected for their moisture content will be mentioned. Sealing barriers for the permanent underground storage of hazardous and non-recyclable waste have to be designed in a way that fluid ingress is prevented for long times. They are often constructed from bentonite or magnesium oxide concrete. Because of the danger of slight dislocation of the ground and degrading connections between the artificial barriers and the cavity walls, leak tightness inspection by regular moisture monitoring of hazardous waste deposits is an absolute must.

Dikes are made from completely different materials. Frequently they consist of a sand core, covered by clay with admixed straw. The seepage through and the stability of such constructions is largely controlled by the water distribution inside the wall. High water content reduces the matric

suction and shear strength of the floodwall material and seepage becomes faster. Again regular moisture determination is an adequate provision to identify the state of the construction and, if necessary, take appropriate measures for its preservation.

Reduced production times as well as innovative combinations of novel with proven materials increase the demands in moisture content control even before the materials are used in building structures. Brick, concrete, and timber are illustrative examples, the thermal, acoustical, and mechanical properties of which depend significantly on their overall moisture content but also on the moisture distribution and thus moisture gradients within the material. In order to enhance the durability and service life of building materials, moisture measurement and control during fabrication is becoming increasingly popular. Crack formation, for instance, is supposed to be effectively reduced by adequate moisture control during concrete curing and timber drying.

1.2.4 Production, storage, quality assessment

Quantitative moisture determination becomes increasingly important for the conditioning of materials in production cycles, such as for paper, foil, textile, leather, films, powders, and pharmaceutics manufacturing. Manufacturing of tablets, for instance, involves first the proper adjustment of moisture in order to improve the flow capability and homogeneity of the material. After mixing the wet mass it is carefully dried to well-defined water content for milling, tableting, and achievement of an acceptable end product [22].

Agricultural products often need also drying and re-wetting cycles to achieve fast production speeds during processing and optimum quality of the end products. A prominent example is green tea which is harvested at moisture content of 350 to 400 % (on a dry basis), first steamed and afterwards dried in a multistep procedure to moisture content as low as 4%. Drying involves up to nine steps, each one relying on critical adjustment of a specific range of moisture. But not only processing procedures necessitate the precise knowledge of the water content of foods and agricultural products. Water content is also an important indicator of quality and a key factor for the durable storability of commodities. Wrong moisture may promote fungi and pest infestation during stocking. On the other hand, adequate moisture enhances a fresh feeling of the end products and thus generates a higher economic return.

Another example is wood-processing. Both the mechanical properties and the decomposition development of wood depend on chemical features

as well as moisture content. Therefore, in advanced wood utilization the wood-drying process is of prime importance for energy saving during drying and particularly for quality assurance of sawn timbers. Present-day kiln-drying is a delicate technology, with the risk of partial degrading or even total loss of timber load. Kiln-drying practice to obtain satisfactory results thus strictly follows moisture-based schedules [23].

1.3 Customary methods and actual demands

The above brief review of the impact of moisture to a variety of natural phenomena as well as manufacturing processes and preservation procedures discloses the considerable but still increasing interest in techniques for quantitative water content determination [24-29].

1.3.1 Definitions

Different definitions exist to express such content [30]. The fractional water content on a dry basis, η, is given as the ratio

$$\eta = m_w/m_d \tag{1}$$

of the mass of water, m_w, to the mass of dry material, m_d. Often the fractional moisture content on a wet basis, ξ, defined as

$$\xi = m_w/(m_d + m_w) = \eta/(\eta + 1) \tag{2}$$

is more convenient. If it is more appropriate to refer to the volume $V = m_t/\rho$ of a piece of material rather than its total mass $m_t = m_d + m_w$, the water concentration

$$k_w = m_w/V = \xi \cdot \rho \tag{3}$$

is used. Here ρ denotes the density of the wet material. Another definition is the volumetric water content

$$\theta_w = V_w/V, \tag{4}$$

where V_w is the volume of the water phase within the total volume V.

1.3.2 Routines for reference measurements

Masses m_t and m_w may be directly determined by simply weighing the masses of a piece of sample before and after drying by heating. In such thermo-gravimetric analysis heating cycles at temperatures between 100 and 110 °C are normally repeated until no further weight loss is observed. Thermo-gravimetric measurements are indeed easy and cost-efficient. They alter, however, the sample and are thus inapplicable in many cases. In addition to water, other vaporizable compounds may disappear during the heating procedure and may lead to wrong water mass. Also the risk of chemical reaction and even material disintegration at higher temperatures exists. Since the method is invasive and not suitable for continuous long-term observations as well as moisture measurements over large regions it is almost solely used as a reference method for the calibration of novel indirect methods of water content determination.

Chemical analysis is also counted among the so-called direct methods of moisture content determination. Chemical methods convert the water into a reaction product that can be quantitatively identified. The familiar Karl-Fischer method [31, 32] is based on the Bunsen reaction [33]

$$SO_2 + I_2 + 2H_2O \leftrightarrow H_2SO_4 + 2HI \tag{5}$$

by which, if water is present, sulfur dioxide is oxidized by iodine. Basically, the reaction medium starts to become brownish, if all water has been used and the iodine is no longer converted into iodic acid. Hence the change in color is utilized as an indicator for the complete consumption of water of the sample. An alternative chemical method is based on the reaction [34]

$$CaC_2 + 2H_2O \leftrightarrow Ca(OH)_2 + C_2H_2 \tag{6}$$

of calcium carbide with water. The acetylene produced thereby is quantitatively detected, for instance by the pressure established in a closed vessel.

Both wet chemistry methods are originally designed for liquid use. They can also be applied to solids if these can be solubilized into working solutions. Both methods provide a high degree of accuracy and are therefore applicable to materials with low moisture content. They are, however, destructive and require handling and disposal of potentially hazardous chemicals. Another drawback is the requirement of a laboratory setting and an adequately trained staff.

Soil moisture is often obtained from its quite complex relation to the suction power which is determined with the aid of a tensiometer. The suc-

tion probe basically consists of a water-filled and airproof porous ceramic cup (pore diameter ≤ 1µm) and a clear standpipe showing the filling level. Measurement of the water content is independent of the salinity of the soil, as, for example, resulting from fertilizer. Typically, tensiometers find applications in automatic irrigation control. A drawback is the slow response and often the punctual determination of moisture content, requiring a considerable array of instruments if lateral and/or vertical moisture distribution is required. In addition, many applications, such as measurement in frozen ground demand special provisions. Applications in dry ground need re-filling of water.

Hence all methods mentioned above suffer from a limited range of applicability and need to be complemented by additional methods both for routine and highly sophisticated measurements. In many cases, however, conventional methods offer a superior accuracy and, as mentioned before, are thus used for testing new techniques and instrumentation.

1.3.3 Prospective techniques criteria

The above short contemplation of a few applications disclosed some clear demands in modern methods for moisture determination. First of all such methods should certainly be non-invasive. An example are moisture-controlled timber-drying procedures which should rely on continuous sensing of the material's moisture rather than the need of regular stops for cutting pieces of timber off to analyze them thermo-gravimetrically. Ideally, the measurement technique should be adapted to the timber size to provide the overall water content or the moisture distribution and not just the punctual result at the sites of the cut samples.

Adaptability to the size of the subject of investigation becomes obvious when moisture measurements of small products are compared to such over large-scale climate zones, like the aforementioned Arctic and boreal forest area. Probing moisture via electromagnetic field interactions offers the unique possibility to use signals in a tremendous range of frequency and thus wavelength and to match the spatial resolution to the subject under consideration. Tiny laboratory-on-a-chip studies of tissue are likewise enabled thereby as investigations into the effects of temperature changes on the soil moisture of global climate zones, including emerging technologies, such as large-scale radar observation [35].

Obviously, both examples addressed above require remote sensing, a feature that is common to most present applications. Moisture determinations in the process control of production lines or on harsh conditions are

prominent examples. In addition, the former need an instantaneous response to changes in the water content and an easy implementation in the production line. Harsh and challenging conditions include online formation water monitoring in subsea wet gas production in which the moisture sensor must withstand extremely high pressure. Of course there is also the common desire in measurement techniques to be non-destructive, non-poisonous, and as versatile as possible.

As already briefly indicated, electromagnetic techniques of moisture measurements comply with most of the desiderata. They thus play an outstanding role among a great variety of indirect methods for water content determination, such as electrical [36-41] and thermal [42-47] conductivity measurements, use of nuclear magnetic resonance techniques [48-56], neutron thermalization [57-59] and activation [60-62], photon absorption and Compton scattering of gamma-rays [63-70], as well as infrared thermography [71-79].

Albeit electromagnetic techniques are widely used in diverse fields of moisture determination, there are still scores of challenging requirements regarding the overall advancement, selective refinement, as well as the target-oriented optimization of the methods. Aiming at a better understanding of electromagnetic field interactions with moist materials in the development of advanced measurement techniques, we thus first present some relevant physical and chemical basics. This part of the book will include aspects of the relations between molecular properties and the dielectric behavior of materials, characteristics of dielectric spectra, and also general principles of electromagnetic measurement techniques. It will be followed by a selection of examples of topical applications of electromagnetic methods for moisture content determination.

2 Molecular Properties and Dielectric Behavior

2.1 Water structure, a side-trip into chemistry

Atoms of unlike elements differ from one another by the number of positively charged protons in their nuclei and, correspondingly, the number of negatively charged electron orbitals around the nuclei. Electrons are located in quantum shells which, depending upon the number of protons in the nucleus, are filled up to a certain amount of their maximum capacity. Higher quantum shells are composed of sub-shells, named s, p, d, and f shell. Quantum physics shows that these sub-shells are capable of 1, 3, 5, and 7 pairs of electrons, respectively. Hence the logic of maximum numbers of electrons in the quantum shells is 2 in the first ($1s^2$), 8 in the second ($2s^2 2p^6$), 18 in the third ($3s^2 3p^6 3d^{10}$), and 32 in the fourth one ($4s^2 4p^6 4d^{10} 4f^{14}$). In this nomenclature the superscript specifies the number of electrons per sub-shell.

2.1.1 Architecture of the water molecule, electrical charge distribution

There is an apparent tendency in the quantum shells to be most stable in the noble gas structure of eight electrons, i.e. the $s^2 p^6$ [80]. Often this tendency is referred to as "octet rule". Applied to second-period carbon with $1s^2 2s^2 2p^2$ electronic structure this tendency means that the atom has to capture four additional electrons in order to reach $2s^2 2p^6$ configuration of its outer electron shell. Carbon (C) resolves this issue by forming covalent "electron-pair" bonds with altogether four hydrogen (H) atoms, each electron pair sharing in one electron from the carbon atom and another one from a hydrogen atom. The resulting tetrahedral methane molecule with four equivalent C–H bonds is sketched in Figure 1. Due to its highly symmetric structure methane does not feature any sites of electrical excess charges.

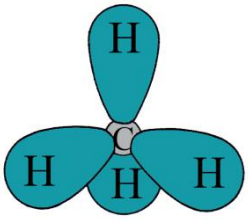

Figure 1. Structure of methane, CH_4. The carbon atom is shown in grey, the turquoise areas represent the binding orbitals to the hydrogen atoms.

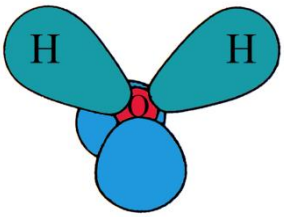

Figure 2. Sketch of a molecule of water, H_2O, as a tetrahedron [80]. The oxygen at the center of the tetrahedron is depicted in red. Turquoise and blue areas indicate the binding orbitals to the hydrogen atoms and the lone pair electrons, respectively.

The electrical charge distribution changes dramatically, however, if carbon, element 6, is replaced by element 8, oxygen (O), with its $1s^2 2s^2 2p^4$ electronic structure. Oxygen needs only two additional electrons to achieve noble gas configuration. It thus binds to two hydrogens to simply form H_2O. As illustrated by Figure 2, the water molecule may again be represented by an almost regular tetrahedron with the comparatively heavy oxygen in its center and with the two light hydrogen atoms at two of its vertices [80]. Both other vertices hold non-binding lone pair electrons. The H–O–H angle of the water molecule is slightly smaller than the tetrahedral angle 109.47°. Experimental values for the water molecule in the gaseous state are 104.47 for the angle and 0.09578 nm for the O–H distance [81]. *Ab initio* calculations yield quite identical values, namely 104.5° and 0.09578 nm, respectively for the isolated molecule [82, 83].

Because of the different electron probability densities in the binding and non-binding orbitals, the electrical charges are not evenly spread across the water molecule. Following Bjerrum [84], the vertices of the tetrahedron may rather be considered poles of charges, as sketched in Figure 3. The binding orbitals hold positive charges at the sites of the hydrogen atoms, reflecting the incomplete shielding of the hydrogen nuclei, the protons, by the binding electrons. Correspondingly, the non-binding lone pair electrons hold the equivalent negative charges and compensate for the positive charges to yield vanishing excess charge of the molecule. Within the framework of the Bjerrum model the charges amount to $\delta^+ = -\delta^- = 0.17e$ [85], where $e = 1.602 \cdot 10^{-19}$ A·s denotes the elementary charge. The

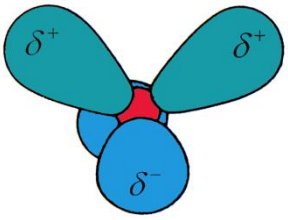

Figure 3. Electrical charge distribution of the water molecule.

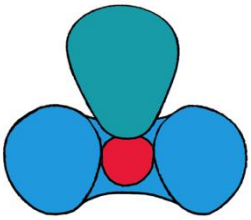

Figure 4. Water molecule with smeared lone pair electrons.

electric polarizability of the water molecule is almost isotropic and amounts to $1.4146 \cdot 10^{-3}$ nm^3 [85].

More recent calculations yield refined charge distributions of the water molecule. Details depend on the supposed molecular geometry and on the method of calculation. Nevertheless the lone pair electrons appear to be not as closely located as in the Bjerrum model but to be rather more evenly smeared out [86, 87] along the line between where the lone pair electrons had been assumed originally (Figure 4). They are also predicted to lie closer to the oxygen atoms. For clearness we shall, however, often sketch the water molecule as the simplified tetrahedral structure shown in Figure 2.

2.1.2 Association, hydrogen bonds

The electrical charge distribution of the H_2O molecule is of prime importance for the properties of water in its condensed phases. Evidently, the positive electrical charges at the only partially shielded protons of a molecule may interact with the negative charges at the lone pair electrons of other molecules to form hydrogen bonds. For a water dimer such a hydrogen bond is sketched in Figure 5: the hydrogen bond donating hydrogen atom forms a covalent bond to one oxygen atom and a hydrogen bond to the oxygen of another water molecule. The strengths of different bonds differ from another by an order of magnitude. The bond energy of the

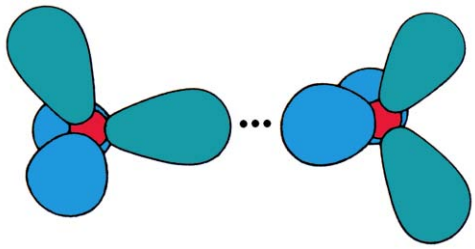

Figure 5. Hydrogen bonded water dimer with ⋯ denoting the H-bond.

covalent bond amounts to 492 kJ/mol [88], whereas the hydrogen bond energy of water accounts for roughly 23 kJ/mol only [89], with the exact value depending on the population of the other hydrogen bonding sites of the participating molecules. The hydrogen bond (H-bond) features predominantly ionic interactions. In most cases, covalent contributions can be neglected.

Hydrogen bonding, i.e. the Coulombic interactions with a neighboring water molecule, tend to weaken the covalent bond of the hydrogen and to reduce the repulsion between the electronic orbitals. Ab initio calculations indicate the O–H distance (0.0991 nm) and the H–O–H angle (105.5°) in liquid water slightly larger [90] than with the isolated molecule (0.0958 nm, 104.5°, as mentioned above). The most stable geometrical configuration of hydrogen bonds in water corresponds with a linear H–O···H structure, where ··· denotes an H-bond.

H-bonds feature a special type of chemical bonds. Their bond energy is indeed one order of magnitude larger than thermal energy at room temperature (RT = 2.5 kJ/mol; R, universal gas constant; T, temperature in Kelvin scale). It is nevertheless sufficiently close to RT to be subject to continual thermal agitation. Consequently the strength of the hydrogen bonds in liquid water fluctuates rapidly.

The special feature of the water molecule to be capable of four hydrogen bonds, with a symmetric distribution of two hydrogen donating and two hydrogen accepting sites, leads to a three-dimensional percolating H-bond network in the condensed water phases. The development of extended

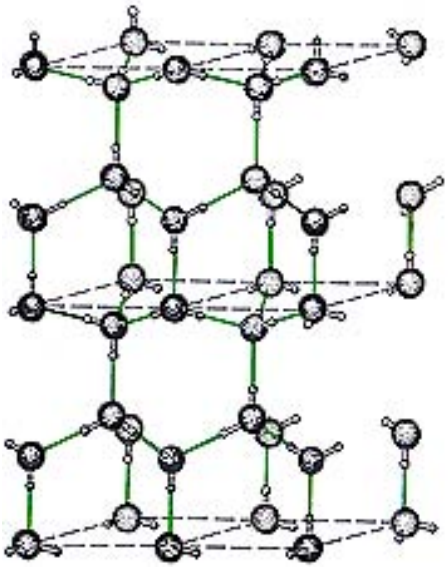

Figure 6. Pauling's sketch of the hexagonal structure of ice Ih. For clearness the hydrogen bonds are marked by green here. Adapted from reference [94].

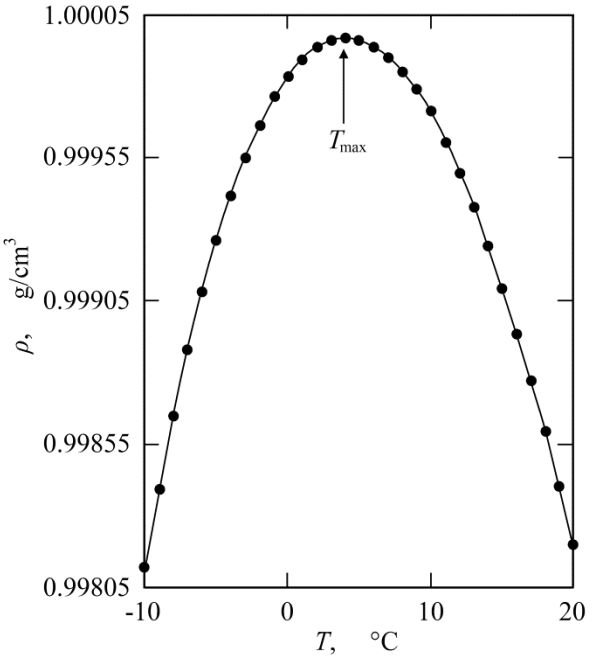

Figure 7. Density ρ of water [98] at temperatures T around T_{max} = 3.984 °C [99]. Data below the melting point of ice refer to supercooled liquid water.

networks is additionally supported by cooperativity effects, tending to enhance the hydrogen bond strengths of associated molecules if another bond is formed between one of the molecules and an additional one [91-93]. The three-dimensional H-bond network of condensed water is illustrated in Figure 6, where a picture by Linus Pauling [94] delineates the regular tetrahedral, almost hexagonal structure of common ice Ih. This rather open structure arranges the oxygen atoms of the water molecules as puckered six-membered rings [95, 96] and features a rather small density (ρ = 0.9167 g/cm^3, 0 °C [81]) as compared to liquid water (ρ = 0.9998 g/cm^3, 0 °C [97]).

The increase in density when ice melts, as well as the density maximum near 4 °C (Fig. 7, [97-101]), along with other water anomalies have inspired a wealth of hypothetical models aiming at an understanding of such experimental findings in a molecular sense. Long before the hydrogen bond had been identified, Röntgen [102] suggested that, when melting, ice was partly converted into a closer-packed fluid in which the remainder dissolved. The fraction of ice-like water was considered to respond to changes of temperature and hydrostatic pressure tending, according to Le Chatelier's principle [103, 104], to eliminate the perturbation effects. This view already implies some bulkiness of the water structure which can be

built up and reduced by processes not existing in "normal" fluids. Though Röntgen noted that similar ideas have been known for a long time, his representation in terms of two types of molecules, ice-like and liquid-like, is considered the prototype of a subsequent series of "mixture" models of water.

After the hydrogen bond had been identified [105] a mixture model, in which the structures of three different intermolecular arrangements are explicitly described, was proposed in a pioneering paper by Bernal and Fowler [95]. Bernal himself, however, stated that the approach postulates a higher degree of order in the liquid than actually exists [96]. He subsequently developed the view of a random network model in which the melting of ice is pictured as a bending of hydrogen bonds which largely remain unbroken. The degree of bond bending is considered the parameter sensitive to changes of state variables such as temperature and pressure. This suggestion keeps the (nearly) tetrahedral local interactions but avoids a high degree of crystalline order [96, 106]. It constitutes the basis of a second class of water models which is often called "uniformist" [107].

In a strict sense the third significant class of models, labeled "interstitial", is a subgroup of mixture models. It proceeds from the assumption that melting of ice is accompanied by dissociation of water molecules from the hydrogen bonded network. Whereas the network is supposed to heal itself, dissociated water molecules are considered to step into the cavities of the puckered ring structure formed by six H-bonded molecules [84, 108-110]. The fraction of lattice sites which are occupied by monomeric "guest" water molecules is taken the parameter sensitive to state variables.

Refined models of the water structure have been developed and are still today subject of considerable scientific debates. Most models are derived to account for a set of parameters or particular observations. In this book the focus will be concepts relevant to the dielectric properties of aqueous systems. For more comprehensive summaries of structure models reference is thus made to the literature [107, 111-115].

As shown in Figure 8, computer simulation studies [116] demonstrate a clear density effect in the water structure (Fig. 8). At reduced density ρ, such as in ice, almost perfect order exists: more than 80 per cent of water molecules are fourfold coordinated. In contrast, a broader distribution of neighboring water molecules emerges for liquid water (ρ = 1 g/cm^3): less than 50 per cent of the water molecules are fourfold coordinated. Quite remarkably, within a 0.33 nm distance, actually one third of all molecules in liquid water is provided with five neighbors. A recent analysis renders a somewhat different probability distribution for the number of hydrogen bonds in liquid water [111]. It predicts an about 60 per cent probability for

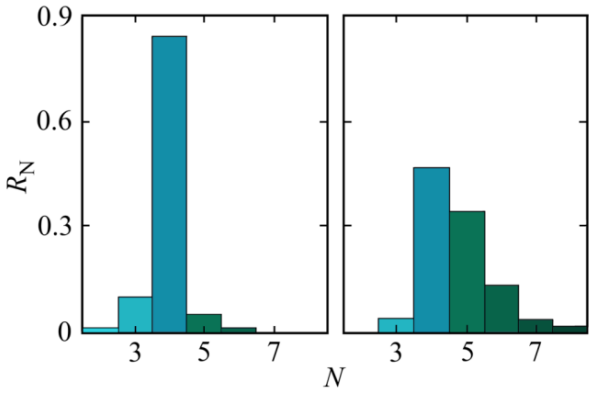

Figure 8. Fraction R_N of molecules with N neighbors within a distance of 0.33 nm for water at 0 °C and normal pressure (ρ = 1g/cm^3, right hand side) and at reduced pressure and density, ρ = 0.75 g/cm^3, left hand side). Results from computer simulation studies [116] are shown.

the existence of fourfold hydrogen bonded water molecules but, analogous to the previous study on the coordination numbers, shows also a considerable content of tri- and fivefold hydrogen bonded molecules. This feature supports the idea of a random network model of liquid water. It will be of major importance in modeling the dielectric relaxation mechanism of water later on.

Despite the distribution of coordination numbers shown in Figure 8, water is exceptional in the capability to form as many hydrogen bonds as it has covalent bonds. Its concentration c^* (= 4c, c = concentration of H_2O molecules) of hydrogen bonding sites is extremely high, namely 221 mol/l at room temperature. This large value compares, for example, to c^* = 74 mol/l of likewise associating methanol (CH_3OH) and is doubtless another special feature of water. It allows water to rather easily respond to changing conditions, such as the presence of differing solutes. It seems that the large c^*, combined with the balanced number of hydrogen bond donating and accepting sites, is the major property that renders water unique as liquid that combines thermodynamic rigidity with high dynamic flexibility. Also the fact that the nearly tetrahedral charge distribution of the water molecule is associated with a permanent electric dipole moment contributes to the uniqueness of the liquid. It gives water the ability to discriminate between polar and non-polar substances and thus to provoke structure formation in solutions, such as the development of cell membranes in biology.

2.1.3 Hydrogen ions, pH value, and proton motion

Another important property of water, especially with a view to its outstanding role in the biosphere, is its auto-ionization or auto-protolysis reaction. Resorting first to a simplified picture by considering only a pair of H_2O molecules and thus neglecting their integration in the three-dimensional hydrogen network, protolysis

$$2\ H_2O \leftrightarrow OH^- + H_3O^+ \tag{7}$$

of water is sketched in Figure 9. It illustrates the basic idea that a proton

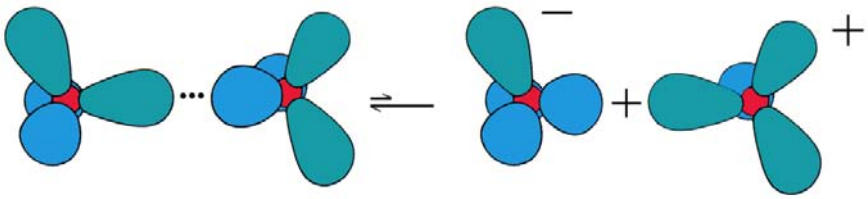

Figure 9. Visualization of the auto-ionization equilibrium of water.

separated from a water molecule approches a neighboring water molecule by changing the type of bond: the proton shifts along the hydrogen bond to form a covalent bond with the new molecule. Due to such shift a hydronium ion, H_3O^+, is established and a hydroxyl ion, OH^-, is left.

Using the common nomenclature and denoting concentrations of a species by square brackets, thus setting $c(X) = [X]$, the equilibrium constant for the auto-ionization reaction is defined by

$$K_{eq} = [H_3O^+][OH^-]/[H_2O]^2. \tag{8}$$

It is normally replaced by the so-called ion product, also named self-ionization constant

$$K_w = [H_3O^+][OH^-]/(\mathrm{mol/l})^2, \tag{9}$$

thereby taking into account that the concentration of the ionic species is small and that $[H_2O]$ thus closely equals the total water concentration (= 55.5 mol/l at room temperature). K_w decreases with temperature T, its

value is 10^{-14} at 25 °C. Since the hydronium concentration is on par with that of the hydroxyl ions, this means that

$$[H_3O^+] = [OH^-] = 10^{-7}. \quad (10)$$

For simplicity, the negative logarithm to base 10 of the H_3O^+ concentration is used and named pH value of the liquid. Hence the pH of an aqueous system is defined as

$$pH = -\log([H_3O^+]). \quad (11)$$

Due to its ampholytic nature water can accept protons from another proton donator (an acid) but can likewise donate protons to another proton acceptor (a base). In any case, in order to keep the ion product (Eq. 9) constant, the OH-concentration must fall if the H_3O^+ concentration rises and *vice versa*.

Because of the extensive hydrogen bond network of water, however, the existence of localized hydronium ions is certainly a strong simplification. Rather the separated proton may be described as a delocalized charge defect shared by multiple molecules [117]. This is an important aspect for the diffusion of protons in water. Despite of their low concentration in liquid water, protons participate in a wide range of phenomena, including biological processes, such as energy transduction in living cells and enzymatic catalysis. Protons distinguish from any other ion by their exceedingly high mobility which is at least 4.5 times larger than that of "normal" cations [118]. This extraordinary mobility corresponds with a diffusion constant ($9.3 \cdot 10^{-9}$ m^2s^{-1} [119]) even four times larger than the self-diffusion constant of water ($2.3 \cdot 10^{-9}$ m^2s^{-1}, 25°C [120]).

Obviously, the uniquely fast proton transfer in water cannot solely be explained by hydrodynamic diffusion of protonated water molecules or clusters. Instead, a combination seemingly exists of diffusion associated with mass transport and a mechanism by which the proton is transmitted from one molecule to another one without noticeable translation of oxygen atoms, i.e. without extensive rearrangement of the center of molecular masses [118, 121, 122]. It is widely accepted that this mechanism shuttles protons between neighboring water molecules similar to the chain conception suggested by Grotthuss more than two centuries ago [122-124]. Nevertheless, the molecular mechanisms behind the shuttling process are not fully conceived and are still today a matter of significant scientific debate.

Whatever the detailed mechanism of proton transfer in water may be, a suitable local structure is required for what is summarized as "Grotthuss

shuttling". Two special protonated complexes have been the focus of much interest: the more stable hydrated protonated water structure $H_9O_4^+$ (= $H_3O^+ \cdot 3H_2O$) proposed by Eigen ("E" [125, 126]) and the Zundel cation $H_5O_2^+$ (= $H_2O \cdot H^+ \cdot OH_2$), in which the proton is located between the oxygens of a water dimer ("Z" [127, 128]). The essential step in the proton transfer is considered an Eigen – Zundel – Eigen (EZE) complex conversion [117-119, 129, 130] in which the EZE partner exchange occurs within just 50 fs. This short period is contrasted with the period of several picoseconds required for the overall proton transport process [117]. The comparatively long characteristic time of the proton transport as well as calculated distant-dependent diffusion constants suggest the proton motions to be coupled to a coordinated rearrangement of the surrounding H-bond network [117, 118, 131, 132]. Obviously, E and Z structures are just limiting and intermediate conformers, respectively, in highly cooperative cluster phenomena, occurring on multiple time and distance scales [117-119, 133]. Water clusters containing some twenty molecules seem to be involved in the proton hopping dynamics [134]. Simulations reveal the proton charge defect to rapidly resonate between three distorted Eigen-type structures [117, 118]. During this process the closest (water oxygen) ligand permanently changes its identity within the first solvation shell. Such activity, suggestively named "special-pair dance", emerges at the location of a suitable configuration for the proton hop. Final proton hopping occurs when the neighboring hydrogen bond network rearranged in a structure favorable for the transfer act. A sketch illustrating the fundamental idea of the special-pair dance is given in Figure 10.

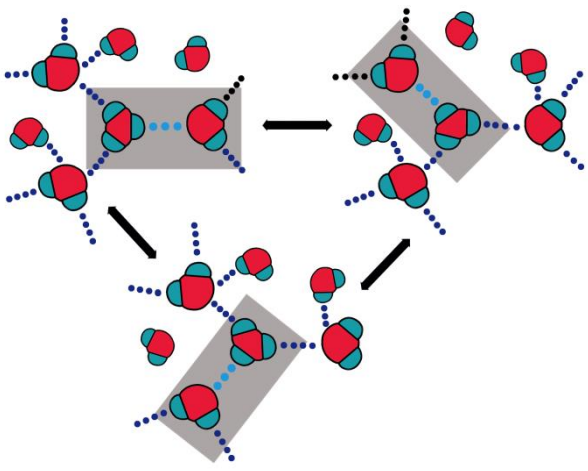

Figure 10. Illustration of the idea of Markovitch et al. [118] to account for the high proton mobility in water by a "special-pair dance" around a protonated water molecule. Water molecules are sketched without the electron lone pair orbitals showing again the oxygen atom by red and the hydrogen atoms by turquoise.

Since proton hopping requires an appropriate local structure, it has been concluded that the mobility of protons should decrease as the structure of the liquid changes [122]. In aqueous HCl solutions, for example, the mobility of the proton at high acid concentration is similar to the chloride ion [135]. Proton transport is then predominantly provided by hydrodynamic diffusion of protonated water molecules [121, 122]. This feature corresponds with the finding that the static permittivity of concentrated HCl solution is reasonably consistent with the results for "normal" cations, as will be discussed below (chapter 4.3).

2.2 Electric field interactions with a dipolar liquid

An implication of the permanent electric dipole moment $\vec{\mu}$ of the water molecule is its usability as natural mark for the investigation of the molecular structure and motions of aqueous systems without any needs for artificial labels. Utilizing this molecular mark just the dipole orientation relative to a given direction is observed, as depicted in Figure 11. The absolute value $\mu = |\vec{\mu}|$ is between 1.83 [83] and 1.87 D [136], with $1D = 1/3 \cdot 10^{-29}$ As denoting the commonly used unit of molecular dipole moments.

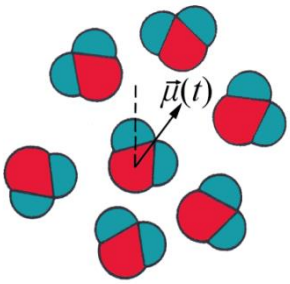

Figure 11. Ensemble of water molecules. For the central molecule the dipole moment $\vec{\mu}(t)$ is shown with its orientation at time t relative to a given direction (dashed line).

2.2.1 Polarization noise: structure and molecular interactions

Consider a dipolar liquid to be contained in a plate capacitor serving as the sample cell (Fig. 12). The spacing of the plate may be small as compared to the lateral plate dimensions. If no electrical field $\vec{E}$ is applied ($E = 0$), the sample is kept in complete thermal equilibrium so that the mean (electric) polarization $\langle \vec{P} \rangle$ vanishes. Angle brackets denote ensemble averages. Thermal fluctuations, however, lead to spontaneous thermal variations $\vec{P}(t)$ in the polarization of the liquid. The varying polarization component perpendicular to the capacitor plates induces electrical charges which tend

to compensate and thus produce a fluctuating current $I(t)$. If the external circuit is provided with a suitable integrator and signal indicator system and if the impedance Z_e of the circuit is negligibly small, the fluctuating charges $Q = \int I(t)\,\mathrm{d}t$ of the capacity plates can be determined. Since these charges are proportional to the polarization perpendicular to the plates and thus, for anisotropic liquids, proportional to the overall polarization $P(t)$. A potential polarization noise signal is displayed in the lower part of Figure 12.

The polarization noise contains different information on the dipolar liquid. The strength of the noise, expressed as the root mean square time average

$$\langle P^2(t)\rangle^{1/2}\,, \tag{12}$$

is related to the number density of dipolar molecules and the amount of their (effective) dipole moment. It thus reflects the structure of the liquid. The autocorrelation function

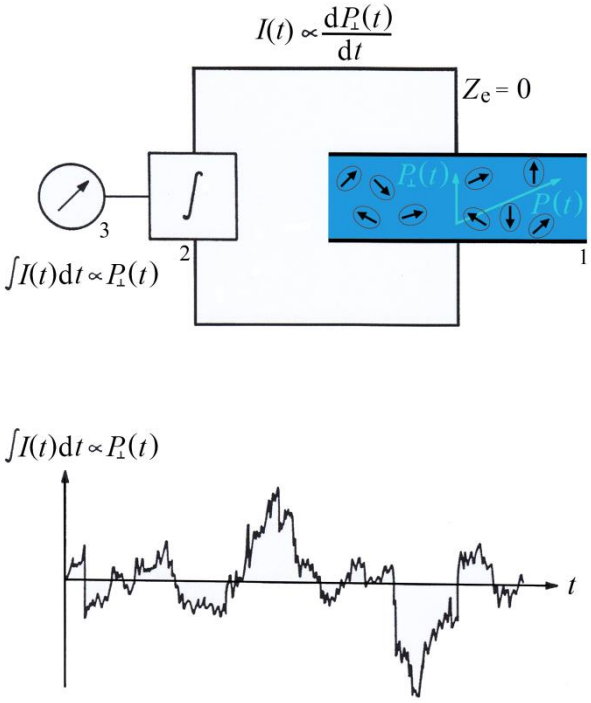

Figure 12. Simplified diagram for the measurement of polarization noise of a liquid in thermal equilibrium (top) and noise signal (bottom). 1, capacitance containing the liquid; 2, integrator; 3, signal indicator.

$$\Psi(t) = \langle \vec{P}(t) \cdot \vec{P}(0) \rangle / \langle P^2(0) \rangle \,, \tag{13}$$

in this normalized format also named "dielectric decay function", yields information about correlations of elementary processes within the sample. Hence it allows for conclusions about molecular interactions, such as hydrogen bonds. In case of uncorrelated white noise, for instance, $\Psi(t) = 0$ follows, whereas, due to the finite lifetime of hydrogen bonds, water is characterized by a non-vanishing auto-correlation function. Actually, as sketched in Figure 13, the autocorrelation function of water at room temperature reveals two different regimes. It starts with a fast changing part at $t < 1$ ps reflecting distortion polarization processes due to the distortion of electron shells and the motions of atomic nuclei relative to one another but containing also contributions from relaxation processes with very short relaxation times. This part is only simplifiedly shown in Figure 13 and needs to be more closely considered in the following chapters. It is followed by an almost perfect exponential decay

$$\Psi(t > t^*) = \Psi(t^*) \exp(-[t-t^*]/\tau_w), \tag{14}$$

with a relaxation time $\tau_w = 8.27$ ps at 25 °C [137] which is considered a characteristic parameter of the hydrogen network dynamics.

$\Psi(t)$ is the autocorrelation function of the experimentally accessible macroscopic polarization. Frequently the interest is, however, the (normalized) auto-correlation function

$$\psi(t) = \langle \vec{\mu}(t) \cdot \vec{\mu}(0) \rangle / \langle \mu^2(0) \rangle \tag{15}$$

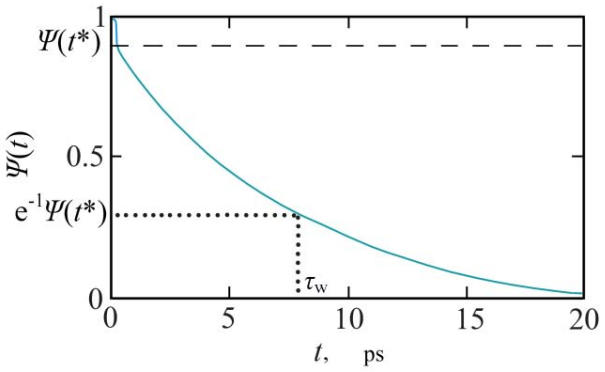

Figure 13. Autocorrelation function $\Psi(t)$ of polarization (Eq. 13) for water at 25 °C.

of the molecular dipole moment $\vec{\mu}$. The relation between the desired ψ(t) and the correlation function $\Psi(t)$ from measurement is a central issue in the theory of dielectrics and a clear finding is available only on favorable conditions [138]. The complexity in the relation between $\psi(t)$ and $\Psi(t)$ are already obvious for liquids with exponential autocorrelation function and identical dipole moments $\vec{\mu}$ of all molecules. The macroscopic polarization of such a liquid

$$P(t) = \frac{1}{V} \sum_{n=1}^{N} \vec{\mu}_n\,(t) \tag{16}$$

is defined by the sum of all N dipole moments $\vec{\mu}_n = \vec{\mu}$, $n = 1,\ldots N$, per volume V. Hence in its nominator autocorrelation function $\Psi(t)$ contains the product

$$\langle P(t) \cdot P(0)\rangle = \langle \frac{1}{V} \sum_{n=1}^{N} \vec{\mu}_n\,(t) \cdot \frac{1}{V} \sum_{n=1}^{N} \vec{\mu}_n\,(0)\rangle \tag{17}$$

which may be written as

$$\langle P(t) \cdot P(0)\rangle = \frac{N}{V^2}\langle \vec{\mu}_n(t) \cdot \vec{\mu}_n(0)\rangle + \frac{N}{V^2}\langle \vec{\mu}_n(t) \cdot \sum_{m\neq n}^{N} \vec{\mu}_m(0)\rangle. \tag{18}$$

The first term on the right hand side corresponds indeed with $\psi(t)$. The second term, however, contains the products of the dipole moments of all unlike molecules and thus reflects the cross correlation function $\gamma(t)$ of the molecular dipole moments. For this reason $\gamma(t)$ is required for the evaluation of the experimental $\Psi(t)$ in terms of $\psi(t)$.

At distinctive short range order, i.e. if at short times $\gamma(t)$ decays significantly slower than $\psi(t)$, the relaxation times of the macroscopic polarization and the molecular dipole moment autocorrelation functions, τ_Ψ and τ_ψ, respectively, are related to one another [138, 139] by the (equilibrium) dipole orientation correlation factor g [140]

$$\tau_\Psi = g\tau_\psi. \tag{19}$$

The g-factor of associating liquids is again a parameter of considerable scientific debate and will be discussed with more details in the low frequency ("static") permittivity section. Interestingly, however, relation (19) has also been derived from a comparison of experimental dielectric relaxation time of pure liquids with single particle correlation times from nuclear magnetic relaxation data [141].

2.2.2 Disturbing fields: step and impulse responses

The above sketched experiment (Fig. 12) at complete thermal equilibrium doubtlessly constitutes a subtle approach to the liquid structure and dynamics. It clearly demonstrates that, in principle, no external electric field is required to produce dielectric polarization. Unfortunately, the polarization noise of liquids is too small to be separable from the inherent noise of the measuring system itself.

For the above reason, in practice, a small electric field is applied to the sample liquid, as illustrated by Figure 14. The strength of the electric field is kept small, so that the electrical energy supplied to the liquid is negligibly small as compared to thermal energy. The benefit of the external field results from its simultaneous coordinated effect on all molecular dipoles. So the response of the field can be filtered and distinguished from the random thermal fluctuations of the measurement system in order to increase the signal-to-noise ratio. In Figure 15 an electrical field step is applied. If the step is sufficiently steep, the step response of the liquid polarization follows the autocorrelation function $\Psi(t)$ of the polarization noise (Figs. 13, 15).

Basically, every convenient signal can be used to disturb the sample if it behaves linear and invariant with respect to time shift. This general statement follows from the fact that, on the one hand, any signal may be considered a series of impulses and, on the other hand, an impulse may be taken a sum of two step functions as delineated in Figure 16. Consider the field steps

$$E_1\,(t < t' + \mathrm{d}t') = E > 0; \quad E_1\,(t > t' + \mathrm{d}t') = 0 \tag{20}$$

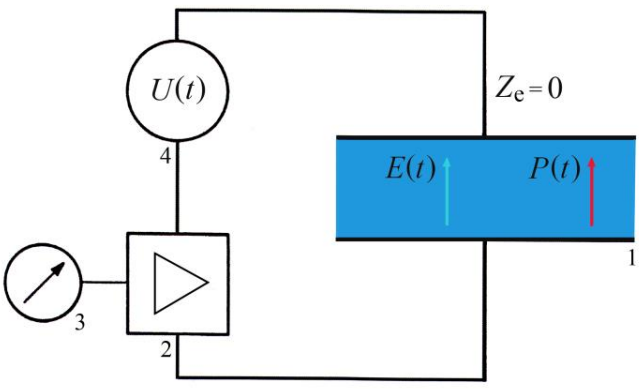

Figure 14. Principle of system to measure the liquid polarization $P(t)$ as response to an external electric field of small field strength $E(t)$. 1, capacitance containing the liquid; 2, amplifier or receiving unit; 3, signal indicator; 4, signal generator.

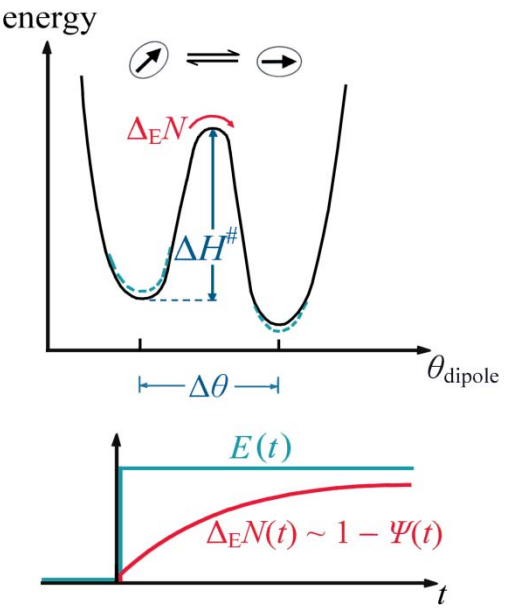

Figure 15. Reaction scheme showing the separation of two dipole moment orientations by a potential energy barrier (top). The orientation difference is denoted by $\Delta\theta$, the activation enthalpy by $\Delta H^{\#}$. Dashed turquoise lines indicate to a disproportionate extend the deformation of the potential minima by an external electric field of strength $E(t)$, as depicted in the lower part of the figure. The development with time of the responding population of the potential minima and thus polarization of the sample liquid is indicated by the red line in the diagram.

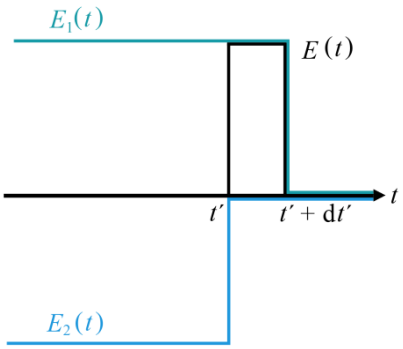

Figure 16. Superposition of two opposing field steps $E_1(t)$ and $E_2(t)$, respectively, with time delay dt'.

and

$$E_2\,(t < t') = -E < 0; \quad E_2\,(t > t') = 0. \tag{21}$$

Linear superposition $E(t) = E_1(t) + E_2(t)$ yields

$$E(t < t') = E(t > t' + dt') = 0; \quad E(t' < t < t' + dt') = E(t') = E \tag{22}$$

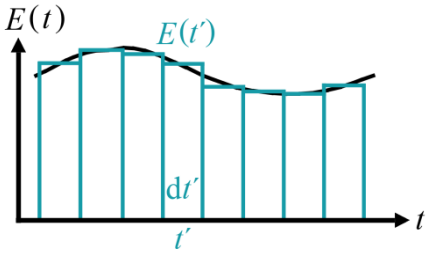

Figure 17. Representation of a signal, shown by a black line, by a complete series of small impulses, pictured in turquoise.

for the field and, if dt' is small,

$$P(t < t') = 0; \quad P(t > t' + \mathrm{d}t') = -[\varepsilon(0) - 1]\varepsilon_0 E(t')\dot{\psi}(t - t')\mathrm{d}t' \tag{23}$$

for the responding polarization. Here $\varepsilon(0)$ denotes the relative „static" permittivity of the liquid, $\varepsilon_0 = 8.8542 \cdot 10^{-12}$ AsV^{-1}m^{-1} the permittivity of free space, and function

$$\dot{\psi}(t) = \mathrm{d}\Psi(t)/\mathrm{d}t \tag{24}$$

is the "impulse response".

In the linear regime, any electrical signal may be represented by a complete series of impulses (Fig. 17). Hence the resulting polarization

$$P(t) = -[\varepsilon(0) - 1]\varepsilon_0 \int_{-\infty}^{t} E(t')\dot{\psi}(t - t')\mathrm{d}t' \tag{25}$$

of a (linear, time-invariant, and causal) system follows as a superposition of the impulse responses. Substituting $t - t' = t''$, this relation may be rewritten to finally read

$$P(t) = -[\varepsilon(0) - 1]\varepsilon_0 \int_{0}^{\infty} E(t - t'')\dot{\psi}(t'')\mathrm{d}t''. \tag{26}$$

2.2.3 Harmonically varying fields: complex permittivity spectrum

Albeit, in principle, any low-amplitude electric field may be applied to measure the responding polarization and to determine the dielectric properties of the sample thereby, only step impulses and harmonically varying (sinusoidal) signals

$$E(t) = \hat{E}\exp(\mathrm{i}\omega t) \tag{27}$$

are normally used. In this equation, $\hat{E}$ is the electric field amplitude, i is the imaginary unit ($i^2 = -1$), $\omega = 2\pi\nu$ is the angular frequency, and ν the (natural) frequency.

Within the framework of the potential energy barrier conception (Fig. 18a) the depths of the energy minima vary periodically when exposed to a sinusoidal field, as indicated by the dashed blue and turquoise lines in the diagram. Since the energy barrier prevents the dipole moments from following the electrical field changes instantaneously, a time lag depending on frequency ν occurs between the polarization of the liquid and the electric field (Fig. 18b). Such time lag involves a phase difference between the responding polarization and the exciting field and thus implies that energy is extracted from the electric field and dissipated as heat. Hence with increasing distance d from a signal source, the amplitude of a plane

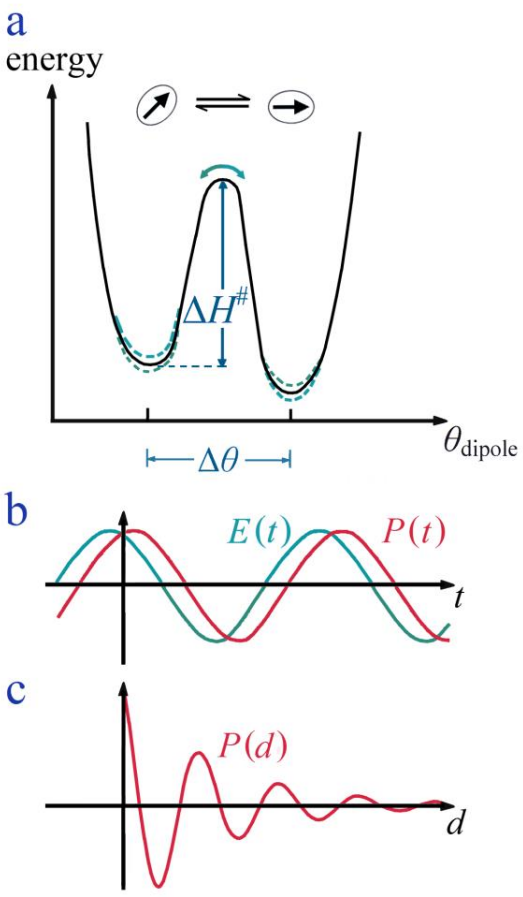

Figure 18. Reaction scheme for dipole reorientation at alternating electric field (a). The variation of the potential energy minima at opposing field directions is indicated by blue and turquoise dashed lines. The time lag between harmonically varying electric field and responding polarization is depicted in part b of the figure. Part c illustrates the decay of the amplitudes of a plane polarization wave (sect. 3.1.1) at increasing distance d from a sinusoidal signal source.

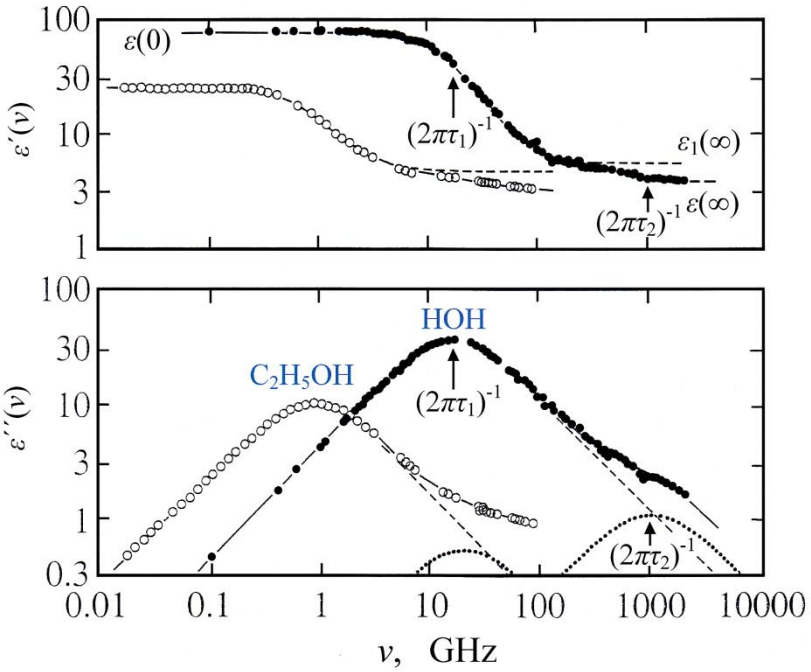

Figure 19. Log-log plot of the complex permittivity spectra [142] for water at 19 °C (● [137, 143-146] and ethanol at 20 °C (○ [147]). The spectrum for water includes data measured at 20 °C and corrected for the small temperature difference [142]. Low-frequency dispersion and absorption terms are indicated by dashed lines. Dotted lines are graphs of the high-frequency absorption terms. For the water spectrum the relaxation frequencies $(2\pi\tau_j)^{-1}$, with τ_j denoting the corresponding relaxation times and j = 1, 2, are shown and also the high-frequency permittivities $\varepsilon_1(\infty)$ and $\varepsilon(\infty)$ as extrapolated from the low and high-frequency dispersions, respectively.

polarization wave set up in the liquid decreases as illustrated in part c of Figure 18.

In addition to the phase lag, the potential energy barrier prevents the polarization from completely following the rapid field changes at high frequencies: dispersion occurs. Both the dispersion in the polarization and the absorption of field energy is taken into account by defining the (dielectric) permittivity, which relates the polarization to the electrical field strength, as a frequency-dependent complex quantity:

$$\varepsilon(\nu) = \varepsilon'(\nu) - \mathrm{i}\varepsilon''(\nu) = P(\nu)/[\varepsilon_0 E(\nu)] + 1. \quad (28)$$

The real part $\varepsilon'(\nu)$ considers the polarization component that is in phase with the electrical capacitor field. It is the part which may be subject to dispersion. The imaginary part takes account of the phase difference by $\pi/2$ and thus reflects the absorption of field energy. Within the frequency range between 10 MHz and 2 THz the complex permittivity spectra for water and ethanol at room temperature are displayed in Figure 19. Both spectra reveal two clear dispersion ($\mathrm{d}\varepsilon'/\mathrm{d}\nu < 0$) and corresponding dielectric loss ($\varepsilon'' > 0$) regions within the frequency range of measurements, indicating relaxation behavior. Interestingly, the spectra resemble each other. Just the static permittivity $\varepsilon(0)$ as well as the relaxation frequencies $(2\pi\tau_1)^{-1}$ and $(2\pi\tau_2)^{-1}$ are larger with water than with ethanol. We shall revisit the water spectrum later when discussing the dielectric properties of aqueous systems with details.

Using Eq. (25) the complex permittivity can be written as Laplace transform

$$\varepsilon(\nu) = [\varepsilon(0) - 1]\int_0^\infty \left[-\dot{\psi}(t)\right]\exp(-\mathrm{i}\omega t)\mathrm{d}t \quad (29)$$

of the impulse response function. Since both, the real part $\varepsilon'(\nu)$ and the negative imaginary part $\varepsilon''(\nu)$ of the permittivity, can be derived from one real function, they cannot be independent from one another. Both parts of the complex permittivity contain basically the same information. Measuring both quantities, however, increases the number of data and thus reduces the overall uncertainty in the spectra.

2.2.4 Charged species: electrical conductivity

Due to the strong interactions of the molecular dipole moments with Coulombic fields water is an excellent solvent for electrically charged species. Shift of these species in an electrical field leads to the magnitude

$$J = \sigma E \quad (30)$$

of electric current density, where σ denotes the specific electric conductivity of the liquid under consideration. Interactions of the ionic particles with the solvent involve internal friction and convert electrical energy into heat. In complex permittivity measurements ion conductivity thus contributes to the imaginary part of the permittivity, resulting in a total

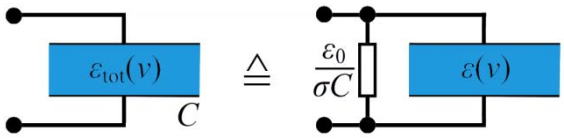

Figure 20. Equivalent circuit representation of a sample with complex permittivity ε and electric conductivity σ in a capacitor C.

dielectric spectrum

$$\varepsilon_{tot}(\nu) = \varepsilon'(\nu) - i[\varepsilon''(\nu) + \sigma/(\varepsilon_0\omega)]. \quad (31)$$

The lumped element representation in Figure 20 evidences the dominating ionic conductivity contributions at low frequencies, where the admittance of the circuit

$$Y(\nu) = \sigma C/\varepsilon_0 + i\omega\varepsilon(\nu)C = [\sigma/\varepsilon_0 + \omega\varepsilon''(\nu)]C + i\omega\varepsilon'(\nu) \quad (32)$$

is primarily given by the σ-term. This feature is relevant to experimental methods to quantify the dielectric properties of electrically conducting samples. Specific measures to improve the accuracy of $\varepsilon(\nu)$ determination

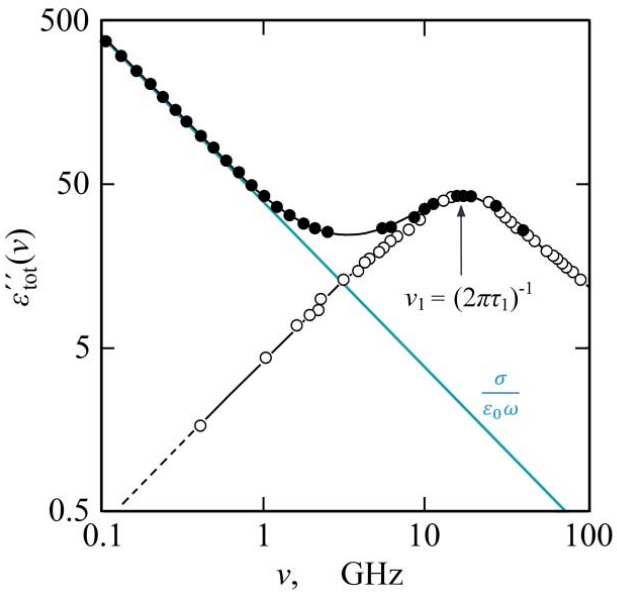

Figure 21. Log-log plot of the (negative) imaginary part of the dielectric spectrum of a solution of NaCl in water at 20 °C (●, [148]). The mass fraction $Y = m_{NaCl}/(m_{NaCl} + m_{water})$ is 0.013, corresponding with a concentration c = 0.224 mol/l of salt. The specific electric conductivity of the solution is σ = 2.04 S/m. Shown for comparison are also data for water at the same temperature (○). The turquoise line indicates the conductivity contribution $\sigma/(\varepsilon_0\omega)$.

for such samples will be presented in chapter 3. Generally, however, it is worth to recall the frequency dependencies of the different terms in Eq. (32), favoring high-frequency permittivity measurements of samples with significant electrical conductivity. This aspect is also illustrated by the total negative imaginary part $\varepsilon''(\nu) + \sigma/(\varepsilon_0\omega)$ of the dielectric spectrum of a saline solution in which even at 100 MHz the conductivity contribution $\sigma/(\varepsilon_0\omega)$ exceeds the dielectric contribution $\varepsilon''(\nu)$ by a factor of about 10^3 (Fig. 21).

3 Dielectric Measurement Methods: Some Basics

3.1 Frequency domain techniques

Methods to measure the dielectric properties of materials [149, 150] are actually available for the enormous frequency range from about 10^{-6} Hz [151-154] to 10^{13} Hz [155-162]. In basic research such a broad applicable dielectric spectrum offers an attractive gateway to a deeper understanding of materials in terms of their molecular properties [163-168]. As mentioned before, both sinusoidal signals and step pulses are commonly applied to excite the samples and the related measurement methods are generally distinguished by terms "frequency domain" and "time-domain" techniques, respectively.

For materials moisture determination different bands of the basically available frequency range are not suitable in equal measure. As obvious from the frequency dependence of ionic conductivity contributions discussed in section 2.2.4, for instance, unavoidable conductivity σ of water-containing materials opposes strict limitations to complex permittivity measurements at very low frequencies. An illustrative example may be highly purified water with σ as small as $5.5 \cdot 10^{-6}$ S/m for which the huge contribution $\sigma/(\varepsilon_0\omega) = 10^{11}$ to the (negative) imaginary part of the complex permittivity (Eq. 31) follows at 10^{-6} Hz. Obviously, resistor $(\varepsilon_0/\sigma)C$ in the equivalent representation of Figure 20 effectively short-cuts the capacitor in the low-frequency regime and thus prevents reliable permittivity measurement of the sample. Similarly, little use has been made so far from measurements in the far-infrared (FIR) or THz region. For these reasons, we shall first focus on the frequency range roughly between 30 MHz and 300 GHz, bridging the low-frequency and the THz-frequency regions.

3.1.1 Microwave measurements

3.1.1.1 Electromagnetic wave propagation

Even though the frequency range considered in this section includes the very-high-frequency (VHF) band, it will be subsumed under the notion "microwave regime" in the following. It is this regime which comprises the predominating dispersion/absorption region of the complex permittivity spectrum of water (Fig. 22). In order to distinguish it from the dispersion/absorption region at around 1 THz its relaxation time had been

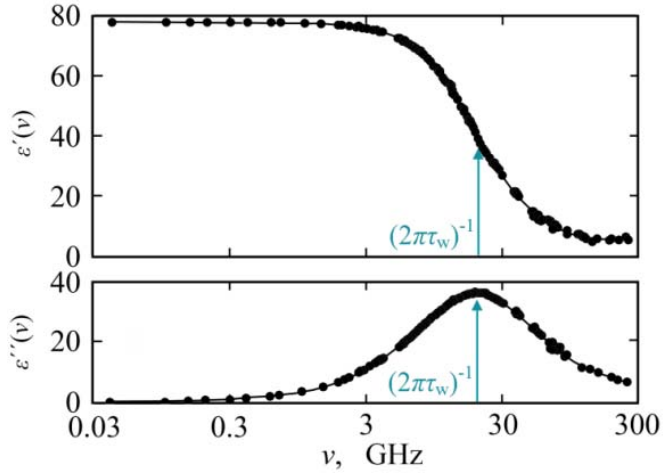

Figure 22. Real part $\varepsilon'(\nu)$ and negative imaginary part $\varepsilon''(\nu)$ of the complex permittivity spectrum of water at 25 °C [137, 169, 170], displayed in the commonly used lin-log format.

named τ_1 in Figure 19. Here we shall refer to τ_w as the principal relaxation time of pure water.

Due to Maxwell's equations time-variable electric fields are accompanied by likewise time-variable magnetic fields. Propagation of the field variations effects coupled transport of electric and magnetic energy in dielectrics via electromagnetic waves. Electric conductors are not required. For non-conducting dielectrics the simple wave equation

$$\frac{\partial^2 E_y}{\partial x^2} = -\mu_0 \mu \varepsilon_0 \varepsilon \omega^2 E_y = -\mu \varepsilon \frac{\omega^2}{c_0^2} E_y. \tag{33}$$

follows if a mono-frequent, plane, and linearly polarized electric field is assumed. In this equation, μ_0 is the magnetic field constant, μ the magnetic permeability, and $c_0 = (\varepsilon_0 \mu_0)^{-1/2}$ the speed of light in free space. In correspondence to the permittivity, the magnetic permeability may be frequency dependent and complex. In the following, however, we shall always presume non-magnetic materials, so that $\mu = 1$ throughout. In deriving Eq. (33) it has been tacitly assumed that the electrical field is restricted to the y direction ($E_z = E_x = 0$) and that the wave propagates in x direction.

Materials are never completely free of dielectric losses. Often, however, the loss factor

$$\tan \delta = \varepsilon''/\varepsilon' \tag{34}$$

is negligibly small, for instance $\tan \delta = 2.1 \cdot 10^{-3}$ for PTFE at 8.5 GHz and room temperature [171], $\tan \delta = 2.4 \cdot 10^{-4}$ for high-density poly(ethylene)

[172], and tan $\delta = 7 \cdot 10^{-5}$ for polyethylene foam at 8.5 GHz and 25 °C [173]. Under these conditions it is justified to consider the electromagnetic field propagating in a loss-free medium ($\varepsilon'' = 0$) and to comply with differential equation (33) simply by a sinusoidal wave, the electrical field strength of which may be written as

$$E_y = \hat{E}_y \exp(\mathrm{i}\omega t - \beta x), \tag{35}$$

where

$$\beta = \frac{2\pi}{\lambda} = \frac{\omega}{c} = \frac{\omega}{c_0}\sqrt{\varepsilon'} \tag{36}$$

denotes the phase constant. Parameters λ and c are the wavelength and phase velocity, respectively, of the wave within the material if, as presumed, $\mu = 1$. The reduced phase velocity c ($< c_0$) within matter follows according to the Huygens principle from the fact that, within the electromagnetic field of a wave, atoms are stimulated to oscillate and thus to emit radiation. Such radiation is subject to a phase shift which adds to the phase shift due to propagation with phase velocity c_0 in free space [174].

Dielectric losses, as, for instance, revealed by the complex permittivity spectrum $\varepsilon(\nu) = \varepsilon'(\nu) - \mathrm{i}\varepsilon''(\nu)$ of water (Fig. 22), lead to a complex propagation constant

$$\gamma = \alpha + \mathrm{i}\beta \tag{37}$$

and thus to the electrical field strength

$$E_y = \hat{E}_y \exp[\mathrm{i}(\omega t - \gamma x)]. \tag{38}$$

As a consequence of the complex nature of the propagation constant, the amplitude

$$\left|E_y(x)\right| = \left|E_y(0)\right| \exp(-\alpha x) \tag{39}$$

of the wave decreases exponentially along the direction x of propagation, as illustrated by Figure 23. Adequate probing of the exponentially decaying wave within the sample offers a direct approach to measure both the wavelength λ and attenuation coefficient α and to thus accurately determine the propagation constant γ, from which in turn the complex permittivity of the sample can be simply derived as

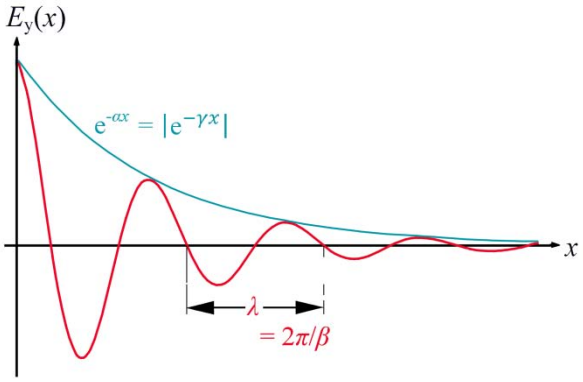

Figure 23. Sketch of a plane wave, propagating with exponentially decaying amplitude in x-direction.

$$\varepsilon(\nu) = \left(\frac{\beta}{\beta_0}\right)^2 - \left(\frac{\alpha}{\beta_0}\right)^2 - 2\mathrm{i}\frac{\beta}{\beta_0}\frac{\alpha}{\beta_0}\,. \tag{40}$$

In this equation, $\beta_0 = 2\pi/\lambda_0$, with $\lambda_0 = c_0/\nu$ denoting the wavelength in free space. Hence

$$\varepsilon'(\nu) = [\lambda_0/\lambda]^2 - [\alpha\lambda_0/(2\pi)]^2 = [c_0/(\nu\lambda)]^2 - [\alpha c_0/(2\pi\nu)]^2 \tag{41}$$

and

$$\varepsilon''(\nu) = \alpha\lambda_0^2/(\pi\lambda) = c_0^2\alpha/(\nu^2\lambda\pi). \tag{42}$$

In deriving the above relations it has been tacitly assumed that wave propagation is not affected by lateral boundaries.

In many applications, probing of waves that are propagated through the material under consideration is less appropriate if not impossible at all. For that reason, access to the dielectric properties is often obtained from waves reflected by the sample. A simple configuration is sketched in Figure 24, where a plane wave propagating in x-direction is subjected to a discontinuity at $x = 0$. This discontinuity is considered to derive from the presence of material with complex permittivity $\varepsilon(\nu)$ at $x > 0$, whereas free space conditions ($\varepsilon(\nu) = 1$) are supposed to exist at $x < 0$. If the material extends over the complete half-space ($x > 0$), any effects from boundaries, except the discontinuity at $x = 0$, can again be neglected. The change in the permittivity at the material surface causes a step in the characteristic wave impedance, which decreases from the value

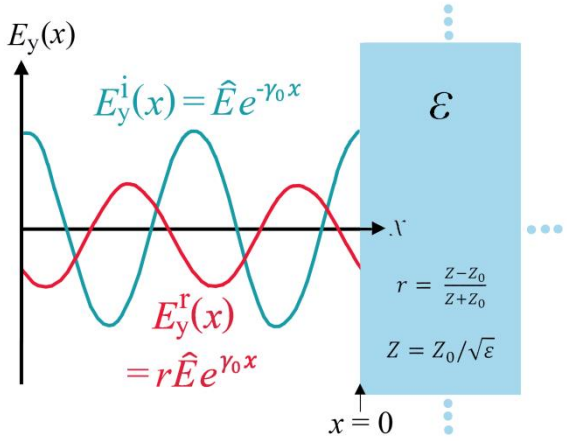

Figure 24. Reflection of a plane wave at a step-like change in the characteristic wave impedance at x = 0. A plane interface between the half space with free space conditions ($\varepsilon(\nu)$ = 1) at x < 1 and material with complex permittivity $\varepsilon(\nu) = \varepsilon'(\nu) - i\varepsilon''(\nu)$ at x > 0 is assumed.

$$Z_0 = (\mu_0/\varepsilon_0)^{1/2} \approx 377\ \Omega \tag{43}$$

in free space to

$$Z = (\mu/\varepsilon)^{1/2} Z_0, \tag{44}$$

which is

$$Z = Z_0/\sqrt{\varepsilon} \tag{45}$$

within non-magnetic materials (μ = 1). Because of the impedance step, only part of the incident wave with electrical field strength E_y^i penetrates the material and propagates forward. This part is not shown in Figure 24. Another part is reflected to propagate backwards. Both waves are controlled by the incident wave as well as the transmission and reflection coefficients

$$d_t = \frac{2Z}{Z+Z_0} = \frac{2}{1+\sqrt{\varepsilon}} \tag{46}$$

and

$$r = \frac{Z-Z_0}{Z+Z_0} = \frac{1-\sqrt{\varepsilon}}{1+\sqrt{\varepsilon}}, \tag{47}$$

respectively. The electrical field of the reflected wave is thus given by the relation

$$E_y^r(x) = rE_y^i(-x) = r\hat{E}\exp(\gamma_0 x). \tag{48}$$

As the reflected wave moves in a lossless medium, its amplitude does not decrease with distance from the plane of reflection. Due to the complex reflection coefficient

$$r = |r|e^{-i\varphi}, \tag{49}$$

with momentum $|r| < 1$ and finite phase angle φ, however, $E_y^r(x)$ reveals a reduced amplitude and a phase shift (Fig. 24). Hence measurement of these parameters can be used to noninvasively determine the complex permittivity of the dielectric material. Some measurement techniques utilizing wave reflection will be discussed in the next section.

3.1.1.2 Transmission and reflection measurement: a short survey

Figure 25 provides a summary of some frequently used configurations in which waves transmitted through or reflected from a specimen cell are used to measure the complex permittivity of a sample [150]. The sample may be solid or liquid. In some configurations liquids need to be held by dielectric windows (c, f, g, i), to be confined by a container (b, h), or to be prevented from flowing through the slit of a slotted line by a suitable sealing (e). Liquids allow for an easy variation of the effective sample length s and thus for complex permittivity determination without the need of calibration measurements. The methods sketched in Figure 25 are not applied at equal values. Some of them are used only to meet special requirements. In the following the focus will thus be the principles of measurement but also techniques suitable for computer-controlled measurement routines and for permittivity determinations without calibration, as required for the dielectric characterization of reference materials. As with the other techniques discussed in the dielectric measurement methods chapter, development specially devoted to electromagnetic moisture determination will be presented below in chapter 5.

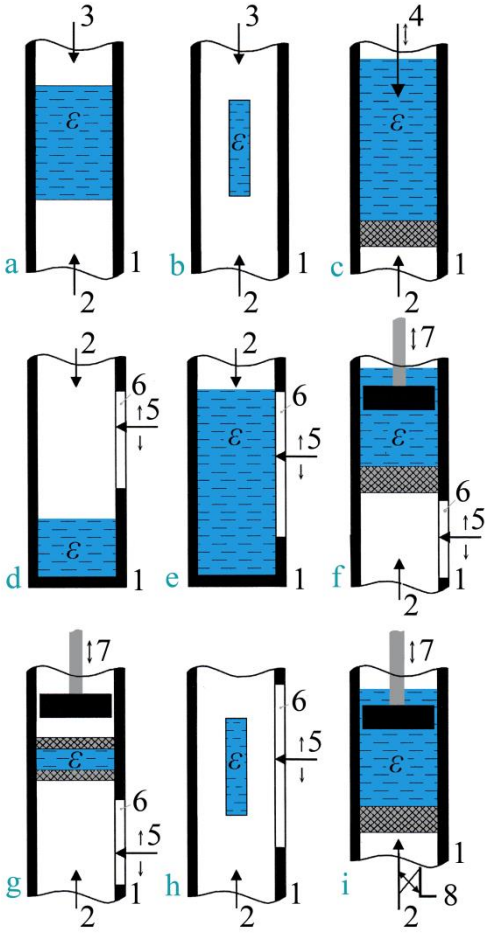

Figure 25. Scheme of configurations for transmission (a-c) or reflection measurement techniques (d-i). The latter may refer to the observation of standing wave patterns (d-h) or reflected waveforms (i). Circular or rectangular waveguide sections are sketched here. Several configurations apply analogously to coaxial lines. a) sample of fixed length completely filling the line section [175, 176]; b) partly filled line section [177, 178]; c) line with movable probe for effective length variation of liquid samples [179-181]; d) standard setting for both liquids and solids [182]; e) completely filled slotted line [183]; f) slotted line combined with length variation of liquid sample [184]; g) equivalent to f) but partly filled with liquid or solid sample [185]; h) partly filled slotted line [186]; i) convenient setting for reflection coefficient determination, with sample length variation for liquids [187-189]. 1, line with ε, sample; 2, feeding line; 3, receiving line; 4, receiving line movable along the direction of wave propagation; 5, movable probe; 6, slotted line; 7, movable shorting plunger; 8, directional coupler.

3.1.1.3 Transmission methods, calibration-free measurement

A prominent example for such techniques of liquid measurement is sketched in part c of Figure 25. A line (4) that is immersed in the liquid can be precisely shifted along the direction of wave propagation and is thus capable of probing the field transmitted through the sample at different cell lengths *s*. Figure 26 shows a simple waveguide (or, alternatively, coaxial line) configuration that has been widely used for measurement of lossy

liquids [190-193]. The variable length transmission cell allows the dielectric properties of liquid samples to be determined without the need for calibrations. Thus, it offers a favorable basis for the measurement of reference liquids.

Reminiscent of radio-frequency bridge circuits the measurement set-up is often called "microwave bridge", but pointing at similarities to optical interferometers, the term "microwave double-beam interferometer" is likewise used. This ambivalent denomination expresses in an obvious manner the intermediate position of the microwave frequency range. In order to demonstrate the principle of operation clearly, Figure 26 displays only the essential components of the bridge. Devices reducing subtle sources of undesired spurious effects and thus increasing the precision of results have been omitted for simplicity.

The variable attenuator (6, Fig. 26) and variable phase shifter (7) of the bridge allow for adjustment of the zero output signal of the bridge at a suitable position s_0 of the probing waveguide or coaxial line (4) of the sample cell (3). Moving the probe and simultaneously re-adjusting the calibrated attenuator (6) yields the zero output signal again at

$$s = s_0 + \lambda \tag{50}$$

if the attenuator setting has been changed by $\alpha\lambda$. Hence the wavelength λ within the liquid as well as the attenuation coefficient α, and thus the

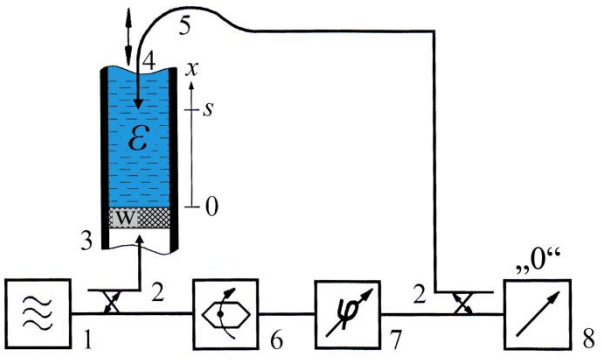

Figure 26. Microwave bridge for complex permittivity measurement of liquids at variable sample length s [190-192]. 1, signal generator; 2, directional coupler; 3, waveguide containing the liquid (ε), with dielectric window (w) and 4, probe movable along the direction x of wave propagation, 5, flexible waveguide or coaxial line; 6, calibrated variable attenuator with constant phase shift; 7, variable phase shifter; 8, zero signal indicator.

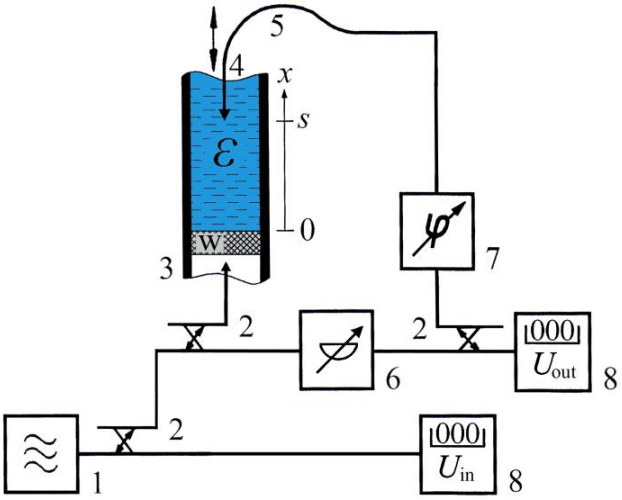

Figure 27. Block diagram of a microwave bridge for complex permittivity measurement of low-to-high-loss liquids [181]. 1, signal generator; 2, directional coupler; 3, waveguide containing the liquid (ε), with dielectric window (w) and 4, probe movable along the direction x of wave propagation; 5, flexible waveguide or coaxial line; 6, variable attenuator; 7, variable phase shifter; 8, level meter.

complex permittivity of the liquid, are just obtained from the readings of the probe positions and the calibrated attenuator. The methods need a sensitive zero signal indicator, however, preferably a superheterodyne receiver, followed by further provisions for noise reduction. Operation of the bridge in this manner also implies attenuation coefficients of the sample sufficiently large to omit any noticeable signals reflected back and forth between the probe at $x = s$ and the dielectric window at $x = 0$.

The set-up can be modified to also apply to low-loss liquids and to enable convenient computer-controlled modes of operation [181]. Figure 27 presents a block diagram which again shows the essential components only. A simple attenuator (6) and a phase shifter (7) are used to just adjust zero output signal U_{out} of the bridge at a suitable position s_0 of the probe (4). Afterwards U_{out} is recorded as a function of sample length s as the probe is shifted along the direction x of wave propagation and the bridge goes out of balance. In order to consider any fluctuations in the signal provided by the generator (1) the input signal U_{in} of the bridge is also recorded. The (scalar) transfer function of the microwave bridge (or double-beam interferometer) is then given by the relation [181]

$$S(x) = U_{out}/U_{in} = \left| |\hat{T}| \frac{\exp(\gamma s)}{1 - \hat{r}\exp(-2\gamma s)} + |T_0| \exp(i\Delta\varphi) \right|, \qquad (51)$$

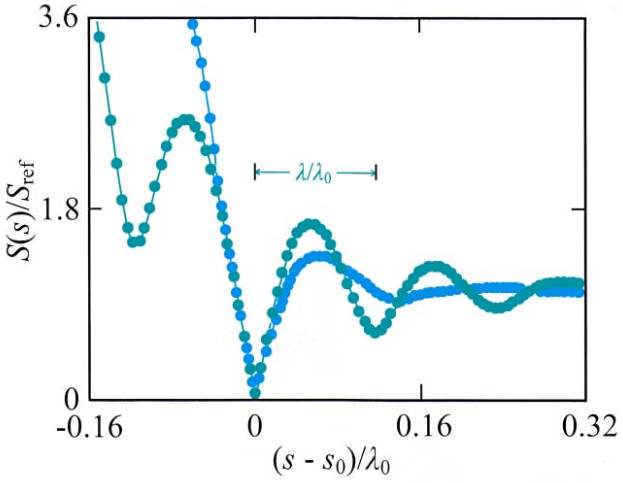

Figure 28. Transfer profiles of a microwave bridge as shown in Figure 27 [181]. Turquoise points refer to data from a cell filled with water at 25 °C and operated at 6.3152 GHz. Blue points show results for an aqueous solution of *n*-heptylammonium chloride at 25 °C and at 17.956 GHz. Lines are graphs of Eq. (51).

where $|\hat{T}|$ and $|T_0|$ denote amplitudes, $\hat{r} = r_{out} \cdot r_{in}$ combines the sample-length-independent reflection coefficients at the liquid-probe and dielectric window-liquid interfaces, respectively, and $\Delta\varphi$ is the phase difference between the measurement and the reference signal. For water at 6.32 GHz ($\tan\delta = 0.30$) and an aqueous solution of a cationic surfactant at 17.96 GHz ($\tan\delta = 0.94$) experimental transfer profiles are displayed in Figure 28 and compared to the graphs of Eq. (51), with parameters as resulted from a nonlinear least-squares regression analysis. Adequacy of the method to low-loss liquid complex permittivity measurement is

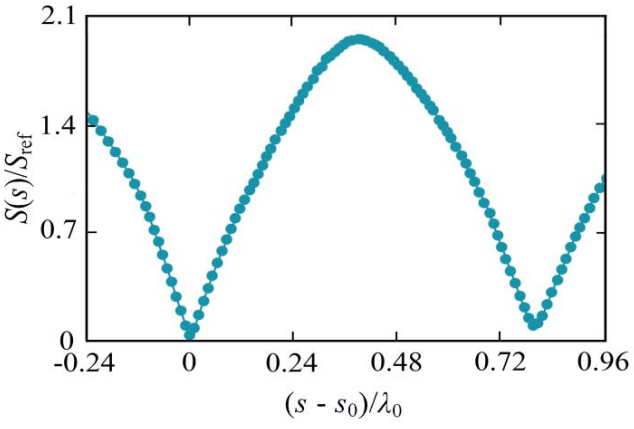

Figure 29. Transfer function as in Figure 28 but for a mixture of *n*-heptanol and *n*-pentane with mole fraction $X_{hept} = 0.1$ of alcohol [181]. The measurement frequency is 7.054 GHz; $T = 25$ °C.

demonstrated by the transfer function of Figure 29 which rather displays a standing wave profile ($\tan\delta = 0.03$).

Waveguide technology offers favorable conditions for complex permittivity measurements at frequencies up to 500 GHz. A drawback of waveguide devices is their limited usable bandwidth which necessitates the application of a series of set-ups in order to reach a reasonable frequency coverage. At frequencies below roughly 50 GHz use of a modern broadband vector network analyzer (VNA) may substantially reduce time and effort. Even if, for optimum operation and reduction of errors from potential higher-order modes, small-band sample cells are applied, a VNA may replace a set of bulky waveguide bridges and facilitate measurement routines considerably.

Figure 30 shows a measuring system that may be used for automated variable-length transmission sample cell measurement to yield transfer function profiles as described before. The VNA provides a measurement signal at his port S (Fig. 30). The signal is splitted to feed part of it back to the reference channel (R). The other part is supplied to the sample cell for the measurement of the signal transmitted through the sample of length *s*. It is then received by the measurement channel (M) of the VNA. Using a stepping motor drive (6, 7) and a digital distance meter (8, 9) the transfer function measurement can be easily controlled by a laboratory computer which also allows $S(x)$ to be directly analyzed in terms of Eq. (51).

Eq. (51) has been derived disregarding any reflections from the upper

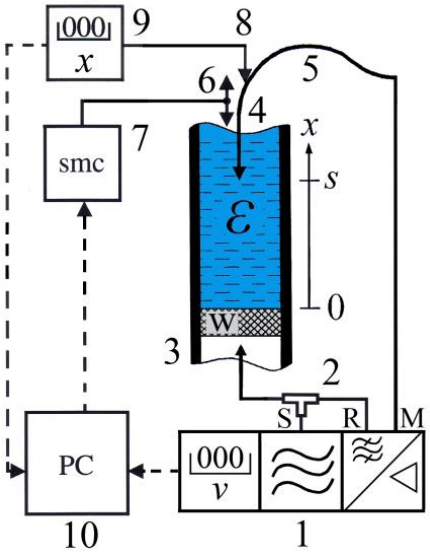

Figure 30. Scheme of sample cell transfer function measurement utilizing a VNA. 1, network analyzer with signal port (S) as well as measurement (M) and reference (R) input channels; 2, power splitter; 3, waveguide containing the liquid (ε) which is held by a dielectric window (w); 4, probe movable along the direction *x* of wave propagation; 5, coaxial line; 6, stepping motor with 7, control unit; 8, digital distance meter with 9, appropriate electronic device; 10, process control computer [149, 194].

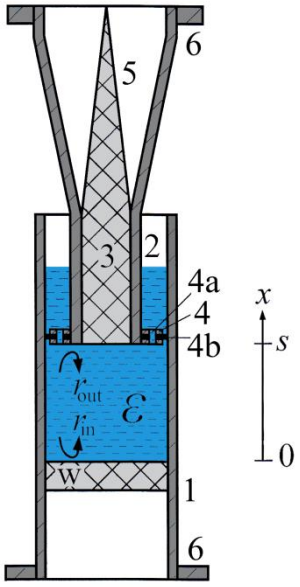

Figure 31. Cross-sectional view of a variable-path-length cell for automated permittivity measurement of liquids with low to high dielectric loss [181]. 1, circular waveguide with dielectric window (w) and sample liquid (ε); 2, circular waveguide moveable along the direction of cell axis and thus along the direction x of wave propagation; 3, solid dielectric filling and sealing the probe (2); 4, contactless reflector ring with thin holes (4a) and ring-shaped insulator (4b); 5, tapered waveguide section; 6, flange.

surface of the sample, i. e. the liquid-air interface. Since the position of that surface varies as the probe is moved, it is difficult to consider such reflections analytically. For that reason, probes preventing the electromagnetic field from reaching the liquid-air interface are preferably used. Construction of a cell from a circular waveguide is shown in Figure 31. The probe, likewise a circular waveguide, is filled with a lossless solid material, the permittivity of which is sufficiently large to enable wave propagation in the complete frequency range covered by the sample waveguide (1). The probing waveguide is provided with a metallic reflector ring (4) that prevents the electromagnetic field from reaching the liquid – air interface. Small holes (4a) in the ring, with diameter far below the cut-off wavelength of the field within the sample, allow flow of the liquid as the probe is moved. The reflector ring is also provided with a ring-shaped insulator (4b), in order to avoid any contact of the probe (2) with the sample waveguide (1). A tapered waveguide section (5) or a waveguide-to-coaxial line adapter establishes the transition between the probing waveguide with reduced diameter and a microwave bridge (Fig. 27).

The transfer function T of the sample waveguide is obtained by summing up the contributions from the waves reflected back and forth at the dielectric window–sample and sample–reflector interfaces with reflection coefficients r_{in} and r_{out}, respectively. As already obvious from Eq. (51),

$$T = \hat{T}\exp(-\gamma s)/[1 - r_{in}r_{out}\exp(-2\gamma s)] \tag{52}$$

follows, with $\hat{T}$ denoting the transfer function of the less interesting sample-length-independent parts of the sample cell. In this context it is important to notice that the propagation constant

$$\gamma = (\beta_c^2 - \varepsilon\beta_0^2)^{1/2} \tag{53}$$

of a wave within a waveguide differs from that in free space by the non-vanishing cutoff constant

$$\beta_c = 2\pi/\lambda_c. \tag{54}$$

In this relation the cutoff wavelength λ_c is the largest wavelength of an electromagnetic field that can be transmitted through the waveguide [174, 195]. For circular waveguides which, due to their easier manufacture, are often used as sample cells,

$$\beta_c = 2j_{11}/d, \tag{55}$$

where $j_{11} = 1.84$ denotes the first root of the first derivative of the Bessel function of first order and first kind and d is the diameter of the waveguide. Hence, instead of Eq. (41), relation

$$\varepsilon'(\nu) = [\lambda_0/\lambda]^2 - [\alpha\lambda_0/(2\pi)]^2 + [\lambda_0/\lambda_c]^2 \tag{56}$$

applies to the permittivity evaluation from measurements using waveguide cells with a completely filled cross-section.

For convenience, waveguide sample cells are often operated at frequencies at which higher-order field modes can propagate. Since existence of such modes may adversely affect the accuracy of the experimental data, care has to be taken to avoid excitation of higher-order field configurations within the cell. A dielectrically homogeneous window (w) with plane faces, precisely aligned perpendicular to the cell axis, is mandatory. Interference of the desired fundamental field configuration with higher-order modes leads to a dependence of the results upon the starting position s_0 of the measurement. Repeated data recording at different s_0 is therefore recommended for verifying absence of undesired modes.

Measurements without variation of the sample length normally require calibrations in order to account for the reflection and transmission coefficients of dielectric windows, containers or any fixtures holding the sample. Even if, as in Figure 25a, a solid sample fills the cross-section of the sample

waveguide completely, calibration measurements using suitable reference materials have to be performed or samples of different length have to be precisely manufactured in order to account for the *a priori* unknown reflection coefficient of the solid. Alternatively, both the reflection and transmission coefficient of the sample cell may be determined and combined in the evaluation procedure as briefly featured below in section 3.1.1.5.

3.1.1.4 Reflection techniques, open-ended coaxial line probe

Due to their noninvasive character reflection measurements are frequently preferred. Figure 32 shows a microwave bridge for the measurement of the signal reflected from the specimen cell relative to a reference signal [196]. The cell is formed by a piece of rectangular waveguide. It is provided with moveable short in order to allow for the variation of the liquid column through which the electromagnetic wave passes. The short circuit is a crucial device because its reflection coefficient should be as close as possible to -1 and should be as accurately as possible maintained when the device is shifted along the *x*- direction. As with the computer-controlled transmission measurement (Fig. 27) the variable attenuator (6) and phase shifter (7) are both just used for the adjustment of an appropriate output signal $U(s_0)$ at a suitable position s_0 of the short. The signal $U(s)$ recorded

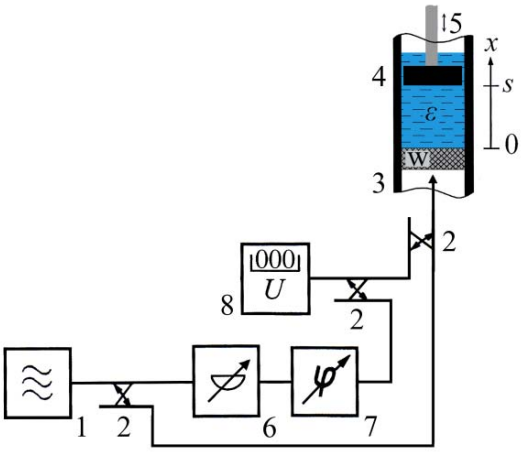

Figure 32. Microwave interferometer for reflection measurements [196], corresponding the microwave bridge for transmission measurements (Fig. 26). 1, signal generator; 2, directional coupler; 3, waveguide containing the liquid (ε), with dielectric window (w) and 4, short circuit shiftable along the direction *x* of wave propagation; 5, short-circuit drive, e.g. stepping motor; 6, variable attenuator; 7, variable phase shifter; 8, level meter.

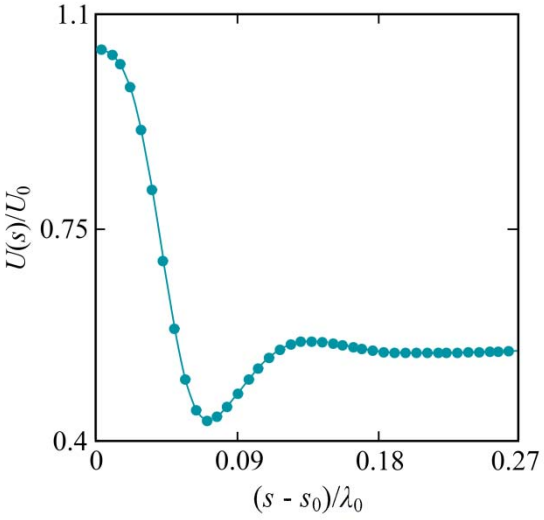

Figure 33. Voltage profile demonstrating the output signal of a reflection coefficient interferometer [144]. The data correspond with the measurement of water ($\varepsilon' = 9.35$, $\varepsilon'' = 16.71$, $\tan\delta = 1.8$) at 30 °C and 90 GHz. A piece of WG 22 waveguide (26.4 to 40.1 GHz) has been used as liquid cell in this measurement. U_0 is the voltage $U(s_0)$ at s_0, λ_0 is the wavelength c_0/ν in free space.

at varying position s of the short can again be evaluated to yield the complex propagation constant γ of the wave and thus the complex permittivity ε of the liquid.

An example of the output signal of a microwave interferometer for reflection coefficient measurement is presented in Figure 33. This example nicely demonstrates that reflection measurements, preferably applied in the investigation of low-loss samples, may be also used for liquids with high dielectric loss.

Many configurations of reflection coefficient measurements, each one matched to special sample properties, have been reported. The short circuit, for example, may be located outside the sample so that it reflects the incident wave after passing the sample [197]. Evidently, such arrangement includes the possibility to measure solids. Similarly spread [182-186, 198-206] have been methods in which slotted lines are used to shift a movable detector along a standing wave pattern, produced by reflection from the sample and superposition with incident wave (Fig. 25d-h). The complex dielectric constant of the sample is the then derived from the voltage ratio VSWR = $U_{max}/U_{min} = U(x_{max})/U(x_{min})$ of the standing field and the shift Δx_{min} of the positions of the minima relative to a reference pattern (Fig. 34). Standing wave approaches are still utilized in certain events [185], but techniques requiring less complex mechanics, preferably entirely without movable devices, are now more popular. They partly compensate for lower demands in the precision mechanics by higher efforts in the calibration

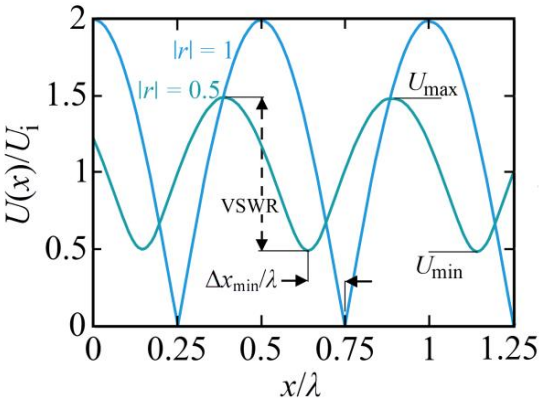

Figure 34. Voltage variation along a transmission line with a sample connected (turquoise curve) and with the line short-circuited at the sample position (blue curve). In this example $|r|$ = 0.5 is assumed at the sample – unloaded line interface so that $U_{max} = U_i \cdot (1 + |r|)$, $U_{min} = U_i \cdot (1 - |r|)$ and VSWR = U_{max}/U_{min} = 3. U_i is the incident signal voltage.

and numerical evaluation procedures.

Much use is made from broadband coaxial line reflection methods. Often they are based on cells of the cut-off variety which offer favorable conditions for the complex permittivity determination of liquids and many materials of relevant moisture content. These conditions include the suitability for frequency domain as well as time domain measurement methods and the applicability in an exceeding frequency band, roughly ranging from 1 MHz to 40 GHz [207, 208]. Cut-off probes are, in addition, increasingly applied [192, 207-229] as easy-to-handle devices which combine the convenience of non-invasive operation with simplicity of on-line implementation in complex measurement systems and control circuits.

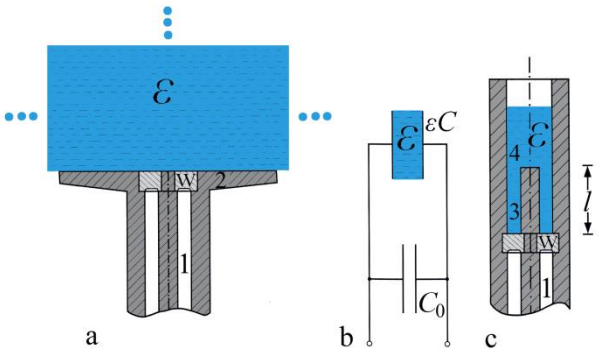

Figure 35. Schematic of open-ended coaxial line sensors (a, c) and their lumped element equivalent circuit (b): a, flanged version with "infinite half-space" geometry; c, shielded coaxial line – to – waveguide transition. 1, feeding coaxial line; w, matched dielectric window sealing the line; 2, ground plane flange; liquid filled coaxial line section of length l; 4, circular "below cut-off" waveguide section.

Originally the shielded circular-to-cylindrical waveguide transition depicted in part c of Figure 35 has been designed in order to allow for simultaneous dc conductivity and complex permittivity measurement of electrolyte solutions by inserting conductivity electrodes in the circular waveguide section [230]. The advantage of such a mode of operation is assurance of identical temperature for both parameters, enabling a superior determination of the dielectric contribution to ε'' to $\varepsilon_{\mathrm{tot}}$ from Eq. (31). If adequately arranged the conductivity electrodes do not disturb the electromagnetic field of the permittivity measurements because the circular waveguide is excited well below the cut-off frequency of its TM01 mode when filled with the liquid [192, 230-233]. The rapidly decreasing evanescent field excited in the circular waveguide section implicates, in addition, the need for sample volumes on the order of 1 cm^3 only and also independency of exact filling level as well as the shape of the liquid meniscus.

The length l ($< \lambda/4$) of the coaxial line section (Fig. 35c) of shielded open-ended cells can be used to match the cell properties to the frequency of measurement and the complex permittivity of the sample. Hence the accuracy of the data obtained may benefit from the use of a set of cells with different l. At sufficiently large l, the shielded cell can be well represented by the simple equivalent circuit of two capacitances in parallel, given in part b of Figure 35. Capacitance εC represents the liquid-filled part. It can be calculated according to transmission line theory, using an effective cell length l_{eff} ($> l$) to take the evanescent field of the circular waveguide into account. Capacitance C_0 considers the feeding coaxial line (1, Fig. 35), including the sealing dielectric window (w). At higher frequencies and larger permittivity of the sample, small lengths l of the liquid-filled coaxial line section, including $l = 0$ (Fig. 36c), are appropriate. On such events, flux lines passing both the dielectric window (w) and the sample (ε) have to be respected. The equivalent circuit of the cell is therefore completed by a serial configuration of capacitances $\varepsilon_{\mathrm{w}}C_1$ and εC_2 in parallel to εC and C_0 (Fig. 36b). The equivalent networks of the shielded open-ended coaxial cells are indeed easy to understand intuitively. They have been, however, theoretically verified by full-wave mode-matching analysis [233]. In practice the input admittance of the cells is calculated as

$$Y(\nu, \varepsilon) = \mathrm{i}2\pi\nu C_{\mathrm{tot}}(\nu, \varepsilon) \tag{57}$$

with

$$C_{\mathrm{tot}} = C_0 + \varepsilon(\nu)C + \varepsilon_{\mathrm{w}}\varepsilon(\nu)C_1C_2/[\varepsilon_{\mathrm{w}}C_1 + \varepsilon(\nu)C_2]. \tag{58}$$

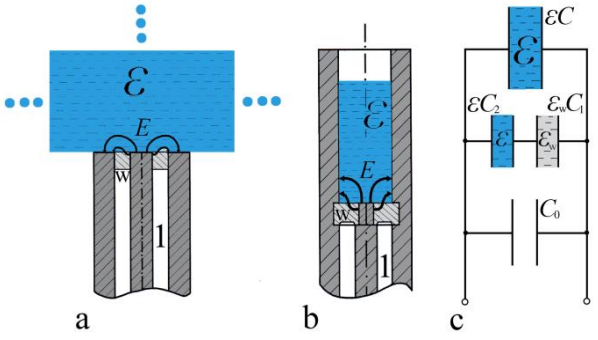

Figure 36. Unflanged coaxial line sensor (a) and cut-off cell with vanishing coaxial line part (l = 0, b) shown with flux lines of the evanescent electrical field of strength E. Part c reveals an equivalent circuit representation of both devices. 1, feeding coaxial line; w, dielectric window.

The values of capacitances C and C_0 as well as C_1 and C_2 are obtained from calibration measurements as will be discussed in more detail below.

Shielded open-ended coaxial cells avoid stray fields and are advantagously applied in liquid studies. Alternatively, open-ended coaxial probes as sketched in parts a of Figures 35 and 36 have been designed. They apply also to tissue measurement or investigation of solid samples. Interaction of the electromagnetic measurement signal with the sample is provided by the fringing field protruding from the end of the coaxial line. In a first approximation the reflection coefficient of the flanged version of such a probe (Fig. 35a) is calculated assuming "inifinite half-space" conditions: the sample is assumed sufficiently large and its dielectric losses sufficiently high to neglect any signals reflected from boundaries except the sensor-sample interface. On such conditions the arrangement at low frequencies can be also represented by two capacitors in parallel as sketched in part b of Figure 35. Here C accounts for the fringing field interacting with the sample. In conformity with the cut-off cell (l = 0, Fig. 36b), the non-flanged open-ended probe needs the consideration of the series configuration of two additional capacitances (Fig. 36c) in order to include flux lines passing the dielectric window and the sample as well. Full-wave analysis of the electromagnetic field at the probe aperture yields an integral equation for which, unfortunately, an analytical solution does not exist [218, 229]. Suitable numerical methods, however, to handle the integral equation are available [222, 234, 235]. Often the simple equivalence circuits of Figures 35 and 36 are used again to evaluate the data.

It is only briefly mentioned that modified sensors have been designed in order to broaden the applicatioin range of the basic devices. Examples are open-ended coaxial probes backed by a conducting plane which are

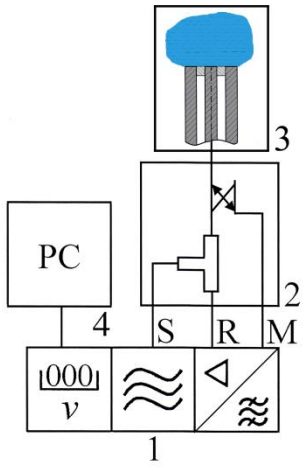

Figure 37. Vector network analyzer set-up for input impedance and reflection factor measurement: 1, VNA with S, signal output port; R, reference input channel; M, measurement input channel; 2, reflection test set; 3, sample cell or electromagnetic sensor; 4, process control computer.

matched to the measurement of thin samples [215, 219, 224, 236].

Adequate to frequency domain measurements with broadband open-ended coaxial sensors are vector network analyzers appendant to a suitable reflection test set (RTS), which is essentially a combination of power splitters and directional couplers. By analogy with the microwave interferometer discussed before (Fig. 32), a plain arrangement is shown in Figure 37. Imperfect operation of both the RTS and the VNA may result in small differences between the indicated ($\tilde{r}$) and the true reflection coefficient

$$r = \frac{Z - Z_0}{Z + Z_0} = \frac{1 - YZ_0}{1 + YZ_0} \tag{59}$$

where $Y = Z^{-1}$ again denotes the input admittance of the cell, i.e.the admittance at the reference plane of the RTS. The true reflection coefficient derives from the indicated coefficient as

$$r = \frac{a_1\tilde{r} - a_2}{a_3\tilde{r} + 1}. \tag{60}$$

The three unknown parameters a_1, a_2, and a_3 are typically obtained from calibration procedures using the open end ($Y = 0$), the short circuit ($Y^{-1} = Z = 0$), and the matched termination ($Y^{-1} = Z_0$) configurations as references. Probes that can be well represented by the simple parallel circuit of two capacitances (Fig. 35) can be included in the calibration procedure by con-

sidering the RTS-VNA configuration in combination with the specimen cell [237, 238]. Bilinear relation

$$\varepsilon(\nu) = \frac{b_1(\nu)\tilde{r}(\nu) - b_2(\nu)}{b_3(\nu)\tilde{r}(\nu) + 1} \tag{61}$$

then describes the complex permittivity $\varepsilon(\nu)$ of the sample as function of the indicated reflection coefficient $\tilde{r}$. Parameters b_1, b_2, and b_3, characterizing the cell together with the measurement system are obtained from calibration measurements using suitable reference materials, such as air, water, and a liquid with permittivity different from air (ε = 1) and water ($\varepsilon(0)$ = 78.36, 25 °C [137]). If the more complicated equivalent circuit of Figure 36 is required for the adequate representation of the probe, more elaborate calibration is unavoidable, for instance by calibrating the network analyzer – reflection test set combination and the cell or probe separately.

3.1.1.5 Cells for measurement at high hydrostatic pressure

The dielectric properties at high hydrostatic pressure are fundamantal in liquid state physics as they provide insights into the liquid structure. Especially water, due to the voluminous arrangement of hydrogen-bonded molecules (Fig. 6) is expected to respond noticeably to pressure variation. The pressure dependence in the complex permittivity of materials is additionally important in various applications, including moisture determination. An example is the monitoring of water formation in subsea oil and wet gas production and transportation [239]. Reflection techniques are convenient for dielectric measurements at hydrostatic high pressure because they need only one sealing window for the connection of the high-pressure sample cell to the electromagnetic measurement system. Open-ended coaxial probes have been used at moderate pressure [240, 241]. Figure 38 shows a schematic of a cell for which a commercial semirigid 2.2 mm coaxial cable is used as dielectric probe. In that arrangement the gap between the inner conductor and outer conductor is simply filled with a PTFE spacer. The cell allows for hydrostatic pressures up to about 20 MPa and covers the frequency range 200 MHz - 20 GHz. An alternative design of an open-ended coaxial line cell utilizes a sapphire bead as high-pressure window at pressures up to 9 MPa and at frequencies up to 2.5 GHz [241].

Significantly higher pressure is reached with the waveguide reflection measurement configuration shown in Figure 39. A highly pressure-resistant self-sealing hemispherically shaped ceramic window (1, Fig. 39)

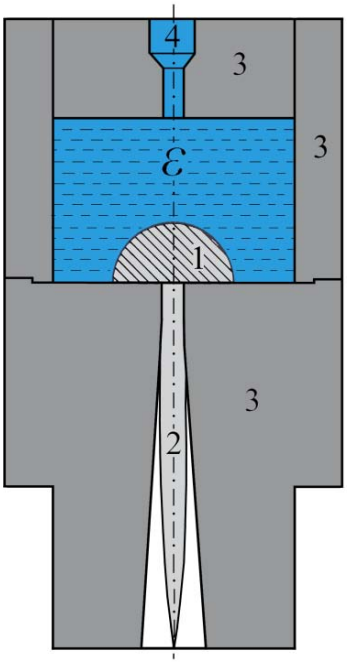

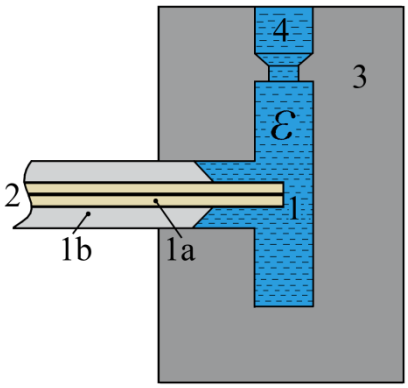

Figure 38. Sketch of a cell for dielectric measurement at increased hydrostatic pressure [240]: 1, semirigid coaxial cable with 1a, PTFE spacer and 1b, high-pressure outer tube; 2, feeding line; 3, pressure-resistant casing; 4, liquid inlet.

Figure 39. Sectional view of high-pressure cells for reflection coefficient measurement in the frequency range 5.5 to 40 GHz [242, 243]: 1, self-sealing hemispherical window from Al_2O_3 ceramic; 2, circular-to-rectangular waveguide transition with specially shaped dielectric rod; 3, pressure-resitant casing; 4, liquid inlet.

closes the sample volume. The reflection coefficient at the sample – window interface is probed at hydrostatic pressures between 0.1 and 200 MPa [242, 243]. The feeding section (2) includes a circular – rectangular waveguide transition to facilitate the use of standard waveguide components in the measuring set-up. The transition includes a ceramic rod with suitable permittivity and computed shape in order to provide wave propagation in the narrow waveguide section. Three analogous devices allow for measurements in the frequency bands 5.3 to 7.9 GHz, 12.4 to 18 GHz, and 26.5 to 40 GHz. Results for the pressure dependence of the dielectric parameters of water and aqueous solutions at ambient temperature are given below in chapter 4.

A cell for high pressure ($p \leq 120$ MPa) and high temperature ($T \leq 750$ °C) has been designed for both reflection and transmission measurement.

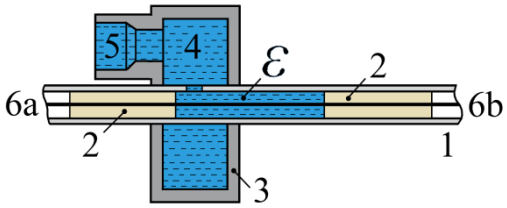

Figure 40. High-pressure cell for microwave transmission measurement [244]: 1, coaxial line; 2, sealing quartz tube; ε, liquid volume; 3, pressure-resistant casing; 4, liquid reservoir; 5, liquid inlet, pressurization; 6a, feeding line; 6b, transmitted signal line.

As sketched in Figure 40 it involves a coaxial line with two quartz tubes (2, Fig. 40) serving as sealing windows between the inner and outer conductor. The signal transmitted through or reflected from the quartz-sample-quartz assembly is recorded using a network analyzer [244].

3.1.1.6 Reflection-transmission techniques

Certainly, the combination of reflection and transmission techniques can enhance the sensitivity in measurement or the versatility in applications. Vector network analyzers are particularly suited for such modes of operation since, in principle, they need only an appropriate directional coupler to feed the signal reflected from the cell in one of the measurement channels of the instrument while the transmitted signal is applied to the second channel (Fig. 41). The somewhat more elaborate relation between the

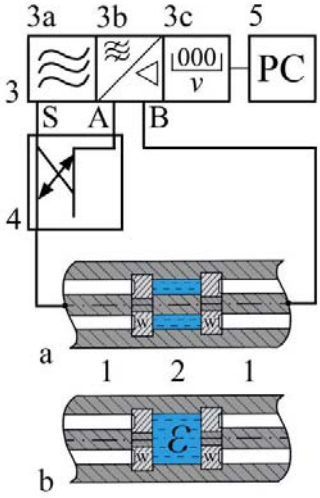

Figure 41. Set-up for combined reflection and transmission measurements using a vector network analyzer (3) combined with a reflection or *S*-parameter test set (4). a, b, coaxial line and waveguide-below-cut-off transmission line cell, respectively with 1, coaxial feeding line and 2, sample volume; 3a, VNA signal generator with signal output S; 3b, two-channel superheterodyne receiver with signal input ports A and B; 3c, synthesizer; 5, process control computer.

measured signals and the complex permittivity of the sample is favorably obtained from a scattering parameter (*S*-parameter) algorithm [245-247] and thus the VNA is combined with a commercial *S*-parameter test set [238, 244, 248-251].

Scattering parameters relate the amplitudes and phases of the signals leaving a complex network at the output lines to the amplitudes and phases of the signal incident at the input lines. For the two-port microwave networks under consideration the relevant (complex) scattering parameters are S_{11}, the input voltage reflection coefficient, and S_{21}, the forward voltage gain, i. e. the output voltage divided by the input voltage.

3.1.1.7 Miniaturized measurement structures, resonators

Both the coaxial line cell and the cell from the waveguide-below-cut-off variety depicted in Figure 41 can be constructed to need a sample volume on the order of 100 µl only. A similarly small sample volume has been reached with miniature flangeless open-ended coaxial probes [208]. For the use with biological materials and pharmaceutical formulations as well as in medical applications measurements at even smaller sample volumes are sometimes required. Considerable efforts have therefore been made in order to reduce the relevant liquid volume.

In Figure 42 the design of a simple cell that takes 200 nl only [252] is sketched. The sample is contained in a narrow capillary made of fused silica. Its inner diameter is as small as 0.2 mm. Two metallic electrodes wrap the capillary and enable the device to be connected to the electronic measurement circuit via the transmitting (3, Fig. 42) and receiving (4) signal lines. An advantage in many applications is the operation of the sample without any metallic contact. The sensitivity of the method, which so far has been used in the frequency range between 50 MHz and 1.6 GHz [252], has been noticeably increased by using an interferometric set-up in which the complex transmission factor of the cell is directly compared to that of an identically constructed reference cell. The latter is typically filled with a liquid of well-known dielectric properties.

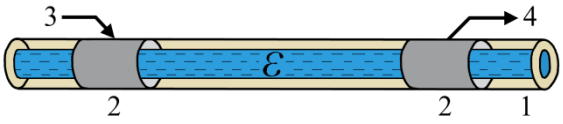

Figure 42. Capillary-based transmission cell for dielectric measurement at 200 nl sample volume [252]: 1, capillary holding the liquid sample (ε); 2, metallic electrodes wrapped around the capillary; 3, feeding line; 4, receiving line.

Many miniaturized measurement sensors in use [253-260] are based on coplanar waveguide structures to which geometrically well-defined micrometerscale fluidic channels are connected [261]. As an example, a two-strip configuration is shown in Figure 43. Devices with three metallic strips are also used and often meandering microfluidic channels are aligned directly above the metallic electrodes. Cells also differ by the substrate material and by the frequency band of measurement, ranging up to 40 GHz [259, 260]. The required sample volume has been reduced to 1 nl by integrating an interdigitated capacitor array into a coplanar waveguide structure [260]. Such devices thus enable microwave dielectric spectroscopy at cellular levels [259, 262]. Avoiding elaborate cleanroom facilities and thus reducing costs of production, a microstrip interferometer for measurement up to 10 GHz has been built by integrating microfluidic channels on a standard radiofrequency printed circuit board [263].

Microfluidic channel sensors include also resonant structures [260] in which the electromagnetic waves are reflected back and forth between places of substantial impedance changes. Because of the multiple reflections the pathway of interaction between the electromagnetic field and the sample is virtually increased, thus providing a superior sensitivity in measurements. The high sensitivity can be utilized to reduce the sample volume, to study low-loss samples, or to indicate small changes in the dielectric properties of samples. The principle of resonator measurement may be illustrated by Figure 44, where a cavity resonator is shown which consists simply of a piece of rectangular waveguide. At its ends the waveguide section is terminated by metallic walls, providing reflection coefficients r_0 and r_l close to -1. The walls are equipped with a dielectric window (or another antenna) to allow for a weak coupling of the resonator to the microwave circuit for transmission measurement.

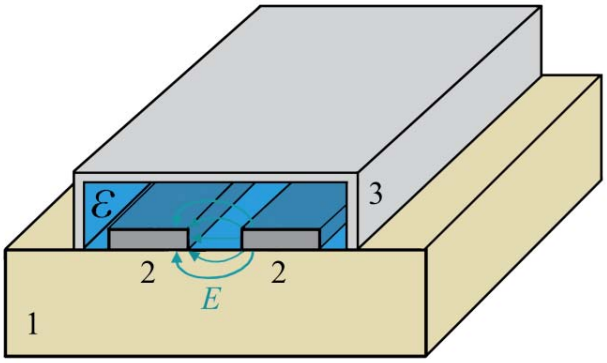

Figure 43. Sketch of a coplanar waveguide cell [261] with two metallic strips (2): 1, substrate; 2, electrode; 3, microfluidic channel containing the sample (ε); E, electrical field lines.

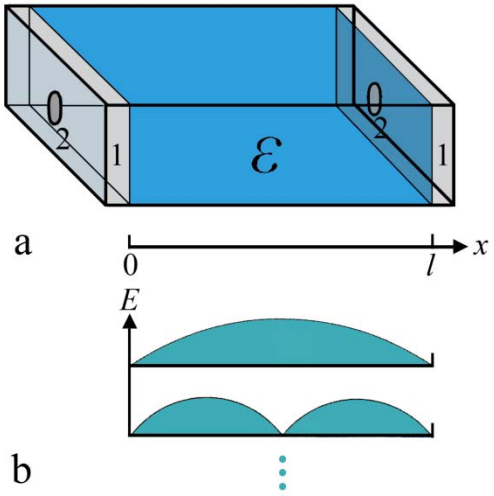

Figure 44. Cavity resonator made from a piece of rectangular waveguide: 1, metallic faces provided with 2, coupling dielectric windows or other suitable antennae (a). Also shown are two examples of possible electric field distributions within the cavity (b).

The electrical field set up in the cavity may be considered as a superposition of a series of waves propaging back and forth within the liquid. Consider first an "ideal" resonator without any losses ($\varepsilon'' = 0$). According to Eq. (53) the propagation constant within the waveguide section is given by

$$\gamma = 2\pi/\lambda, \tag{62}$$

where

$$\lambda = (\lambda_c^{-2} - \varepsilon' \lambda_0^{-2})^{-1/2} \tag{63}$$

is the wavelength. Since the electrical field strength must vanish at the positions $x = 0$ and $x = l$ of the metallic walls, i.e. in case r_0 and r_l are assumed exactly -1, a signal is transmitted by the resonator only if

$$\sin(2\pi l/\lambda) = 0, \tag{64}$$

i.e.

$$2\pi l/\lambda = \mathrm{p}\pi \text{ or } \lambda/2 = l/\mathrm{p}, \quad \mathrm{p} = 1, 2, \ldots . \tag{65}$$

Hence the spectrum of the ideal resonator is a series of equidistant delta functions at every integer multiple of a half wavelength of the electrical field within the cavity. Since according to Eq. (63) λ is related to the real

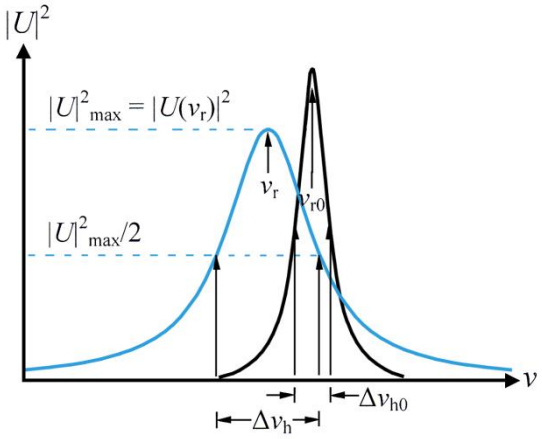

Figure 45. Resonance curves of an unloaded (black curve) resonator and a cavity resonator filled with a dielectric (blue curve): ν_{r0} and ν_r denote the resonance frequencies of the empty and filled resonator, respectively. $\Delta\nu_{ho}$ and $\Delta\nu_h$ are the corresponding half-power bandwidths.

part of the permittivity of the sample, ε' can be directly obtained from the difference

$$\nu_p - \nu_{p\text{-}1} = c_0/(2l\sqrt{\varepsilon'}) \tag{66}$$

of subsequent resonance frequencies.

Due to unavoidable losses, however, the resonance curves from real experiments display always a finite half-power bandwidth $\Delta\nu_h$, as depicted in Figure 45. The empty resonator experiences losses because of the finite electrical conductivity of the wall material and the coupling of the device to the measurement set-up. The loaded cavity is normally also subject to sample losses because of a nonvanishing imaginary part ε'' of the material's permittivity and the thus complex propagation constant $\gamma = \alpha + i\beta$ of the electromagnetic waves within the resonator. Neglecting first the (typically small) intrinsic losses of the empty cell, the partial waves which, due to reflection, propagate can be added together to yield the transfer function

$$|T(\nu)| = [\sinh^2(\alpha l) + \sin^2(\beta l)]^{-1/2}\,. \tag{67}$$

At small losses (αl « 1) this function can be developed for a frequency range around a given resonance frequency ν_r (= ν_p, Fig. 45) to yield relation

$$\alpha\lambda = \pi\Delta\nu_h/\nu_r = \pi Q^{-1}, \tag{68}$$

where

$$\Delta\nu_h = \nu_{h+} - \nu_{h-}, \tag{69}$$

denotes the half-power bandwidth and $Q = \nu_r/\nu_h$ the quatity factor. In Eq. (69) ν_{h+} ($> \nu_r$) and ν_{h-} ($< \nu_r$) are defined by $|T(\nu_{h\pm})|^2 = |T(\nu_r)|^2/2$.

Due to the intrinsic losses of the cell, the half-power bandwidth $\Delta\nu_{h,meas}$ from measurement contains contributions $\Delta\nu_{h,s}$ and $\Delta\nu_{h,0}$ from both the sample and the empty cell. To account for the latter, energy losses are assumed to be additive. Applying the above definition of the quality factor analogously, relation

$$1/Q_s = 1/Q_{meas} - 1/Q_0 \tag{70}$$

is used to obtain the relevant quality factor Q_s from Q_{meas}. The quality factor of the empty cell is normally determined from reference measurements. Eqs. (69, 70) show that Q_0 must be high in order to permit a high sensitivity of the method.

The above considerations are based on the assumption of field similarity, i. e. on almost identical resonance frequencies in the sample and reference measurements. Because of $\varepsilon' \geq n^2 \approx 2$, n = optical refractive index, the resonance frequency of the cavity resonator changes substantially when completely filled with a sample. For that reason partly filled configurations are normally employed. An example is shown in Figure 46, where a plane layer of sample (ε) is contained between two dielectric windows (w). Different field configurations may be used and also the positions of the sample and the windows may be shifted along the x direction to either feature strong interaction of the dielectric with the electric field, as appropriate to low-loss materials, or to offer reduced interaction, as adequate to samples with large permittivity.

The resonance curve of such a cell can be favourably calculated with the aid of the impedance transmission formula for homogeneous lines [174]

$$Z(x_b) = Z_0[Z(x_a) + Z_0\tanh(\gamma\Delta x)]/[Z(x_a)\tanh(\gamma\Delta x) + Z_0] \tag{71}$$

which relates the impedance at position x_b to the impedance at position x_a. Here Z_0 is again the characteristic impedance of the line and $\Delta x = x_b - x_a$. Hence zero impedance at $x = 0$ can be successively transformed to x_1, x_2, x_3, x_4, and finally x_l (Fig. 46). Boundary condition $Z(x_l) = 0$ yields an implicite complex relation for the permittivity $\varepsilon' - i\varepsilon''$ of the sample which needs to be solved numerically.

Small sample volumes are achieved if the sample is contained in a thin capillary which is placed in a suitable position of the resonator (Fig. 47). Now, however, the cylindrical geometry of the sample is no longer matched to the rectangular geometry of the cavity so that the analytical

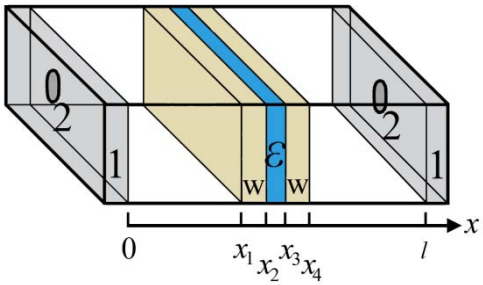

Figure 46. Cavity resonator, as the one shown in Figure 44, made from a piece of rectangular waveguide but only partly filled with sample (ε): 1, metallic faces provided with 2, dielectric coupling holes or other suitable antennae; w, dielectric windows holding the sample.

description of the resonator cell is complicated [264, 265]. In general, the surface admittance of the cylindrical sample with radial field is given by Bessel functions of zeroth and first order [149, 195]. If wave propagation of the radial field within the sample can be neglected ($\sqrt{\varepsilon}\beta r_s \ll 1$, $r_s = d_s/2$) development of these functions reveals the admittance (when looking towards decreasing radii) of the sample as

$$Y = i\omega\varepsilon\varepsilon_0 r_s^2/h. \tag{72}$$

Hence it equals that of a cylindrical capacitor of height h if h is the height of the resonator. On such conditions, i. e. at a uniform electric field within the sample, perturbation methods are often employed in which insertion of the sample is considered a small disturbance of the original resonator field and in which geometrical details are combined in a so-called filling factor η_f [266-273]. If η_f is known from theoretical considerations or calibrations the real and imaginary parts of the sample permittivity are obtained for

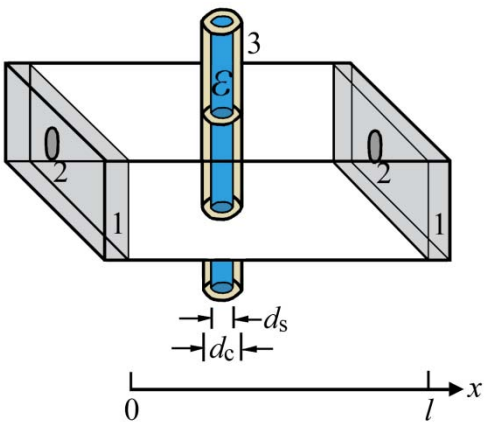

Figure 47. Linear cavity resonator as in Figures 44 and 46 but with capillary containing the sample (ε): 1, metallic faces provided with 2, dielectric coupling holes or other suitable antennae; 3, capillary of outer diameter d_c and inner diameter d_s.

arbitrarily shaped objects as [268]

$$\varepsilon'(\nu_r) = 1 + 2\,\eta_{f'}(\,1 - \nu_r/\nu_{r0}) \tag{73}$$

and

$$\varepsilon''(\nu_r) = \eta_f/Q_s = \eta_{f'}(1/Q_{meas} - 1/\,Q_0). \tag{74}$$

Alternatively, the resonator geometry may be matched to the geometry of the capillary. Employing cylindrical cavities with the sample placed in their axis (Fig. 48), in correspondence to the linear configuration of Figure 46 the electrical field can be exactly calculated [274-276]. Impedance transmission formulas for radial transmission lines [195, 277] may be applied to reveal the relation between the resonance frequency and half-power bandwidth of the resonator and the complex permittivity of the sample. Applying suitable antenna systems, again different field configurations can be excited (Fig. 48b) in order to match the electrical field

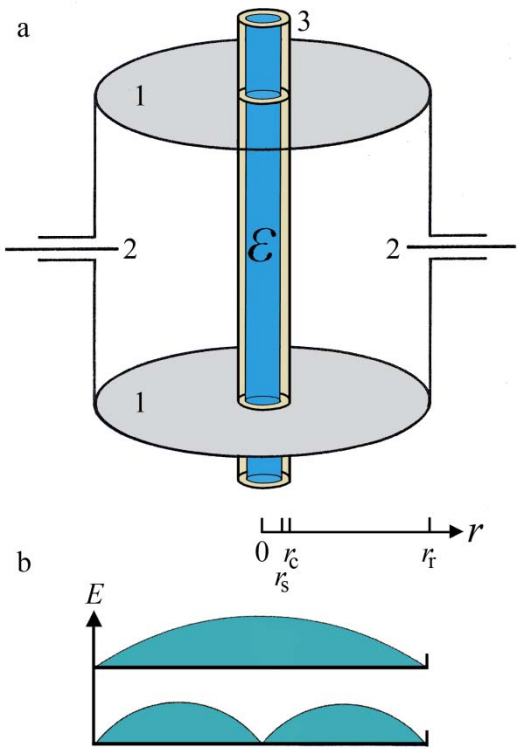

Figure 48. Sketch of a cylindrical cavity resonator with calculable geometry. 1, metallic wall; 2, coupling antenna; 3, capillary holding the sample (ε) placed along the axis of the cavity (a). Two electric field distributions (b) indicate configurations in which the sample is placed at sites of maximum (e.g. TM_{010} mode) and minimum (e.g. TE_{011} mode) field strength.

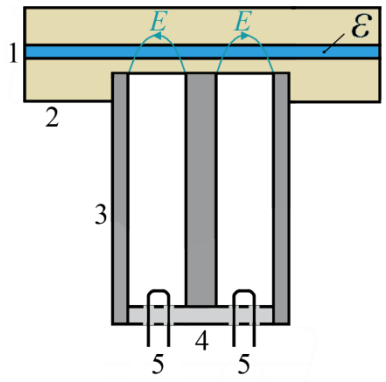

Figure 49. Schematic of a resonant coaxial sensor which, with the aid of its fringing electric field (E), probes a sample (ε) contained in a microchannel: 1, microchannel; 2, substrate; 3, coaxial resonator with 4, metallic face; 5, antenna for coupling the device to the measurement circuit.

strength at the cavity axis to the dielectric properties and magnitude of the sample.

A variety of specially designed resonant devices for complex permittivity measurement of materials have been designed. An example are microwave resonators probing a sample-filled microchannel [278-280] as sketched in Figure 49. Since the sample is contained in an appropriate substrate, by analogy to the capillary devices shown in Figures 42, 47, and 48, excellent chemical and biological compatibility is offered by the sensor. The microwave part of the configuration may be considered an open-ended coaxial sensor (Fig. 36a) which is operated in a resonant mode. So far rather bulky resonators with lengths around 8.4 and 17.5 cm have been used in order to reach resonance frequencies as small as 1.25 and 0.6 GHz, respectively. Hence at those frequencies the advantage from miniaturization of the channel holding the sample is partly compensated by the large dimensions of the resonator. The method proves, however, that, at the expense of broadband applicability, the sensibility of open-ended sensors can be increased by a resonant mode of operation.

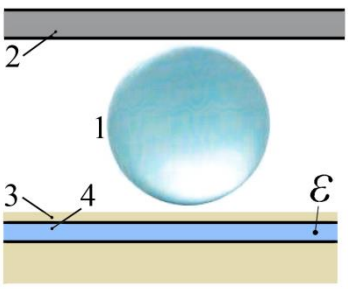

Figure 50. Whispering gallery mode resonator combined with a sample-filled microchannel [281]: 1, spherical resonator made of sapphire; 2, dielectric waveguide; 3, substrate containing the microchannel (4) that is filled with the sample (ε).

Resonator techniques often enable measurements at one fundamental frequency only and are thus notoriously smallband. To a certain extent this disadvantage is overcome by whispering-gallery-mode resonators which, due to their rich resonance frequency spectrum, offer a broader frequency range of measurement [281-285]. Dielectric spheres or discs made from materials with extremely small dielectric loss, such as sapphire, are utilized as resonant device (1, Fig. 50). It is coupled to the microwave set-up via a dielectric waveguide (2). Electromagnetic fields excited in the resonant body may re-phase after a complete turn and thus lead to sharp resonances. Appropriate adjustment of the body's permittivity results in total reflection of the field at the surface and thus largely restricts the resonant modes of whispering gallery type to the interior. However, still present weak evanescent fields outside the resonator body provide coupling not just to the waveguide (2) but also to the microfluidic channel (4) containing the sample under test (ε). Such a resonator – sample interaction affects the resonance frequencies and half-attenuation frequencies of the whispering gallary modes so that these parameters can again be used to determine the sample's complex permittivity.

Modern microwave electronics offer easy access to fast measurements of complete resonance curves and subsequent numerical analysis. The multipoint determination of resonance frequencies ν_r and half-power bandwidths $\Delta\nu_h$ from total curves greatly enhances their accuracy as compared to the direct identification of the ν_r and $\Delta\nu_h$ values. It allows, in addition, a careful inspection of the resonance curves for undesired disturbances, such as from spurious higher-order modes. Network analyzers or level meters permit accurate and fast automatic measurements. In principle, scalar measurements are sufficient to determine the absolute value $|T(\nu)|$ of the resonator transfer function. Complex measurements, including the phase φ of $T(\nu)$, yield, of course, additional information. Phase slope $\mathrm{d}\varphi(\nu)/\mathrm{d}\nu$ has been shown to be a favourable function for resonator evaluation [286].

Evidently, instead of the signal transmitted by, the signal reflected from the device can be also measured for resonance curve determination. However, since the absolute value of the resonator's reflection coefficient is close to 1 the resonance curve appears just as a small dip in the frequency dependence of the reflected signal. In order to enable an adequate resolution of the dip, a careful compensation for the prevailing frequency-independent background contribution is thus required. This endeavor may countervail the advantage of only needing one antenna for the connection of the resonator cell to the electronic set-up.

3.1.1.8 Free-space configurations

As obvious from the intermediate position of the microwave region within the electromagnetic spectrum, free-space techniques for the determination of the dielectric properties of materials are an alternative to the above methods in which the samples are contained in separately designed specimen cells. Especially *in-situ* tests often ask for probing electromagnetic wave propagation in free space. Figure 51 sketches free-space configurations of the three main classes of measurement, namely transmission (a), reflection (b), and resonance (c) observations. The measurement signal is transmitted from and received by adequate antennae, typically horn antennae. It can be divided by a beam splitter (5) as required for the coupling of open resonators (c) which, by analogy to optics, are also named interferometers.

Interferometers have been widely used to expand the upper limit of microwave measurements up to 300 GHz [287-297]. Avoiding wall losses and thus providing a superior Q_0, they are particularly adapted to low-loss materials. Michelson [287], Mach-Zender [291], and Fabry-Perot [294] type configurations have proven appropriate. In correspondence with many cavity resonator systems, the resonance curve may be also recorded at fixed frequency by slightly varying the interferometer dimensions, i. e. by precisely moving a reflector (or mirror; 8, Fig. 52).

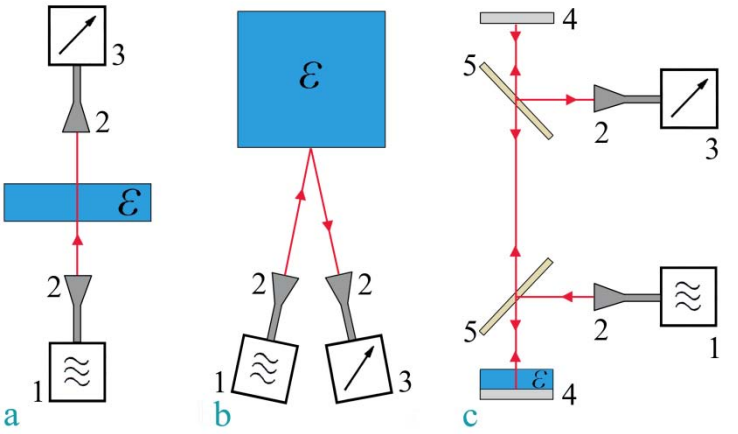

Figure 51. Schematics of transmission (a), reflection (b), and resonance (c) measurement configurations in free-space technology: 1, signal source; 2, horn antenna; 3, detector; 4, metallic reflector; 5 beam splitter; ε, sample.

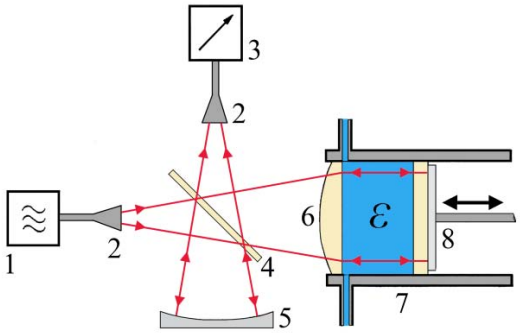

Figure 52. Microwave Michelson interferometer [287]: 1, signal source; 2, horn antenna; 3, detector; 4, beam spitter; 5, spherical mirror, 6, plano-convex lense; 7, cell holding the sample (ε); 8, movable reflector (mirror).

3.1.2 Audio- and radio-frequency range, lumped-element technology

3.1.2.1 Electric conductivity, admittance derivative method

Due to the excellent hydration of ions, aqueous solutions are often subject to a significant electrical conductivity, largely masking the dielectric properties of the materials. As has been shown before (Eq. 32) the admittance of a capacitor, filled with a conducting sample, is simply given by

$$Y(\nu) = [\sigma/\varepsilon_0 + \mathrm{i}\omega\varepsilon(\nu)]C, \tag{75}$$

if C denotes the void capacitance and $\varepsilon(\nu)$ the dielectric part of the complex permittivity. Evidently, the admittance derivative $\mathrm{d}Y(\nu)/\mathrm{d}\nu$ is independent of the specific electric conductivity σ and may thus be the preferred measurement category in low-frequency investigations of conducting samples [298, 299]. Modern automated electronics easily allow for frequency modulation and thus direct determination of the derivative. Alternatively, they enable at every frequency ν_m of measurement to also record data at a closeby frequency $\nu_\mathrm{m} + \Delta\nu_\mathrm{m}$ and to thus obtain the admittance derivative as the differential ratio $\Delta Y(\nu_\mathrm{m})/\Delta\nu_\mathrm{m} = [Y(\nu_\mathrm{m} + \Delta\nu_\mathrm{m}) - Y(\nu_\mathrm{m})]/\Delta\nu_\mathrm{m}$. The admittance derivative mode of operation greatly benefits from the perfect compensation of the conductivity contributions because of simultaneous measurement of the permittivity data and the notoriously temperature-sensitive specific conductivity.

According to Eq. (75)

$$\mathrm{d}Y(\nu)/\mathrm{d}\nu = 2\pi\mathrm{i}C[\nu\mathrm{d}\varepsilon(\nu)/\mathrm{d}\nu + \varepsilon(\nu)] = 2\pi\mathrm{i}C[\mathrm{d}\varepsilon(\nu)/\mathrm{d}\ln\nu + \varepsilon(\nu)] \tag{76}$$

follows. Hence in addition to the spectrum itself the logarithmic derivative

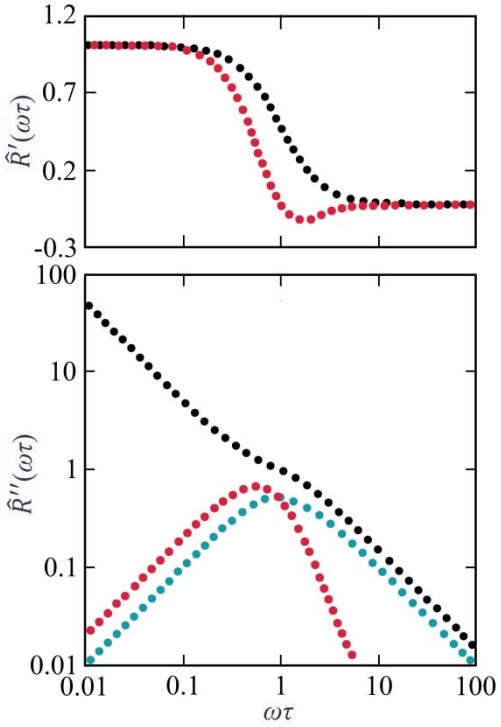

Figure 53. Lin-log and log-log plots of the real part $\hat{R}'(\omega\tau)$ and negative imaginary part $\hat{R}''(\omega\tau)$, respectively, of normalized relaxation spectral function $\hat{R}(\omega\tau) = \hat{R}'(\omega\tau) - i\hat{R}''(\omega\tau)$: $\hat{R} = [\varepsilon_{tot} - \varepsilon(\infty)]/\Delta\varepsilon = [\varepsilon - i\sigma/(\varepsilon_0\omega) - \varepsilon(\infty)]/\Delta\varepsilon$ (Eq. 30; black curves); $\hat{R}'' = \varepsilon''/\Delta\varepsilon$ (turquoise curve); $\hat{R} = [S - \varepsilon(\infty)]/\Delta\varepsilon$ (Eqs. 79, 80; red curves).

$d\varepsilon(\nu)/d\ln\nu$ of the dielectric part of the complex permittivity spectrum is involved. The conduction-free sum function

$$S(\nu) = d\varepsilon(\nu)/d\ln\nu + \varepsilon(\nu) \tag{77}$$

within the square bracket of Eq. (75) features some secondary beneficial characteristics. Figure 53 illustrates such quality for material with Debye-type relaxation behaviour for which [300]

$$\varepsilon(\nu) = \varepsilon(\infty) + \frac{\varepsilon(0)-\varepsilon(\infty)}{1+i\omega\tau} = \varepsilon(\infty) + \frac{\Delta\varepsilon}{1+i\omega\tau} \tag{78}$$

and thus

$$S'(\nu) = \varepsilon(\infty) + \Delta\varepsilon\frac{1-\omega^2\tau^2}{(1+\omega^2\tau^2)^2} \tag{79}$$

as well as

$$S''(\nu) = 2\Delta\varepsilon\frac{\omega\tau}{(1+\omega^2\tau^2)^2}\,. \tag{80}$$

In addition to the elimination of the conductivity contribution, the dispersion and dielectric loss region of the spectrum extends over a smaller frequency range and is shifted toward lower frequencies as compared to the original $\varepsilon(\nu)$ spectrum. Furthermore the more distinctive shape of the $S'(\nu)$ function, revealing a relative minimum well above the relaxation frequency ω_r ($[S(\omega_r) - \varepsilon(\infty)]/\Delta\varepsilon = 1/2$), is helpful in the analysis of experimental spectra.

We mention that blocking of electrical conductivity by insulating electrode layers normally leads to worsening rather than improvement of the signal analysis [301]. The careful analysis of the effect of insulation layers also showed [301] that thin insulating films (< 0.5 µm) can be used with little detriment in order to avoid contact between sample and metal if necessary.

3.1.2.2 LCR bridges, impedance analyzers

Low-frequency frequency domain techniques to measure the complex permittivity of materials are often based on refinements [302-304] of sensitive methods for impedance compensation as originally designed as, for instance, Wheatstone [305, 306], Wien [307], Schering [308], and Scheiber [309] bridge circuits. The principle of operation at the basis of all bridge methods is illustrated by Figure 54.

The sample with permittivity $\varepsilon(\nu) = \varepsilon'(\nu) - i[\varepsilon''(\nu) + \sigma/(\varepsilon_0\omega)]$ is contained in a capacitor C which along with the series connection of resistance R_0 and capacitor C_0 forms one arm of the bridge. In the figure, capacitor C is represented by the equivalent parallel arrangement of capacitor C_x with capacitance $\varepsilon' C$ and resistor R_x with resistance $[\omega\varepsilon'' + \sigma\varepsilon_0]C$. If a sinusoidal voltage with frequency $\nu = \omega/(2\pi)$ is applied between positions A and B of the circuit, zero signal between points D and E is adjusted on the

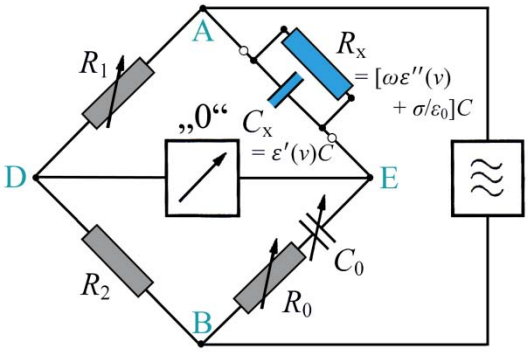

Figure 54: Wien-type bridge circuit for the measurement of the complex capacitance
$C_x + (i\omega R_x)^{-1}$
$= \varepsilon_{tot}(\nu)C$
$= [\varepsilon(\nu) - i\sigma/(\varepsilon_0\omega)]C$.

condition

$$Z_x/Z_0 = Z_1/Z_2 = R_1/R_2 \tag{81}$$

where

$$Z_j^{-1} = R_j^{-1} + i\omega C_j\,, \qquad j = 0, 1, 2, x. \tag{82}$$

Hence the bridge is balanced if

$$C_x/C_0 = (R_1/R_2 - R_0/R_x) \tag{83}$$

and

$$\omega^2 = (C_x R_x C_0 R_0)^{-1}. \tag{84}$$

Auto-balancing bridge methods are based on the simplified diagram shown in Figure 55. A current, flowing through the unknown impedance Z_x, also flows through resistor R. The potential at point L is maintained at 0 V since, due to the operational amplifier, the current through R balances with that through Z_x. Because of the high input impedance of the amplifier (3, Fig. 55) the voltage across resistor R effectively measures the current. Hence the unknown impedance is calculated using voltage measurement at terminal H and across R, also determining the phase of the signal. Commercial instruments differ by the degree of sophistication of the phase detectors and other modules. Two channel vector voltage analyzers may be used for voltage and phase measurement of both voltages. This type of automated bridges is capable of a maximum frequency around 100 MHz.

A variety of modifications of the measurement principle sketched in Figure 55 have been designed, such as the Fourier correlation analyzer [167] and the so-called dielectric converter depicted in Figure 56. The

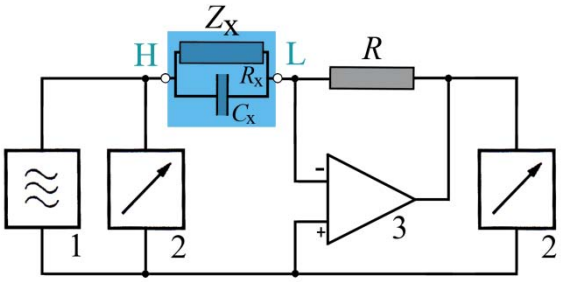

Figure 55: Schematic of auto-balancing bridge for measuring the complex impedance Z_x of a specimen cell ($Z_x^{-1} = R_x^{-1} + i\omega C_x$): 1, signal source; 2, voltage meter; 3, operational amplifier.

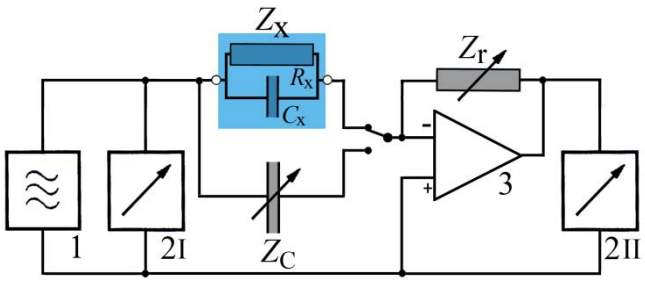

Figure 56: "Dielectric converter" principle at ν < 100 kHz [310]: 1, signal generator; 2I, 2II, vector voltage analyzer, channels I and II; 3, operational amplifier.

latter offers a superior accuracy from a reference measurement with a precisely known capacitor. Knowledge of impedance Z_r can then be avoided by calculating the unknown impedance according to

$$Z_x = - Z_C V_C / V_x, \tag{85}$$

where

$$V_j = U_{II}/U_I, \quad j = x, C \tag{86}$$

are the ratios of voltage readings at analyzers II and I, respectively, with the sample (x) and the reference measurement (C).

Alternatively, a two-channel network analyzer may be used. The block diagram of an instrument that can be rather easily built from commercial components is displayed in Figure 57 where the measurement and reference channels are distinguished by light grey and moderate yellow. Consider briefly one of the identically constructed channels.

The sinusoidal measurement signal with frequency ν is provided by a direct digital synthesizer DDS (1, Fig. 57) and is amplified by the terminal amplifier 3. After passing the unknown impedance Z_x or reference impedance Z_r, respectively, it is operated by a superheterodyne receiver. For this purpose it is combined in a mixer (4) with the signal of frequency ν_+ which, generated by a second DDS, is shifted by 10 kHz with respect to ν. If the mixer is operated in its linear regime the amplitude of the intermediate-frequency (IF) signal is proportional to the magnitude $|U_o|$ of the unknown (or reference) impedance output. In order to reduce annoying noise, the IF signal is amplified by a smallband 10 kHz amplifier (5) and analog/digital converted (6). It is combined in the digital processor (DSP) board (7) of a minicomputer (8) with a reference signal, the amplitude of which is proportional to the magnitude $|U_i|$ of the input signal of Z_x (or Z_r). The real and

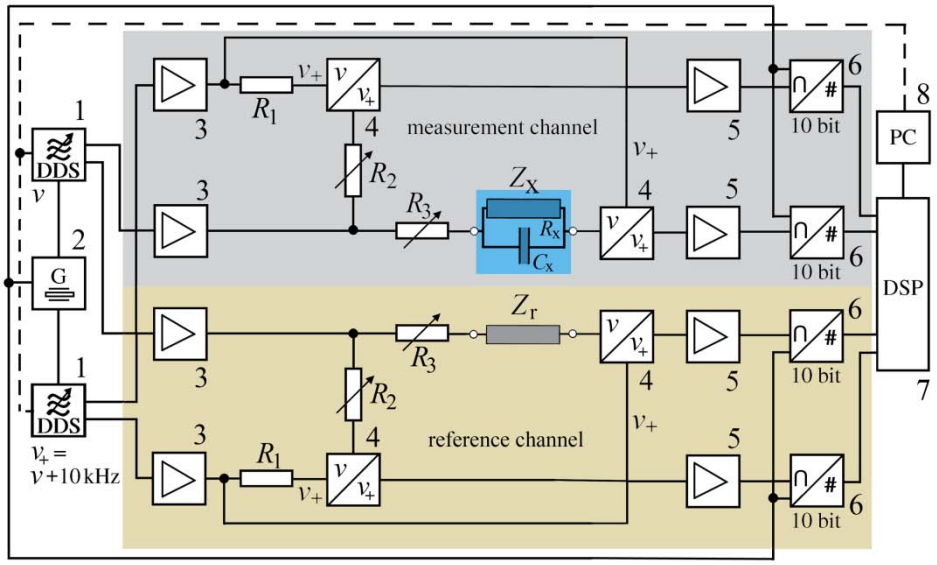

Figure 57. Low-priced home-made two-channel vector network analyzer for measurement up to MHz frequencies [311]: 1, direct digital synthesizer (25 MHz); 2, quartz-controlled generator (50 MHz); 3, terminal amplifier; 4, mixer; 5, small-band amplifier 10 kHz; 6, analog/digital converter; 7, digital processor board of 8, process control computer. Z_x is the unknown impedance and Z_r the impedance of the reference.

imaginary parts of the transfer functions of Z_x (or Z_r), i. e. the voltage ratios $U_o(\nu)/U_i(\nu)$ are obtained from sampling U_o both, in phase with U_i and at phase shift $\pi/2$ with respect to U_i. Such phase shift simply corresponds with a fixed delay ΔT_{IF} (= 25 µs) of a quarter period in the 10 kHz intermediate frequency signal. In order to ensure high frequency stability of the instrument, the DDS generators (1) and A/D converters (6) may be controlled by a 50 MHz clock (2).

Appropriate sampling enables efficient calculation of the the desired transfer functions $U_o(\nu)/U_i(\nu)$ of the unknown and reference impedances. If the mth sample value of voltage U is denoted by U_m, the amplitude $\hat{U}$ of signal $U(t) = \hat{U}\sin(\omega t)$ results as [311]

$$\hat{U} = \left(\frac{\pi}{4M}\right) \sum_{m=0}^{M} |U_m| \qquad (87)$$

and the phase difference may be obtained from the consideration of each voltage also at $m + M/4$, where its phase is shifted by π/2. Here M is the

total number of samples taken in the discretization process. Using the average φ of the phase shifts at all different m, the complex transfer functions for both channels of the analyzer follow as

$$(U_o/U_i)_{x,r} = (\widehat{U}_o/\widehat{U}_i)_{x,r}\exp(i\varphi_{x,r}). \tag{88}$$

3.1.2.3 Specimen cells, electrode polarization

Whereas a variety of sophisticated LCR bridges, impedance analyzers, and network analyzers are commercially available for low-frequency measurements, the design of adequate specimen cells is still a challenging task and a topic of intense scientific debate. In particular two problems have to be resolved in careful complex permittivity determinations, the effect from fringing fields at the edges of capacitor cells and the impact of electrode polarization due to retarded discharge of ions.

Fringing fields are widely known for plate capacitors which till this day are popular cells for measurement in the frequency range between 10^{-6} and 10^{7} Hz [312-317]. As already discovered by Kirchhoff [315], the fringing field contributions to the capacitance of a spherical plate capacitor filled with a sample of complex permittivity $\varepsilon_{tot}(\nu) = \varepsilon(\nu) - i\sigma/(\varepsilon_0\omega)$ amount to

$$C_f(\nu) = \varepsilon_{tot}(\nu)[\ln(16\pi r_C^2/d) - 1], \tag{89}$$

where r_C denotes the radius of the capacitor plates and d their spacing. Hence the total measured capacitance

$$C_m(\nu) = C(\nu) + C_f(\nu) = \varepsilon_{tot}(\nu)r_C[\pi r_C/d + \ln(16\pi r_C/d) - 1] \tag{90}$$

may exceed the capacitance $C(\nu) = \pi r_C^2\varepsilon_{tot}(\nu)/d$ of the ideal resonator without fringing fields by a considerable amount. As suggested intuitively, the edge effects are especially strong at large d. In measurements at small sample conductivity σ, as small as possible d/r_C ratios are thus to be preferred.

Alternatively, contributions from fringing fields may be avoided by three-terminal guard-ring capacitor cells [313, 315, 317-320]. As indicated by the schematic in Figure 58, the guard ring and the shielded center electrode are kept at identical potential but, in order to prevent contributions from the fringing field, only the current charging the center electrode is measured.

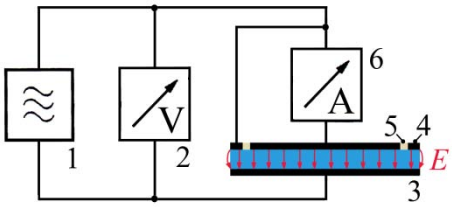

Figure 58. Simplified diagram of a system using a guard-ring capacitor cell: 1, signal generator; 2, voltage meter; 3, three-terminal capacitor with 4, guard ring and 5, insulating ring; 6, current meter. Electrical field lines are shown in red.

Guard ring capacitors can be also used in order to reduce electrode polarization effects. Usually the electrodes along with their polarization layers are represented by a resistance $R_\mathrm{p}(\nu)$ in series with a capacitance $C_\mathrm{p}(\nu)$. If $Z_\mathrm{x}(\nu)$ denotes again the sample impedance and $Z_\mathrm{p}(\nu)$ the impedance of one of the electrode polarization layers of a circular capacitor with radius r_C, the total impedance of the cell is given by [321]

$$Z_\mathrm{C}(\nu) = 2Z_\mathrm{p}(\nu) + Z_\mathrm{x}(\nu) = 2R_\mathrm{p}(\nu) - \frac{i}{\pi\nu C_p(\nu)} + \frac{d}{\sigma(\nu) r_C^2} \frac{1-\frac{2i\pi\nu\varepsilon_0\varepsilon(\nu)}{\sigma(\nu)}}{1+[\frac{2\pi\nu\varepsilon_0\varepsilon(\nu)}{\sigma(\nu)}]^2}, \qquad (91)$$

where d is the electrode spacing and $\sigma(\nu)$ the sample conductivity. So as to accentuate the sample term relative to the electrode polarization term, the electrode spacing d should be as large as possible, at variance with the requirement for small effects from fringing fields (Eq. 90). Obviously, guard-ring cells can best account for such conflicting requirements. Use of electrode material with lowest possible resistance and largest possible capacitance leads to a reduction of the electrode polarization parts in Eq. (91) and thus also contributes to distinguish the sample part. For that reason platinum black electrodes are preferably employed. With many samples, however, requirements for easy cleaning of the cell call for polished electrode surfaces.

Since electrode resistance $R_\mathrm{p}(\nu)$ and capacitance $C_\mathrm{p}(\nu)$ are unknown from theory, measurements at different electrode spacing are required [302, 317, 322-328]. At two frequencies the results from measurements of an aqueous suspension at varying electrode distance d is displayed as apparent permittivity

$$\varepsilon'_a(\nu,d) = -\,\mathrm{Im}\{1/Z_\mathrm{C}(\nu,d)\}/[2\pi\nu C(d)]$$

$$= Z''_C(\nu,d)d/[2\cdot|Z_\mathrm{C}(\nu,d)|^2\varepsilon_0\pi^2\nu r_C^2] \qquad (92)$$

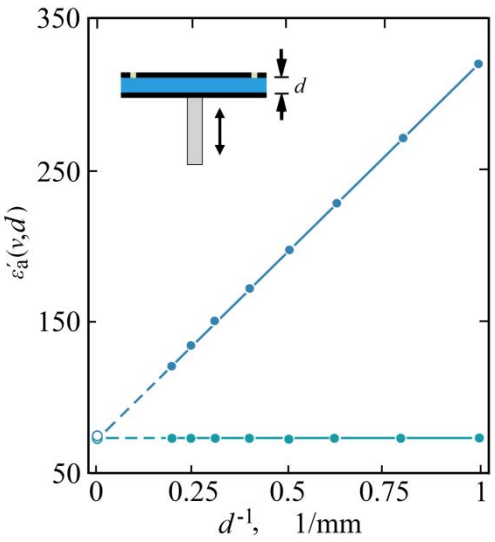

Figure 59. Real part $\varepsilon'_a(\nu,d)$ of the apparent permittivity (Eq. 92) of an aqueous solution of a phospholipid bilayer vesicle suspension at 30°C, displayed as function of inverse electrode distance d^{-1} [329]. The lipid concentration is 0.1 mol/l, the electrical conductivity 0.0077 S/m. Points represent experimental data (blue: 10.1 kHz; turquoise: 500.1 kHz), circles indicate extrapolation to $d^{-1} = 0$. The inset shows a sketch of guard ring capacitor with variable d ($r_C = 3.4$ mm).

in Figure 59. Hence $\varepsilon'_a(\nu,d)$ is calculated on the assumption of an ideal capacitor. The data clearly shows independency from d and thus vanishing electrode polarization effects at 500 kHz. At 10 kHz, however, the contributions from the undesired electrode layers predominate at $d < 5$ mm. Presuming, at sufficient spacing, the polarization layers independent of d, the $\varepsilon'_a(\nu,d)$ data can be extrapolated to yield the "true" $\varepsilon'(\nu)$. For the present sample $\varepsilon' = 73.8 \pm 0.5$ results at 500.1 kHz and $\varepsilon' = 74.0 \pm 1.5$ at 10.1 kHz. This example also shows that a meaningful determination of the sample permittivity by electrode distance variation is imposible at significantly lower frequencies or distinctly larger electric conductivity. Various numerical techniques have been proposed [330-334] for postprocessing experimental data for further reduction of influences from electrode polarization layers.

A different approach to determine the permittivity of conducting samples at low frequencies is the use of four-electrode instead of three-terminal cells. Such devices are provided with two electrode pairs as sketched in Figure 60. One pair is used for feeding the current, the other one for measurement of a potential difference outside the electrode polarization layers [335-339]. The concept procedes from the idea that the correct current is measured by the amperemeter and that the measurement of the potential difference with thin electrodes outside the polarization layer zones of the current electrodes remains unaffected of these layers. Electrode polarization effects at the potential electrodes are further reduced

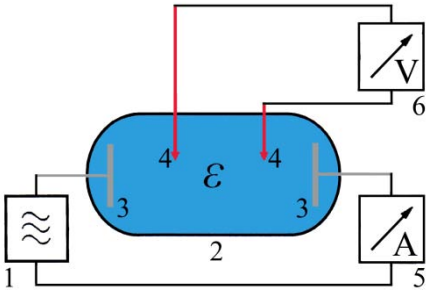

Figure 60. Four-electrode cell for measurement of dielectric materials (ε) at low frequencies: 1, signal source; 2, sample cell; 3, ample current electrodes; 4, thin electrodes to determine the potential difference between two sites; 5, amperemeter; 6, high-impedance voltage meter.

by a high input impedance, i.e. by reducing current flow to a minimum. Nevertheless electrode polarization effects are not easily diminished [334]. For that reason, using sophisticated electrode design and arrangement the available measurement range at given sample conductivity can indeed be extended to lower frequencies. But interferences can not be completely eliminated.

From a theoretical point of view electrodeless measurement of the dielectric properties of materials by exposing the sample to the electromagnetic field of a coil instead of a capacitor is a promising alternative [340]. In practice, however, the coupling of dielectric samples to the field of the coil is too weak to enable a sufficient accuracy in quantitative measurements.

3.1.3 THz spectroscopy

There is a continuing interest in the properties of materials in the far infrared (FIR) region, now often named the THz frequency range. These properties are capable of providing valuable deeper insights into the intermolecular interactions of condensed matter. An illustrative example is the dielectric spectrum of water (Fig. 19) the THz part of which is accentuated in the complex plane representation of data in Figure 61. In such representation, also called Cole-Cole plot [341], the negative imaginary part $\varepsilon''(\nu)$ of the complex permittivity (Eq. 28) is displayed as function of the real part $\varepsilon'(\nu)$, the frequency ν being parameter. The benefit of such a (Cartesian) plot is the often simple locus of the data. If we take the Debye relaxation function (Eq. 78) as example, the negative imaginary part reads

$$\varepsilon''(\nu) = \frac{\Delta\varepsilon\omega\tau}{1+(\omega\tau)^2} \tag{93}$$

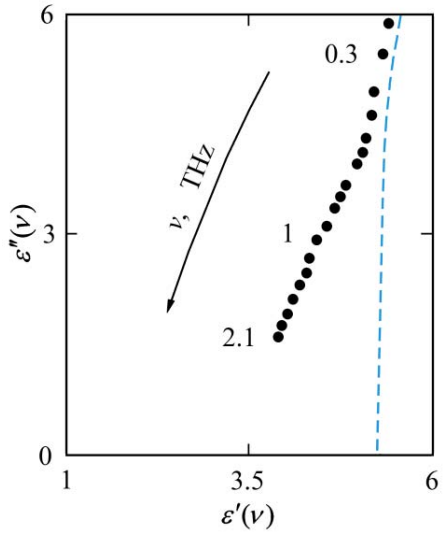

Figure 61. High-frequency part of the dielectric spectrum of water at 19 °C (Fig. 19) in a complex plane representation. Points show the experimental data in the THz region. The dashed blue line depicts the extrapolation from the dominating Debye relaxation with relaxation frequency in the microwave region (Fig. 19).

and the real part

$$\varepsilon'(\nu) = \varepsilon(\infty) + \frac{\Delta\varepsilon}{1+(\omega\tau)^2}, \tag{94}$$

where again $\Delta\varepsilon = \varepsilon(0) - \varepsilon(\infty)$ denotes the relaxation amplitude. Hence relation

$$[\varepsilon'(\nu) - \varepsilon(\infty) - \Delta\varepsilon/2]^2 + [\varepsilon''(\nu)]^2 = \Delta\varepsilon^2, \tag{95}$$

holds, revealing the data to follow a semicircular arc with diameter $\Delta\varepsilon$ and center at $\varepsilon' = \varepsilon(\infty) + \Delta\varepsilon/2$ and $\varepsilon'' = 0$.

The experimental data in Figure 61 clearly disclose a relaxation in the THz frequency range in addition to the principal relaxation that governs the microwave dielectric spectrum of water. This THz relaxation is an essential attribute of the molecular dynamics of water and is of paramount significance for modelling the hydrogen network fluctuations of the liquid. Likely THz technologies will therefore also contribute to the future development of electromagnetic moisture measurements. This is particularly true as recent progress in THz spectroscopy [159, 342, 343] has greatly facillitated measurements procedures and increased experimental accuracy as compared to previous submillimetre wave Fourier transform techniques [344-347] which are based on weak continuous radiation from

suitable lamps. Also worth mentioning are methods utilizing coherent signal sources [348-350], such as the vector network analyzer approach introduced below.

The THz network analyzer set-up sketched in Figure 62, combining broadband applicability with a superior signal-to-noise ratio, corresponds to common practice in radio frequency and microwave measurements. It involves a conventional microwave vector network analyzer (VNA, Fig. 62), the frequency ν_{mw} of its output microwave signal being transformed to the required THz range by diode multipliers (3). The resulting signal with frequency $\nu = n\nu_{mw}$ (n integer > 1) propagates in a free-space geometry, marked by moderate yellow in the figure. With the aid of a beam splitter (5), part of the THz signal is received by an antenna (8) and downconverted by a mixer (10). For this purpose the mixer is provided with the signal from a local oscillator (9) which is locked to the generator of the microwave VNA. At suitably chosen frequency ν_{lo} harmonics of the local oscillator signal provide appropriate beat signals when mixed with the measurement signal of frequency ν. The beat signal with intermediate frequency is received by the reference input port (R) of the VNA. The other part of the THz signal is focused to the specimen cell (7) and, after transmission

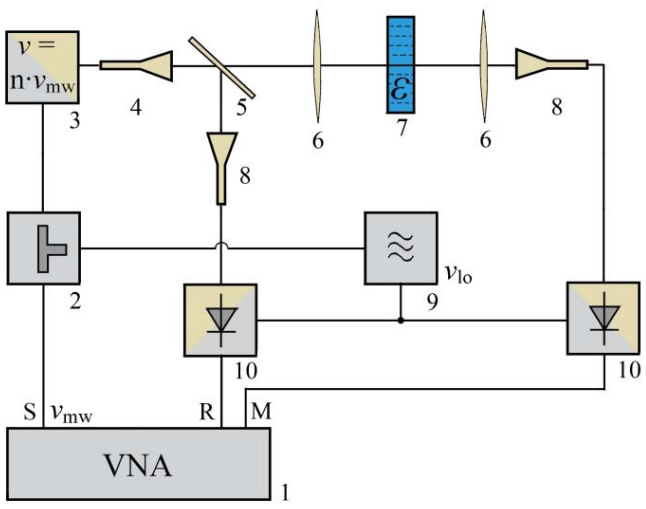

Figure 62. Schematic of a THz vector network analyzer arrangement: 1, microwave network analyzer with signal port (S) and reference signal (R) as well as measurement signal (M) inputs; 2, signal splitter; 3, harmonic multiplier; 4 transmitting antenna; 5, beam splitter; 6, lens; 7, sample cell; 8, receiving antenna; 9, local oscillator; 10, mixer and signal detector. The microwave part of the set-up is colored by grey, the THz part by moderate yellow.

through the sample, received by another antenna (8). In correspondence with the reference branch the sample signal is also downconverted by mixing (10) with the signal from the local oscillator (9) and is fed to the measurement input port (M) of the VNA. A reflection-transmission mode is easily feasible by supplying the reference port (R) of the VNA with the signal reflected from the sample cell [349].

Using such an arrangement, frequency-domain measurements over the range of 0.065 to 0.72 THz have been reported. Likely, the usable range will extend to even higher frequencies in the near future. An attractive alternative are THz TDS techniques, which will be discussed in the time domain techniques chapter below (section 3.2.4).

3.2 Time domain techniques

The favored term "time domain spectroscopy", mostly referred to as "TDS", comprises various measurement methods. Time domain reflection techniques are frequently applied so that the short term "TDR" is often used instead of the more generell abbreviation TDS. The majority of TDS techniques in use consist of the observation of the sample response to exciting pulses. In so-called slow-response techniques the relaxation of the sample properties after excitation by a step-voltage pulse is directly observed (section 3.2.2). Such techniques aim at the elucidation of processes with relaxation times significantly larger than the rise-time of the exciting pulses. On the contrary, fast-response TDS techniques (section 3.2.3) are applied to processes with relaxation times on the order of the rise time of the pulses, which may be as small as 15 ps. Hence in fast response TDS the change in shape of pulses when reflected from or transmitted through a sample is evaluated. THz TDS employs subpicosecond pulses (section 3.2.4) which are split to utilize one part for sample excitation and the other one for probing the sample at different times after excitation.

Fundamentally, the pulses used to excite the sample feature an unfavourable concentration of energy in a short range of time and thus make high demands on the linearity of the sample and the dynamic range of the experimental setup. Exposure of the sample to (pseudorandom) noise combined with cross-correlation analysis between the exciting signal and the response to it [351-353] yields the desired autocorrelation function $\Psi(t)$ of polarization (Eq. 13) in a more favorable manner. The noise spectrum is flat and thus the energy is distributed over a tremendously broad frequency range. Unfortunately, even though noise excitation of the sample has been applied in FIR Fourier transform spectroscopy [346] for long,

little use is made of it in radiofrequency and microwave measurements of materials.

In addition to time domain spectroscopy, time domain techniques are employed to yield the dielectric properties of materials from transient times and thus group velocity determination. Alternatively, if the group velocity is known or additionally measured, dielectric property profiles can be obtained from transient times of reflected pulses. Such approaches at a preselected single frequency are briefly discussed in the following section.

3.2.1 Transient time measurement, permittivity profiles

If, for simplicity, the losses are assumed negligibly small ($\varepsilon'' \approx 0$), i.e. if $\alpha\lambda \ll 2\pi$ (Eq. 41), the real part $\varepsilon'$of the permittivity can be simply obtained from phase velocity measurements using Eq. (36) as $\sqrt{\varepsilon'} = c_0/c$. Convenient methods in use obtain c from the time interval Δt which a sharp pulse needs to propagate through a distance Δx within the sample. Strictly, however, this time interval is controlled by the group velocity

$$c_g = \mathrm{d}\omega/\mathrm{d}\beta, \tag{96}$$

namely the propagation velocity for amplitude-modulated signals. From $c = \omega/\beta$ follows

$$\mathrm{d}\omega = c\mathrm{d}\beta + \beta\mathrm{d}c \tag{97}$$

and thus

$$c_g = c + \beta\mathrm{d}c/\mathrm{d}\beta \tag{98}$$

as well as

$$c_g^{-1} = c^{-1} + (\nu/c^2)(\mathrm{d}c/\mathrm{d}\nu). \tag{99}$$

Hence the group velocity c_g of medium equals the phase velocity c only if no dispersion exists ($\mathrm{d}c/\mathrm{d}\nu = \mathrm{d}\varepsilon'/\mathrm{d}\nu = 0$). According to the fluctuation-dissipation theorem [354, 355] and the Kramers-Kronig relations [356, 357], missing dispersion corresponds with the presumed absence of dielectric loss ($\varepsilon'' = 0$).

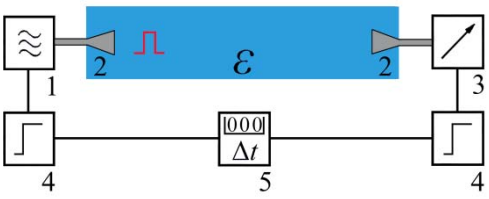

Figure 63. Scheme of transient time measurement in material with permittivity ε using sharp pulses: 1, signal source; 2, antenna; 3, signal detector; 4, trigger; 5, start-stop timer.

The principle setting of a set-up for velocity determination by transient time measurement is sketched in Figure 63. A sharp pulse is transmitted through the material using a transmitting and receiving antenna (2), respectively, and suitable trigger control (4) simply activates a start-stop timer.

Figure 64 illustrates the idea of permittivity profile observation from transient time measurements. If the phase (or group) velocity of the material is known or if it is obtained from additional measurement, such as sketched in Figure 63, an antenna array may be used to determine the positions of changes in the dielectric properties of the material under observation. Often the atennas are operated in a reflection mode, using a multiplexer to scan the array.

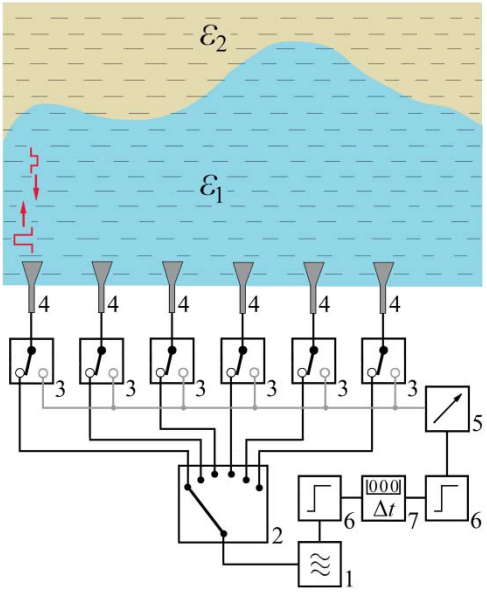

Figure 64. Schematic of antenna array for permittivity profile determination. Transient time measurements of pulses reflected at the interface between permittivities ε_1 and ε_2 of the material are used: 1, signal generator; 2, multiplexer; 3, switch; 4, antenna; 5, signal detector; 6, trigger; 7, start-stop timer.

3.2.2 Slow response spectroscopy

In slow response time domain spectroscopy, an electrical field is suddenly applied or removed from a capacitor filled with (or a probe attached to) the sample under consideration and the responding transient current or electrical charge is monitored. If the rise time t_s of electrical field and the charge time $t_c = R_0 C_x$ of the capacitor (or probe) are distinctly smaller than the relaxation time τ of the sample permittivity, the autocorrelation function $\Psi(t)$ of polarization (Eq. 13) can be directly taken from the transient current (Fig. 65). Here R_0 is the resistance of the cicuit and $C_x = \varepsilon(\nu)C$ the capacitance of the sample cell, where C denotes the void capacitance. Slow response techniques are applied in measurements at times between roughly 10^5 and 10^{-7}s, corresponding with the frequency range from about 1 μHz to 1 MHz [358-363]. They are thus especially adapted to studies of extremely slow relaxation phenomena, such as molecular processes in supercooled liquids [363, 364] or in the glassy state [152]. An example accentuating the capability of dc transient current methods is shown in Figure 66, where the dielectric spectra of poly (vinyl acetate) are shown at four temperatures. As common practice in time domain spectroscopy, the experimental data has been converted to the frequency domain using Laplace transform (Eq. 29).

Slow-response time-domain techniques in use are mostly based on a charge compensation method as sketched in Figure 67. Step voltage generators (1, Fig. 67) provide positive (U_+) and negative (U_-) voltage steps which are applied across the sample capacitor $C_x = \varepsilon C$ and the reference capacitor C_r, respectively. The charge detector, basically an operational amplifier (4) with feedback capacitor C_f, yields an output voltage $U_o = (Q_r - Q_x)/C_f$ proportional to the net charge induced by the step voltages. Here Q_r and Q_x are the charges of the reference and the sample capacitor, respectively. The integrating circuit, formed by the operational amplifier and its feedback capacitor, virtually causes zero signal at the amplifier input. It therefore ensures that the potentials of the sealed measurement and

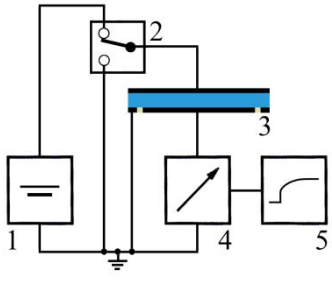

Figure 65. Basic set-up of slow-response time-domain spectrometer [358]: 1, dc voltage source; 2, switch for charging or discharging the 3, guard-ring sample capacitor; 4, signal detector, e.g. electrometer; 5, display unit.

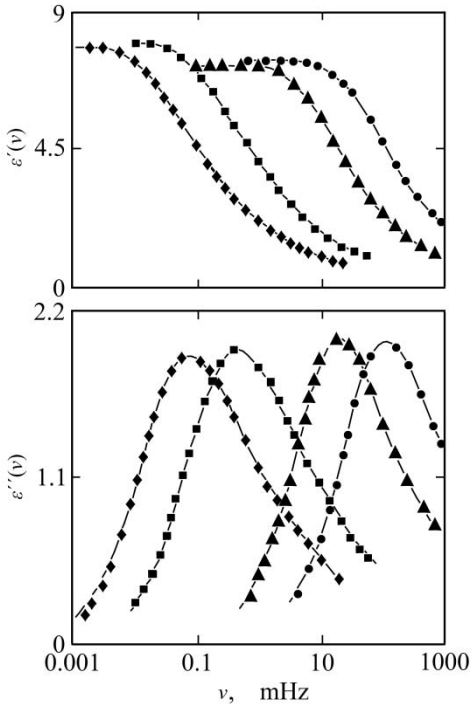

Figure 66. Real part $\varepsilon'(\nu)$ and negative imaginary part $\varepsilon''(\nu)$ of the complex dielectric spectrum of poly(vinyl acetate) at four temperatures [151]: ♦, 28.10 °C; ■, 29.75 °C; ▲, 36.01 °C; ●, 38.00 °C. The data in the frequency range 10^{-6} to 1 Hz have been obtained with the aid of two slow-response time-domain apparatus.

reference capacitor electrodes precisely follow that of the guard rings. The symmetric structure of the set-up reduces significantly the dynamic-range requirements and thus warrants linearity in the measured response function.

Applying special pulse sequences and utilizing the time as an explicite variable thereby allows for a considerable extension of the area of application [363]. Emphasis may thus be placed on suppression of specific

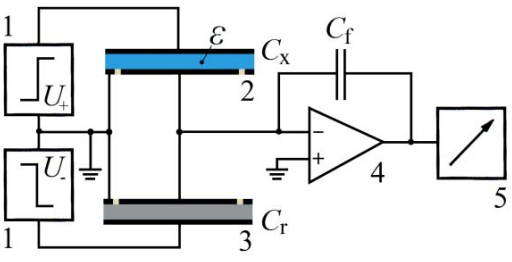

Figure 67. Circuit for slow-response time domain spectrometry against a reference [362]: 1, positive and negative step-voltage generators; 2, guard-ring sample capacitor; 3, reference capacitor; 4, operational amplifier with feedback capacitor C_f; 5, detector.

contributions to the relaxation function and also on the observation of non-equilibrium conditions, offering, for example, the possibility to study memory effect as relevant in glass-forming liquids.

3.2.3 Fast response spectroscopy

In studies of polarization processes with shorter relaxation times ($\tau < 10^{-7}$ s) the finite rise time t_s of the exciting pulse and/or the charge time t_c of the sample cell act a noticeable influence on the transient current. On such events the change in shape of a step-voltage pulse after reflection by or transmission through the sample is observed and analyzed in terms of the material properties. Normally, the complex permittivity spectrum is obtained as the ratio of Fourier transforms of the responding and the incident waveforms [231, 365-372]. Transformation to the frequency domain can indeed be avoided by direct evaluation of the dielectric properties from a real-time analysis of the waveforms in the time domain [373-375]. Because of their approximate character, however, the range of applicability of such procedures is limited. In addition, Fourier transformation permits an easy inclusion of frequency domain data in the evaluation and discussion of dielectric spectra.

Fast-response TDS rests upon coaxial line technology (Fig. 68). A train of fast rising pulses with rise time shorter than 35 ps is produced by a tunnel diode step generator (2, Fig. 68) and propagated along a suitable

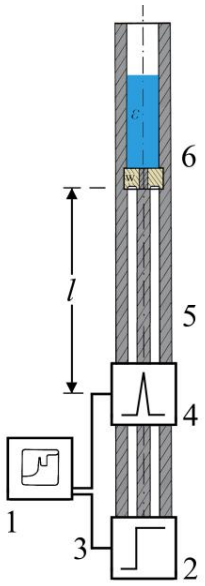

Figure 68. Scheme of a fast-response time-domain reflectometer: 1, sampling scope combined with minicomputer for process control as well as data acquisition and evaluation; 2, tunnel diode step-voltage generator; 3, trigger line; 4, sampling head; 5 coaxial line; 6, sample cell or dielectric probe.

coaxial line (5). In the commonly applied time domain reflectometry (TDR) the pulses are reflected at the impedance mismatch caused by the sample cell (6). Both the incident and the reflected waveforms are detected at some point of the coaxial line by a voltage probe (4), essentially the gate of a sampling system (1). Being thus transformed to an extended time scale the signals are analogue / digital converted and further processed by a computer. Automated data processing is unavoidably necessary in fast-response TDS measurements because the information about the sample properties is contained just in a deformation of the non-ideal responding pulses. Hence a detailed numerical analysis is required for the proper extraction of the dielectric properties from the measurement signals.

In correspondence to bridge circuits (Fig. 54) and microwave interferometers (Figs. 26, 27, 32) in frequency domain spectroscopy, as well as charge compensation set-ups (Fig. 67) in slow-response TDS, fast response time domain spectroscopy may also benefit from difference methods [192, 373-376]. Using such methods the sensitivity in the measurements is noticeably enhanced by comparison of signals $S(t)$ and $S_r(t)$ as reflected from the sample and reference cell, respectively (Fig. 69). Furthermore, errors due to unwanted reflections from impedance mismatch within the coaxial line system largely cancel each other if identical cells (or probes) are used and if the dielectric properties of the reference material are chosen to closely match to those of the sample. An important aspect is the identical long-time stationary value of $S(t)$ and $S_r(t)$ if, in investigations of

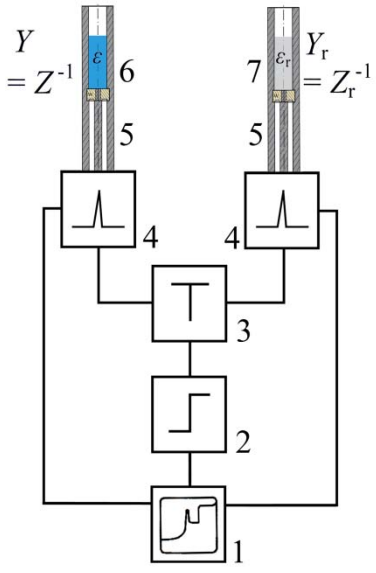

Figure 69. Schematic circuit of a two-channel fast-response time-domain reflectometer: 1, sampling scope combined with a minicomputer; 2, tunnel diode step-voltage generator; 3, power splitter; 4, sampling head; 5, coaxial line; 6, sample cell or dielectric probe; 7, reference cell or probe.

electrically conducting samples, the conductivity of the reference is appropriately adjusted.

Transmission line theory yields

$$r_{\mathrm{r}}(\nu) - r(\nu) = \frac{2}{(1+ Z_0 Y_r)^2} \cdot \frac{Z_0(Y-Y_r)}{1+\frac{Z_0(Y-Y_r)}{1+Z_0 Y_r}} \tag{100}$$

for the difference of the reflection coefficients $r_r(\nu)$ and $r(\nu)$ of the reference and the sample cell, respectively. Here Y_{r} and Y are the corresponding input admittances of the cells, as indicated in Figure 69, Z_0 is the characteristic impedance of the feeding coaxial lines. With $C(\nu) = -\mathrm{i}Y(\nu)/\omega$ and $C_{\mathrm{r}}(\nu) = -\mathrm{i}Y_{\mathrm{r}}(\nu)/\omega$ follows

$$C(\nu) - C_{\mathrm{r}}(\nu) = \frac{s_r(\nu)-s(\nu)}{i\omega Z_0 u(\nu)} \cdot \frac{(1+Z_0 Y_r(\nu))^2}{2-(1+Z_0 Y_r(\nu))(s_r(\nu)-s(\nu))/u(\nu)} \tag{101}$$

Hence at low frequencies, where the cells or probes, like the open-ended devices (Fig. 35) can be represented by a parallel circuit of two capacitances, the sample permittivity

$$\varepsilon(\nu) = \varepsilon_{\mathrm{r}}(\nu) C(\nu)/C_{\mathrm{r}}(\nu) \tag{102}$$

is directly given by the permittivity $\varepsilon_r(\nu)$ of the reference. In equation (101) $s(\nu)$ and $s_r(\nu)$ are the Fourier transforms of the reflected $S(t)$ and

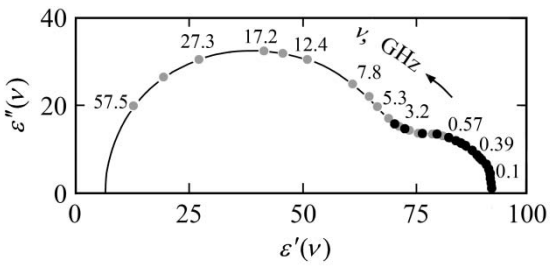

Figure 70. Complex plane representation of the dielectric part of the dielectric spectrum of a 0.1 mol/l solution of $Al_2(SO_4)_3$ in water at 25 °C: σ = 2.1 S/m, pH = 2.0 [192]. Black points show TDR data at 10 MHz ≤ ν ≤ 3 GHz, grey points indicate data from frequency domain measurements in the range 500 MHz ≤ ν ≤ 58 GHz. In addition to the solvent relaxation at high frequencies, the spectrum reveals contributions from dipolar ion complex structures at lower frequencies. Such structures will be discussed in chapter 4.

$S_r(t)$, respectively, and $u(\nu)$ is the Fourier transform of the incident pulse $U(t)$. The performance of the TDR difference method is demonstrated by the spectrum of a strongly conducting aqueous electrolyte solution displayed in Figure 70. Regardless of the considerable conductivity contributions to the total permittivity, the time domain data nicely displays a dielectric relaxation at low frequencies and they also fit well to the frequency domain results for the same sample.

The TDR data in Figure 70 has been obtained with a shielded cut-off cell with vanishing coaxial line part (b, Fig. 36). Such cells as well as the flanged (a, Fig. 35) and unflanged (a, Fig. 36) coaxial line sensor are most popular in TDR measurements. In spite of the merits of two-channel fast-response time domain reflectometry, TDS investigations into the properties of electrolyte solutions have, of course, to also carefully consider electrode polarization effects. Like in frequency domain measurements, provisons can be made to reduce the disturbances by such effects [331].

Present advanced electronics restrict jitter, time drift and fluctuations in the sweep frequency of time domain spectrometers effectively. As a result dielectric spectra up to 25 GHz are obtained from the pulse response signals [377]. Sophisticated high-speed sampling techniques contribute also to the stability and time resolution of the measurement systems and are an important element in the extension of the applicability of time domain spectroscopy to high frequencies. A high accuracy in TDS measurements is achieved by parallel-time non-uniform sampling techniques, enabling a superior time resolution in probing the most relevant parts of signals $U(t)$, $S(t)$, and $S_r(t)$ and allowing also for an adequate probing of the long time behavior of these waveforms [363]. Such means help to effectively reduce baseline and truncation errors.

3.2.4 THz time-domain spectroscopy

As a complement of the THz network analyzer measurement technique presented in section 3.1.3, THz time-domain spectrometry has been applied with considerable success [146, 157-160, 378-383]. An example of a THz time-domain spectrometer is depicted in Figure 71. The pulse train provided by a femtosecond pulse laser (1, Fig. 71) is divided in two parts with the aid of a beam splitter (2). One part is used for generating the THz signal that is applied to the sample. The other one is used as a probe signal for the gated detection of the THz measurement pulses. The latter pulses are produced when the optical pulses strike the emitter (6), i.e. a metal-semiconductor-metal structure forming a photoconductive switch. The

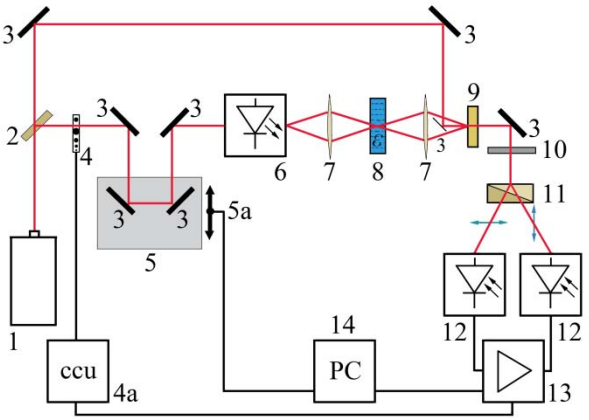

Figure 71. Terahertz time-domain transmission spectrometer [379]: 1, femtosecond laser; 2, beam splitter; 3, mirror; 4, chopper with 4a, chopper control unit; 5, delay stage with 5a, position control; 6, emitter; 7, lens; 8, sample cell; 9, electro-optic crystal; 10, quarter wave plate; 11, Wollaston prism; 12, photodiode; 13, lock-in amplifier; 14, process control computer.

measurement pulses are focused onto the sample (8) and combined with the probe pulses so that both beams arrive simultaneously at the sampling detection system, consisting of an electro-optic crystal (9), a quarter-wave plate (10), a Wollaston prism (11), and a pair of balanced photodiodes (12). A photocurrent is induced in the electro-optic crystal when a probe pulse coincides both spatially and temporally with a THz pulse. Since the probe pulses are distinctly shorter than the THz pulses they can be used to repeatedly sample the THz waveforms utilizing an optical delay line (5). Since the bandwidths of the detected pulses are limited by the finite detector response, measurements are normally made relative to a reference, such as an identical cell without sample.

Time domain measurement techniques of this type have been used to obtain THz permittivity data for water, as included, for instance, in the spectrum shown in Figure 19.

3.3 Dielectric imaging

During the past years considerable progress has been achieved in electromagnetic imaging, especially in biomedical applications [384, 385]. Nameable examples are ventilation and perfusion monitoring [386-391], breast cancer detection [392-397], brain activity observation [398-401], and fetomaternal examination [402-404]. Industrial utilization involves systems for multiphase flow imaging [405-409], for semiconductor junction [410] and nanocrystal [411] characterization, as well as for non-intrusive densi-

ty mapping of wood [412, 413]. Betimes dielectric imaging techniques will likely play a significant role also in the monitoring of varying moisture distribution of materials [414]. On that account principles of the prevailing imaging methods are briefly reviewed below.

3.3.1 Scanning microwave microscopy

The combination of network analyzer measurement performance with superior scanning microscope spatial resolution enables unique microwave images of materials [415-422]. In the standard mode of operation a microwave signal of a VNA is fed to a thin probe tip. Microwaves at frequencies up to 6 GHz are commonly applied to the tip. A set-up is shown in Figure 72. The central part is a coaxial cavity resonator which is used to reach optimum sensitivity by operating the device close to the resonance frequency. The signal reflected from the tip depends on the load impedance of the tip. As the load impedance reflects the electrical field between the tip and the sample under test, the reflected signal contains information on the local dielectric properties of the sample, including the electrical conductivity. Hence the sample's dielectric properties act an influence on the resonance frequency and the half-power bandwidth of the cavity resonator. Evaluation of the resonance curve at a given position of the sample thus yields information on its local dielectric properties so that variation of the sample position in a controlled mode allows for the scanning of the dielectric properties across the sample. A movable short circuit (7, Fig. 72) enables optimum adjustment of the cavity resonator.

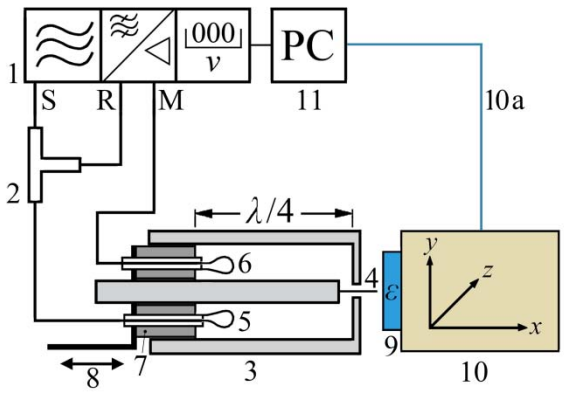

Figure 72. Scheme of a scanning microwave microscope using a tunable coaxial resonator for sensitivity enhancement [415]: 1, network analyzer; 2, power splitter; 3, coaxial cavity resonator with 4, probing tip, 5, feeding antenna, 6, receiving antenna, and 7, moveable short; 8, short circuit drive; 9, sample; 10, *x, y, z* – stage; 10a, control line; 11, process control computer.

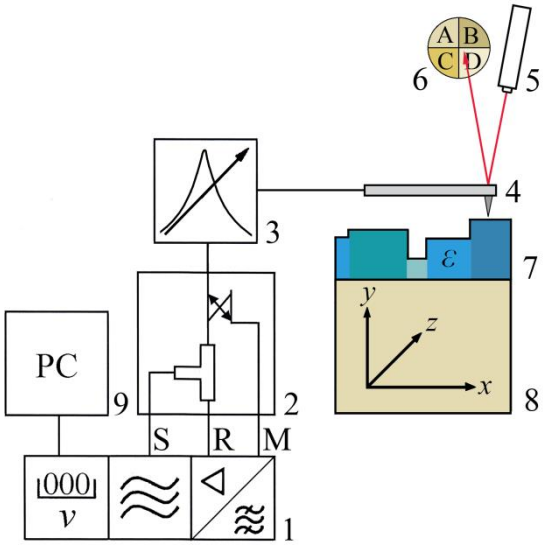

Figure 73. Principle of a scanning microwave microscope based on a standard atomic forth microscope (AFM): 1, microwave network analyzer; 2, reflection test set; 3, resonance structure for impedance matching; 4, AFM cantilever; 5, laser; 6, photodetector; 7, sample; 8, *x, y, z* – stage of AFM, 9, process control computer, control lines are not shown [422].

If, during the scanning process, the tip is not kept at constant distance to the sample the microwave signal provides a convolution of the sample's topography and its dielectric properties. For that reason the scanning microwave microscope is often simultaneously operated as atomic force microscope in order to record the topography separately. A set-up referring to this is sketched in Figure 73. Via an appendant reflection test set (2, Fig. 73) the microwave signal from a network analyzer (1) is applied to the tip of an atomic force cantilever (4). The signal reflected from the tip, which again holds information about the local dielectric properties of the sample (7), is received by the measuring channel (M) of the VNA and further processed by the computer (9). As with the device shown in Figure 72, a challenging task is the implementation of the broadband microwave path to the tip. Again a resonant structure, such as a half-wavelength coaxial cavity resonator [422], may be used as shown in Figure 73. Standard AFM equipment (5,6) is used to keep the distance between the tip and the sample surface constant when the sample is moved (8). The AFM control signal provides the desired information about the sample topology.

In order to minimize the effect from fringing fields around the tip and thereby enhance the spatial resolution of microwave microscopes, specially designed tips are used. Examples are parallel strip-line tips formed of two aluminium layers deposited on a tapered quartz bar [417, 419]. Other designs separate the sensing probe from the exciting probe employing micro-fabricated silicon nitride cantilevers onto which coplanar waveguide structures have been patterned [419].

A special system is the scanning nonlinear dielectric microscope using a lumped element *LC* probe to measure the sample capacitance under the central tip of the probe [423-426]. Connected via a small inductance to a concentrically arranged ring electrode the tip forms a resonant circuit which acts as part of the feedback circuit of an oscillator. The capacitance under the central tip affects the total capacitance of the feedback circuit so that the frequency of the oscillator can be used to measure the capacitance changes of the samples when the sample is scanned. Oscillator frequencies are typically in the range 1 to 6 GHz. Variations in the capacitance on the order of 10^{-22} F are accessible to measurement and spatial resolution to the atomic scale is reached [424].

3.3.2. Electrical tomography

In close relationship to X-ray tomography, but using non-ionizing electromagnetic fields, techniques have been developed for obtaining cross-sectional images of the impedance or permittivity distribution inside a body [384, 427, 428]. Electrical impedance tomography (EIT [390, 394, 403, 407, 429-432]) and electrical capacitance tomography (ECT, [405, 433-436]) have established promising methods for the imaging, monitoring, and controlling in medical and industrial applications. Electrical tomography methods for local tissue mapping [437] and on-chip EIT techniques for imaging of biological cells [438] have been also described recently.

Electrical impedance tomography collects images of the internal impedance distribution with an array of external electrodes, distributed around the body under test. Typically, a small electrical current is applied to the body by means of one electrode pair and the resulting currents are concurrently measured at all other electrode pairs. Successively activating all available electrode pairs, the current injection is rotated around the body. After complete rotation the electrical impedance (or complex permittivity) image can be calculated from the voltage profiles using suitable algorithms. Capacitance tomography reconstructs a cross-sectional image of the permittivity inside a pipe or vessel from inter-electrode capacitances. In many ECT applications cylindrical-based geometries are preferred. Hence the sensor is an array of electrodes placed on the outside of an electrically non-conducting pipe that surrounds the cross-section to be examined. The capacitances between all different combinations of electrode pairs are determined and evaluated with the aid of an appropriate algorithm to yield the permittivity distribution within the sensor area.

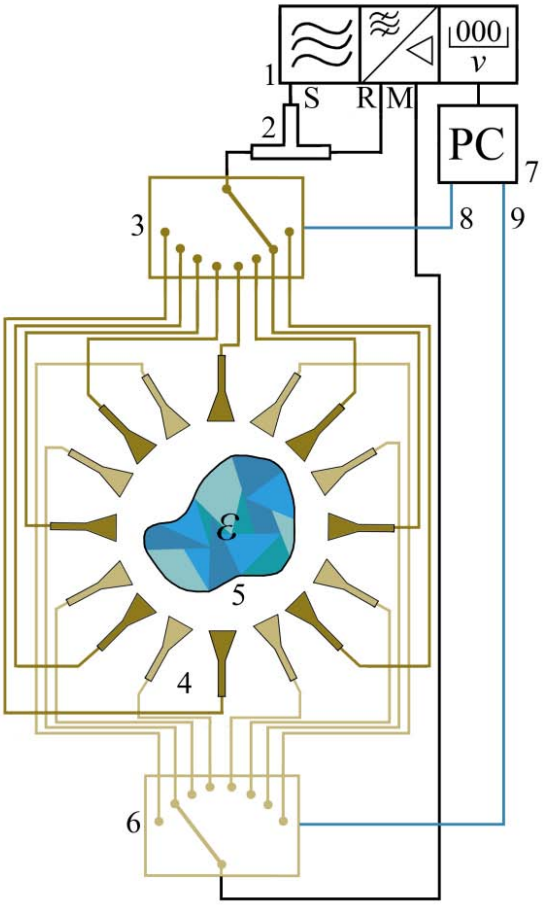

Figure 74. Scheme of a microwave tomography system: 1, network analyzer with signal output (S) as well as reference (R) and measurement (M) input ports; 2, power splitter; 3, multiplexer for the feeding signal; 4, antenna array; 5, sample; 6, multiplexer for transmitted signals; 7, process control computer; 8, 9, lines for multiplexer control.

As mentioned before, an advantage of electrical tomography techniques is the small-amplitude non-ionizing fields employed in the measurements. In addition, EIT and ECT are non-invasive, non-intrusive, robust, withstanding high temperatures and hydrostatic pressures, they are low cost and fast [436]. A repetition rate up to 10^3 frames/s can be reached [430], permitting multiphase-flow monitoring in many industrial processes. A drawback with respect to X-ray and nuclear magnetic resonance tomography is the minor spatial resolution. In order to enhance the resolution, tomographic systems operated at microwave rather than radio frequencies have been proposed [407]. The scheme of a set-up for imaging in the range 2 to 4 GHz is given in Figure 74. Again a vector network analyzer is used for signal generation and reception. With the aid of a suitable multiplexer, the measurement signal is successively applied to the particular

antenna of an array, shown in brown (Fig. 74). After transmission through the sample under test the signals from the transmitting antennae are received by another array of antennae (light brown), sampled by a second multiplexer, fed to the measurement input port of the VNA, and processed by a computer for image reconstruction.

In order to improve the EIT spatial resolution, magnetic resonance electrical impedance tomography (MREIT) has been also suggested recently [439]. MREIT is based on the idea that a current injected into the body under test does not just alter the interior current density and the voltage between electrodes but also the magnetic flux lines inside the subject. Adding the magnetic-flux-density data from a magnetic resonance imaging scanner to the voltage data is expected to substantially enhance the resolving power of electromagnetic imaging techniques [439].

Since the corresponding inverse problem is ill-posed, image reconstruction is still a challenging endeavour in electrical tomography [440]. Considerable efforts are therefore currently made to optimize algorithms in view of both the quality of reconstructed images as well as computational efforts and computing time [441-447].

3.3.3 Spectroscopic imaging

Since network analyzers provide rather fast frequency scans the combination of imaging and spectroscopy is also possible [448-451]. A potential measurement set-up in the microwave region is sketched in Figure 75. It is

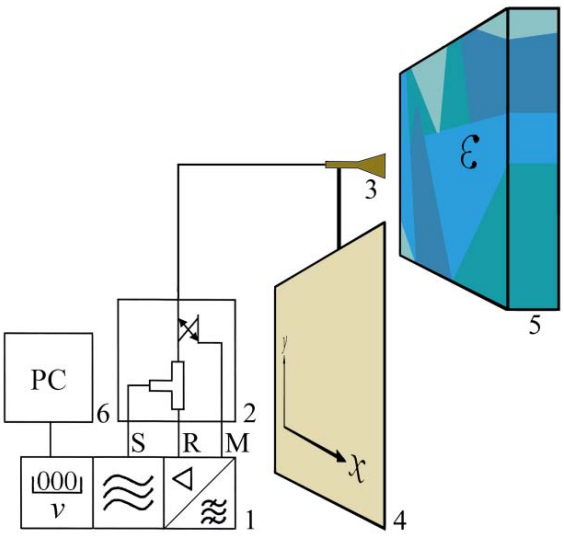

Figure 75. Schematic of system for frequency resolved microwave imaging of materials: 1, vector network analyzer; 2, reflection test set; 3, transmitting and receiving antenna; 4, stage for positioning the antenna; 5, material under test; 6, process control computer, control lines are omitted.

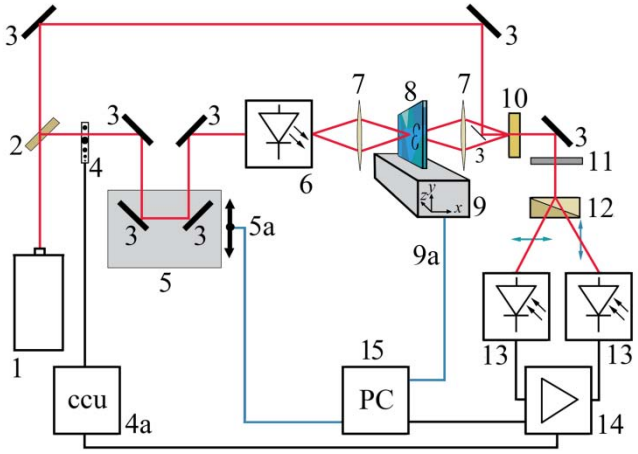

Figure 76. Scanning THz microscope: 1, femtosecond laser; 2, beam splitter; 3, mirror; 4, chopper with 4a, chopper control unit; 5, delay stage with 5a, position control; 6, emitter; 7, lens; 8, sample cell; 9, *x, y, z*-stage; 9a, line for stage control; 10, electro-optic crystal; 11, quarter wave plate; 12, Wollaston prism; 13, photodiode; 14, lock-in amplifier; 15, process control computer.

designed as a free space system to scan materials by varying the position of an antenna (3, Fig. 75) that transmits the measurement signal and at the same time receives the signal reflected from the material under test. Scanning the frequency at each position of the antenna provides additional valuable spectroscopic information and thus allows for the construction of dielectric images at different frequencies.

A THz microscope yielding dielectric images at different frequencies is shown in Figure 76. Actually this version of a spectroscopic microscope simply derives from the spectrometer sketched in Figure 71. The instrument is modified by placing the sample on a suitable stage for spatial scanning (9, Fig. 76). Again a frequency scan may be taken at each sample position.

4 Dielectrics of Water and Aqueous Solutions

4.1 Pure water: effects of temperature and pressure

As shown before, techniques for dielectric measurement at THz frequencies are indeed well developed. So far, however, they have been scarcely applied in liquid measurements and applications to moisture determination are almost non-existent. For those reasons the following review on the dielectric properties of water in its different states of interaction will be largely restricted to the frequency range up to 100 GHz.

In the relevant temperature range liquid water displays a relaxation at microwave frequencies (Fig. 77) which can be analytically represented by the simple Debye-type relaxation function (Eq. 78) with discrete relaxation time. The parameter values of the Debye function are collected in tabular

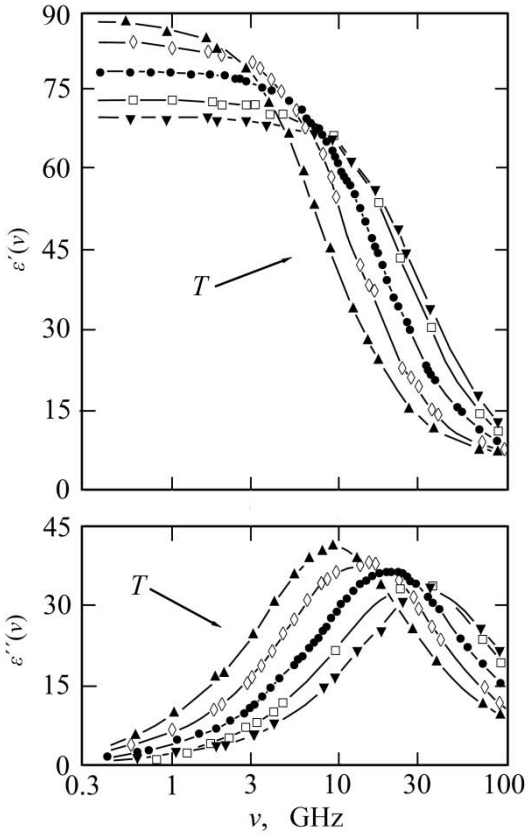

Figure 77. Real part $\varepsilon'(\nu)$ and negative imaginary part $\varepsilon''(\nu)$ of the microwave complex permittivity spectrum of water at five temperatures: ▲, 0 °C; ◊, 10 °C; ●, 25 °C; □, 40 °C; ▼, 50 °C [137, 145].

form in reference data section (chapter 6) and are briefly discussed in the following. Since the extrapolated high-frequency permittivity $\varepsilon(\infty)$ is of minor importance for the principal dispersion ($d\varepsilon'/d\nu < 0$)/dielectric loss ($\varepsilon'' > 0$) region of water, the focus of the discussion will be the static permittivity $\varepsilon(0)$ and the dielectric relaxation time which, as mentioned above, will be denoted by τ_w in order to accentuate the reference to pure water.

4.1.1 Static permittivity, Kirkwood-Fröhlich theory, dipole orientation correlation

Owing to its relatively large permanent electric dipole moment μ = (1.84 D, sect. 2.2) of the isolated water molecule, liquid water exhibits a considerable static permittivity. At normal pressure it is as large as $\varepsilon(0) = 107 \pm 2$ for supercooled water at -35 °C and decreases with temperature to reach $\varepsilon(0) = 55.67 \pm 0.1$ at 100 °C. A set of data from the literature is plotted in Figure 78. This data has been fitted to the empirical relation

$$\varepsilon(0) = 87.853\exp[-0.00457(T/\mathrm{K} - 273.15)] \qquad (103)$$

in which T denotes the absolute temperature. In the temperature range from -15 to 100 °C, Eq. (103) represents the experimental data well within

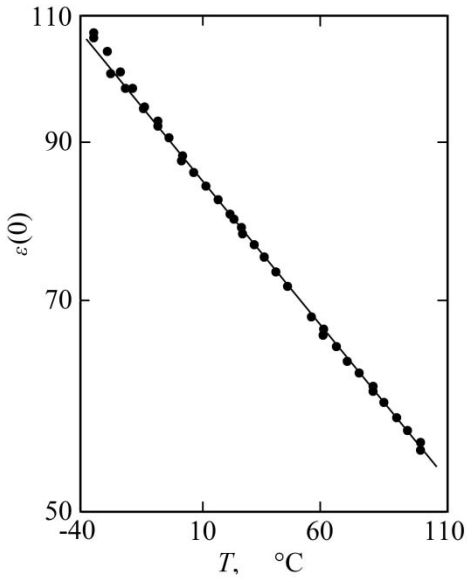

Figure 78. Static permittivity $\varepsilon(0)$ of liquid water, including the supercooled region, plotted on a logarithmic scale against temperature T. Symbols show literature data measured at low frequency [452-457] as well as extrapolated from microwave spectra [137, 144, 145]. The line represents the empirical interpolation relation defined by Eq. (103).

their limits of uncertainty. Only with supercooled water at lower temperature the deviations slightly exceed experimental uncertainty.

Whilst providing a reasonable way to interpolate static permittivity data of water at temperatures between -25 and 100 °C, the above empirical relation (Eq. 103) does not permit physical insigths into the nature of the low-frequency (static) polarization of the dipolar liquid. Such insights are offered by theoretical models, such as the elaborate Kirkwood-Fröhlich theory [140, 458-462] which yields

$$\frac{(\varepsilon(0)-\varepsilon_\infty)(2\varepsilon(0)+\varepsilon_\infty)}{\varepsilon(0)} = \frac{N_A c}{9\varepsilon_0 k_B T}(\varepsilon_\infty + 2)^2 \mu_g^2 g. \qquad (104)$$

In this equation N_A (= $6.022 \cdot 10^{23}$ mol^{-1}) is Avogadro's number, k_B (= $1.381 \cdot 10^{-23}$ J/K) Boltzmann's constant, and ε_0 (= $8.854 \cdot 10^{-12}$ F/m) the electrical field constant as before. Parameter c is the (molar) concentration of dipols with dipole moment μ_g in the gaseous (i.e. the isolated) state. Quantities ε_∞ and g, a high-frequency permittivity and the Kirkwood dipole orientation correlation factor, respectively, need special attention and are discussed in further detail below. However, it is worth mentioning first that the rather complicated structure of the relation, namely the fact that the static permittivity is not simply proportional to the squared electric dipole moment, reflects the interactions between the dipole field and the polarizable surroundings. Also the enlargement of the dipole moment μ_g of the isolated molecule to the value $\mu = \mu_g \cdot (\varepsilon_\infty + 2)/3$ in condensed matter is due to its polarization of the medium in which it is embedded.

The dipole orientation correlation factor g considers effects of ordering of dipole moments. As is well known from ferroelectrics, preferential parallel alignment of dipole moments leads to enhanced static permittivities ($g > 1$) of materials. If, for example, g dipoles form a domain with the molecular dipole moments μ perfectly aligned, its total dipole moment amounts to $g \cdot \mu$. At the same time the concentration of polar species indeed decreases by the factor g. Since, however, the dipole moment enters Eq. (104) quadratically, a net enhancement results so that the effective dipole moment is $\sqrt{g} \cdot \mu$. Basically, this feature reflects the finding that, in thermodynamic equilibrium, a rotation of a complete domain with g dipoles in the direction of an electrical field is more likely than the independent rotation of g individual dipoles in the same direction. As obvious from the above arguments, antiparallel ordering of dipole moments leads to reduced permittivities ($g < 1$), whereas the stochastic distribution of the dipole directions conforms with $g = 1$.

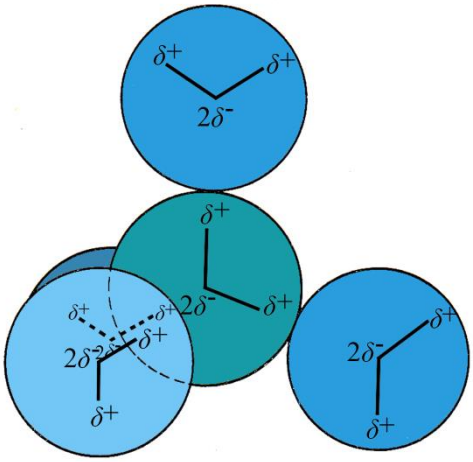

Figure 79. Tetrahedral coordination of water molecule according to Bernal and Fowler [95]. In correspondence to Figure 3, the positively charged sites at the hydrogens are marked by δ^+, the position of the oxygen is indicated by $2\delta^-$.

In regard to the high static permittivity of water, Kirkwood [140, 458] proceeded from the tetrahedral coordination of the molecules (Fig. 79) and, taking only nearest neighbors into account, calculated the correlation factor from geometric considerations as

$$g = 1 + 4\cos^2(50°) = 2.65. \qquad (105)$$

This value agrees well with the one derived from Eq. (104) if the high frequency permittivity in that relation is identified with the squared optical refractive index ($\varepsilon_\infty = n^2 = 1.33^2 = 1.77$). However, within the broad limits between the squared optical refractive index and the extrapolated high-frequency permittivity $\varepsilon(\infty)$ the correct value of ε_∞ to be used in Eq. (104) is unknown $n^2 \le \varepsilon_\infty \le \varepsilon(\infty)$. Furthermore, the results from Eq. (104) depend sensitively upon ε_∞. If, for example, the high-frequency permittivity $\varepsilon(\infty)$ as extrapolated from the microwave permittivity data ($4.0 \le \varepsilon(\infty) \le 6.0$ [463]) is used, $g < 1$ is found. Hill [464] has shown that $g = 1$ is compatible with ε_∞ between 4.35 (0 °C) and 4.05 (60 °C). By comparison of single-particle correlation times from nuclear magnetic resonance data with dielectric relaxation times of water (Eq. 19), a g-value of 1.7 has been more recently proposed for water at room temperature [141]. Contrary to that, the static permittivities of aqueous solutions of non-dipolar solutes (sect. 4.2.2 below) may be taken to indicate a small effect of dipole orientation correlation only. Because of the unresolved issue of the correct orientation correlation factor of liquid water, solute-induced changes in the static permittivity of aqueous solutions are often discussed relative to the properties of the pure solvent instead of speculating on potential variations in

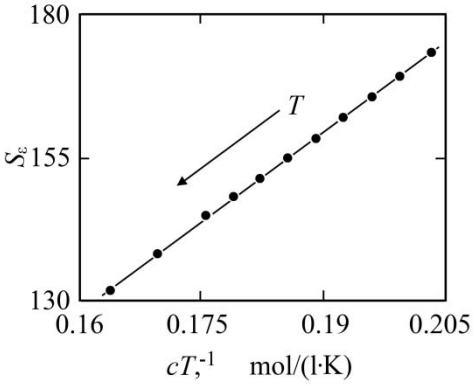

Figure 80. Quantity $S_\varepsilon(T)$ representing the left hand side of Eq. (104) for water versus $c(T)/T$. Data for the temperature range 0 to 60 °C are shown on the assumption $\varepsilon_\infty = n^2 = 1.77$.

the g-factor. This path will be followed below.

The temperature dependence in Eq. (104) points at thermal agitation, which more strongly promotes stochastic distribution of the electric dipole moments and thus more strongly impedes their rotation in direction of an external electric field as temperature is increased. Neglection of the high-frequency permittivity ($\varepsilon_\infty \ll \varepsilon(0)$) on the left hand side of Eq. (104) shows that the static permittivity of water is roughly inversely proportional to T. In order to realize the correct temperature dependence in the static permittivity data of water, the left hand side of Eq. (104), namely quantity $S_\varepsilon(T) = [\varepsilon(0) - \varepsilon_\infty][2\varepsilon(0) + \varepsilon_\infty]/\varepsilon(0)$, is displayed as a function of $c(T)/T$ in Figure 80. Since the uncertainty in the extrapolated high-frequency permittivity $\varepsilon(\infty)$ is high, $\varepsilon_\infty = n^2 = 1.77$ has been used in the calculation of the S_ε data. In doing so, a marginal temperature dependence of n^2 has been neglected. The data in Figure 80 nicely follows a straight line and thus indicates a temperature independent slope $dS_\varepsilon/d(c/T)$. Since the other parameters in the slope are constants or quantities almost independent of T (Eq. 104), this result may be taken to indicate that the dipole orientation correlation factor of water, if different from $g = 1$ at all, does not noticeably depend upon temperature.

4.1.2 Dielectric relaxation time, Eyring behavior

Within the framework of the reaction scheme discussed in section 2.2 a higher temperature means that the potential energy minima are filled up to a higher level. This effect is sketched in Figure 81 where identical minima are shown since the hydrogen bond energy does not depend on the orientation of the water molecule. Obviously, the potential energy barrier

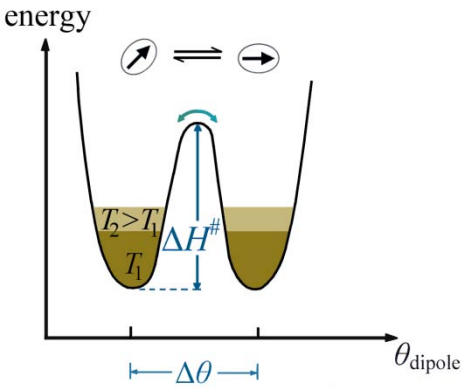

Figure 81. Reaction scheme showing the separation of two dipole moment orientations by a potential energy barrier (Figs. 15, 18). Brown and light brown coloring indicates the filling of the potential energy minima at temperatures T_1 and $T_2 > T_1$, respectively.

Figure 82. Eyring plot of the relaxation time τ (= τ_w) of the (principal) dielectric relaxation of water in the microwave region. Data refer to the temperature range -20 to 100 °C (black and blue points: data from references 137 and 170, respectively). The full line is discussed in the text, the dashed line indicates Eyring behavior (Eq. 106) with activation entropy $\Delta S^{\#} = 0$ and enthalpy $\Delta H^{\#} = 17.5$ kJ/mol.

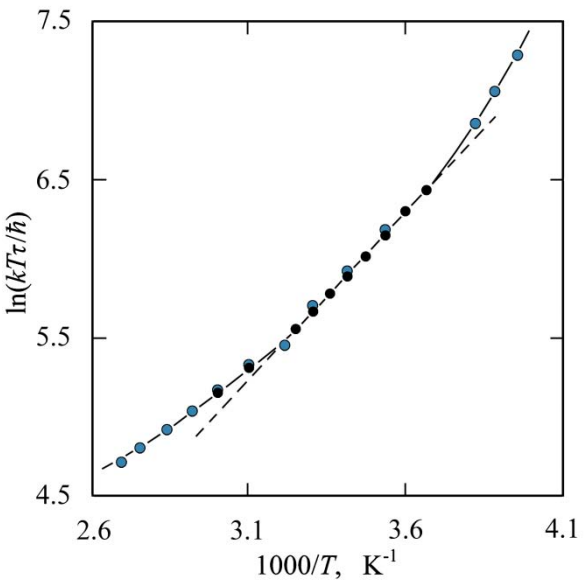

to be surpassed for reorientation appears to be smaller at higher than at lower T. Therefore, the probability that thermal activation is sufficiently strong for surpassing the barrier increases with temperature. Consequently, the relaxation time is expected to decrease with T. This feature is expressed by the Eyring equation [465, 466]

$$1/\tau = \frac{k_B T}{\hbar} C_f \exp(-\Delta G^{\#}/RT), \qquad (106)$$

where

$$\Delta G^{\#} = \Delta H^{\#} - T\Delta S^{\#} \quad (107)$$

denotes the Gibbs free energy of activation with activation entropy $\Delta S^{\#}$. In Eq. (106) $\hbar$ is Planck's constant divided by 2π, C_f is a dimensionless factor, and $R = k_B N_A$ is the gas constant. Prefactor $k_B T C_f/\hbar$ may be considered the frequency with which the molecule at thermal equilibrium is vibrating in the potential energy profile. The faster the vibrations, i. e. the more attempts are made per second to surpass the energy barrier, the shorter will be the period after which reorientation occurs.

The dominating factor in the relaxation time is, however, the ratio of the Gibbs free energy of activation and thermal energy (Eq. 106). In most parts of the relevant temperature range, namely between 0 and 60 °C, the principal dielectric relaxation times of water follow Eyring temperature behavior with activation enthalpy $\Delta H^{\#} = 16.7$ kJ/mol and entropy $\Delta S^{\#} = 23$ J/(mol·K). Using these parameter values the Eyring function is depicted in that temperature range by the full line in Figure 82. Outside that range the line is drawn just to guide the eyes. In the somewhat reduced temperature range from 0 to 50 °C the relaxation time data can be also well described assuming a vanishing activation entropy and $\Delta H^{\#} = 17.5$ kJ/mol. With these parameter values the Eyring function is represented by the dashed line in Fig. 82. Hence at the most important tempertures for our daily lives an activation enthalpy on the order of the hydrogen bond interaction enthalpy $\Delta H = 20$ kJ/mol of water follows.

The relaxation behavior of viscous liquids, especially glass-forming

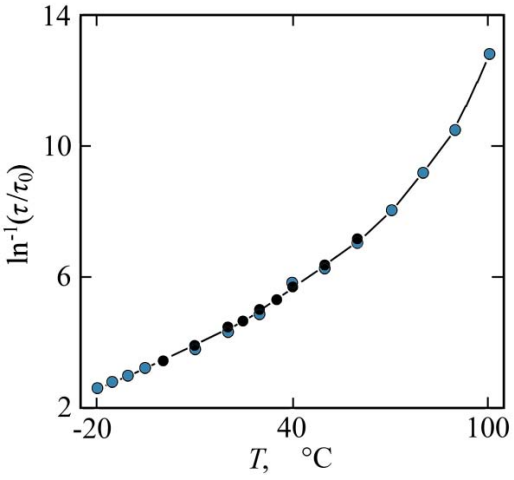

Figure 83. Vogel-Fulcher-Tammann-Hesse representation (Eq. 108) of the principal dielectric relaxation time τ (= τ_w) of water at temperatures between -20 and 100 °C: τ_0 = 1 ps.

substances, is often described by the relation

$$\ln(\tau/\tau_0) = E_{VFTH}/(T - T_0) \tag{108}$$

which Vogel [467], Fulcher [468], as well as Tammann and Hesse [469] first applied to experimental viscosities. Here τ_0 is a reference relaxation time, E_{VFTH} is a parameter related to an energy and T_0 is a specific temperature, for example the glass temperature. The plot of $1/\ln(\tau/\tau_0)$ for water as a function of temperature (Fig. 83), however, does not reveal a straight line, clearly disclosing that the Vogel-Fulcher-Tammann-Hesse model is not applicable.

4.1.3 High hydrostatic pressure, wait-and-switch relaxation model

When water with its relatively open structure is compressed one might expect an increase in the dielectric relaxation time because of added internal friction. As shown by Figure 84, however, the opposite is true: τ_w decreases with hydrostatic pressure p. Likewise surprising on a first glance is the trend observed in computer simulation studies [116] for the molecular mobility of water. Lowering the density from 1 to 0.85 gcm^{-3}, the mobility decreases, in conformity with the increase in the reorientational mobility at increasing pressure.

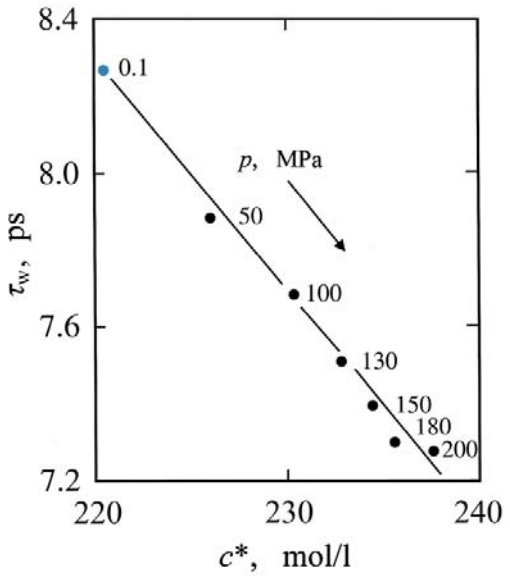

Figure 84. Principal relaxation time τ_w of water at 25 °C and various hydrostatic pressures p plotted as function of concentration c^* (= 4[H_2O]) of hydrogen bonding sites [242, 243]. The blue point marks the value at normal pressure.

The above results suggest a correlation between the dielectric relaxation time of water and the concentration c^* of hydrogen bonding sites, which is already considered in the presentation of pressure-dependent data in Figure 84: the relaxation time decreases with c^*. This feature is described by the so-called wait-and-switch model of dipole reorientation [142]. The model proceeds from previous ideas of dipole orientational motions in alcohols [470] and from results of computer simulation studies for water [116, 471-477]. Still assuming the reorientation of the water dipoles to comply with an activated jump mechanism, as again sketched by the reaction scheme in Figure 85, let us consider the direction of the dipole moment of a selected molecule. This dipole moment is marked by an arrow. Its direction (a, Fig. 85) may correspond to one of the potential energy minima in the reaction scheme. In order to be able to rotate in another direction the potential energy barrier has to be surpassed by the molecule, implying the breaking of several hydrogen bonds. Computer simulations reveal rapid fluctuations, with correlation times as small as 0.1 to 1 ps, of hydrogen bond strength [472, 473, 477]. Within these fluctuations,

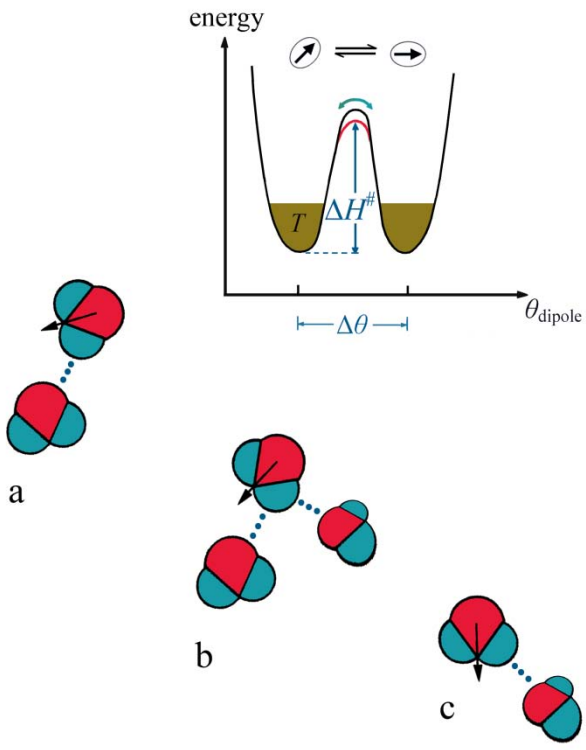

Figure 85. Sketch of the potential energy barrier between two dipole orientations. The red line shows the reduction of the activation enthalpy due to the formation of a bifurcated hydrogen bond when an additional neighbor molecule is present. Also sketched are three situations of a given water dipole: a, the original hydrogen bond and dipole orientation; b, bifurcated bond to the primary partner molecule and an additional neighbor; c, hydrogen bond to the latter molecule after the switch of dipole orientation.

however, the hydrogen bonds normally weaken and just reform again. The situation changes substantially, when another hydrogen bond partner appears at a suitable site [116, 471, 475-477]. Since water is predominantly tetrahedrally coordinated (Fig. 8) this additional partner is also named the "fifth neighbor" [475]. Presence of a fifth neighbor in a suitable position leads to the formation of a bifurcated (branched) bond, including both the original bond partner and the new neighbor (b, Fig. 85). The bifurcated bond causes a reduction of the potential energy barrier, as indicated by the red line in Figure 85. Thereby the considered water molecule can more easily surpass the barrier, thus rotate its dipole orientation and form a normal hydrogen bond with the new partner (c, Fig. 85). The dipole rotation itself occurs again within the short period of around 0.1 ps [472, 473, 477] and therefore resembles a switching. Because the reorientation itself is so fast, the greater proportion of the relaxation time is the period for which a molecule has to wait until an additional neighbor occurs in a suitable position. This aspect reflects the correlation between the dielectric relaxation time and the concentration of hydrogen bonding sites c^*: the larger c^* the higher the probability density for the occurrence of a suitable new hydrogen bond partner, the shorter the waiting period, and thus the smaller the relaxation time.

The idea of the wait-and-switch model applies, at least in a qualitative manner, to many features of aqueous systems as well as other associating liquids. The large difference in the dielectric relaxation times of liquid water and ice, at 0 °C disagreeing by a factor of more than 10^6, may be attributed to the higher degree of tetrahedral order in the solid state which is associated with a reduced probability density for catalyzing reorientational motions by structural defects. In this context it is worth mentioning that not only fivefold coordinated water molecules may initialize switching

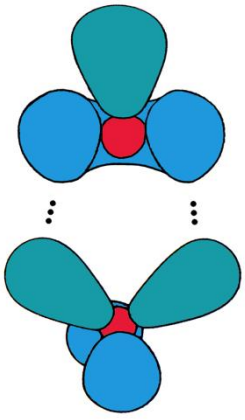

Figure 86. Hydrogen bonding between the positively charged sites at the hydrogen atoms of one water molecule and the smeared lone pair electron charges of another molecule.

of the dipole moment and the formation of a new hydrogen bond. Threefold coordinated structures, as resulting if both hydrogen atoms of a water molecule interact with the smeared lone pair electrons of another molecule (Fig. 86), can likewise act as defect that promotes reorientational motions.

Some favorable examples for aqueous solutions will be discussed in sections 4.2 and 4.3 below, including such for which the model fails to explain relaxation times in an obvious manner. Figure 87 supports the idea of a wait-and-switch model. It shows relaxation times τ_1 for the principal relaxation process for water and the series of normal alcohols up to

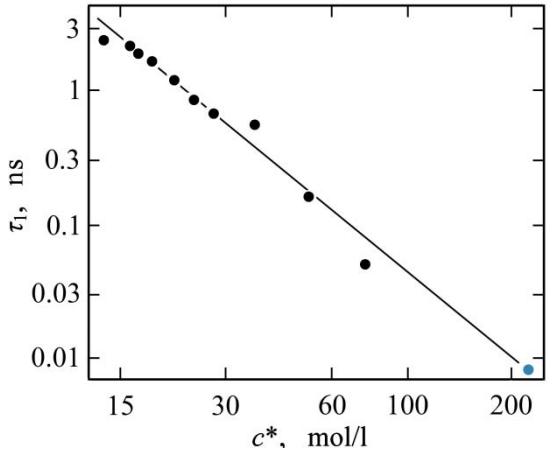

Figure 87. Log-log plot of the relaxation time τ_1 of the principal (microwave) relaxation of normal alcohols [$CH_3(CH_2)_{n-1}OH$, n = 1 ,..., 12] as function of the concentration of hydrogen bonding sites. The τ_w value for water at 25 °C is also included (blue point). Alcohol data refer to 25 and 20 °C [147, 478-483].

dodecanol. Again the τ_1 values decrease with concentration of hydrogen bonding sites. Since the hydrogen bond energy is almost identical for all normal alcohols, Figure 87 highlights again the impact of the density of hydrogen bonding sites for the dielectric relaxation of associating liquids. It is this density which successively decreases when going from methanol (or even water) to dodecanol and thus provokes increasing periods of waiting for a suitable new hydrogen bond partner. Additionally, translational diffusion of normal alcohols is noticeably affected by interactions between $-CH_2-$ and $-CH_3$-groups. For each additional group of an alkyl chain of normal alcohols up to *n*-octanol an increase in the activation enthalpy by 3.5 kJ/mol has been found [147, 484]. Hence the waiting period of higher homologues of methanol is further extended by interactions of alkyl groups.

A converse example is the dielectric relaxation times for mixtures of

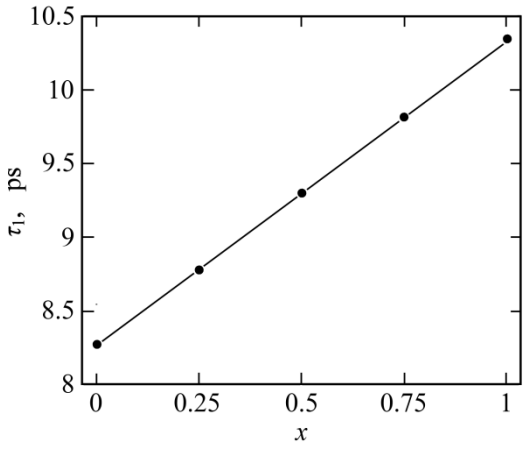

Figure 88. Dielectric relaxation time of the principal relaxation process in mixtures of heavy water (D_2O) and normal water (H_2O) at 25 °C versus mole fraction x of D_2O [485].

heavy water with water. They increase linearly from 8.27 ps for H_2O at 25 °C to 10.37 ps for D_2O at the same temperature (Fig. 88). This happens although the concentration c^* of hydrogen bonding sites of both liquids is identical. Since measurements at different temperatures reveal also nearly identical activation enthalpies [486], the larger relaxation times of heavy water appear to be due to a different C_f in Eq. (106). Due to its larger mass, the frequency of vibrations in the potential energy minimum (Figs. 81, 85) is smaller with D_2O than with H_2O. Consequently, in D_2O less attempts are made per time unit to surpass the potential energy barrier in the reaction scheme of Figure 85. A reduced probability density for achieving favorable conditions for dipole moment switching and thus enhanced dielectric relaxation time follows.

4.2 Aqueous solutions of polar and non-polar molecules

Aqueous solutions of non-ionic non-dipolar solutes reveal comparatively simple spectra (Fig. 89), connatural to Debye-type relaxation behavior. They differ, however, in three points. The (extrapolated) static permittivity $\varepsilon(0)$ and thus the relaxation amplitude $\Delta\varepsilon = \varepsilon(0) - \varepsilon(\infty)$ is smaller than with pure water, the dispersion ($d\varepsilon'(\nu)/d\nu < 0$) and dielectric loss ($\varepsilon''(\nu) > 0$) region extends over a somewhat broader frequency band, and the relaxation frequency ν_r is shifted to smaller values, pointing at an enhanced relaxation time $(2\pi\nu_r)^{-1}$. For a moment the relaxation frequency may be just defined as the frequency at which the dielectric loss adopts its relative maximum ($d\varepsilon''(\nu)/d\nu = 0$, $d^2\varepsilon''(\nu)/d\nu^2 < 0$ at $\nu = \nu_r$). More particulars of such spectra will be discussed below, starting with the broadened

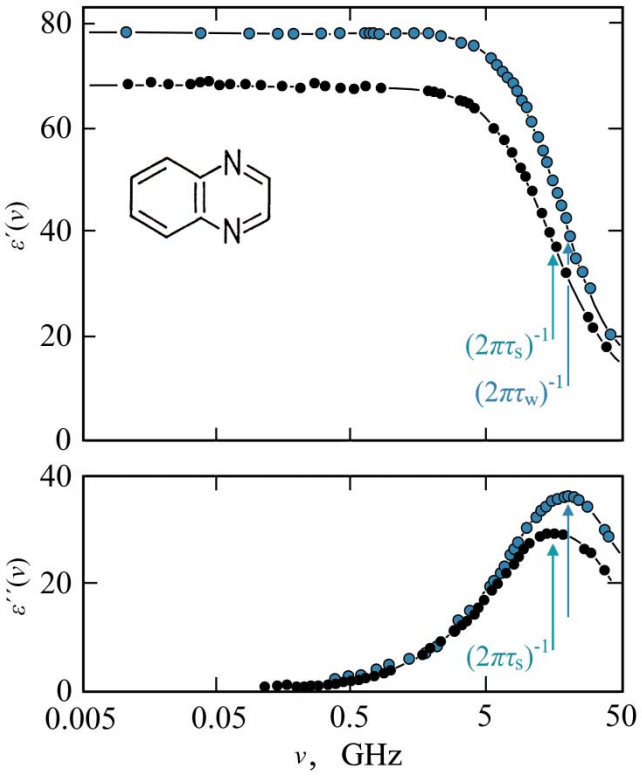

Figure 89. Real parts $\varepsilon'(\nu)$ and negative imaginary parts $\varepsilon''(\nu)$ of the complex permittivity spectra of water (blue points) and a 1 mol/l aqueous solution of quinoxaline at 25 °C (black points [487]). The structure of the solute molecule is also delineated. Parameters τ_s and τ_w are the principal relaxation time of the Havriliak-Negami spectral function (Eq. 113) and the Debye function (Eq. 78), respectively.

frequency range of relaxation.

4.2.1 Relaxation time distribution, hydration model

4.2.1.1 Continuous relaxation time distribution

Often the broadening of the relaxation region is accounted for by the assumption of a continuous distribution $G(\tau)$ of relaxation times, by which the complex permittivity spectrum is expressed as

$$\varepsilon(\nu) = \Delta\varepsilon\int_0^\infty \frac{G(\tau)}{1+i\omega\tau}\mathrm{d}\tau + \varepsilon(\infty), \tag{109}$$

with normalization relation

$$\int_0^\infty G(\tau)\mathrm{d}\tau = 1. \tag{110}$$

Since both the frequency band of measurement and the measurement accuracy are usually too small to extract the relaxation time distribution function directly from the experimental spectra, empirical spectral functions are used to analytically represent the complex permittivity data and to conclude on the underlying relaxation time distribution from the best fitting analytical description of experimental spectra.

Popular relaxation functions are the Cole-Cole function [341, 488]

$$\varepsilon(\nu) = \varepsilon(\infty) + \frac{\Delta\epsilon}{1+(i\omega\tau_{\mathrm{CC}})^{1-h}} \tag{111}$$

and the Davidson-Cole function [489]

$$\varepsilon(\nu) = \varepsilon(\infty) + \frac{\Delta\varepsilon}{(1+i\omega\tau_{\mathrm{DC}})^{(1-b)}}\,. \tag{112}$$

When $\tau G(\tau)$ is plotted versus $\ln(\tau/\tau_{\mathrm{CC}})$ the relaxation time distribution underlying the Cole-Cole function is symmetrically bell-shaped with principal relaxation time $\tau_s = \tau_{\mathrm{CC}}$ (part b, Fig. 90). The complex plane representation of the spectrum follows a circular arc with its center below the ε' axis. The Davidson-Cole distribution is asymmetric (a, Fig. 90). The principal relaxation time $\tau_s = \tau_{\mathrm{DC}}$ is not just the one with largest weight, but, at

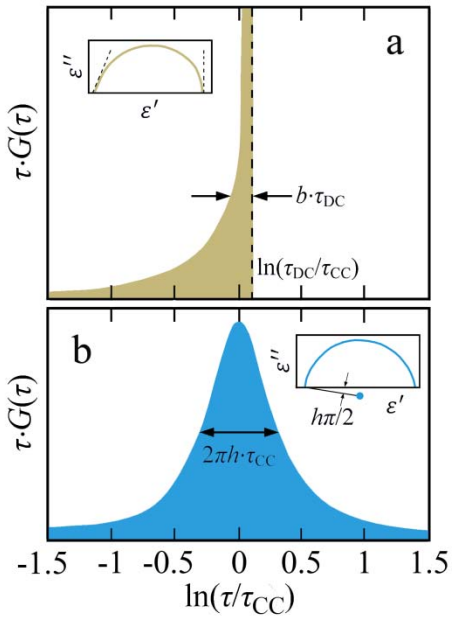

Figure 90. Relaxation time distributiom functions corresponding with the Davidson-Cole (Eq. 112) and the Cole-Cole (Eq. 111) spectral functions. The former is shown in the upper part (a), the latter in the lower part (b) of the Figure. Also sketched are the corresponding spectra in the complex plane representation.

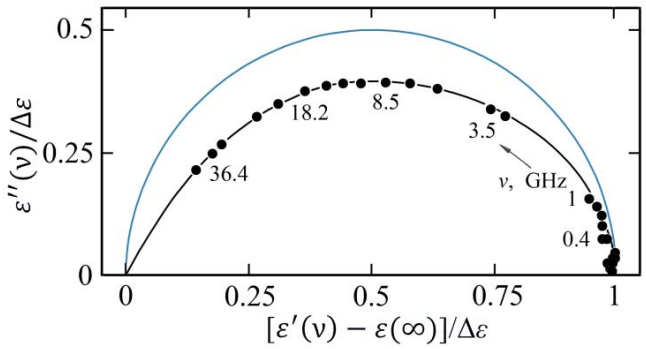

Figure 91. Complex plane representation of normalized permittivity data for a 5 mol/l solution of quinoxaline in water at 25 °C [487]. The black line is the graph of a Havriliak-Negami function (Eq. 113) with h = 0.09 and b = 0.11. The blue line indicates the Debye function (Eq. 78) as applying to pure water.

the same time, is also the largest relaxation time. In the complex plane representation the spectral function constitutes a skewed arc. Parameters h and b ($0 \le h,b < 1$) control the width and shape of the relaxation time distribution function and thus the deviations from simple Debye relaxation behavior.

A combination of Eqs. (111) and (112) yields the so-called Havriliak-Negami spectral function [490]

$$\varepsilon(\nu) = \varepsilon(\infty) + \frac{\Delta\varepsilon}{(1+(i\omega\tau_{\mathrm{HN}})^{1-h})^{1-b}} \tag{113}$$

with principal relaxation time $\tau_s = \tau_{\mathrm{HN}}$ and with two relaxation time distribution parameters. A spectrum with almost balanced Cole-Cole and Davidson-Cole distribution parameters (h = 0.09 ± 0.02; b = 0.11 ± 0.06 [487]) is shown in Figure 91.

Various other empirical relaxation spectral functions have been proposed. Within the limits of typical experimental uncertainties, most of these functions are well reproduced [491, 492] by the Hill function [491, 493, 494]

$$\varepsilon''(\nu) = \frac{[\varepsilon(0)-\varepsilon(\infty)](\omega\tau_{\mathrm{H}})^m}{[1+(\omega\tau_{\mathrm{H}})^{2s}]^{(m+n)/(2s)}} \tag{114}$$

which is available in complete form for the negative imaginary part of the permittivity spectrum only. This function includes three distribution parameters ($0 < m, n, s \le 1$) which are related in an obvious manner to the

shape of the spectral function: at low frequencies ($\omega\tau_H \ll 1$) the dielectric loss spectrum increases as ω^m, towards high frequencies ($\omega\tau_H \gg 1$) it decreases as ω^{-n}, and around its relative maximum ($\omega\tau_H \approx 1$) it is mainly controlled by *s*. However, because of its rather large number of parameters and since consideration of the real part of the permittivity function needs numerical transformation, little use is made of the Hill function.

4.2.1.2 Basic hydration model

Instead of assuming a continuous relaxation time distribution the broadening of the relaxation region with respect to pure water spectra can be principally accounted for by considering a sum of a limited number of Debye relaxation terms. Generally, at moderate solute concentrations two Debye terms are sufficient to represent the dielectric spectra of solutions. In addition, the relaxation time of one term may be fixed at the value τ_w of pure water at the relevant temperature. Based on these findings, it is an obvious attempt to identify the relaxation terms of the solutions with water that is unaffected and water around the solute, the relaxation time τ_h (≠

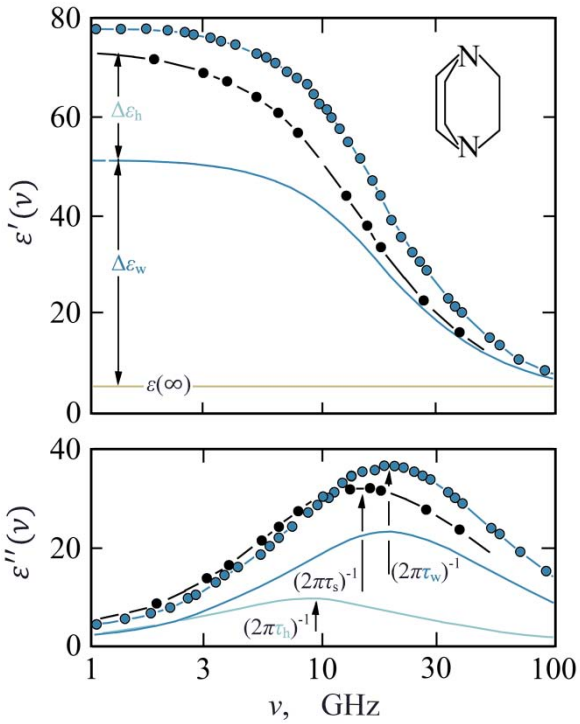

Figure 92. Real parts $\varepsilon'(\nu)$ and negative imaginary parts $\varepsilon''(\nu)$ of the complex permittivity spectra of water (blue points) and a 0.67 mol/l aqueous solution of triethylenediamine (TED) at 25 °C (black points [495]). The subdivision of the latter spectrum into pure water and hydration water contributions is indicated by blue and turquoise lines. The inset shows the structure of the solute molecule.

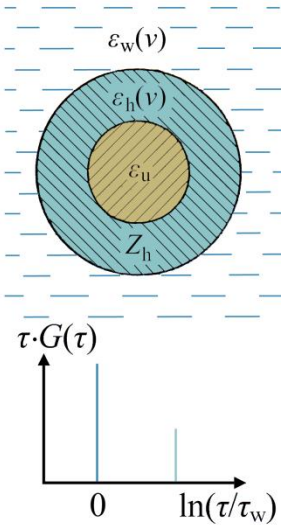

Figure 93. Sketch of hydration model (top). The solute in the center is given the permittivity ε_u. It is surrounded by Z_h hydration water molecules with relaxation time τ_h ($\neq \tau_w$). The hydrated solute is embedded in unperturbed water with pure water complex permittivity $\varepsilon_w(\nu)$. Also shown is the relaxation time distribution corresponding with this model (bottom).

τ_w) of the latter thus being controlled by the solute. Applying this model, the experimental spectra are analytically represented by the function

$$\varepsilon(\nu) = \varepsilon(\infty) + \frac{\Delta\varepsilon_w}{1+i\omega\tau_w} + \frac{\Delta\varepsilon_h}{1+i\omega\tau_h} \tag{115}$$

where $\varepsilon(\infty) + \Delta\varepsilon_w + \Delta\varepsilon_h = \varepsilon(0)$ and where $\Delta\varepsilon_h$ is related to the concentration cZ_h of hydration water. If identical dipole orientation correlation factors (section 4.1.1) are assumed for both, the hydration water and the unperturbed water, equation

$$cZ_h = c_w\Delta\varepsilon_h/(\Delta\varepsilon_h + \Delta\varepsilon_w) = c_w\Delta\varepsilon_h/(\varepsilon(0) - \varepsilon(\infty)) \tag{116}$$

may be simply used to estimate Z_h.

As it proceeds from only two different kinds of water this basic concept of hydration model is certainly an oversimplification of the structure of aqueous solutions. In reality there will be a more smooth transition from strongly affected water at the solute's surface to unaffected water. Also, the dipole orientation correlation factor of the hydration water may be different from that of pure water [496]. Nevertheless, this simple model impresses by its clarity and its small number of adjustable parameters: $\varepsilon(\infty)$, $\varepsilon(0)$, $\Delta\varepsilon_h$, and τ_h instead of $\varepsilon(\infty)$, $\varepsilon(0)$, τ_{CC}, and h or $\varepsilon(\infty)$, $\varepsilon(0)$, τ_{DC}, and b with the Cole-Cole or Davidson-Cole models, respectively.

4.2.1.3 Solute contribution to the spectra

So far non-dipolar solutes such as quinoxaline and triethylenediamine have been considered. With these molecules the partial dipole moments at the opposing nitrogens compensate each other because the molecular structure is stabilized by delocalized electrons or by the bicyclic composition, respectively. Dielectric spectra of solutions change significantly when solutes themselves bear a significant dipole moment. An example is shown in Figure 94, where spectra of 3 mol/l solutions of dipolar purine and non-polar quinoxaline are compared to one another. Due to its permanent electric dipole moment (μ_g = (4.5 ± 0.2) D [497]), purine adds its own contribution to the permittivity spectrum, with relaxation amplitude $\Delta\varepsilon_u = \varepsilon(0) - \varepsilon_{sw}$ and relaxation time τ_u. Here ε_{sw} denotes the water contribution to the static permittivity (Fig. 94).

In the purine solution spectrum shown in Figure 94, the solute and solvent relaxations are well separated from one another, so that the analysis in terms of two relaxation processes

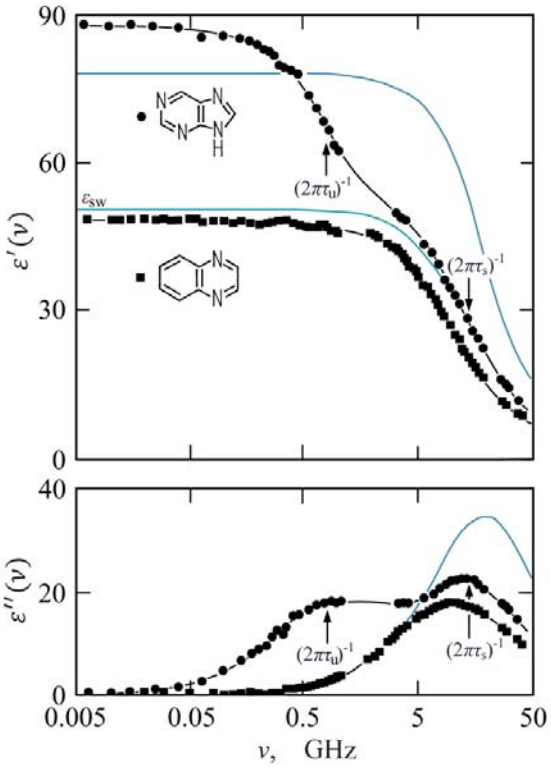

Figure 94. Real parts $\varepsilon'(\nu)$ and negative imaginary parts $\varepsilon''(\nu)$ of the complex permittivity spectra of 3 mol/l aqueous solutions of purine (●) and quinoxaline (■) at 25 °C [497]. The blue lines reflect the water spectrum at the same temperature. The turquoise line reveals the contribution of the solvent water to the real part of the purine spectrum. Insets show the structures of the solvent molecules.

$$\varepsilon(\nu) = \varepsilon(\infty) + \frac{\varepsilon(0)-\Delta\varepsilon_u-\varepsilon(\infty)}{(1+i\omega\tau_s)^{(1-b)}} + \frac{\Delta\varepsilon_u}{1+i\omega\tau_u} \tag{117}$$

is quite easily possible. If the relaxation times τ_s and τ_u are closely spaced, however, assumptions have to be made either by calculating $\Delta\varepsilon_u$ from the solute dipole moment or by fixing ε_{sw} based on results for solutions of non-dipolar solutes. Such results will be discussed in the next section.

The situation is even more complicated if experimental spectra for solutions of dipolar solutes are treated in terms of the hydration model. As illustrated by Figure 95 at least three relaxation terms are required,

$$\varepsilon(\nu) = \varepsilon(\infty) + \frac{\varepsilon(0)-\Delta\varepsilon_u-\Delta\varepsilon_h-\varepsilon(\infty)}{1+i\omega\tau_w} + \frac{\Delta\varepsilon_h}{1+i\omega\tau_h} + \frac{\Delta\varepsilon_u}{1+i\omega\tau_u}, \tag{118}$$

with the hydration water term located between that for the unaffected water and the one for the solute. On such conditions, it is particularly helpful in the regression analysis of experimental spectra if at least one of the parameters can be fixed at a reasonable value.

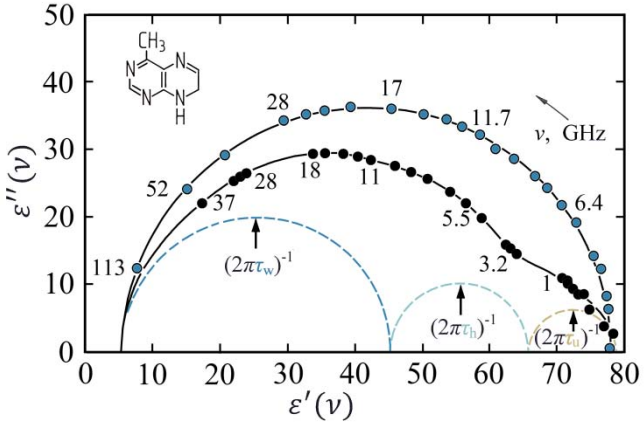

Figure 95. Complex plane representation of the spectra for water (blue points) and a 1.11 mol/l solution of 6-methyl-purine (black points) at 25 °C [497]. The subdivision of the latter into Debye relaxation terms for unaffected water (w), hydration water (h), and solute (u) is indicated by blue, turquoise, and light brown color, respectively. The structure of the dipolar solute is also shown.

4.2.2 Static permittivity, mixture models

4.2.2.1 Experimental findings

The static permittivities $\varepsilon(0)$ of aqueous solutions of non-dipolar molecules generally decrease with increasing volume fraction v_u of solute (Fig. 96). The smaller $\varepsilon(0)$ values are for the most part due to the dilution of the dipolar solvent and thus reduced concentration of dipole moments (Eq. 104). Depolarizing fields, resulting from polarization charges at the internal solute-solvent interfaces, also contribute to the reduction of $\varepsilon(0)$. Unfortunately, the internal fields cannot be rigorously treated. Rather mean field approaches are required even for comparatively simply structured solutions of spherically shaped solutes. Because of some ambiguity in the mean field approximations, a variety of mixture relations exist even for solutions of globular solutes [458, 500-506]. In Figure 96 graphs of two prominent mixture relations for such solutions are shown, assuming a solute permittivity $\varepsilon_u = 2$ and a solvent permittivity $\varepsilon(0) = \varepsilon_w = 78.35$, corresponding with the permittivity of water at 25 °C. The Maxwell-Wagner model [507-509] proceeds from the idea that the permittivity of the solvent close to solute particles agrees with the permittivity $\varepsilon(0)$ of the pure solvent. It is thus assumed to preferentially apply at small volume fractions v_u of solutes. The Maxwell-Wagner relation for the permittivity ε_m of

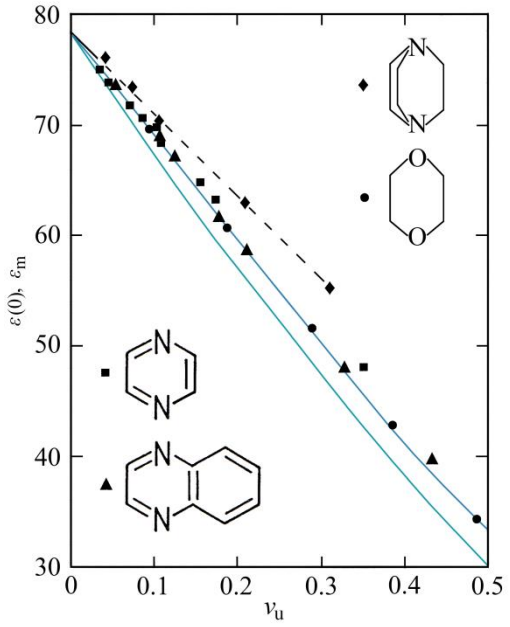

Figure 96. Static permittivity $\varepsilon(0)$ versus volume fraction v_u of solute for aqueous solutions of some non-dipolar heterocyclic molecules at 25 °C: ⧫, bicyclic triethylenediamine (TED, [497]; •, 1,4-dioxane [498]; ■, aromatic pyrazine as well as 2-methyl- and 2,6-dimethyl-pyrazine [499]; ▲, quinoxaline and 2-methylquinoxaline [499]. Dashed line accentuates the TED solution data. Blue and turquoise lines are graphs of mixture relations, Eqs. (119), (120), respectively, providing mixture permittivity ε_m.

mixtures with water as solvent reads

$$\varepsilon_{\mathrm{m}} = \varepsilon_{\mathrm{w}} \frac{2\varepsilon_{\mathrm{w}}(1-v_{\mathrm{u}})+\varepsilon_{\mathrm{u}}(1+2v_{\mathrm{u}})}{\varepsilon_{\mathrm{w}}(2+v_{\mathrm{u}})+\varepsilon_{\mathrm{u}}(1-v_{\mathrm{u}})}. \tag{119}$$

Contrary to the above assumption, Bruggeman suggested the permittivity of the surroundings of a solute to equal that of the solution, ε_{m}. His relation [510]

$$\frac{\varepsilon_{\mathrm{m}}-\varepsilon_{\mathrm{u}}}{\varepsilon_{\mathrm{w}}-\varepsilon_{\mathrm{u}}}\left(\frac{\varepsilon_{\mathrm{w}}}{\varepsilon_{\mathrm{m}}}\right)^{1/3} = 1 - v_{\mathrm{u}} \tag{120}$$

may thus be considered more suited for concentrated solutions. Irrespective of the variance in the theoretical predictions, the experimental data tend to slightly exceed the mixture relations. This tendency is deemed to express effects of hydrophobic hydration which will be discussed with more details below. It is, however, interesting to realize that the largest $\varepsilon(0)$ data at given v_{u} result for triethylenediamine solutions. From an elementary point of view, TED is the most hydrophobic chemical among the water soluble substances. It offers only two lone pair electrons for hydrogen bonding with water but comprises six $-CH_2$-groups. The hydrophilic-hydrophobic balance looks quite different for 1,4-dioxane: four lone pair electrons are accompanied by four $-CH_2$-groups. Hence, from the character of its groups, this non-dipolar molecule is rather hydrophilic. 1,4-dioxane is miscible with water in any proportion.

In this context, it is worth to notice that the numbers of hydrophilic and hydrophobic groups per molecule are indeed important factors in influencing the water around the solute. They are, however, not the exclusive parameters controlling the water properties. An illustrative example is symmetric and thus non-dipolar 1,3,5-trioxane with its six hydrogen bonding sites per just three $-CH_2$-groups. Despite of this favorable hydrophilic – hydrophobic balance trioxane is soluble up to 221 g/l only, corresponding with 2.45 mol/l. Such behavior may be taken to indicate that other factors, such as steric and configurational aspects of solutes, are important in influencing the water properties around them.

4.2.2.2 Mixture relations

The above discussion reflects the specific relevance of mixture relations. The impact of a solute on the dielectric properties of the solvent is typical-

ly inferred from comparison of experimental permittivity data with theoretical predictions for the mixture permittivity ε_m. In electromagnetic aquametry, mixture relations are applied in an inverse mode for deriving the volume fraction v_w of water from the overall (effective) permittivity ε_m of the material under consideration. Since, for reasons mentioned before, no rigorous universal mixture relation exist, discovery of an adequate relation for particular applications is a challenging problem that has been illuminated by various reviews [458, 500-506]. Some demonstrative points will be briefly given in this section in order to direct attention to potential sources of error.

Both the Maxwell-Wagner (Eq. 119) and the Bruggeman (Eq.120) relation are not symmetric in the solute and solvent permittivities and should thus not be applied at large volume fractions of solutes. The symmetric formula ($v_w = 1 - v_u$)

$$\varepsilon_m^{1/3} = v_w \varepsilon_w^{1/3} + v_u \varepsilon_u^{1/3} , \tag{121}$$

i.e.

$$v_u = (\varepsilon_m^{1/3} - \varepsilon_w^{1/3})/(\varepsilon_u^{1/3} - \varepsilon_w^{1/3}) , \tag{122}$$

has been proposed by Looyenga, Landau, and Lifshitz [511, 512]. As shown

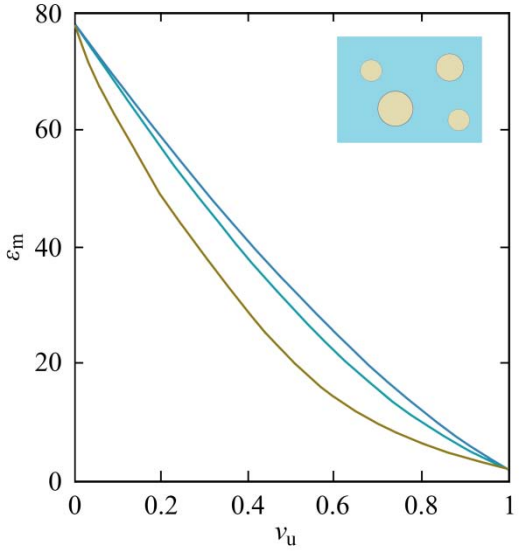

Figure 97. Maxwell-Wagner (blue line; Eq. 119), Bruggeman (turquoise line; Eq. 120), and Looyenga-Landau-Lifshitz (brown line; Eq. 121) effective permittivity ε_m as function of volume fraction v_u. Calculating the ε_m values, spherically shaped solute particles with permittivity ε_u (= 2) and volume fraction v_u are assumed to be embedded in water with permittivity ε_w (= 78.36) and volume fraction v_w = (1 - v_u). See the inset for a sketch of the mixtures.

by Figure 97, the mixture permittivities predicted by the Looyenga-Landau-Lifshitz model ($\varepsilon_{m,LLL}$) deviates substantially from those calculated with the aid of the Maxwell-Wagner ($\varepsilon_{m,MW}$) and the Bruggeman ($\varepsilon_{m,B}$) relations. At $v_u = v_w = 0.5$, for example, $\varepsilon_{m,LLL} = 20.7$ only, whereas $\varepsilon_{m,MW} = 30.0$ and $\varepsilon_{m,B} = 33.6$. These figures clearly express the different approximations made in the models, i.e. the different consideration of internal, predominantly depolarizing electric fields.

Different depolarizing internal fields lead also to the quite unequal mixture relations for water-in-oil and oil-in-water emulsions. Figure 98 reveals the tremendous difference in the effective permittivity of the differently structured liquids. In that figure the permittivity data is displayed as a function of the volume fraction of the respective spherically shaped solvent, i.e. of v_u with the oil-in-water and v_w with the water-in-oil emulsions. In order to accentuate the effect of internal depolarizing fields the simple linear relation

$$\varepsilon_m = v_w\varepsilon_w + v_u\varepsilon_u, \quad v_w = 1 - v_u, \tag{123}$$

disregarding internal electric fields completely, is also shown. The figure clearly reveals ineffectiveness of electromagnetic moisture determination of water-in-oil emulsions at volume fractions v_w larger than roughly 0.1: depolarizing fields largely mask the water droplets so that their

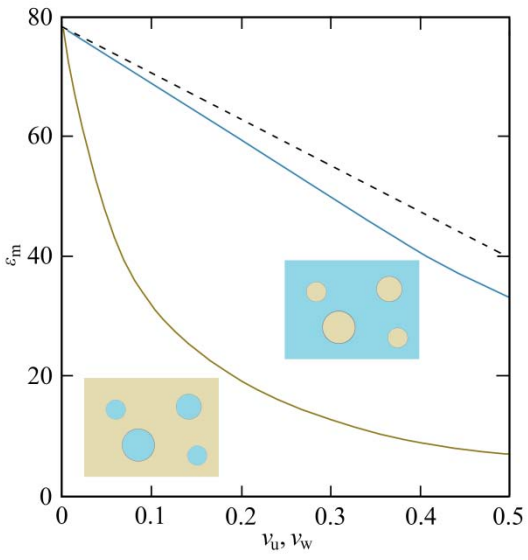

Figure 98. Maxwell-Wagner mixture permittivity (Eq. 119, blue line) for a solution of spherically shaped nonpolar solute (light brown) with permittivity $\varepsilon_u = 2$ in water with permittivity $\varepsilon_w = 78.36$, plotted versus volume fraction v_u of solute. This line reproduces the MW relations of Figures 96 and 97. Also shown in brown is the Maxwell-Wagner relation for the corresponding emulsion of globular water droplets in nonpolar material. Dashed line depicts relation (123).

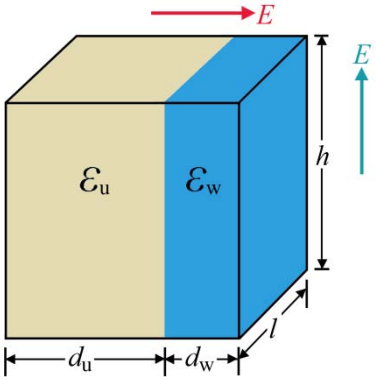

Figure 99. Simply shaped sample made of water (permittivity ε_w, volume fraction $d_w/(d_u + d_w)$) and other material with permittivity ε_u and volume fraction $d_u/(d_u + d_w)$. Different field directions are indicated by red and turquoise arrows.

contribution to the mixture permittivity is small and likewise small is its variation $d\varepsilon_m/dv_w$ with water content.

Another aspect is an often anisotropic structure of samples. A geometrically simple example is sketched in Figure 99. Again the sample is made of water with permittivity ε_w and a second material with permittivity ε_u. The mixture relation for the electric field directions marked by colour can be easily calculated assuming the sample to be placed in a parallel plate capacitor. For the field direction indicated by the turquoise arrow the total capacitance is given by the equation

$$\varepsilon_m(d_u + d_w)l/h = \varepsilon_w d_w l/h + \varepsilon_u d_u l/h, \tag{124}$$

which immediately yields the above mixture relation for samples without effects of depolarizing fields (Eq. 123). For the other field direction the total capacitance follows as

$$(d_u + d_w)/(hl\varepsilon_m) = d_w/[hl\varepsilon_w] + d_u/[hl\varepsilon_u], \tag{125}$$

so that

$$1/\varepsilon_m = v_w/\varepsilon_w + v_u/\varepsilon_u \tag{126}$$

and thus

$$\varepsilon_m = \varepsilon_w \varepsilon_u/(v_w\varepsilon_u + v_u\varepsilon_w) \tag{127}$$

results. This example demonstrates that, depending on the structure of the sample, internal fields may act a tremendous influence on the effective

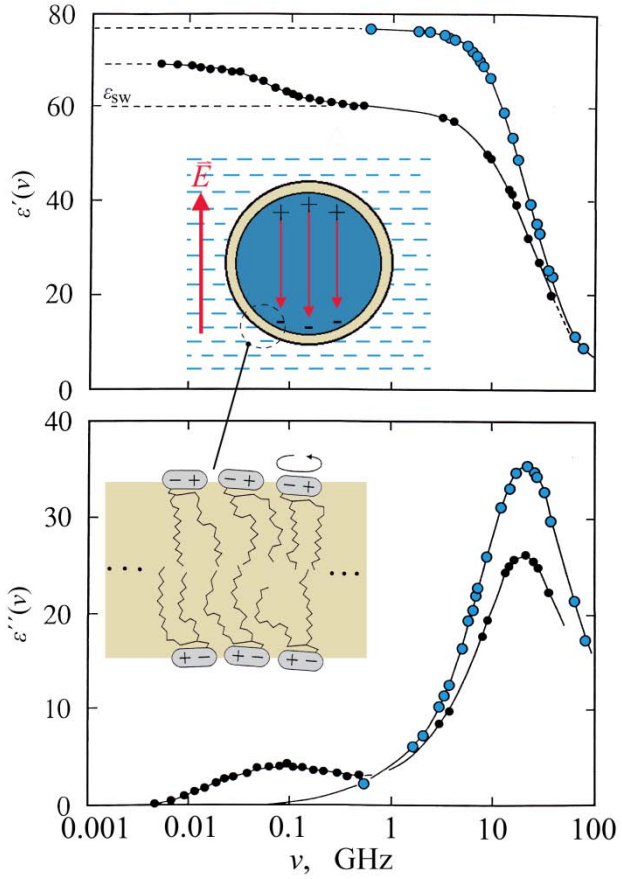

Figure 100. Real part ε' and negative imaginary part ε'' of the complex permittivity spectra for water and a 0.17 mol/l solution of C_{14}-lecithin in water at 30 °C [513, 514]. The insets show the structure of the solutions, in which the amphiphilic phospholipid molecules associate to form bilayers. This way the dipolar lipid head groups shield the nonpolar (hydrophobic) hydrocarbon groups from contact with water. The bilayers in turn self-assemble to nearly globular vesicles.

permittivity. Considering again a sample with balanced volume fractions ($v_u = v_w = 0.5$), Eq. (126) yields $\varepsilon_m = 3.9$ if $\varepsilon_w = 78.36$ and $\varepsilon_u = 2.0$ is assumed. In contrast, at missing depolarizing field (Eq. 123), the mixture permittivity amounts to the more than ten times larger value 40.2.

The strong correlation between the material structure, its internal electric field, and thus the permittivity of the material is also demonstrated by the dielectric properties of biological cell suspensions and by vesicle solutions, which are considered simple models to simulate biomembrane structure and functions. Biological membranes contain significant amounts of phospholipid molecules which are made of a hydrophilic (polar) head group and a hydrophobic (nonpolar) part. The latter consists typically of two alkyl groups, as shown in the lower inset of Figure 100. When dissolved in water, in order to prevent the hydrophobic groups from contact with the dipolar solvent, the phospholipid molecules spontaneously self-

aggregate to form bilayers which simultaneously build more or less globularly shaped vesicles (upper inset in Figure 100). Since the permittivity of the bilayers is small when compared to the permittivity of water, the water in the vesicle core is subject to considerable depolarizing electric fields. Hence the bilayer largely prevents the core water to interact with external electric fields and to contribute to the permittivity of the solution. This dielectric invisibility is evidenced by the comparatively small water contribution ε_{sw} to the static permittivity of a 0.17 mol/l aqueous solution of C_{14}-lecithin (1,2-dimyristoylglycero-L-3-phosphatidylcholine, Fig. 100). It follows also from the permittivity ε_v of a homogeneous dielectric sphere corresponding with a dielectrically heterogeneous vesicle. If the vesicle is assumed perfectly spherically shaped with core radius r_c, core permittivity ε_w, bilayer thickness d, and bilayer permittivity ε_b, theory yields [500]

$$\varepsilon_v = \frac{2\varepsilon_b+\varepsilon_w - 2(\varepsilon_b-\varepsilon_w)v_c}{2\varepsilon_b+\varepsilon_w+(\varepsilon_b-\varepsilon_w)v_c}, \tag{128}$$

where $v_c = (r_c/r_v)^3$ and $r_v = r_c + d$. Using r_c = 36 nm, r_v = 40 nm, ε_w = 76.6 at 30 °C, and ε_b = 6 this relation yields ε_v = 31, which compares to 57.5 from analogous application of Eq. (123), i.e. from neglection of internal fields. It is only mentioned here that the low-frequency relaxation at around 100 MHz (Fig. 100) is due to the reorientational motions of the dipolar phospholipid head groups on the surface of the bilayers.

The above discussion of rather simply composed and clearly structured materials discloses difficulties in finding the adequate mixture formula for the description of any composite dielectric. The set of problems increases with most applications to moisture determiniation in which often multicomponent systems with complicated structure are the focus of interest. Physically based models usually need to be matched empirically to the properties of the materials under consideration [515]. On many events empirical per se calibration rules need to be applied to a class of specific materials [516-520], aiming, of course, at a unified description of an as broad as possible variety of species within such class [521, 522]. In this context, particular interest is directed toward density-independent relations [522-526].

4.2.3 Dielectric relaxation time, hydrophobic hydration

4.2.3.1 Relative molal shift of principal relaxation time

Let us first consider dielectric spectra of aqueous solutions which can be well represented by the assumption of a continuous relaxation time distribution (Fig. 91) or for which the water contribution (Fig. 100) can be described supposing such distribution. It is found that, at small solute content, the relevant principal dielectric relaxation time increases linearly with molal concentration m of the solute. For two non-dipolar solutes some data is displayed in Figure 101 as example. In this context, it is important to recollect the molal concentration as a measure of the amount of substance (in moles) per given mass of solvent, in contrast to the more common molar concentration which refers to the volume of the entire solution.

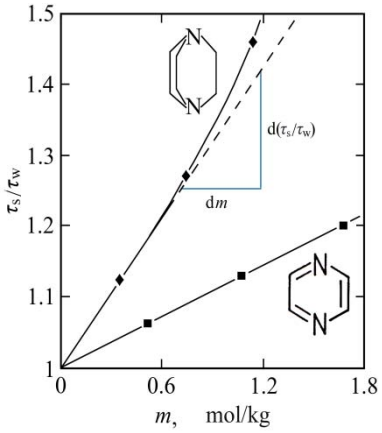

Figure 101. Relaxation time ratio τ_s/τ_w versus molal concentration m of solute for some aqueous solutions of triethylenediamine (⧫, [497]) and pyrazine (■, [499]) at 25 °C.

As clearly evidenced by Figure 101, the effect of different solutes on the water behavior presents itself by the initial slope in the relaxation time – versus – molality relations. Hence, in order to omit the rather obvious influence of solute concentration, the relative molal shift in the dielectric relaxation time at infinite dilution

$$B_d = \frac{1}{\tau_w} \lim_{m \to 0} \left(\frac{d\tau_s}{dm} \right) \tag{129}$$

is considered instead of τ_s itself when discussing solution properties. Some illustrative B_d values for aqueous solutions of nonpolar and dipolar (pyridine, urea and their derivatives) are presented in Table 1. The B_d values

Table 1: Relative molal shift B_d at 25 °C of the principal dielectric relaxation time of water for aqueous solutions of some nonpolar [487, 495, 499, 527] and dipolar molecules [499, 528, 529].

Heterocyclic hydrocarbons	B_d kg/mol	Urea and derivatives	B_d kg/mol
Pyrazine	0.13	Urea	0.03
Methylpyrazine	0.19	Methylurea	0.08
2,3-Dimethylpyrazine	0.24	*n,n*-Dimethylurea	0.17
2,5-Dimethylpyrazine	0.27	*n,n*'-Dimethylurea	0.18
2,6-Dimethylpyrazine	0.25	Ethylurea	0.13
Ethylpyrazine	0.21	Trimethylurea	0.24
2,3,5-Trimethylpyrazine	0.32	*n*-Propylurea	0.19
Quinoxaline	0.19	Tetramethylurea	0.30
2-Methylquinoxaline	0.24	*n,n*-Diethylurea	0.30
Pyridine	0.19	*n*-Butylurea	0.21
2-Methylpyridine	0.27	Bicyclic heterohydrocarbon	B_d kg/mol
3-Methylpyridine	0.22		
2,4-Dimethylpyridine	0.27	1,4-Diazabicyclo [2,2,2]octane	0.36
2,6-Dimethylpyridine	0.28		

are positive throughout, indicating that the relaxation time generally increases when organic molecules are dissolved in water. The data also reveals an overall trend to increase when hydrophobic (methyl) groups are added to a molecule, for example B_d increases from 0.13 $(mol/kg)^{-1}$ for pyrazine to 0.19 $(mol/kg)^{-1}$ for the methyl derivative, to 0.26 $(mol/kg)^{-1}$ for the 2,6-dimetyl derivative, and to 0.32 $(mol/kg)^{-1}$ for 2,3,5-trimethylpyrazine. This trend is a well-known feature of hydrophobic hydration. Within the framework of the wait-and-switch model of dielectric relaxation (sect. 4.1.3) it expresses the reduced density of hydrogen bonding sites in the neighborhood of hydrophobic groups or particles. The lower the density of such sites, the smaller the probability for the occurance of a suitable new hydrogen bond partner and the larger the waiting period for conditions promoting switching of the dipole direction of a water molecule near the solute. Also the large difference between the B_d values of urea (0.03 $(mol/kg)^{-1}$) and triethylenediamine (1,4-diazabicyclo[2,2,2]octane, 0.36 $(mol/kg)^{-1}$) supports the idea of the wait-and-switch model. In terms of the balanced number of hydrogen bond accepting and donating sites

and of the concentration c^* of hydrogen bonding sites urea ($O=C(NH_2)_2$) is very near to water. Its four donating sites at the hydrogens and four lone pair electrons (two at the oxygen and one at each nitrogen) lead to c^* = 174 mol/l, which compares to the slightly larger extreme value c^* = 221 mol/l for water (sect. 2.1.2). Because of this large c^* the waiting period for the availiability of a suitable new hydrogen bond partner is almost identical for water dipoles near urea and in pure water. Therefore the dielectric relaxation time of water increases only marginally when urea is added and thus B_d is small. The counterpart, triethylenediamine ($N(CH_2CH_2)_3N$), possesses only two hydrogen accepting sites, namely one at each nitrogen, but six hydrophobic -CH_2-groups. It is thus characterized by the abnormally small c^* = 17 mol/l, causing a long waiting period in the relaxation time of its neighboring water.

Additional details in the relaxation behavior of water in solutions will be discussed below when the dielectric spectra are considered in the light of the hydration model. In section 4.3.2.2 below, attention will be also given to effects from the steric distribution of alkyl groups, for instance to the finding of B_d as large as 0.30 $(mol/kg)^{-1}$ with tetramethylurea but only 0.21 $(mol/kg)^{-1}$ with isomeric *n*-butylurea (Table 1).

4.2.3.2 Hydration water relaxation time and concentration

The above discussion of B_d values combines the influence of solute molecules on the properties of water in one parameter. Hence it does not enable the separate evaluation of changes in the relaxation time provoked by the solute and of changes in the spatial extent of the modifications in the dielectric properties of water. More detailed information like this can be obtained from the hydration model introduced in sect. 4.2.1.2 as it provides both the hydration water relaxation time τ_h and the number Z_h of

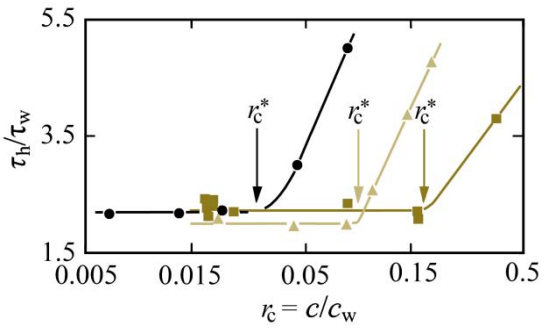

Figure 102. Hydration water-to-pure water relaxation time ratio τ_h/τ_w versus solute-to-solvent concentration ratio c/c_w for aqueous solutions of triethylenediamine (•, TED, [497]), polyvinylpyrrolidone (▲, PVP, [530]), as well as poly(ethylene glycol) (■, PEG, [531]).

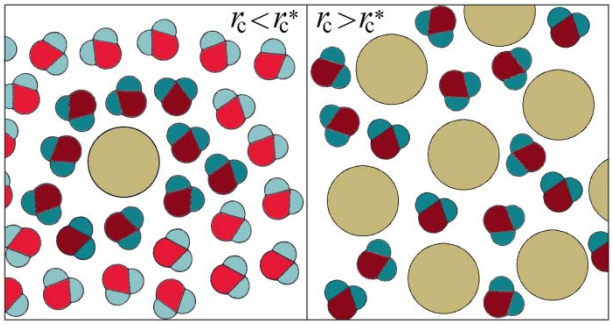

Figure 103. Sketch of aqueous solutions at low (left) and high (right) solute concentration. Solute particles are shown by light brown, affected and unaffected water, resp., is distinguished by dark and light colour.

hydration water molecules per molecule of solute. Relaxation times shown in Figure 102 for solutions of a low-weight molecule and two polymers confirm congruity of the hydration model. At comparatively low solute concentration ($r_c = c/c_w < r_c^*$) the relaxation times and also the corresponding numbers Z_h of hydration water molecules are independent of r_c and thus of c, as required for a meaningful hydration model. Only if the concentration cZ_h of hydration water exceeds the total water concentration c_w, i.e. if there is no unaffected water left (Fig. 103), the relaxation time increases distinctly and, for the systems under consideration, reaches values up to five times the pure water relaxation time. This particular concentration is marked by r_c^* ($\approx 1/Z_h$) in Figure 102.

The strong increase in the dielectric relaxation time of water in solutions with low water content ($r_c > r_c^*$, Fig. 102) attracts attention. It confirms the idea that the reorientational motions of water are not only governed by the strength of hydrogen bonds but also by the probability of forming new bonds. If the concentration of new hydrogen bonding sites is small, the waiting period for a new hydrogen bonding site is large, implicating a long relaxation time. This finding is an important aspect in the discussion of the properties of so-called "bound water".

Also the hydration water relaxation times at $r_c < r_c^*$ feature a noticeable facet as they cover a rather restricted range of values only (Fig. 102). This small range is further illustrated by a collection of data in Table 2, where results for some oxygen as well as nitrogen containing solutes are presented, including low-weight molecules, oligomers and polymers. Surprisingly, all τ_h/τ_w data falls in the small range between 1.5 and 2.3. There are still some indications of an increase in the hydration water relaxation time when alkyl groups are added to a solute molecule: $\tau_h/\tau_w = 1.5$ for pyrazine, but 1.9 for 2,6-dimethylpyrazine. Yet different solutes seem to act a more specific influence on the number Z_h of hydration water molecules than on

Table 2. Hydration water-to-pure water relaxation time ratio τ_h/τ_w for some organic solutes. Oxygen and nitrogen containing substances are discriminated by yellow and blue colour. Darker colour indicates polymers. Solutes with carbonyl group are marked by turquoise [497, 499, 529-532].

Solute	τ_h/τ_w	Solute	τ_h/τ_w
1,4-Dioxane	1.6	Pyridine	1.8
Ethylene glycol	2.0	1,4-Diazabicyclo[2,2,2]octane	2.2
Triethylene glycol	1.9	Urea	2.1
Triethylene glycol dimethylether	2.0	Aceteamide	2.1
Poly(ethylene glycol) 400	2.1	Dimethylamide	2.1
Poly(ethylene glycol) 600	2.1	Purine	1.9
Pyrazine	1.5	6-Methylpurine	2.1
2-Methylpyrazine	1.6	Poly(ethylene imine)	2.0
2,6-Dimethylpyrazine	1.9	Poly(propylene imine)	1.8
Quinoxaline	1.9	Polyvinylpyrrolidone	2.0
2-Methylquinoxaline	2.2	Polyacrylamide	2.3

the relaxation time τ_h itself. This tendency is, for instance, exposed by the data for the counterparts urea (B_d = 0.03 (mol/kg)$^{-1}$; $\tau_h = 2.1\tau_w$) and triethylene diamine (1,4-diazabicyclo[2,2,2]octane; B_d = 0.36 (mol/kg)$^{-1}$; $\tau_h = 2.2\tau_w$). Though the B_d values differ significantly, the hydration water relaxation times almost agree. Hence the large difference in the relative molal shift of the principal relaxation time reflects substantially different numbers of hydration water molecules. With triethylenediamine (Z_h = 23) the hydration region exceeds the nearest neighbor water layer around the solute by a considerable amount. In contrast, urea (Z_h = 3) affects just about one third of its neighboring water molecules in their reorientational motions. It is suggested that the overall shape and the steric configuration of the nitrogens of triethylene diamine are particularly suited to promote hydrophobic hydration around it, whereas quite hydrophilic urea offers only small areas in which changes in the dielectric relaxation of adjacent water are induced.

4.3 Electrolyte aqueous solutions

4.3.1 Extrapolated static permittivity

Apart from the conductivity contribution to the negative imaginary part of the complex permittivity (Fig. 21) the dielectric spectra of solutions of 1:1

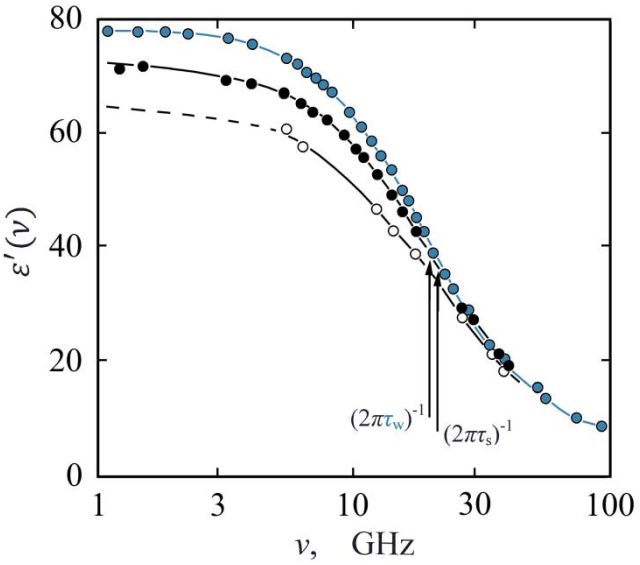

Figure 104. Real part of the complex permittivity spectra for water (blue points) as well as 0.5 mol/l aqueous solutions of NaCl (•, [533]) and HCl (○, [534]) at 25 °C.

valent and many 2:1 and 3:1 valent electrolytes resemble those of solutions of non-polar solutes. Aqueous solutions of some 2:1 and 3:1 valent salts, however, and particular such of 2:2 and 3:2 valent salts exhibit contributions from dipolar ion complexes due to incomplete dissociation of the solutes [535-538]. These contributions will be introduced below in chapter 4.3.3. In general, ion cloud relaxation may also contribute an extremely small-amplitude relaxation to the dielectric spectra of electrolyte solutions [536, 537, 539-541]. It originates from the oppositely charged ionic atmosphere surrounding an ion in diluted solution. In our context, however, the effects from ion cloud contributions may be neglected because of their diminutiveness. Hence the focus here is the influence of ions on the dielectric properties of water. Compared to the solutions of uncharged solutes, two features of the water contribution to the spectra (or of the spectra at all, if 1:1 valent electrolytes are considered, Fig. 104) are remarkable. First, the (extrapolated) static permittivity is significantly reduced even if the water concentration changes only marginally when the ionic solutes are added to the pure solvent. Second, the relaxation frequency $(2\pi\tau_s)^{-1}$ may also become larger. Hence in electrolyte solutions the dielectric relaxation time may be shorter than with pure water.

4.3.1.1 Experimental evidence

The substantial reduction in the (extrapolated) static permittivity of electrolyte solutions is demonstrated by Figure 105, where $\varepsilon(0)$ data for 1 molar aqueous solutions of 1:1 valent electrolytes is presented. In correspondence with solutions of nonpolar molecules (Fig. 96) the permittivities for solutions of bromides of large organic cations tend to exceed the predictions from the Bruggeman mixture relation. This result confirms the idea of a hydrophobic hydration effect mentioned before. With decreasing cation radius r^+, however, the $\varepsilon(0)$ data falls more and more below the Bruggeman mixture permittivity. The effect is particularly strong for hydrochloric acid with its exceedingly large ionic conductivity. The data in Figure 105 also reveal a comparably small influence of the anion on the static permittivity of the electrolyte solutions.

On a first glance, the strong dielectric decrement in the static permittivity of solutions of low-weight electrolytes may be globally assigned to the existance of bound water. Yet in the following sections a somewhat more sophisticated picture of the solutions will be drawn.

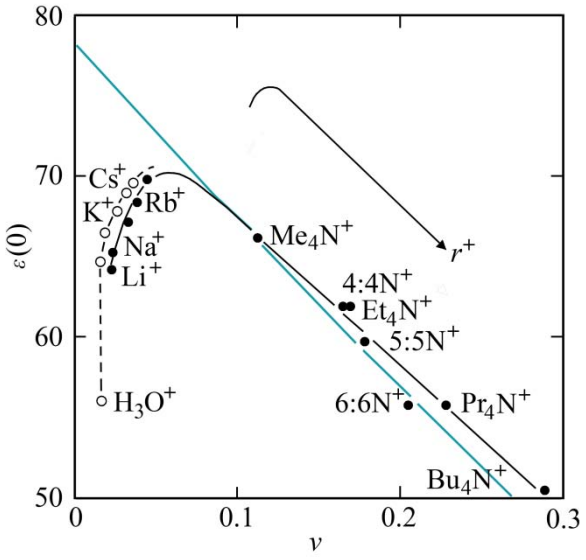

Figure 105. Static permittivity $\varepsilon(0)$ versus volume fraction of solute for 1 mol/l aqueous solutions of hydrochloric acid [534], as well as chlorides (○) and bromides (•) of alkali ions [542, 543] and of some 1-valent large organic cations [544]. X_4N^+ denote tetraalkyl ammonium ions, notation $Y{:}YN^+$ is used to symbolize azoniaspiroalkane ions. The turquoise line shows the Bruggemann mixture relation (Eq. (120), Figs. 96, 97). Full and dashed black lines are given to indicate the trend in the data. All data refer to 25 °C.

4.3.1.2 Kinetic depolarization

Onsager, when contemplating peculiar static permittivity data for sulfuric acid [545], suggested a coupling between hydrodynamic effects and the dielectric properties of electrically conducting liquids. As sketched in Figure 106, an ion moving in an external electrical field sets up a non-uniform hydrodynamic flow [546, 547]. Thereby the solvent dipolar molecules are rotated opposed to the direction promoted by the electrical interaction with the external field [548]. Within the framework of the continuum theory by Hubbard and Onsager ('HO' [549]), the resulting kinetic polarization deficiency of aqueous systems can be expressed by the decrement

$$\delta\varepsilon_{\mathrm{HO}} = \frac{2}{3}\frac{\varepsilon_{\mathrm{w}}(0)-\varepsilon_{\mathrm{w}}(\infty)}{\varepsilon_0\varepsilon_{\mathrm{w}}(0)}\sigma\tau_{\mathrm{w}} \qquad (130)$$

in the static permittivity. In deriving Eq. (130) perfect slip boundary conditions on solvent flow at the ion surface have been assumed.

Hence the Onsager-Hubbard continuum model predicts the kinetic dielectric decrement proportional to the specific ionic conductivity σ of the solutions and to the dielectric relaxation time τ_{w} of a solvent. The larger σ the more dipolar solvent molecules are rotated by the hydrodynamic flow in the direction opposed to that promoted by the electrical interaction with the external field. The larger the solvent relaxation time, the longer the dipole moments remain in the opposed direction.

Both plausible dependencies of $\delta\varepsilon_{\mathrm{HO}}$ are globally reflected by experimental findings. The dominating role of the specific electric conductivity

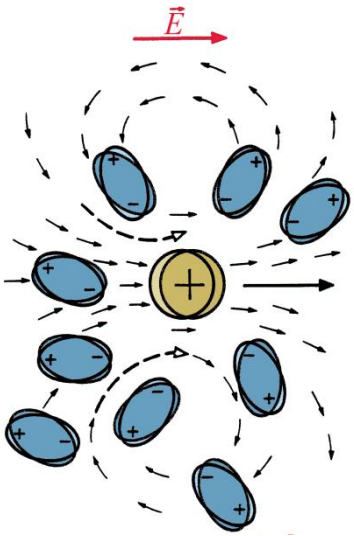

Figure 106. Illustration of the coupling between hydrodynamic and dielectric properties of electrolytre solutions. Movement of an ion in an electrical field $\vec{E}$ produces a solvent flow (small black arrows) that tends to rotate dipolar solvent molecules.

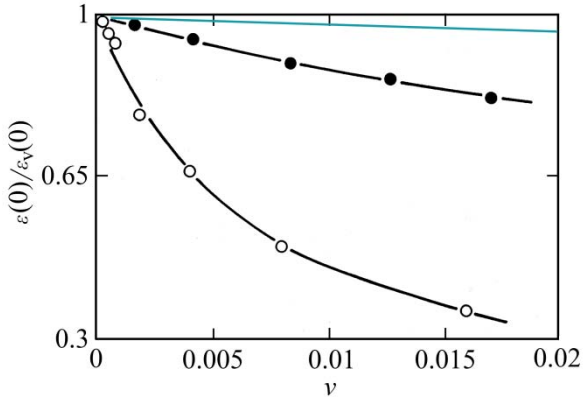

Figure 107. Solution-to-solvent static permittivity ratio $\varepsilon(0)/\varepsilon_v(0)$ as function of volume fraction v of solute for aqueous solutions of lithium chloride in water (•, τ_w = 8.27 ps) and methanol (○, τ_s = 50.9 ps) at 25 °C [550, 551]. The turquoise line is the graph of the Bruggeman relation (Eq. 120). Full lines are given to guide the eyes.

follows, for instance, from the small effect of kinetic depolarization in the static permittivity of solutions with comparably small σ, such as those containing large organic cations (Fig. 105). Likewise the large kinetic decrement for acids may be taken to confirm the $\delta\varepsilon_{HO}(\sigma)$ relation. In this context, it has to be recalled, however, that proton motion occurs hardly by Stokes transport but rather by shift of protons along hydrogen bond networks (sect. 2.1.3). Insofar the fact that the static permittivity decrement of acids

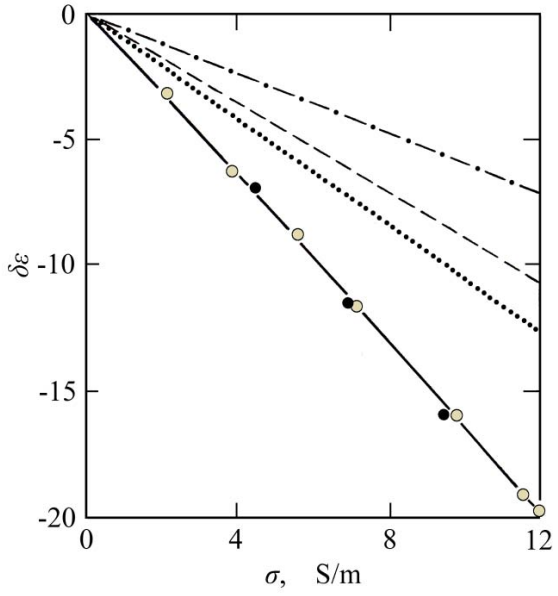

Figure 108. Static permittivity decrement $\delta\varepsilon = \varepsilon(0) - \varepsilon_m$ versus specific electric conductivity σ for aqueous solutions of lithium chloride (light brown points) and lithium nitrate (black points) at 25 °C [551]. The dash-dot curve is the graph of the continuum model relation (Eq. 130), the dashed curve shows predictions by the molecular model [552], the dotted curve those from the microscopic model [553].

nicely fits to concepts for other electrolytes is not completely conceived and needs further attention.

The impact of the relaxation time is demonstrated by the relative static permittivities $\varepsilon(0)/\varepsilon_v(0)$ for solutions of LiCl in water and methanol (Figure 107). In conformity with the significantly larger principal relaxation time of methanol ($\tau \approx 6\tau_w$, 25 °C) the $\varepsilon(0)/\varepsilon_v(0)$ values of the methanolic solutions decrease noticeably stronger with volume fraction v of electrolyte than those of the aqueous solution.

Molecular models reveal the kinetic polarization deficiency to depend on the ion radius [552-555]. They also yield different predictions for the extent of dielectric decrements (Fig. 108). With most electrolyte solutions under consideration, however, the experimental decrement exceeds the predictions from either model. This aspect is discussed in further detail in the next section.

4.3.1.3 Dielectric saturation

In Figure 109 experimental static permittivity values for some aqueous solutions of lithium chloride are shown to disclose again the difference between the $\varepsilon(0)$ data and the predictions from the mixture relation (Eq. 120). As already mentioned before, even if the effect of kinetic depolarization is taken into account there is still a considerable gap left. For reasons of simplicity, only the Hubbard-Onsager continuum model of the kinetic dielectric decrement is considered in the following. Hence according to

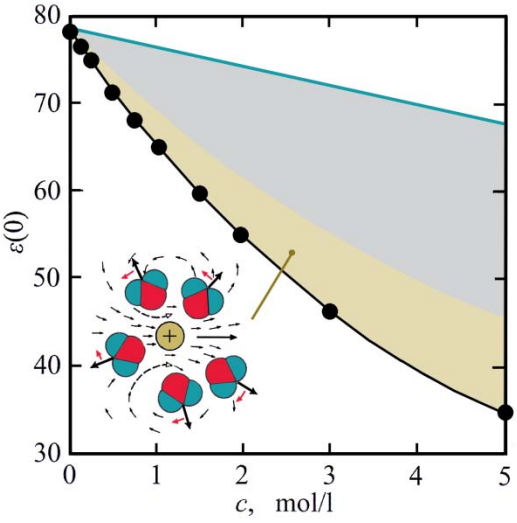

Figure 109. Extrapolated static permittivity $\varepsilon(0)$ of aqueous solutions of LiCl as function of salt concentration c [535]. Light brown area shows the effect of kinetic depolarization according to Eq. (130). The grey area indicates the remaining dielectric decrement with respect to the Bruggeman mixture relation (Eq. 120, turquoise line). The inset illustrates the process of kinetic depolarization.

results shown in Figure 108 the effect of kinetic depolarization may be somewhat underestimated.

It appears nevertheless useful to assume the remaining gap between the experimental static permittivity data and the prediction by the mixture relation (Eq. 120), i.e. the grey area in Figure 109, to result from dielectric saturation, also named structure saturation. The idea behind this term is sketched in Figure 110: water molecules in the strong Coulombic fields of small ions may be restricted in their motions and the direction of their electrical dipole moment may be primarily governed by the dipole interactions with the ionic field. In such situations the (dielectrically saturated)

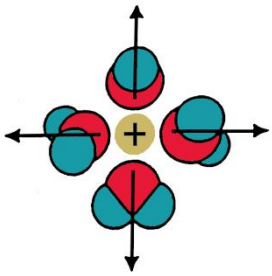

Figure 110. Illustration of dielectric saturation of water in strong Coulombic fields of small ions.

	d^0	d^{10}	d^0	d^{10}	d^0	d^{10}
	Li^+ 3.9		Be^{2+} 6.5			
	Na^+ 2.6		Mg^{2+} 7.0		Al^{3+} 11.5	
H_3O^+ 0	K^+ 0		Ca^{2+} 6.4	Zn^{2+} 4.3		
	Rb^+ 0	Ag^+ 0	Sr^{2+} 7.0	Cd^{2+} 1.3	Y^{3+} 12.7	In^{3+} 3.9
	Cs^+ 0		Ba^{2+} 5.4		La^{3+} 13.4	

Figure 111. Numbers Z^+ of apparently saturated water molecules per cation. Light brown points and turquoise fields indicate the areas of bare ions and of the dielectrically saturated solvent regions, respectively, on an arbitrary scale. The cations are ordered according to their electrical charge, the structure of their outer electron shell, and their radius.

water molecules will hardly respond to an external field and will thus lead to a reduction in the static permittivity of the relevant electrolyte solution. Numbers Z^+ of apparently dielectrically saturated water molecules per cation are presented in Figure 111. Since we have just one parameter to estimate these numbers, we can only derive apparent values, which are based on the assumption of completely saturated (i.e. completely irrotationally bound) water molecules per ion. Unfortunately, because of missing more sophisticated information, the consideration of any distribution in the degree of saturation is impossible. Nevertheless, the apparent numbers of saturated water molecules feature some interesting aspects:

- The hydronium ion does not provoke saturation. The considerable dielectric decrement (Fig. 105) can be solely explained by kinetic depolarization if the Hubbard-Onsager continuum model (Eq. 130) is adopted. As mentioned before, however, relevance of Stokes-like motions of the hydronium ion may be questioned because of the special proton transport mechanism.
- The small monovalent lithium ion reveals about four completely saturated water molecules, corresponding roughly with the number of nearest neighbors.
- With the sodium ion the effect of dielectric satutration is already smaller and either does not comprise all nearest neighbors or the dipole orientations of nearest neighbors are not completely fixed in the ionic field.
- With the larger alkali ions and with monovalent silver ion dielectric saturation is missing completely.
- The Z^+ values ($5.5 \le Z^+ \le 7.0$) of the two-valent alkaline earth metal ions slightly exceed the numbers of nearest neighbors. Also striking is the small variation of the number of saturated water molecules with cation radius.
- Three-valent aluminium, transition metal yttrium, and rare-earth metal lanthanum ions reveal also a comparatively small range of Z^+ values ($11.5 \le Z^+ \le 13.4$). With these cations dielectric saturation extends even beyond the layer of next nearest water molecules.
- Most conspicuous, ions with d^{10} outer electron shell exhibit distinctly smaller Z^+ values than equally (or similarly) sized ions with d^0 shells. This is a remarkable result as for the isolated ions both electron configurations are spherically symmetric. Hence it suggests that, in aqueous solutions, the hybridization of electronic orbitals of the d^{10} ions is partly abolished and thus symmetry is broken.

This suggestion is supported in a very obvious manner by evidence from the dielectric spectra of relevant electrolyte solutions. In contrast to cations with d^0 outer electron shells, such with d^{10} electronic structure tend to form ion complexes with monovalent anions in water, as will be dicussed in section 4.3.3. Ion complex formation reduces the electrical field

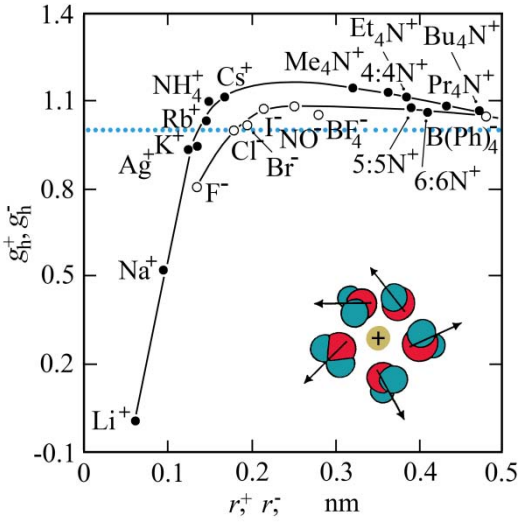

Figure 112. Cationic and anionic orientation correlation factors g_h^+ and g_h^-, respectively for the nearest neighbor water of monovalent ions, displayed versus ionic radii r^+ and r^-. X_4N^+ and Y:YN$^+$ denote the tetraalkyl ammonium and azoniaspiro alkane ions (see also Fig. 105), $B(Ph)_4^-$ is the short term of the tetraphenalborate ion. Dotted blue line indicates vanishing correlation ($g_h^\pm$ = 1). The inset sketches incomplete dielectric saturation ($g_h^+ > 0$).

strength and thus the ion-water interactions around the ions. For monovalent ions the effect of short-range ion-solvent interaction is shown in an alternative manner in Figure 112 . Orientation correlation factors $g_h^\pm$ are presented which have been calculated according to the relation

$$g_h^\pm = 1 - Z^\pm / Z_{nn}^\pm, \tag{131}$$

with $Z_{nn}^\pm$ denoting the number of nearest neighbor water molecules per ion. Hence applying this equation, it is assumed that only the nearest neighbors are subject to short-range ion-water interaction. As already shown before, the nearest water molecules of the lithium ion are almost completely saturated. Among the other monovalent ions, only Na^+ and F^- reveal a weak effect of dielectric saturation. For ions with radii roughly larger than that of a water molecule (when presumed spherically shaped), the correlation factors are slightly larger than one, indicating the trend that is characteristic of the hydration water of hydrophobic solutes (Fig. 96, sect. 4.2.2.1).

According to our expectations the numbers of saturated water molecules decrease with increasing salt concentration *c*, as shown for lithium chloride solutions in Figure 113. With increasing *c* hydration regions and also the electric fields of different ions overlap. At small salt concentration neutron diffraction measurements disclosed indeed the dipole moments of water molecules adjacent to cations radially orientated [556]. At larger salt concentrations, however, a with *c* increasing tilt angle between the direction of the ionic field and that of the dipole directions emerged. More and

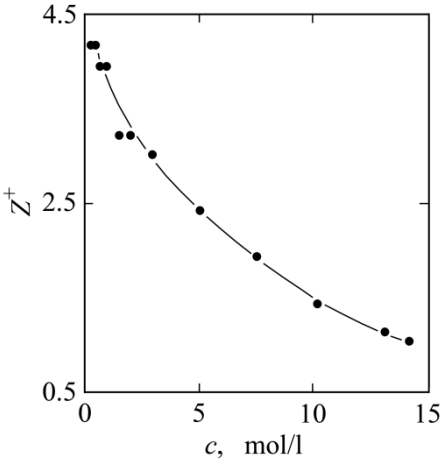

Figure 113. Number Z^+ of apparently saturated water molecules per lithium ion in aqueous solutions of LiCl at 25 °C, displayed as function of salt concentration c.

more water molecules are thereby enabled to contribute to the static permittivity. According to the results shown, the number of saturated water molecules per ion likely increases toward smaller salt concentration. At even smaller salt content (c < 0.2 mol/l), however, the accuracy in the extrapolated $\varepsilon(0)$ is insufficient to extract small amounts of saturated water with adequate accuracy.

The data displayed in Figure 113 has been evaluated using the Onsager-Hubbard continuum relation (Eq. 130) which had been derived for diluted solutions. Depending on detais in the modelling of dielectric spectra, the numbers of dielectric saturated water molecules per ion may deviate from those presented in this section. Somewhat larger values have in fact been reported for some series of ions [557, 558]. The absolute $Z^{\pm}$ numbers should thus not be overvalued. Their trend, however, may be taken to exemplify the ion-water interactions realistically and to illustrate the molecular mechanisms behind the reduction of the extrapolated static permittiviy of electrolyte solutions.

4.3.2 Dielectric relaxation time

Ion-water interactions do not just affect the orientational polarizability of the solvent, but, as expected intuitively, also its relaxation time. Other than molecules in aqueous solution, elctrolytes may also induce a reduction of the relaxation time of water. Both effects are depicted in Figure 114. As already described in section 4.2, highly hydrophobic triethylenediamine

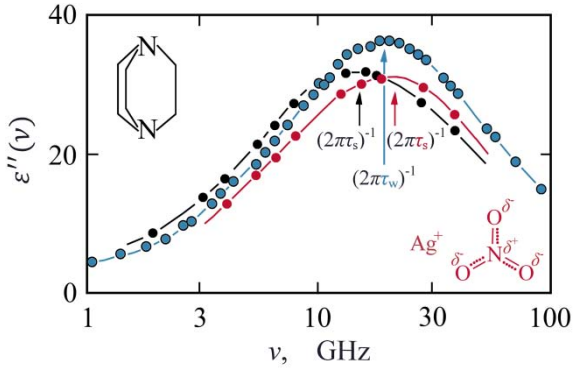

Figure 114. Negative imaginary part ε'' of the dielectric spectra of water (blue points), as well as aqueous solutions of triethylene diamine (0.67 mol/l, black points) and $AgNO_3$ (0.82 mol/l, red points) at 25 °C. Insets show the structure of the solutes.

shifts the dielectric spectrum towards smaller frequencies, correspondent with an increase in τ_s. Silver nitrate, however, causes the relaxation frequency of the solvent to rise with respect to pure water. Hence it provokes a reduction in the dielectric relaxation time. It is true that minor amounts of ion pairs are seemingly formed in the $AgNO_3$ solution. In either case, however, their concentration too small [559] to noticeably affect the principal dielectric relaxation time.

4.3.2.1 Positive, negative, hydrophobic hydration

For some monovalent ions hydration water relaxation times (Fig. 115) substantiate the existence of both τ_h values larger and smaller than τ_w. At $r < 1.5r_w$ the hydration water relaxation times decrease monotonuously with ion radius, from $\tau_h \approx 2.5\tau_w$ for the lithium ion to $\tau_h \approx 0.5\tau_w$ with iodide. As explained in chapter 4.3.1 before, the water around small Li^+ and Na^+ is subject to preferential orientation of dipole moments in the direction of the ionic fields. Molecular reorientation is thus largely restricted to the proton-around-proton motions around the direction of the electric dipole moment. Therefore relaxation time data from nuclear magnetic relaxation measurements is shown in Figure 115. Because the small ions attract the water molecules strongly, such motions are decelerated with respect to pure water and thus reveal increased relaxation times. This special effect is often considered the normal property of ion hydration. In order to distinguish it from quite different hydration behavior, it is more completely named 'positive' hydration.

As obvious from Figure 115, medium-sized ions ($1 < r/r_w < 2$) induce a quite different effect. The water molecules in their hydration layer are able to reorientate faster than in pure water. For a long time such 'negative'

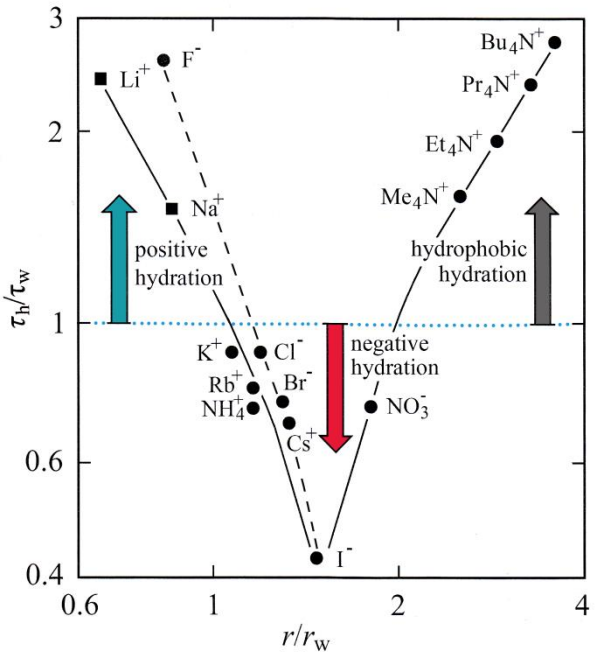

Figure 115. Relaxation time ratio τ_h/τ_w versus ratio of ion radius r to radius r_w of the water molecule (if assumed spherically shaped). The τ_h values (●) have been evaluated assuming only coordination water molecules to be affected, including evidence from NMR measurements [542]. Relaxation times for dielectrically saturated water around Li^+ and Na^+ ions (■) are completely taken from NMR data [560, 561].

hydration has been considered to reflect the structure breaking actions of ions which are too large to attract water molecules strongly but which can still affect the water hydrogen network by their Coulombic field. Within the framework of the wait-and-switch model of dielectric relaxation negative hydration is simply a consequence of a high density of hydrogen bonding sites in a more general meaning. In Figure 116 the situation is illustrated by a water molecule near iodide, which may be taken as a prime example of negatively hydrated ion. With its extended soft electron shell iodide offers a large angle range in which a positively charged hydrogen site of a water molecule can interact with the anion, corresponding with a high concentration of hydrogen bonding sites. Due to this increased probability for hydrogen bond-like interactions the waiting period in the dielectric

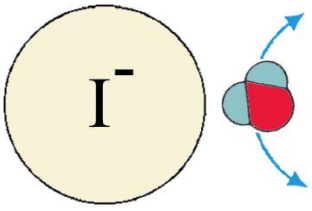

Figure 116. Sketch of a water molecule neighboring a comparatively large negatively charged iodide ion.

Table 3. Cationic and anionic radii r^+ and r^- [562] as well as relative molal shifts B_d^+ and B_d^- [542, 543], respectively, of dielectric relaxation times at 25 °C for some mono-, bi-, and trivalent ions.

Cation	r^+ nm	B_d^+ kg/mol	Ion	r^+, r^- nm	B_d^+, B_d^- kg/mol
Li^+	0.060	-0.04	Al^{3+}	0.050	-0.07
Na^+	0.095	-0.07	Y^{3+}	0.093	-0.07
K^+	0.133	-0.07	La^{3+}	0.115	-0.10
Rb^+	0.148	-0.07	F^-	0.136	0.05
NH_4^+	0.148	-0.04	Cl^-	0.181	-0.01
Cs^+	0.169	-0.05	Br^-	0.195	-0.03
Be^{2+}	0.031	-0.08	I^-	0.216	-0.05
Mg^{2+}	0.065	-0.14	BF_4^-	0.28	-0.13
Ca^{2+}	0.099	-0.16	NO_3^-	0.29	-0.05
Sr^{2+}	0.133	-0.13	$B(Ph)_4^-$	0.38	0.44
Ba^{2+}	0.135	-0.17	CO_3^{2-}	0.25	0.18

relaxation time decreases as outlined before. The impact of a soft electron structure on the hydration characteristics of ions is also demonstrated by the nitrate ion with its delocalized electrons and its negative charges at the three oxygen atoms (Fig. 114).

The hydration water relaxation times of Figure 115 will be further discussed later. It is interesting to first briefly examine the relative molal shifts in the principal dielectric relaxation time (Table 3) induced by some ions. Curiously, most ions reveal negative B_d^+ or B_d^- values. This is also true for Li^+ and Na^+ for which increased hydration water relaxation times result from nuclear magnetic relaxation measurements (Fig. 115). This apparent discrepancy follows from the finite residence times τ_h^* and τ_w^* of water molecules within the hydration regions and the bulk phase, respectively. Due to thermal motions and collisions, water molecules permanently exchange between the areas of different dielectric properties and contribute to the dielectric spectrum, corresponding with an effect in the time dependence of the polarization. At strong dielectric saturation (g_h = 0, Fig. 112), for example, the dielectric decay function (Eq. 14) becomes

$$\Psi(t > t^*) = \Psi(t^*)\{(\tau_w^{-1} - p_2)\exp(-p_1\Delta t) - (\tau_w^{-1} - p_1)\exp(-p_2\Delta t), \qquad (132)$$

where

$$\Delta t = t - t^* \tag{133}$$

and

$$p_{1,2} = 0.5(\tau_w^{-1} + \tau_w^{*-1} + \tau_h^{*-1} \pm q^{1/2}) \tag{134}$$

as well as

$$q = (\tau_w^{-1} + \tau_w^{*-1} + \tau_h^{*-1})^2 + 4(\tau_w^{*-1}\tau_h^{*-1})^{-1} \tag{135}$$

[563]. Using these relations to calculate the residence time of water molecules in the hydration shell of Li^+, $\tau_h^* \approx 40$ ps follows, in close agreement with nuclear magnetic relaxation measurement [564]. With bi- and trivalent cations the situation is even more complicated. The residence time of water in the inner hydration shell is too long (e.g. $\tau_h^* \geqslant 1$ µs, Al^{3+} [565]) to act a noticeable influence on the microwave dielectric spectrum. But reorientational motions as well as exchange processes in partly saturated hydration shells outside the first shell of strongly saturated water may contribute to the negative shift in the principal relaxation time. A region of increased mobility ($\tau_h < \tau_w$) may probably also arise from an increased density of hydrogen bonding sites at the surface of strongly saturated shells. Even though the full details of the hydration properties of multivalent ions are missing, in view of applications it is important to notice that in solutions of small and multiply charged ions a negative shift of the principal dielectric relaxation time may exist.

At larger ion radii ($r > 2r_w$) the relaxation time ratio increases with r, as demonstrated for the series of tetraalkyl ammonium ions in Figure 115. The electrical field at the surface of the large organic ions is too weak to noticeably affect the water reorientational motions. In correspondence to hydrophobic molecules, these ions offer an inert surface to neighboring water molecules, thereby effectively reducing the local concentration of hydrogen bonding sites and thus the waiting period in the relaxation time. The effect of hydrophobic hydration is nicely demonstrated by principal relaxation times for solutions of a cationic surfactant shown in Figure 117. At solute concentrations below the critical micelle concentration *cmc* the organic cations are molecularly dispersed and thus completely hydrated. Owing to the long hydrocarbon chain, the principal relaxation times of the solutions increase considerably with molal concentration m, yielding $B_d = 0.41$ $(mol/kg)^{-1}$. In the concentration range around the *cmc* the cations start to self-aggregate in order to form micelles and to prevent considerable parts of the alkyl chains from contact with water. Since, in the micelles, only alkyl groups close to the hydrophilic head groups encounter water,

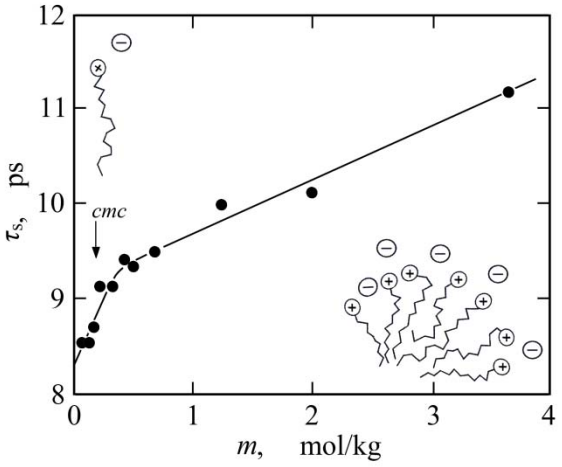

Figure 117. Principal dielectric relaxation time τ_s versus molal concentration m of solute for aqueous solutions of *n*-octyl ammonium chloride at 25°C [566, 567]. The insets draft molecularly dispersed solute as well as part of an almost globular micelle.

the distinctly smaller relative slope $\hat{B}_d$ = 0.05 (mol/kg)$^{-1}$ results. Here the slope is defined as

$$\hat{B}_d = \frac{1}{\tau_w}\left(\frac{d\tau_s}{dm}\right)_{c>cmc} . \qquad (136)$$

This is another exemplification of the effect of hydrophobic groups on the reorientational mobility and thus dielectric relaxation time of water.

4.3.2.2 H-bonding sites, structure, and flexibility of solute

So far the hydration behavior of solutes has been considered in the light of the wait-and-switch model of hydrogen network fluctuations. This model offers indeed a convenient path to consistently subsume a varity of features of water's dielectric relaxation. There are, however, also indications that factors other than the local concentration of hydrogen bonding sites may act an influence on the dielectric relaxation of water and dipolar solvents in general. Some evidence will be presented in this section.

A prominent example is the hydration water relaxation times of three series of organic cations shown in Figure 118. Within each series, τ_h increases with molar volume ϕ^+ of cations, in conformity with the increasing hydrophobic character of the solute and, in turn, the decreasing local concentration c^* of hydrogen bonding sites. At comparable sizes, however, the hydration water relaxation times of differently shaped cations differ

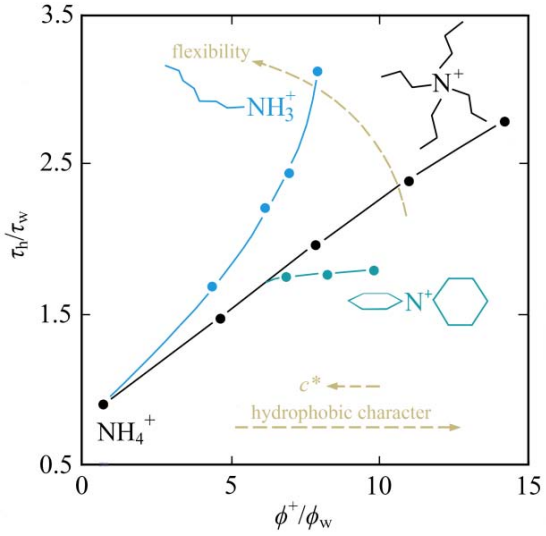

Figure 118. Hydration water–to-pure water relaxation time ratio τ_h/τ_w at 25 °C versus cation-to-water molar volume ratio ϕ^+/ϕ_w for three series of organic cations deriving from NH_4^+: blue points, *n*-alkylammonium ions [566]; black points, tetraalkyl ammonium ions; turquoise points, azoniaspiroalkane ions [544].

substantially. The *n*-alkyl ammonium ions display the largest relaxation times. Evidently they promote a comparatively stable hydration water structure. Distributing the hydrocarbon groups around the positively charged nitrogen to form tetraalkyl ammonium ions results in a reduction of the τ_h values. These values decrease again when, as with the azoniaspiroalkanes, closed loops are formed from the hydrophobic chains. Hence properties not considered so far, such as the existence of terminal methyl groups and the flexibility of the solute, seem to be major parameters conditioning the hydration water.

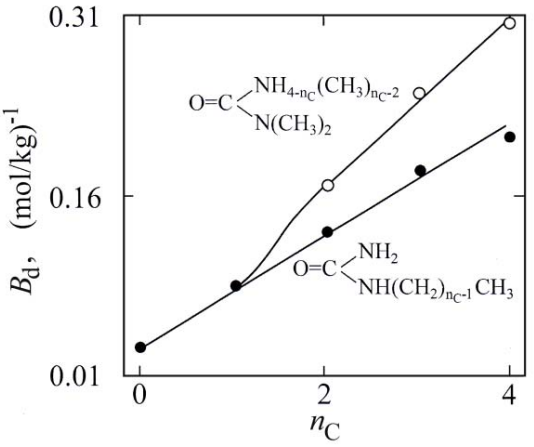

Figure 119. Relative molal shift B_d of the principal dielectric relaxation time of the water contribution to the spectra of aqueous solutions of urea derivatives, at 25 °C displayed as function of number n_C of methyl groups per molecule [529]: ●, *n*-alkyl derivatives; ○, dimethyl-, trimethyl-, and tetramethylurea.

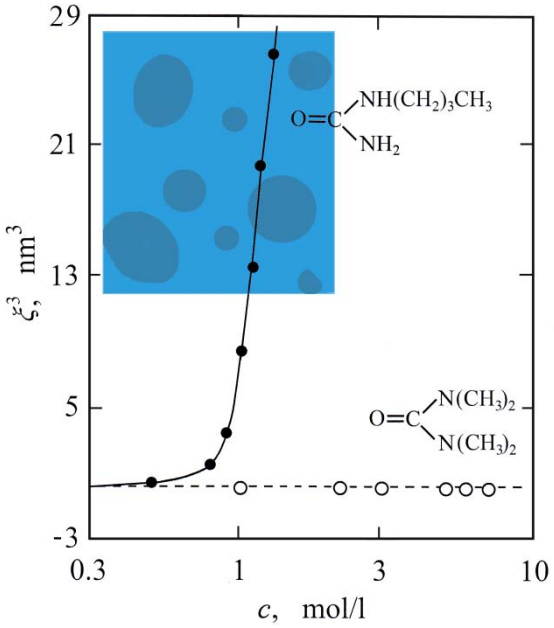

Figure 120. Fluctuation correlation volume ξ^3 at 25 °C, as following from broadband ultrasonic spectra for aqueous solutions of tetramethylurea (○) and *n*-butylurea (●, [568]). The sketch delineates the subdivision of the solution in a phase with solute content larger than the mean concentration *c* and, consequently, another one with solute content smaller than *c*.

Another representative of the effect of structural isomerization of solutes on the dielectric relaxation of hydration water is the B_d values for the water contribution to the dielectric spectra of urea derivatives (Fig. 119). With those solutes a different behavior emerges: at identical n_C the series of *n*-alkyl derivatives exhibits smaller shifts in the water dielectric relaxation time than that with methyl groups distributed around the urea structure. The reason appears to be a microheterogeneous structure of the solutions with extended alkyl chains of the solute. By some analogy with micelle formation solutes with long hydrophobic chains tend to induce two phases in solution, one with solute concentration slightly larger than the mean concentration *c* and, correspondingly, the other one with solute concentration somewhat smaller than *c*. The distribution of such concentration differences fluctuates rapidly. The fluctuation correlation time

$$\tau_\xi = \xi^2/(2D) \tag{137}$$

is controlled by the fluctuation correlation length ξ, measuring the mean spatial extent of the fluctuations and by the mutual diffusion coefficient *D* [568, 569].

Figure 120 reveals the fluctuation correlation volume of aqueous tetramethylurea solutions to be constant up to very high solute concentrations and, in addition, to be on the order of the molecular volume of the solute.

Hence tetramethylurea is molecularly dispersed in water so that its hydrophobic groups are completely exposed to the solvent. In contrast, *n*-butylurea tends to cluster in order to partly shield its alkyl chain. This way the hydration shells around the hydrophobic butyl group are not fully developed, thus causing only a reduced shift in the principal dielectric relaxation time of water.

Other conspicuous systems are carbohydrate aqueous solutions. Carbohydrates, the 'waters of carbon', characterized by the simple empirical formula $C_m(H_2O)_n$, play multiple roles in the design of life on molecular and cellular levels. Because of their exceptional structural flexibility and rich conformational variety, they offer an additional alphabet in the biosphere which is commonly used for signaling, cell-cell recognition, or molecular and cellular communication [570-574]. Probably the outstanding flexibility of the molecules also provokes the unusual dielectric properties of carbohydrate aqueous solutions, as for two series of monosaccharide solutions exemplified by their dielectric relaxation times in Figure 121. For reasons of comparison, data for monohydric alcohol-water mixtures are also shown. They roughly follow the trend to increase with decreasing concentration c^* of hydrogen bonding groups and water molecules ($c^* = c + c_w$), as predicted by the wait-and-switch model and as already demonstrated by Figure 87. Contrasted with this behavior, the relaxation times for the solutions of monosaccharides ($c^* = 6c + c_w$) increase considerably stronger with c^*. When represented by power law

$$\tau_1/\tau_w = (c^*/c_w)^{-\zeta}, \tag{138}$$

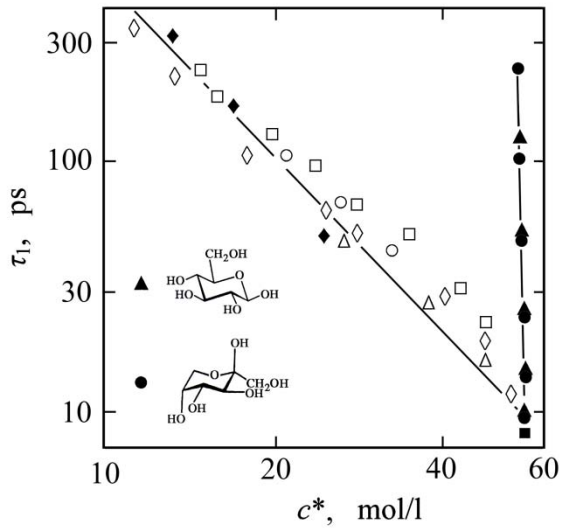

Figure 121. Principal dielectric relaxation time τ_1 at 25 °C, versus the sum of hydrogen bonding groups and water concentrations for solutions of D-glucose (▲) and D-fructose (●, [575]), methanol (Δ, [576]), ethanol (○, [577]), isopropyl alcohol (□, [576]), as well as *tert*-butyl alcohol (◊, [578]). Pure water (■) and alcohol (⧫) data are also shown.

exponent $\zeta \approx 100$ follows for the carbohydrates instead of $\zeta \approx 2$ for the alcohols. With each series of liquids both the water molecules and the dipolar solute groups contribute to the (low-frequency) principal relaxation term under consideration. Different behavior of the alcoholic OH-groups and the exocyclic hydroxyl and hydroxy methyl groups of the saccharides, however, can hardly account for the large difference in the relaxation times. The rotatable exocyclic groups are exemplified by the molecular structures of the β-pyranose tautomers in the inset of Figure 121. These tautomers are the most frequent conformations of D-glucose and D-fructose in aqueous solution.

It has been speculated that an almost perfect correspondence of the saccharide OH-group topology to the water hydrogen network structure [575] may be the reason for the exceptional features of the dielectric relaxation times. Though our knowledge of the dielectric relaxation of saccharide solutions is still incomplete, these systems may nevertheless be taken to show that reasonable care is necessary when applying apparently universal rules to the properties of aqueous system.

4.3.3 Dipolar solute structures

It is obvious that dipolar solutes or rotatable dipolar solute groups contribute to the complex dielectric spectra of solutions and that such contributions may feature their own relaxation terms, as discussed in section 4.2.1.3 and as illustrated, for example, by the spectra in Figures 94 and 95. Extra relaxation terms, however, may also result from temporary ion structures. Some few examples are given below.

4.3.3.1 Ion complexes

Salts from multivalent ions have been known for a long time to dissociate incompletely in water and to form fluctuating ion complex structures in doing so [579, 580]. A prominent example is magnesium sulfate which has been identified to be essentially responsible for the strong and frequency-dependent absorption of ultrasonic (sonar) signals in sea water [579-583]. Incomplete dissociation means that a salt from m-fold positively charged metal ions M^{m+} and l-fold negatively charged ligand L^{l-} does not completely decompose to form hydrated ions in water. Additional complexes exist in which water molecules in the hydration shell of the cation-aquo complex are substituted by an anion. The chemical equilibrium between the different ionic species is generally represented by the reaction scheme

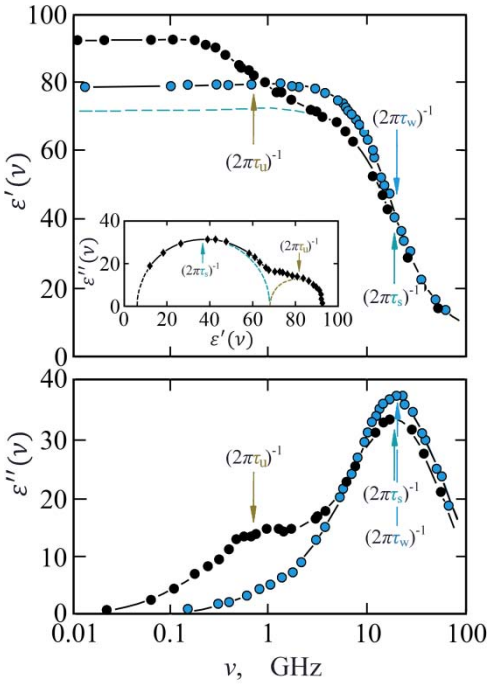

Figure 122. Real part $\varepsilon'(\nu)$ and negative imaginary part $\varepsilon''(\nu)$ of the complex permittivity for water (blue points) and an aqueous solution of $Al_2(SO_4)_3$ (●, 0.1 mol/l) at 25 °C. Arrows mark the relaxation frequencies of pure water ($1/(2\pi\tau_w)$), of the water in the solution ($1/(2\pi\tau_s)$), and of the ion complex contribution ($1/(2\pi\tau_u)$). Dashed turquoise line indicates the water contribution to $\varepsilon'(\nu)$. The inset shows a complex plane representation for the spectrum of a 0.15 mol/l solution of $Al_2(SO_4)_3$. Dashed turquoise and brown lines represent the water and ion complex contributions [192]. The conductivity part (Eq. 31) in ε'' is generally omitted.

(139)

$$(ML)_{aq}^{(m-l)+} \rightleftarrows (M^{m+}(H_2O)L^{l-})_{aq} \rightleftarrows (M^{m+}(H_2O)_2L^{l-})_{aq} \rightleftarrows (M^{m+})_{aq} + (L^{l-})_{aq}$$

in which the contact ion pair $(ML)_{aq}^{(m-l)+}$ is denoted the inner sphere complex, the solvent separated species $(M^{m+}(H_2O)L^{l-})_{aq}$ the outer sphere complex, and $(M^{m+}(H_2O)_2L^{l-})_{aq}$ the outer-outer sphere complex. Evidently these complexes are provided with an electric dipole moment and thus contribute to the dielectric polarization. Examples for spectra of solutions of an incompletely dissociated 3:2 valent salt are displayed in Figure 122. They clearly reveal a water contribution and, at lower frequencies, a contribution from dipolar ion complexes and resemble the spectra for aqueous solutions of polar molecules (Figs. 94, 95).

The discovery of ion complexes to add relaxation terms to the spectra of aqueous solutions of salts from multivalent ions [191, 535] has inspired a variety of dielectric spectroscopy studies [192, 536, 537, 584-587] and has also directed interest towards ion pairing in solutions of 1:2 [588, 589], 2:1 [590], and even 1:1 valent [591] electrolytes. Surprisingly, in spite of the clear evidence of the existence of dipolar ion complex structures (Figs.

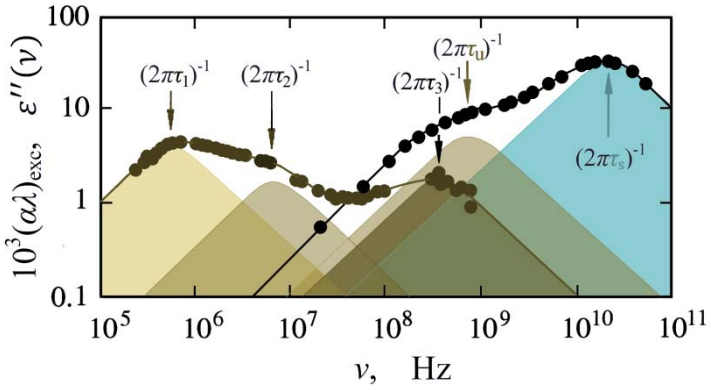

Figure 123. Ultrasonic excess attenuation (brown points, [592]) and dielectric loss (black points) spectra for $Sc_2(SO_4)_3$ in water (0.1 mol/l, 25°C, [192]). The relaxation term for water (τ_s) in the ε'' spectrum is indicated by turquoise color, the term due to ion complexes (τ_u) by brownness. Differently strong brown colors also distinguish the ion complex contributions to the $(\alpha\lambda)_{exc}$ spectrum.

122 and 123), there are no explicit indications for the presence of differently polar species as suggested by the reaction scheme of equation (139). Due to the different molar volume of these species the transitions between the ion complexes of that scheme are nicely reflected by the ultrasonic excess attenuation spectra of aluminium or scandium sulfate solutions [592] which clearly reveal three relaxation terms (Fig. 123). Interestingly, the relaxation frequency $(2\pi\tau_u)^{-1}$ of the ion complex term in the dielectric spectra are larger than the relaxation frequencies $(2\pi\tau_n)^{-1}$, n = 1, 2, 3, in the corresponding ultrasonic excess attenuation spectra. This result supports the idea that dielectric spectroscopy is largey unaffected by the ion pair formation and disintegration processes because it is sensitive to reorientational motions of the ionic structures: the faster reorientational motions of the species short-circuits the dipole moment variations by transitions between the different species in the chemical equilibria shown by Eq. (139).

The situation is even more demanding with zinc(II)chloride aqueous solutions. This electrolyte features an intricate reaction scheme as it forms mono-, bi-, tri-, and even tetrachloro complexes which, in addition, may exist as contact (inner sphere) and as solvent separated (outer sphere) complexes [593-596]. Activated zinc ions seem to also exist [596], i.e. ions with one hydration molecule less than the sixfold coordinated ground state. Since the linear dichloro, the planar trichloro and the tetrahedral tetrachloro complexes are considered nondipolar, however, only the monochloro complex is assumed to contribute to the solute relaxation in the

dielectric spectra of $ZnCl_2$ aqueous solutions (Fig. 124). Evaluation of the relaxation amplitude disclosed a considerable amount of outer sphere complexes $(Zn(H_2O)Cl)^+$ in the solutions [590].

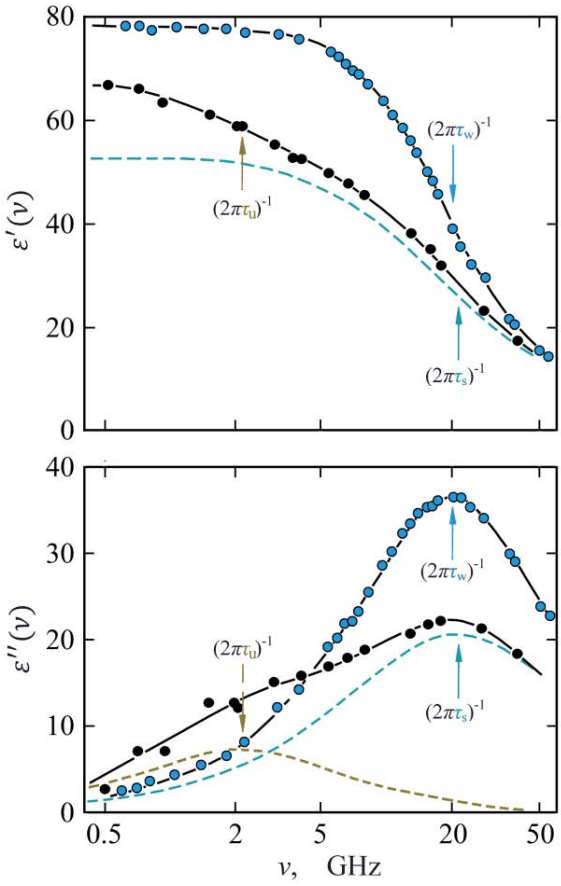

Figure 124. Real part $\varepsilon'(\nu)$ and negative imaginary part $\varepsilon''(\nu)$ of the complex dielectric spectrum for water (blue points) and a 2.04 mol/l solution of $ZnCl_2$ in water (●) at 25 °C [590]. Arrows mark the relaxation frequencies of pure water $(1/(2\pi\tau_w))$, of the water in the solution $(1/(2\pi\tau_s))$, and of the ion complex contribution $(1/(2\pi\tau_u))$. Dashed turquoise lines indicates the water contribution to the complex spectrum of the solution. The dashed brown line shows the contribution of the ionic species to the dielectric loss $\varepsilon''(\nu)$. Again the conductivity contribution has been subtracted from the total loss using Eq. (31).

4.3.3.2 Polyelectrolytes, giant dispersion

Considerable contributions to the complex permittivity spectra of ionic solutions may also result from limited motions of ions in polyelectrolyte systems. Examples are motions of counterions at the surface of roughly globularly shaped ionic micelles or vesicles and motions along linear or folded polyelectrolytes, such as biopolymers [503, 597-602]. Because of

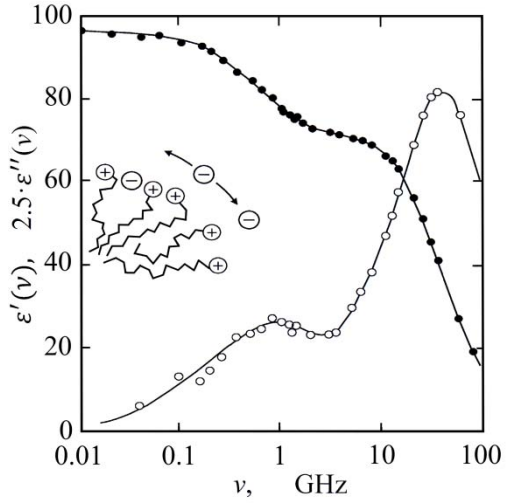

Figure 125. Real part (●) and negative imaginary part (○) of the complex dielectric spectrum of a solution of ionic surfactant *n*-hexadecyltrimethylammonium bromide (0.15 mol/l) in water at 25 °C [603]. The contribution of the ionic conductivity is omitted. In the inset counterion motions on a micelle surface are sketched.

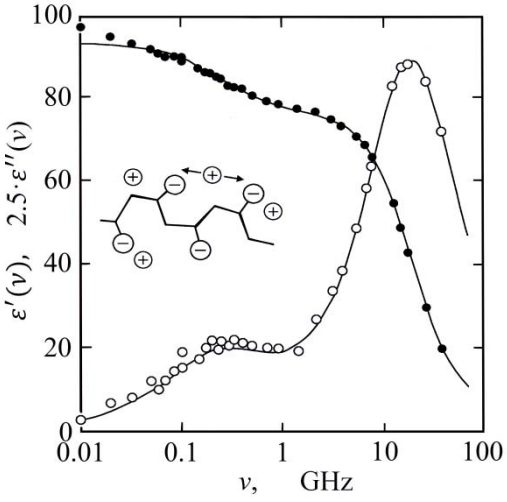

Figure 126. Complex permittivity spectrum of an aqueous solution of sodium polyacrylate ($H[-CH_2-CH(CO_2Na)-]_nH$, with n = 555, c = 0.123 mol/l, and T = 25 °C [604]). The inset delineates the counterion motions relative to the polyelectrolyte chain.

the Coulombic forces most counterions are condensed at the polyelectrolyte surface. Hence they cannot freely drift and contribute to the electrical conductivity of the system like free ions in a low-weight salt solution. Since the dimension of the surface is limited, ions in the diffuse counterion layer moving relative to the polyelectrolyte, cause a fluctuating dipole moment and thus a relaxation term in the dielectric spectra. The relaxation amplitudes and relaxation times depend strongly upon the shape and size of the polyelectrolyte and on various further parameters of the solutions, such as the salt concentration and pH value of the suspending bulk phase [503,

605-607]. Figures 125 and 126 show spectra for solutions of a cationic surfactant and an anionic linear polymer, respectively. With both polyelectrolyte solutions the limited counterion motions extend over comparatively small dimensions so that the low-frequeny solute relaxations are located at frequencies similar to those of ion complex reorientations (Fig. 122). Also the relaxation amplitudes reveal comparable magnitudes. At larger polyelectrolyte dimensions both the relaxation time and relaxation amplitude may be significantly larger. This is true, for instance, with ion motions in suspensions of biological cells.

4.4 'Bound water'

'Bound water' is an enigmatic term in liquid state physics. The nature of bound water is insufficiently understood and it will be a challenging future task to clearly identify and specify bound water in moist materials.

The term springs from the idea that water at the surface of (non-aqueous) substances may feature characteristics distinctly different from normal water. It is especially suggested that such water is strongly bound to the non-aqueous surfaces. In bulk solutions, however, evidence of bond (or activation) energy significantly larger than the hydrogen bond energy of pure water is virtually non-existent [608]. On the other hand, isolated surfaces with thin (monomolecular) water layers are difficult to investigate and it is also unclear how such a layer changes its properties when water is added to the system.

The incomplete definition of bound water's properties leads to discrepancies in the results from different techniques: diverse amounts of special water are typically derived from different parameters. As long as such water is not fully characterized, it may be useful to name it specifically in view of its unusual property, for example 'unfreezable water'. In electromagnetic aquametry water that seems to be invisable in the dielectric spectrum of the system under test is often considered 'bound'. However, this may be a rash conclusion, as will be briefly summarized below.

4.4.1 The mixture problem

In the majority of cases moist materials of interest display a complicated internal structure. It is therefore impossible to represent their dielectric properties by exact analytical models. Even for solutions of simply spherically shaped particles mean field approximations are necessary in order to consider the effects from internal electric fields theoretically. Since there is

some ambiguity in selecting the mean field approach, a variety of mixture relations exists even for such simply structured systems (sect. 4.2.2.2). For those reasons, only partly deterministic, probabilistic, or even completely empirical relations are applied in order to model the resulting permittivities of the composite materials. Frequently the parameters of such relations are adjusted to the specific material under investigation (e.g. [609]). Due to the deficient knowledge of the suitable mixture relation from theory, inadequate evaluation of experimental findings may lead to a discrepancy between the measured and the real water content which, in turn, is accounted for by the assumption of bound water that contributes to the material permittivity in a reduced manner (with respect to normal water).

An example for lack of clarity when deducing the existence of bound water from experimental mixture permittivity ε_m is the modified Looyenga formula [609-611]

$$\varepsilon_\mathrm{m}^\alpha = v_\mathrm{w}\varepsilon_\mathrm{w}^\alpha + v_\mathrm{bw}\varepsilon_\mathrm{bw}^\alpha + (1 - v_\mathrm{w} - v_\mathrm{bw})\varepsilon_\mathrm{u}^\alpha \tag{140}$$

in which the original exponent 1/3 (Eq. 121) is replaced by the adjustable parameter α. Using this relation, potentially ill-founded modifications in α can be widely compensated for by the additional bound water term with unknown volume fraction v_bw and permittivity ε_bw.

The effect of orientation in isotropically structured materials has been demonstrated for layered systems in section 4.2.2.2. Here we mention the considerable variation in the mixture permittivity that may even result from elliptic deformation of originally globular solutes. Consider a solution of ellipsoids of revolution with axis a and b and with permittivity ε_u. As before, the volume fraction of solute may be v_u. If the permittivity of the material neighboring a solute particle is assumed to equal the permittivity ε_w of the solvent the mixture permittivity, at random orientation of the ellipsoids and small v_u (< 0.1), follows as [500-502, 612]

$$\varepsilon_\mathrm{m} = (1 - \frac{1}{3}v_\mathrm{u})\varepsilon_\mathrm{w}\sum_{n=a,b,b}\frac{\varepsilon_\mathrm{w}-\varepsilon_\mathrm{u}}{\varepsilon_\mathrm{w}-D_n(\varepsilon_\mathrm{w}-\varepsilon_\mathrm{u})}. \tag{141}$$

For spherical particles the ellipsoidal depolarization factors in Eq. (141) are $D_\mathrm{a} = D_\mathrm{b} = 1/3$ and the formula agrees with the Maxwell-Wagner relation (Eq. 119) at small v_u:

$$\varepsilon_\mathrm{m} = \varepsilon_\mathrm{w}\left[1 - 3v_\mathrm{u}\frac{\varepsilon_w-\varepsilon_\mathrm{u}}{2\varepsilon_\mathrm{w}+\varepsilon_\mathrm{u}}\right]. \tag{142}$$

Mixtures of thin oblate ellipsoids of revolution ($a \ll b$, $D_a = 1$, $D_b = 0$), however, are represented by

$$\varepsilon_m = \varepsilon_w \left[1 - \frac{1}{3} v_u \frac{\varepsilon_w - \varepsilon_u}{\varepsilon_u}\right]. \quad (143)$$

Consider solutions of nondipolar particles ($\varepsilon_u = 2$) in water ($\varepsilon_w = 80$). At small volume fraction $v_u = 0.05$ Eq. (143) yields ε_m as small as 25.4, whereas Eq. (142) predicts $\varepsilon_m = 74.2$ for solutions of spherical solutes. Hence if a spherical instead of a more or less ellipsoidal particle shape is untruly assumed experimental permittivities may appear smaller than estimated from the water content and may thus suggest existence of some dielectrically invisible water. Corresponding results follow for the inverse material structure, i.e. for solutions of dipolar spheroids in nonpolar solvent. Interchanging indexes "w" and "u" in Eqs. 141-143 leads to $\varepsilon_m = 2.28$ for solutions of globular particles ($D_a = 1/3$) and $\varepsilon_m = 2.03$ for the limiting case of oblate ellipsoids ($D_a = 1$). Figure 127 shows the effect from ellipsoidal deformation of dispersed solutes which is minor at small deviations from the globular shape.

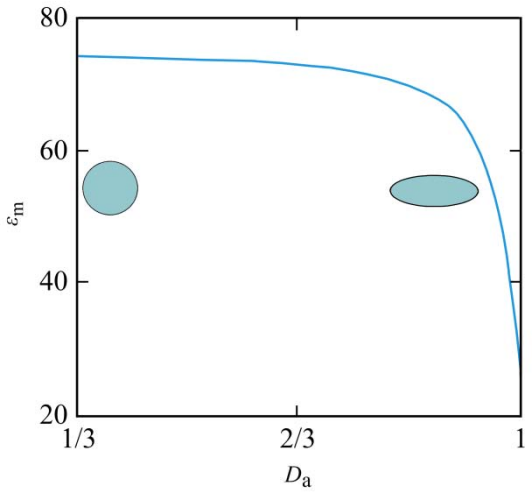

Figure 127. Mixture permittivity ε_m versus depolarization factor D_a for solutions of nonpolar oblate ellipsoids of revolution (permittivity $\varepsilon_u = 2$) in water (permittivity $\varepsilon_w = 80$). The volume fraction of solute is $v_u = 0.05$. $D_a = 1/3$ characterizes globular solute (Eq. 142), $D_a = 1$ the limiting case of thin disc-shaped solute (Eq. 143).

4.4.2 Extra dielectric decrement in electrolyte solutions

Figure 128 shows again the extrapolated static permittivity $\varepsilon(0)$ of aqueous solutions of 1:1 valent salts to point at the substantial decrement of electrolyte solutions. The extra polarization deficiency with respect to

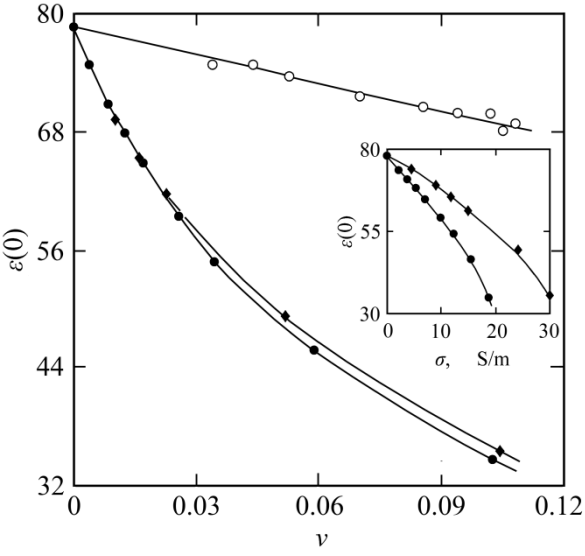

Figure 128. Extrapolated static permittivity $\varepsilon(0)$ of aqueous solutions of LiCl (●) and KF (⧫) [550, 551] at 25 °C, displayed versus volume fraction v of salt. Some data for solutions of uncharged non-dipolar molecules in water (○, [497-499]) are also presented. For the LiCl and KF solutions the inset shows the dependence of their $\varepsilon(0)$ data on the specific electric conductivity σ of the liquids.

solutions of uncharged solutes is partly explained by kinetic depolarization. This involves high mobility of dipolar solvent molecules which, within the hydrodynamic field around moving ions, are rotated in the direction opposed to that dictated by the external electric field (sect. 4.3.1.2, Fig. 106). Incomplete consideration of kinetic depolarization may likely lead to the (wrong) conclusion that dielectrically invisible or 'bound' water exists in the sample even if all water dipole moments are freely rotatable.

The inset of Figure 128 indicates that, in addition to kinetic depolarization, another effect contributes to the dielectric decrement of the salt solutions. Otherwise the extrapolated static permittivities of the two series of liquids, when plotted against the specific electric conductivity σ, should almost condense on one curve. The second effect is the before discussed dielectric saturation (sect. 4.3.1.3), the extensive radial restriction of the direction of solvent electric dipole moments in the strong Coulombic fields of small ions, predominantly cations. For some mono-, di-, and tri-valent cations the extent of dielectric saturation of water around them is again depicted in Figure 129, where numbers Z^+ of apparently totally saturated water molecules per ion are shown. Dielectrically saturated water molecules may indeed be considered bound, even though strictly they are able to perform more or less fast proton-around-proton motions at fixed electric dipole moment orientation. Also their residence time in the saturated water shell is finite. Hence water molecules switch between the saturated

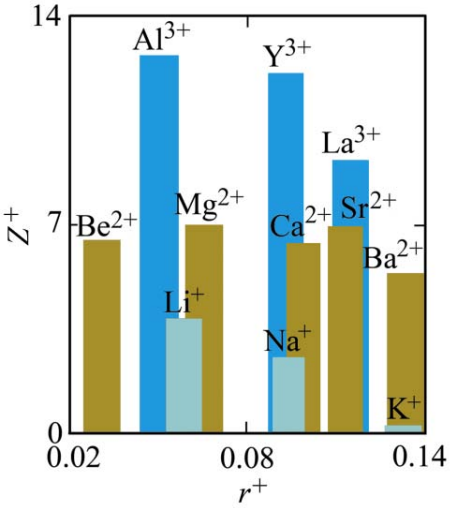

Figure 129. Numbers Z^+ of apparently completely saturated water molecules around some cations as function of the Pauling ion radius r^+ (data from Fig. 111).

region and the bulk phase. The dielectrically saturated water molecules around Li^+, for example rotate with relaxation time $\tau_h \approx 2.4 \cdot \tau_w \approx 20$ ps [560] and their residence time in the dielectrically saturated shell is $\tau_h^* \approx 5 \cdot \tau_w \approx 40$ ps [564], as briefly mentioned in sect. 4.3.2.1. Water in the saturated regions of multivalent ions moves, of course, slower, for instance $\tau_h^* \geq 1$ µs with the inner shell of Al^{3+} [565].

Since water in the strong fields of small ions is not bound in a close sense, it may be more clearly named 'dielectrically saturated' instead of 'bound' water.

4.4.3 Slowed hydration water reorientation

Non-aqueous materials may not just cause a decrement $\delta\varepsilon(0)$ in the static permittivity of materials but also reveal a shift $\delta\nu_r$ in the relaxation frequency $\nu_r = (2\pi\tau)^{-1}$. An extreme example is given in Figure 130, where the complex dielectric spectra for liquid and solid water at 0 °C are shown. The static permittivities of water and ice differ only marginally. Nevertheless, experimental data in the broad frequency range, roughly marked in light blue in the upper part of the figure, yield substantially smaller $\varepsilon'(\nu)$ values for ice than for water. This is true though the static permittivity of the former is even slightly larger than that of the latter.

The spectrum of ice may be taken as the typical dielectric behavior of bound water. The activation enthalpy $\Delta H^\# = 58.6$ kJ/mol has been reported for dielectric, NMR spin lattice, and elastic relaxation in ice at -10 °C [613].

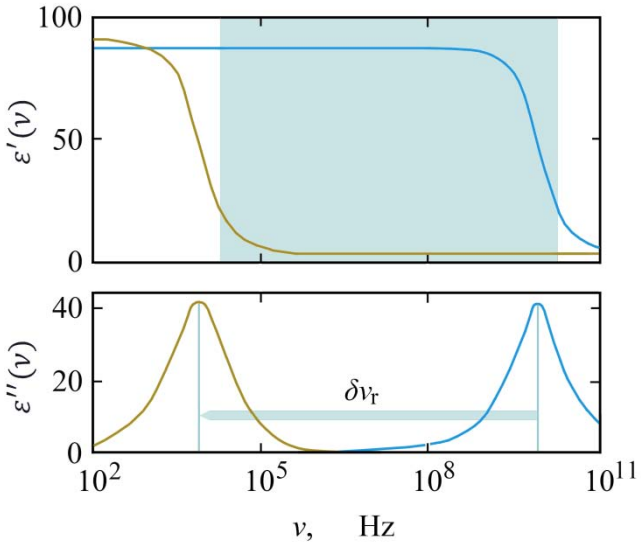

Figure 130. Real part $\varepsilon'(\nu)$ and negative imaginary part $\varepsilon''(\nu)$ of the complex dielectric spectrum for liquid water (blue lines) and ice (brown lines) at 0 °C [608]. The light blue arrow indicates the tremendous shift $\delta\nu_r$ in the relaxation frequency when water freezes.

This value compares to the activation enthalpy $\Delta H^{\#}$ = 17 kJ/mol and the hydrogen bond interaction enthalpy ΔH = 20 kJ/mol for water at ambient temperature (sect. 4.1.2). The larger value for solid water manifests a clear effect of dynamic stability in terms of a substantially increased potential energy barrier (Fig. 81) when compared to the liquid. The high activation enthalpy of ice is worth noting because Pauling has estimated 21 kJ/mol as reasonable value for the hydrogen bond interaction energy of ice [614], close to the value for water given above.

At ambient temperatures, systems containing liquid water, such as aqueous solutions, display incomparabibly smaller shifts in the relaxation frequency. These shifts are moderate even if large amounts of inorganic or organic solutes are added to water. An example is the 1,4-dioxane-water mixture, with roughly identical volume fractions of dioxane and water, for which the complex permittivity spectrum is shown in Figure 131. As outlined before in chapter 4.2.3, the comparably small shifts in the relaxation frequency (or relaxation time) are rather due to reduced local concentrations of hydrogen bonding sites than to enhanced activation enthalpies. Unfortunately, however, only a few relevant mixtures have been investigated so far as a function of temperature [608]. Therefore a clear-cut conclusion on variations in the activation enthalpy (and even more the hydrogen bond energy) of aqueous solutions is impossible at present. This situation suggests the use of term ‘hydration water’ instead of ‘bound water’ in order to characterize water that is affected in its reorientational motions by solute materials.

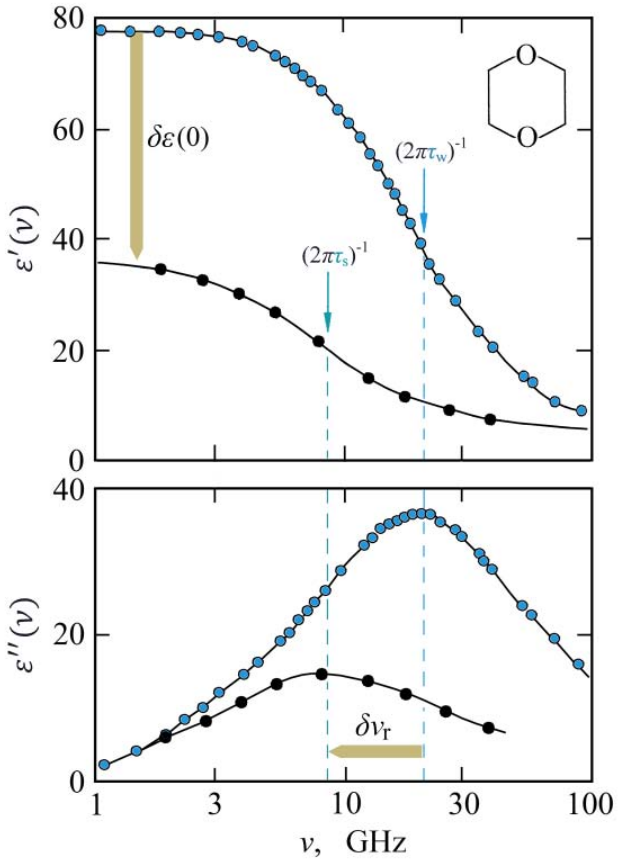

Figure 131. Real part $\varepsilon'(\nu)$ and negative imaginary part $\varepsilon''(\nu)$ of the complex dielectric spectrum for water (blue points) and a solution of nonpolar 1,4-dioxane in water (●, c = 6 mol/l [603]) at 25 °C. Light brown arrows show the tremendous shift $\delta\varepsilon(0)$ in the static permittivity due to the dilution of water by the solvent as well as the moderate shift $\delta\nu_r = (2\pi\tau_s)^{-1} - (2\pi\tau_w)^{-1}$ in the relaxation frequency. The inset sketches the structure of the nonpolar solute.

Care must be taken in the assignment of reduced permittivities to dielectrically invisible water, if measurements are performed in a limited frequency range. Failing to notice relaxation frequency shifts, as characteristic to hydration water, may pretend permittivity reduction and thus lead to erroneous conclusions on the existence of bound (or dielectrically saturated) water.

4.4.4 Supercooled water

So far the focus was water and aqueous systems above the freezing point. However, several applications, including food processing, pharmaceutics, and cryopreservation, may include temperatures significantly below 0 °C. Much efforts have been made during the past years in order to elucidate the puzzling behavior of liquids at cold non-crystalline states [615].

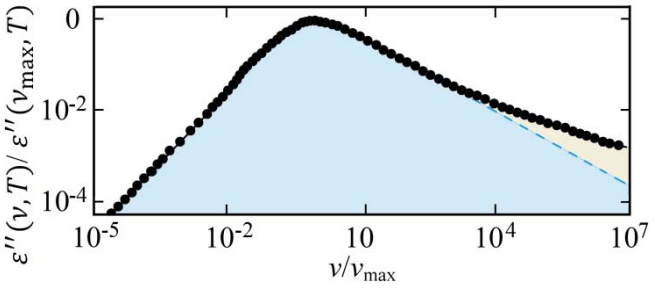

Figure 132. Normalized plot of the imaginary part of the spectrum of a mixture of glycerol and water with mole fraction 0.75 of the alcohol [622]. Data at temperatures T between 197 and 230 K are shown in this master plot. Paramter $\nu_{max} = \nu_{max}(T)$ is the frequency of the relative maximum in the $\varepsilon''(\nu, T)$ spectra at the respective temperature of measurement. The light blue area reveals the dominating primary relaxation term, the light brownish area indicates the high-frequency excess dielectric loss.

Supercooled water has been specifically investigated in mixture with glass-forming solutes which often allow for studies over broad temperature ranges. Prominent examples are aqueous solutions of carbohydrates [616, 617], ethylene glycol and propylene glycol oligomers and monomethyl ethers [618-620], glycerol [621, 622], as well as proteins [623-625]. If the conductivity contribution (Eq. 31, Fig. 21) is omitted, dielectric spectra of supercooled aqueous systems typically reveal two relaxation terms (Fig. 132). The primary relaxation term, named α-relaxation, is subject to a considerable relaxation time distribution. The second relaxation term appears at frequencies above the relaxation frequency of the primary term. This secondary contribution to the spectra may appear either as a distinct relaxation in terms of a high-frequency shoulder, or as a so-called excess wing on the α-relaxation term [626, 627]. It is normally represented by a Cole-Cole function (Eq. 111) or simply a Debye function (Eq. 78).

Over relevant ranges of temperature the relaxation time of the α- term follows Vogel-Fulcher-Tammann-Hesse law (Eq. 108), whereas that of the high-frequency excess dielectric loss largely conforms Eyring behavior (Eq. 106). These findings and the fact that, contrary to that of the α-term, the relaxation strength of the high-frequency contribution increases with water content have suggested the high-frequency contribution to reflect the local relaxation of spatially restricted reorientational motions of water. Since the relaxation time of these motions is largely independent of the structure and concentration of the other constituent [618], such motions are considered uncoupled. Due to an appreciable similarity to the relaxation behavior of ordinary glass formers the α-relaxation term is mostly assigned to cooperative motions in which both the organic constituent and

water participate. This view implies water molecules (at high solute content) to be physically coupled to solute molecules and suggests the respective water to be bound.

The above reasoning involves the idea of a microheterogenous structure of the supercooled liquid. It is only briefly mentioned that dynamic microheterogeneity is also found with ordinary solutions at ambient temperatures. Examples are aqueous solutions of solutes with extended alkyl chains mentioned in sect. 4.3.2.2 and also carboxylic acid-water mixtures. The analysis of complex dielectric spectra of the latter has suggested two microscopic phases, with water concentrations smaller and larger than the mean, respectively [628].

4.4.5 Interference with solute contributions

As briefly summarized in chapter 4.3.3 polarization due to dipolar solutes, including dipolar ion structures, may feature contributions to the dielectric spectra with relaxation times well separated from the water relaxation time. Such contributions carry the inherent danger of being mistakenly considered to result from specially bound water. This is particularly true if measurements are conducted over a too limited frequency range to enable a clear analysis of the experimental data in terms of different contributions.

If the solute dipole moments are large and the (local) concentration of solute is high the low-frequency solute relaxation term may largely mask the minor solvent term. An illustration is the spectrum of a zwitterionic amino acid solution in Figure 133. On such condition it is virtually impossible to draw conclusions about special water from the dielectric spectra.

In several instances solute and water relaxation times are too close together to enable a meaningful separation into different contributions. A prominent example is aqueous solutions of saccharides (Fig. 121). The hydrogen bond group topology of the cyclic molecules seems to fit almost perfectly to the water structure so that the solute and solvent reorientational motions are coupled [629-631]. At higher saccharide concentration the description of the dielectric spectra of glucose and fructose aqueous solutions may indeed be represented by two relaxation terms [629]. However, neither term can be consistently assigned to sole carbohydrate or water contributions. Rather, by analogy with the carboxylic acid-water mixture mentioned before, those terms seem to likewise reflect relaxations from two composite liquid phases, i. e. carbohydrate–water mixtures of different composition. This view involves again a (dynamically) microheterogeneous structure of the liquids associated with fluctuations in the

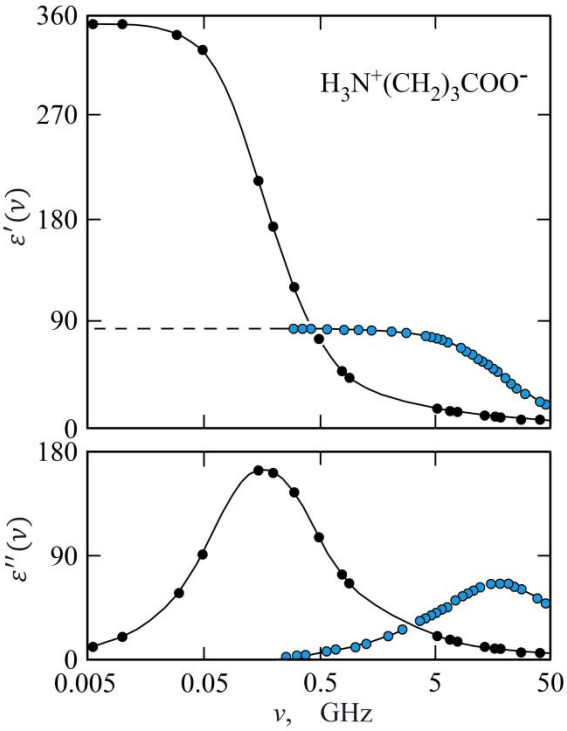

Figure 133. Real part $\varepsilon'(\nu)$ and negative imaginary part $\varepsilon''(\nu)$ of the complex dielectric spectrum for pure water (blue points) and a 6 mol/l aqueous solution of zwitterionic 4-aminobutyric acid (●, [632]) at 25 °C. The inset shows the structure of the zwitterion.

local concentration as already briefly discussed in sections 4.3.2.2 and 4.4.4.

4.4.6 Maxwell-Wagner relaxation

Ion accumulations at internal interfaces of materials may also lead to extra contributions to the dielectric spectra. Such ion accumulation results if at least one constituent possesses an electrical conductivity and if either the conductivities or permittivities of the materials are different. Since the electrical conductivity is finite, the formation and disintegration of internal charge distributions need a certain time so that a relaxation process ("Maxwell-Wagner relaxation" [509]) results. As a simple example, let us consider a spherical particle that is covered by a thin layer of different material, as depicted in Fig. 134. The particle may be taken as a rough model of shelled fruits, such as corn or peanuts. For clearness let us assume the core with radius r_c to be filled with aqueous solution of specific electric conductivity σ. If we focus on frequencies well below the water

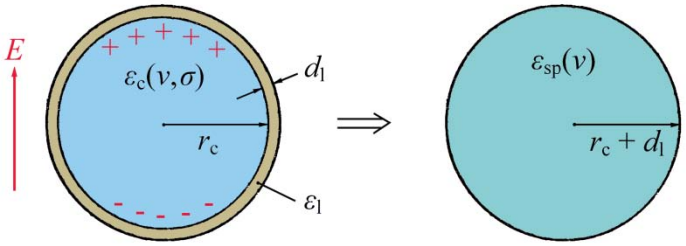

Figure 134. Sketch of a spherical particle made of a core with radius r_c and a concentric layer of thickness d_l (left side). Core and layer are made of material with permittivity ε_c and ε_l, respectively. Plus and minus signs indicate the accumulation of charges if an electrical field E is applied and if the specific electric conductivity of the layer is smaller than that of the core. The right-hand side shows the dielectric substitute with homogeneous permittivity ε_{sp} of the composite sphere.

relaxation and if we restrict ourselves to small electrolyte concentrations the complex permittivity of the core is given by the relation

$$\varepsilon_c = \varepsilon_w(0) - i\sigma/(\varepsilon_0\omega). \tag{144}$$

The layer of thickness d_l may be made of nonpolar material with permittivity $\varepsilon_l = 2$. According to the Maxwell-Wagner theory the composite dielectric may be substituted by a dielectrically homogeneous sphere with radius $r_c + d_l$ and with permittivity [500]

$$\varepsilon_{sp}(\nu) = \varepsilon_l \frac{2[(r_c+d_l)^3 - r_c^3]\varepsilon_l + [(r_c+d_l)^3 + 2r_c^3]\varepsilon_c}{[2(r_c+d_l)^3 - r_c^3]\varepsilon_l + [(r_c+d_l)^3 - r_c^3]\varepsilon_c}. \tag{145}$$

If $d_l \ll r_c$, $(r_c + d_l)^3 \approx r_c^3 + 3r_c^2 d_l$ results and Eq. (145) reduces to

$$\varepsilon_{sp}(\nu) = \varepsilon_l \frac{\varepsilon_c r_c + (\varepsilon_c + 2\varepsilon_l)d_l}{\varepsilon_l r_c + (\varepsilon_c + 2\varepsilon_l)d_l}. \tag{146}$$

Using Eq. (144) to include the frequency dependence of ε_c, this equation may be rewritten to read

$$\varepsilon_{sp}(\nu) = \varepsilon_{sp}(\infty) + \frac{\varepsilon_{sp}(0) - \varepsilon_{sp}(\infty)}{1 + i\omega\tau_{sp}}, \tag{147}$$

where

$$\varepsilon_{\mathrm{sp}}(\infty) = \varepsilon_{\mathrm{w}}(0)\frac{\varepsilon_{\mathrm{sp}}(0)}{2\pi\sigma\tau_{\mathrm{sp}}}\ , \tag{148}$$

$$\varepsilon_{\mathrm{sp}}(0) = \varepsilon_{\mathrm{l}}(r_{\mathrm{c}}/d_{\mathrm{l}} + 1), \tag{149}$$

and

$$\tau_{\mathrm{sp}} = 2\varepsilon_0[\varepsilon_{\mathrm{l}}(r_{\mathrm{c}}/d_{\mathrm{l}}) + \varepsilon_{\mathrm{w}}(0)]/\sigma\ . \tag{150}$$

With $\varepsilon_{\mathrm{w}}(0) = 80$, $\varepsilon_{\mathrm{l}} = 2$, $d_{\mathrm{l}}/r_{\mathrm{c}} = 0.01$, and $\sigma = 10^{-3}$ S/m follows $\varepsilon_{\mathrm{sp}}(\infty) = 4.6$, $\varepsilon_{\mathrm{sp}}(0) = 202$, and $\tau_{\mathrm{sp}} = 5$ ns, corresponding with a relaxation frequency $\nu_{\mathrm{sp}} = (2\pi\tau_{\mathrm{sp}})^{-1} = 30$ MHz. This elementary, easily-to-handle analytical example may be taken to indicate that Maxwell-Wagner contributions can considerably affect the permittivity spectra of dielectrically heterogeneous materials. Many materials of interest reveal a much more complicated structure so that Maxwell-Wagner effects are difficult to distinguish from the input of other polarization mechanisms, such as the relaxation of potentially existing special water.

5 Selected Moisture Measurement Applications

5.1 Note on measurement signals

Methods in use for electromagnetic moisture content determination and control rely commonly on pulse transit time and pulse profile evaluation, applying time domain techniques. Likewise popular are frequency domain methods including both, spot frequency microwave approaches as well as broadband techniques based on network analyzer facilities. Because of the diverse effects in the dielectric spectra of aqueous systems, wide-band signals for moisture sensing are preferred because they provide substantially more information than monofrequent or narrow-band approaches. Wide-band signal processing is, of course, more costly and increases measurement time. That may be one reason why little attention has been devoted to techniques in which the samples are excited other than by the classical (swept) harmonically varying signals (sect. 2.2.3) or short pulses with their unfavorable spectrum (2.2.2).

Some variants of moisture determination have been described in which the samples were excited by pseudo-random maximum-length binary sequences [633]. The measurement signal was generated with the aid of a digital shift register which was controlled by a stable clock with frequency ν_c. Figure 135 presents the low-frequency part of the power spectrum of a suitable measurement signal. Maximum-length binary sequences feature a line spectrum, with the line spacing depending upon ν_c as well as the length of the shift register. The envelope corresponds to a squared sinc-function. A quite flat signal spectrum exists in the frequency band up to $\nu_c/2$. This band thus defines the optimum range of operation in

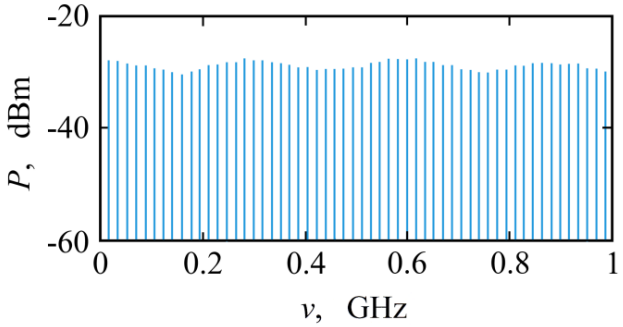

Figure 135. Part of the power spectrum of a maximum-length sequence provided by a 9th order shift register, triggered by a 9 GHz clock (adapted from Fig. 2 of [633]).

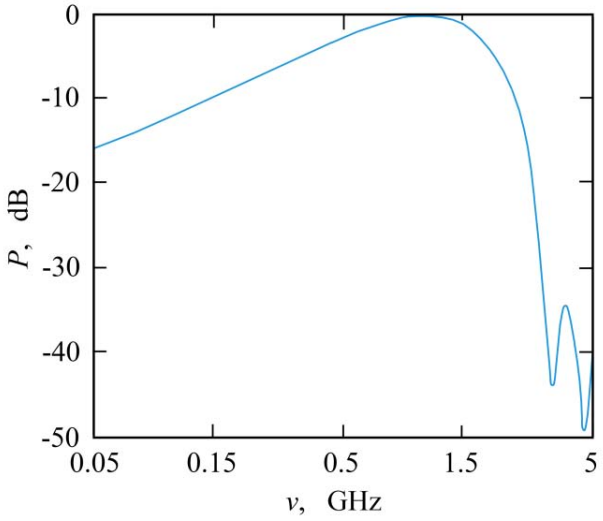

Figure 136. Power spectrum of ultra-wide-band quasi-Gaussian monocycle pulse (adapted from Fig. 1 of reference [634]).

measurements. Current technology easily permits a bandwidth of 7.5 GHz.

As an attractive alternative in various applications, the use of sub-nanosecond ultra-wideband pulses has been proposed [634]. The power spectrum of a wideband quasi-Gaussian monocycle pulse with a cycle width of about 0.4 ns is shown in Figure 136 as an example. Such a pulse provides a rather flat spectrum containing components between about 20 MHz and 3 GHz with spectral power larger than –20 dB compared to the maximum power.

Apart from the use of such innovative measurement signals, electromagnetic moisture determination is mostly based on the principles described in chapter 3. Even when using the classic harmonic signals or short pulses, a multitude of challenging demands result from the adaptation of sensor and instrumentation principles to the specific applications in moisture determination and control. Often the design and development of measurement systems requires a compromise in order to reasonably consider widely differing and conflicting aspects, such as noninvasiveness, high precision, resilience, reliability, remote control and operation, simple networking, marginal needs for service and maintenance, ease of use, and low costs.

Some prominent versions of moisture determination systems as well as a few more recent examples will be discussed in the following to prove how successful topical instruments comply with the different requirements in their performance.

5.2 Soil moisture

Spatial distributions and temporal variations of soil moisture play an important role in many physical and biological processes on our planet. Soil moisture properties are relevant on vast ranges of scales, including characteristic length scales from a few centimeters up to several kilometers and even global dimensions. Characteristic time scales of soil moisture dynamics vary from a few seconds up to years [635, 636]. The knowledge of soil moisture profiles is evidently important for optimizing procedures in agriculture and forestry but also for a better understanding of climate [637, 638] and biogeophysical processes [639]. Within this wide field of applications, electromagnetic methods now dominate soil moisture determination [635, 640-644]. Figure 137 shows a space-time diagram that relates electrical and electromagnetical measurement capabilities to scales at which hydrological processes can be investigated. Remote sensing applying electromagnetic soil moisture sensors with rather small support are already widely used for measurements on a field scale. Much interest is presently also directed towards large-scale soil moisture assessment by evaluating

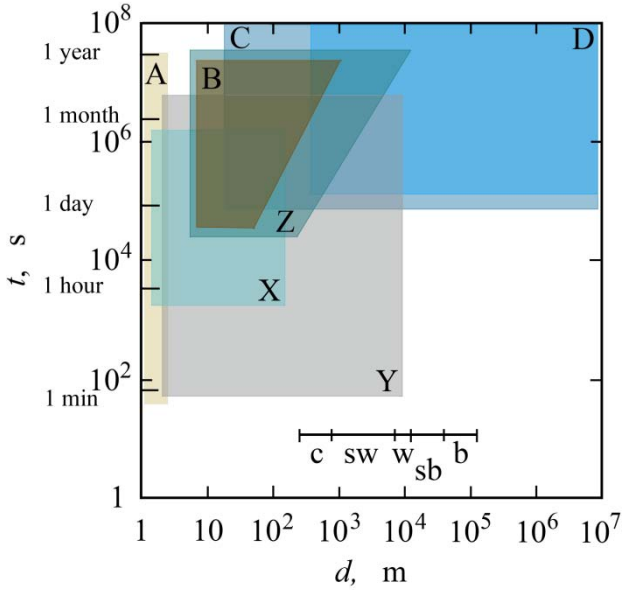

Figure 137. Scheme showing the estimated spatial extent d of measurements and their spacing t in time. Current techniques are restricted to scales represented by areas A (TDR sensor array), B (mobile TDR), C (airborne remote sensing), and D (satellite remote sensing). Emerging methods include electrical resistivity imaging (X), sensor network operation (Y), and electromagnetic induction technologies (Z). c, catchment (0.1-1 km^2); sw, subwatersheed (1-80 km^2); w, watershed (80-250 km^2); sb, subbasin (250-2500 km^2); b, basin (2500-25000 km^2). Adapted from Fig. 3 of reference [635].

propagation characteristics of low-frequency electromagnetic surface waves or by using ground-based microwave radiometry as well as backscattered radar signals acquired on airborne or space-borne sensing platforms. There is nevertheless a gap in the current capabilities of soil moisture determination, especially for monitoring comparatively fast variations of extended ecosystems (Fig. 137). Future work will thus focus on sensor and geophysical networks which may help to close the gap in the measurement techniques and may thus enable study of processes on space – time scales that are currently inaccessible [636]. Without intending to be exhaustive, some measurement systems in use will be described below.

5.2.1 Invasive sensors

Climate change and decreasing water availability in many parts of the earth call for intensified efforts in order to improve water efficiency in agricultural irrigation and to maximize yields thereby. Effective irrigation control requires to be equipped with a two-dimensional structure of moisture sensors, preferably each one providing a depth profile of the water content. Efficient operation needs the sensors to be remotely run in a multiplex mode.

The large amount of sensors required to cover the farming area at reasonable sensor spacing necessitates low sensor costs. Electromagnetic methods have proven to adequately comply with all requirements. Most of them utilize sensors which probe either capacitance or signal velocity changes on moisture content variations. Hence basically the aim is the soil permittivity (Eq. 31)

$$\varepsilon_{\mathrm{tot}}(\nu) = \varepsilon(\nu) - \mathrm{i}\sigma/(\varepsilon_0\omega) \tag{151}$$

which then is evaluated in terms of the volumetric moisture content θ_{w} (Eq. 4) using appropriate empirical relations. Such relations are essentially soil-type specific. A prominent example is the so-called Topp-equation [645]

$$\theta_{\mathrm{w}} = -0.053 + 2.92\cdot10^{-2}\,\varepsilon_{\mathrm{a}} - 5.5\cdot10^{-4}\varepsilon_{\mathrm{a}}^2 + 4.4\cdot10^{-6}\varepsilon_{\mathrm{a}}^3 \tag{152}$$

in which ε_{a} denotes the apparent permittivity

$$\varepsilon_{\mathrm{a}} = \left(\frac{2l}{c_0\Delta t}\right)^2 \tag{153}$$

as following from transient time measurements using time domain methods (sect. 3.2.1). In Eq. (153) Δt is the period which a pulse needs to be transmitted back and forth through a non-dispersive material of length l. This period

$$\Delta t = \frac{2l}{c_0}\sqrt{\varepsilon_\mathrm{a}}\,, \tag{154}$$

because of

$$\varepsilon_\mathrm{a} = \frac{\varepsilon'(\nu)}{2}\left\{1 + \left[\left(\frac{\varepsilon''(\nu)+\sigma/(\varepsilon_0\omega)}{\varepsilon'(\nu)}\right)^2 + 1\right]^{1/2}\right\}, \tag{155}$$

is given by both the real and imaginary part of the material permittivity $\varepsilon_\mathrm{tot}(\nu)$ as characterized by Eq. (151). For many soils it can also be assumed that $\varepsilon'(\nu)$ does not vary with frequency and that dielectric losses are negligible ($\varepsilon''(\nu) \approx 0$). However, the delay time Δt, the apparent permittivity ε_a, and, consequently, the estimated moisture content θ_w depend also upon the soil specific conductivity σ. Hence Topp's equation (Eq. 152) preferably applies to soils with minor conductivity ($\sigma/(\varepsilon_0\omega) \ll \varepsilon'(\nu)$).

This example suggests the need for soil-specific calibrations in order to appropriately relate the measured permittivity value to the actual moisture content. In practice this need is often no serious restriction because applications mostly refer to particular farming areas or soils with well-known composition and texture.

5.2.1.1 Rod antennae, pulse delay time and capacitance measurements

Due to their basically simple design and their comparatively easy insertion into the soil by applying force, such as hammering, when indicated, rod antennae have been used for a long time for soil moisture determination [645]. Various geometrical configurations of rod antennae have been proposed, ranging from a pair of parallel rods up to seven-rod structures [645-652]. Rod antennae are preferably operated in a reflection mode (sect. 3.1.1.2) using either pulse transient time measurements (sect. 3.2.1) or frequency domain electrical capacity measurements.

Figure 138 delineates a two-rod and a three-rod antenna both used as sensing part of a time-domain reflectometer. In field monitoring applications small hand-held TDR meters, designed to comply with the requirements of *in-situ* operation, are usually employed [653, 654]. Such

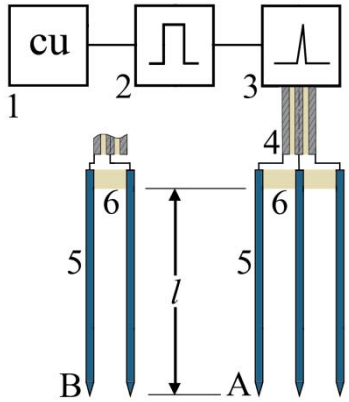

Figure 138. Schematic of three-rod (A) and two-rod (B) antenna, respectively, operated by a transient time measurement system. 1, control unit combined with process control computer; 2, signal generator; 3, sampling unit; 4 coaxial feeding line; 5, rod antenna; 6, insulating (plastic) holder.

instruments, based on low-cost high-speed integrated circuit technology, can be integrated on printed circuit boards including field programmable gate arrays [653]. They can be powered by a battery for a time of several months and do not need an external control setup.

Depth profiles of the soil water distribution, especially in the rizosphere,

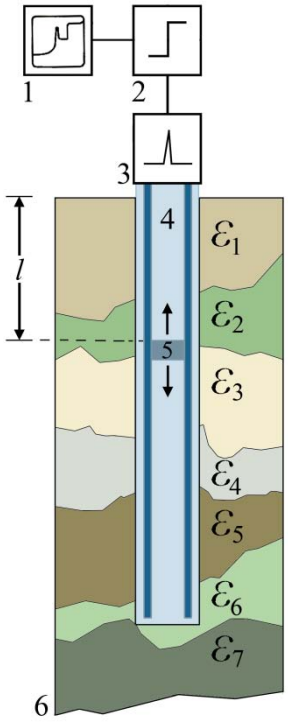

Figure 139. Two-wire antenna (dark blue) provided with movable short circuit (5) for variation of the actual line length *l* when probing soil (6) with vertical variation of its dielectric permittivity (ε_i, i = 1, ...,7). 1, sampling scope combined with process control computer; 2, step-voltage generator; 3, sampling head; 4, antenna housed in a polytetrafluorethylene pad (light blue); 5, movable short; 6, layered soil (adapted from Fig. 1 of ref. [651]).

can be determined by exchanging the rods of an antenna for such of different length *l* or by using a set of differently long antennae [645]. Such a procedure requires, however, multiple placement of the rods and thus increased distortion of the soil, potentially accompanied by preferential water flow. An alternative is the sensor sketched in Figure 139. It consists of a two-rod antenna embedded in a polytetrafluorethylene pad and provided with a movable short circuit [651]. The position of the short can be accurately changed by a stepper motor utilizing a thread rod. This way the apparent permittivity profile of the surrounding soil can be recorded with a resolution better than 1 cm in the vertical position *l*. Depth profiles may be alternatively determined by using PIN-diodes to switch active sections of a one-rod sensor [655].

An example of alternative frequency domain techniques is shown in Figure 140. Measuring the complex reflection coefficient and thus the electrical impedance (3.1.1.1) of the loaded piece of antenna transmission line yields the soil complex permittivity [650, 656]. Therefore such techniques enable not just the moisture content but also the soil conductivity to be determined at frequencies preferably below the dispersion/dielectric loss region of water and above the predominating conductivity range in the total dielectric spectra (100 MHz $\lesssim \nu \lesssim$ 1 GHz). In correspondence with transient time determinations specially designed low-cost electronics are used in most applications instead of multi-purpose laboratory network analyzers. Commercial sensors (e.g. ThetaProbe [657, 658]) are provided with a matched signal generator in their waterproof probe body.

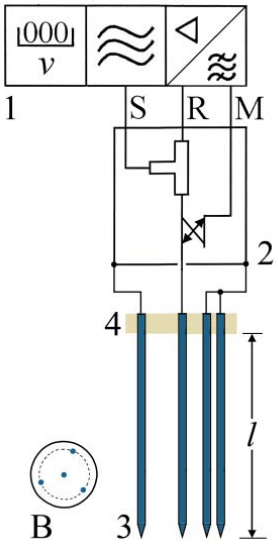

Figure 140. Principle of reflection coefficient measurement of soil using a four-rod antenna with the signal rod in the center and concentrically arranged shield rods (B). 1, vector network analyzer with S, signal output port; R, reference port; M, measurement input channel; 2, reflection test set; 3, four-rod antenna; 4, insulating setting holding the rods.

Whereas two-rod probes cause a minimum disturbance when inserted in the soil, they produce an unbalanced signal resulting in unwanted noise and unfavorable signal-to-noise ratio [648]. Information loss can be reduced by a balancing transformer inserted in the probe head [659] or by the use of three- or more-rod antennae. The latter, however, may provoke larger soil disturbance [660], including the development of air gaps or water pockets.

5.2.1.2 Flat ribbon cables, TDR-inversion for spatial moisture distribution

Flat ribbon cables carved in the soil may be considered a modification of rod antennae. An essential difference is the usable length *l*. Depending on the soil's electric conductivity, *l* of the former may be as large as 40 m [661] whereas with the latter it usually does not exceed a few decimeters. Another difference is the covering of the antenna copper strips by poly(ethylene) insulation, rendering the sensor suitable for the application to highly conducting (saline) soils at reasonable cable length. Flat ribbon cable sensors have been successfully used in a variety of applications, such as the monitoring of soil liquefaction [661], soil water flow processes [662], snow wetness [663], dyke tightness [664], salt-mine barrier behavior [665] and, with some modified implementation, large building durability [21, 666].

A short piece of a flat ribbon cable is depicted in Figure 141. The electrical field is concentrated around the copper conductors. With cables in use (spacing of copper wires about 3 cm, characteristic sensor impedance approximately 200 Ω) it provides a sensing area of 3 to 5 cm around the cable. The dielectric properties of the material surrounding the cable sensor affect signal propagation and cause partial reflection. In order to reconstruct the spatial moisture distribution from the reflected signals a fast

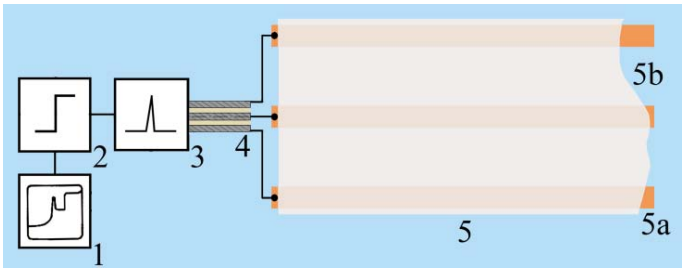

Figure 141. Flat ribbon cable used as TDR sensor. 1, sampling scope; 2, step-voltage generator; 3, sampling head; 4, coaxial line; 5, ribbon cable with 5a, three copper wires embedded in 5b, polyethylene insulation [661].

TDR-inversion technique is applied [661, 664, 667-669]. The procedure requires the information about the complex permittivity of the soil as typically obtained from fast response time domain spectroscopy (sect. 3.2.3). Hence the measurement system needs to involve a time domain spectrometer providing sharp pulses and enabling adequate sampling.

Neglecting higher-order modes and radiation of electrical energy from the cable sensor, the relation between the TDR signal and the (complex) permittivity distribution of the soil has been derived from the telegraph equations

$$\frac{\partial}{\partial x}U(x,t) = -R(x)I(x,t) - L(x)\frac{\partial}{\partial t}I(x,t) \tag{156}$$

$$\frac{\partial}{\partial x}I(x,t) = -G(x)U(x,t) - C(x)\frac{\partial}{\partial t}U(x,t) \tag{157}$$

refering to the equivalent circuit depicted in Figure 142 for a line of infinitesimal length [667]. Series resistance R and inductance L of this circuit are usually considered independent of the material surrounding the cable whereas shunt conductance G as well as capacitance C depend on the total permittivity $\varepsilon_{\mathrm{tot}}(\nu)$ as defined by Eq. (151). Both C and G have been obtained from numerical field calculations [668]. For cables embedded in lossless dielectrics ($\varepsilon'' = 0,\ \sigma = 0$) the resulting dependenc of capacity C upon ε (= ε') suggests the capacitance equivalent network as shown in part A of Figure 143. Hence the total capacitance is given by

$$C(\varepsilon) = C_1 + \varepsilon(\nu)C_2C_3/(C_2 + \varepsilon C_3). \tag{158}$$

Extending this relation by using $\varepsilon_{\mathrm{tot}}(\nu)$ instead of $\varepsilon(\nu)$ leads to the adequate representation of both C and G (part B, Fig. 143)

$$C(\varepsilon_{\mathrm{tot}}) + \mathrm{i}\frac{G(\varepsilon_{tot}(\nu))}{\omega} = C_1 + \frac{\varepsilon_{tot}C_2C_3}{C_2+\varepsilon_{tot}C_3}. \tag{159}$$

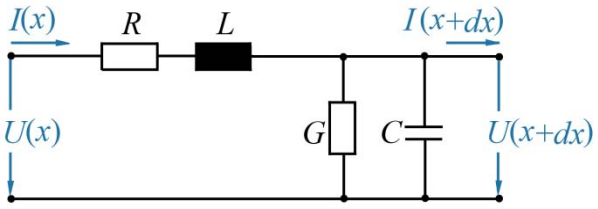

Figure 142. Equivalent circuit of a piece of transverse electromagnetic transmission line with infinitesimal length dx [667].

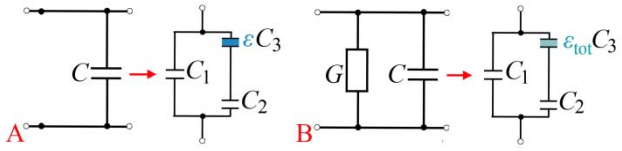

Figure 143. Capacitance (A) and capacitance-conductance (B) model of loaded flat band cable [667].

Parameters C_m, m =1,...,3, can be derived from numerical field evaluation but also from calibration measurements in which the cable sensor is embedded in materials of well-known permittivities [668].

The spatial resolution of flat-ribbon-cable applications can be significantly improved by providing the sensor with fast high-frequency switches at both of its ends (Fig. 144). Such a setting enables the time domain reflection signal to be recorded from both sides of the sensor, thus increasing the sensitivity of measurements. This is especially true when this signal is strongly attenuated due to a large moisture conductivity. Involvement of switches also enables reflection coefficient measurements at different sensor terminations such as the matched or the open-ended line and, furthermore, it offers the possibility to calibrate the measuring system on complete reflection conditions at the transition between the coaxial feeding line and the sensor. The information gained by the different modes of measurement is used in the algorithms reconstructing the moisture profiles from TDR signals. As believed intuitively, the additional information results in an enhanced spatial resolution in the moisture distribution of the material surrounding the cable sensor.

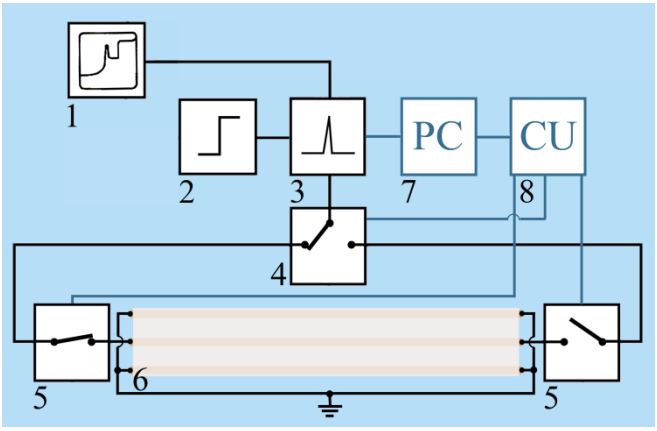

Figure 144. Set-up for flat ribbon cable operation utilizing switches at both sensor ends [670]. 1, sampling scope; 2, step-voltage generator; 3, sampling head; 4, multiplexer; 5, RF switch; 6, cable sensor; 7, process control computer; 8, control unit for multiplexer and driver for switches. TDR signal lines are shown in black, control lines in dark blue.

5.2.1.3 Resonance-type and ring oscillator-based sensors

Some soil moisture measurement methods take advantage of the high sensitivity of resonant circuits to its impedance. Figure 145 sketches a set-up in which part of the resonance frequency-setting circuit is formed by ring electrodes. Placed in a suitable thin-walled low-permittivity tube the electrodes can be placed into the soil where the fringing electrical field interacts with the surrounding soil. Thereby the impedance of the electrodes, and thus the resonant frequency of the circuit, depends on the soil moisture content. A design has been reported in which the resonance frequency ν_r = 230 MHz with a sensor surrounded by air changes to ν_r = 170 MHz when the ring electrode is inserted in saturated soil [671].

The electrical field interaction with the soil leads not just to a shift in the resonance frequency but, due to dielectric losses or electrical conductivity, also to a broadening of the resonance curve, correlated with a reduction of its amplitude (section 3.1.1.7). Hence if, in addition to the resonance frequency, also the half-power bandwidth of the resonance curve is determined both the moisture content and the salinity is obtained. Moisture (and salinity) profiles can be determined either by shifting a pair of ring electrodes vertically within the tube and by recording the resonance curve of the system at each antenna position [671]. Alternatively, the holding

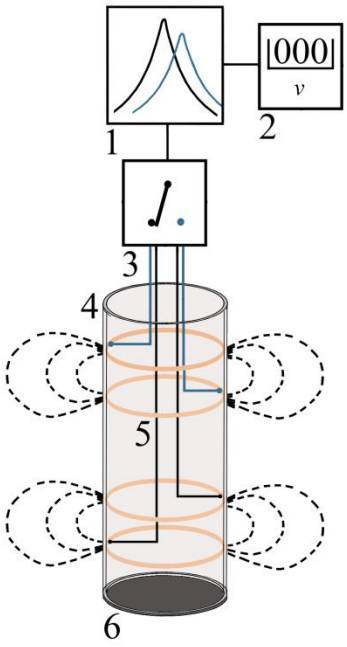

Figure 145. Principle of resonance circuit for soil moisture measurement in the frequency domain [671, 672]. 1, resonant circuit; 2, frequency counter; 3, multiplexer; 4, tube made, for instance, of glass fiber [670]; 5, ring electrodes made of copper; 6, sealing bottom of the tube (4). Dashed lines indicate electrical field lines.

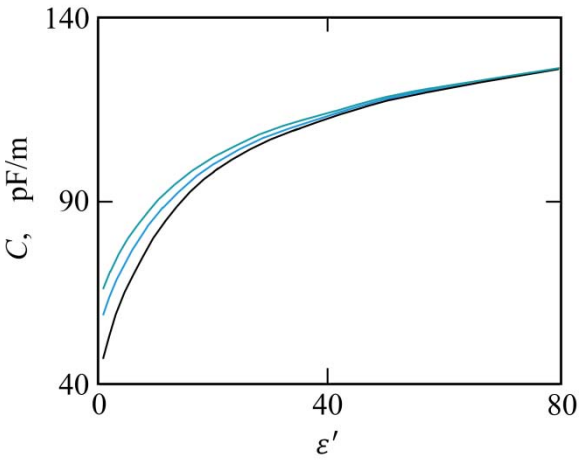

Figure 146. Capacitance of ring electrode antenna as function of soil permittivity ε' and at three different gaps separating the sensor and the soil [672]. Black line: no gap. Blue and turquoise lines: water-filled gaps 0.5 and 1.0 mm thick, respectively.

tube may be provided with several pairs of ring electrode which are sequentially operated via a multiplexer (Fig. 145).

The careful installation of the sensor into the soil is of eminent importance for reliable measurements. Gaps between the sensor tube and the soil may offer a path of preferential water flow and thus change the properties of undisturbed soil significantly. Furthermore, the capacitance of the loaded ring-electrode sensor is very sensitive to air gaps which, expressed in terms of an equivalent circuit, act like a small capacitance in series to the actual soil-affected capacitance. Because of the large permittivity of water the effect is much smaller with water-filled gaps but is still intolerable at small soil permittivities (Fig. 146).

The ring-electrode system has been also used in TDR measurement as well as the frequency-determining device of a ring oscillator [672-675]. Figure 147 illustrates operation of a ring oscillator when combined with a planar transmission line as sensing antenna. The core element is an inverter (3 in Fig. 147) or a cascade of inverters [676] which acts like a driver of a delay line (2). Since the end of the line is fed back to the input of the inverter the system oscillates: if the logic 1 state travels along the transmission line it will become the locic '0' state when it reaches the inverter at the end of the line. This distortion is now propagated along the transmission line until it is transformed into the logic 1 state by the inverting line driver and so forth. Hence the line driver toggles with a frequency determined by the propagation velocity of the positive and negative voltage pulses along the transmission line, standing for both logic states. The propagation velocity, and thus the frequency of the ring oscillator, depends on the permittivity of the material surrounding the transmission line.

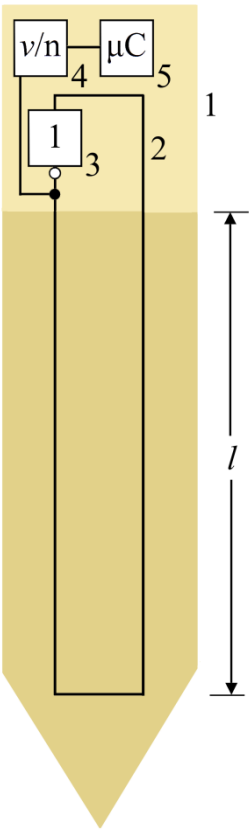

Figure 147. Sketch of a simple planar sensor [672] realized on a multilayer epoxy printed circuit board (1). The upper part holds the ring oscillator with its transmission line (2) of which part of length *l* is introduced in the soil [672-675]. Other essential parts of the oscillator circuit [676] are the inverter (3) and the frequency divider (4). The microcontroller (5) may be also placed on the board.

Sensors with frequencies of 305 MHz in air and 225 MHz in water have been reported [674]. Such a frequency variation offers a favorable sensitivity for soil moisture determination. The width of lancet-shaped printed circuit board is about 30 mm, its length may vary due to the specific application [673]. Typical lengths vary between 100 and 200 mm. Because of the beneficial properties of the glass fiber substrate such boards are rigid and flexible as well and can thus be easily inserted into the soil.

Low-cost moisture depth profile sensors for field application, such as for monitoring the vertical soil water distribution when irrigating agricultural crop land, can be simply derived from the above planar sensor (Fig. 147) by placing several ring oscillator units on one printed circuit board. An external microcontroller is then used to multiplex the basic sensor systems and to support interfaces for process control and data logging [674, 675]. The number and size of the individual units can be easily matched to the specific needs. For agricultural use profile sensors with five basic ring

oscillator units, each one covering an area of about 100 mm by 100 mm, have proven suitable [674, 675]. Besides, this sensor technology is most convenient for the additional large area monitoring of the lateral moisture distribution. For this purpose, a number of sensors, distributed at appropriate spacing over the area of interest, is provided with wireless nodes to form a network. The control unit activates the sensors at suitable intervals and transmits the measured data back to the base station where they are stored and evaluated. This way the three-dimensional moisture distribution of agricultural crop land can be automatically recorded and used, for example, to optimize irrigation procedures [672].

5.2.1.4 Sensors matched to time domain transmission measurement

When processed in the reflection mode transient time measurements using sharp pulses (section 3.2.1) often suffer from unwanted reflections reducing the accuracy of the method. For that reason pulse transmission measurements are preferred in many cases when monitoring dielectrically inhomogeneous materials because the first pulse transmitted through the sample is not affected by reflections. However, this mode of operation, commonly named time domain transmissiometry (TDT [642, 677-681]), requires a sensor design which, in principle, offers a receiving device at the

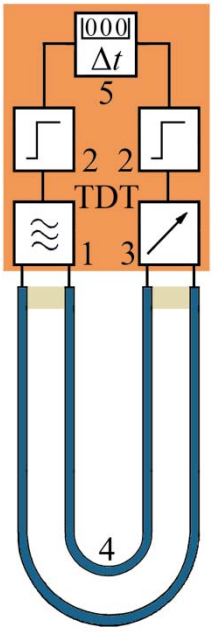

Figure 148. Principle of time domain transmissiometry sensors using loop antennae [642, 680]. The TDT measurement system is indicated by reddish brown color and provided with the principle scheme of Fig. 63. 1, signal source; 2, trigger; 3, signal detector; 4, transmission line; 5, start-stop timer.

end of the transmission line. In soil moisture applications such a measurement port is normally difficult to realize. For that reason, special sensors, matched to the TDT requirements are currently in use.

One TDT sensor group simply uses rod antennae (section 5.1.1.1) which are bent to a loop (Fig. 148) in order to lead the end of the lines back to the transmitter port [642, 680]. In correspondence to two-wire sensors in reflection measurements, the electrical field concentrates mainly between both wires so that the dominant effect on the pulse transient time results from the material between the wires. Since, in field applications, the soil matrix may be significantly disturbed by the loop antenna the measured water content may noticeably deviate from that of the intact material.

The disturbance of the soil can be reduced by using so-called helical sensors [680]. With such sensors a two wire line is helically wrapped round a cylindrically shaped dielectric. One end of the line is directly connected to the transmitting port of the TDT system, the other end is directly fed back to the receiving port by a line proceeding in the interior of the dielectric cylinder. Helical sensors can be easily inserted, they cause less soil disturbances and, due to their line structure, they offer a superior sensitivity when compared to unwrapped two-line sensors. A drawback is the dielectric properties of the supporting cylinder which also act an influence on the measured transit time.

Alternative approaches are concentric sensors for bore hole application [678-682]. Figure 149 exhibits the miniaturized version of such a device. At both ends the cylindrical sensor consists of two concentric coaxial lines (2, 7) bordering the sensing one-wire line structure (5, 6) which is named obstacle. The pulse from the signal port (S) of the TDT system is fed to the outer coaxial line which is formed by the outer (2) and the inner conductor (3) which at the same time serves as the outer conductor of the inner coaxial line. After this feeding section the signal passes a piece of sensor where the central conductor (3) serves as a one-wire line. In order to enhance the sensor sensitivity the diameter of the one-wire sensor is increased using the so-called obstacle (5,6). For impedance matching diameter enlargement is performed in two steps. The obstacle causes the interaction of the electromagnetic field with the surrounding soil and thus influences the propagation velocity of the pulse. The receiving unit consists of a reversion coupler. Basically it is realized by the concentric coaxial lines with the outer conductor (7) provided with a short circuit (8). The inner conductor (4) of the inner coaxial line is indeed connected to the short but the central line (3) is interrupted for a distance *d*. By this means the electromagnetic field of the outer coaxial line couples to the inner line and the pulse provided by the TDT system is transmitted back to its measurement port (M). Identical wave impedances of the coaxial lines support coupling. Combined

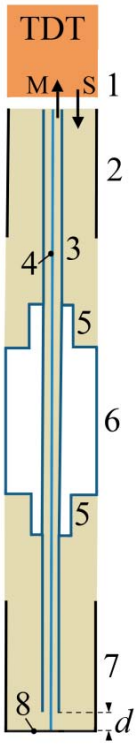

Figure 149. Sectional view of miniaturized concentric TDT sensor [682]. 1, TDT measurement system with signal (S) and measurement (M) port; 2, outer conductor of the outer coaxial line; 3, central conductor, i.e. inner conductor of the outer and outer conductor of the inner coaxial line; 4, inner conductor of the inner coaxial line; 5, 6, obstacle: pieces of one-wire lines with diameter different from the central conductor; 7, 8, concentric reversion coupler with 7, outer conductor and 8, short circuit. Beige color indicates a dielectric (polytetrafluorethylene, $\varepsilon(0) = 2.1$) to mechanically stabilize the sensor.

with an optimized distance d from a numerical simulation a reasonable signal strength is reached for detection.

A prototype of a miniaturized sensor has been constructed with 7.9 mm outer diameter, 150 mm total length, and 40 mm long sensitive part (6) of the obstacle [682]. As long as matching conditions are fulfilled the geometrical dimensions of the device can be varied in wide ranges. At increased diameters [678-681] the TDT measurement system has also been housed inside the obstacle (6).

5.2.2 Miniaturized planar sensors

Microelectromechanical (MEMS) and printed circuit board (PCB) technologies have greatly facilitated the development of miniaturized planar moisture sensors which can easily be inserted into the soil [683] or can be simply placed noninvasively on the surface of the soil under consideration [680, 684, 685]. Other modules, such as soil water potential sensors and temperature measuring devices [683] may be situated close to the mois-

ture sensor so that different soil parameters can be measured at the same site. Depending on the measurement principle, the use of packaged microelectronics may also allow for the integration of the electronic parts on the same printed circuit board, thus forming a compact stand-alone sensor [683, 685].

Because of their physical dimensions miniaturized moisture sensors catch only small soil areas. The small price and low costs render their suitability for punctual moisture determination and distributed sensing as, for instance, required for application in irrigation scheduling [683]. Several methods in use are based on resonant circuit evaluation. A microstrip antenna, for example, has been characterized by the resonance frequency [684]

$$\nu_\mathrm{r} = \frac{c_0}{4h + 2L\sqrt{\varepsilon_\mathrm{eff}}} \tag{160}$$

with height h of the device and length L of the radiating patch and with effective permittivity ε_eff depending upon the permittivities of the material under investigation and of the antenna substrate. Only the real parts of the permittivities have been considered.

Figure 150 shows resonance curves from measurements of some differently moist sands. The resonance curves have been obtained from TDR measurements. The waveforms obtained from fast response time domain spectroscopy have been transformed to the frequency domain to yield the frequency dependencies [684].

The half-power bandwidth of the resonance curves increases with water content of the samples, indicating that the imaginary part of the material's permittivity should be also considered in the theoretical model of the

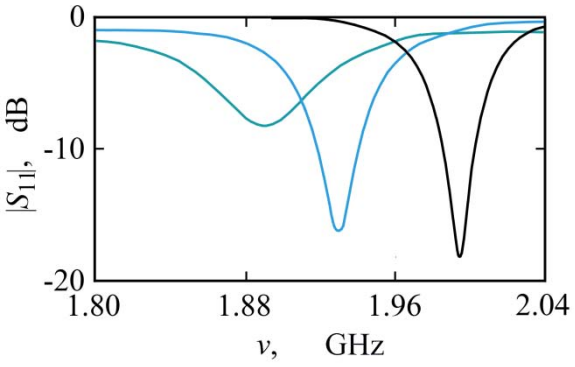

Figure 150. Magnitude $|S_{11}(\nu)|$ of scattering parameter S_{11} of microstrip antenna with length L = 40 mm of radiating patch. Curves show results for the antenna applied to different sands: black, dry sand (water content θ_w = 0, $\varepsilon' = 3.9$); blue, θ_w = 0.062, $\varepsilon' = 4.7$; turquoise, θ_w = 0.124, $\varepsilon' = 8.33$ [684].

loaded micro-strip antenna. The results also demonstrate inadequacy of the small antenna for the investigation of materials with large permittivity ($\varepsilon' \gtrsim 12$), because the broadness of the resonance curves does no longer allow for a reliable evaluation of the resonance frequency ν_r.

In another mode of operation the measurement area of the sensor and the soil act as a parallel circuit of an inductance L and a capacitance C. This circuit is utilized as the frequency determining component of an oscillatory unit, the resonant frequency of which is simply given by the relation

$$\nu_r = (2\pi\sqrt{LC})^{-1}. \tag{161}$$

Since inductance and capacitance depend on the soil properties, the characteristic frequency ν_r of the oscillatory unit can be used to determine the soil moisture via commonly applied empirical relations between the soil permittivity and its water content.

Figure 151 shows the dependence of the characteristic frequency of the oscillatory circuit upon the real part of the material permittivity. The slope $d\nu_r/d\varepsilon'$ is particularly large at small ε', i.e. for dry soils. The printed circuit board of the actual sensor contains further measuring areas. The tight arrangement of two overlying porous matrixes for soil water potential determination in close combination with dielectric moisture content measurement has proven a valuable improvement for applications, such as irrigation scheduling. Because of its comparatively low frequency of operation the dielectric sensor, as briefly discussed before, is less suited for soils with high salinity.

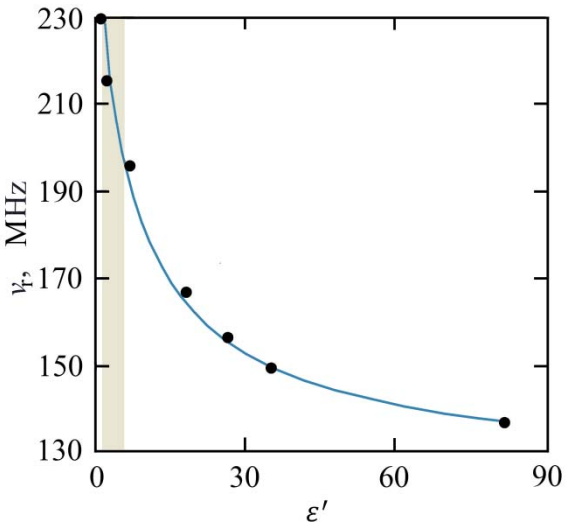

Figure 151. Characteristic frequency ν_r (Eq. 161) of an oscillatory circuit versus real part ε' of the permittivity of several liquids [683]. Light brown area indicates the range of permittivities of dry soil.

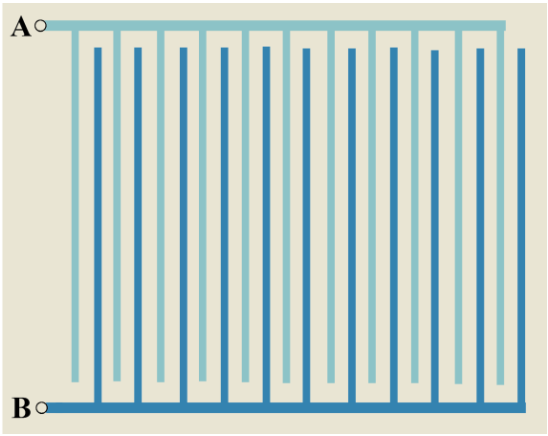

Figure 152. Sketch of two so-called 'interdigitated' electrode systems with electrical contacts A and B [685].

An obvious sensor design is sketched in Figure 152. It basically consists of two 'interdigitated' electrode configurations on a substrate [685]. In the figure both configurations are distinguished by different colors. Each configuration involves n strips of area A, stacked in parallel and separated by a distance d from one another, in the substrate material. Each electrode strip of a configuration is electrically connected to a common electrode, with contacts A and B (Fig. 152), respectively, to the electronic measurement system. When a voltage is applied between the electrode configurations, the fringing field interacts with the surrounding material. Hence the capacitance of the device depends on the permittivity ε of the dielectric. The capacitance of the sensor has been approximated as [685]

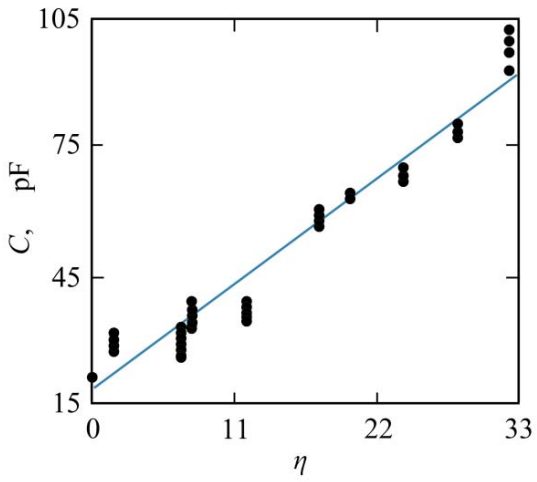

Figure 153. Capacitance C of the interdigitated electrode sensor (Fig. 152) versus soil fractional water content η on a dry (mass) basis. The blue line is taken the calibration line of the instrument [685].

$$C \approx (n\text{-}1)\varepsilon A\gamma/d, \tag{162}$$

where γ (≥ 1) denotes a fringing scale factor.

Using a LCR meter at 100 kHz the sensor capacitances C = 16.5 pF in air and C = 152.3 pF when fully submerged in water at room temperature have been measured for an array 10 mm by 8.5 mm, consisting of 29 interdigitated electrode strips [685]. This result suggests an offset C_0 in the capacity and thus the relation

$$C = \Delta C{\cdot}\varepsilon + C_0, \tag{163}$$

with $C_0 \approx$ 14.8 pF and $\Delta C \approx$ 1.72 pF. Figure 153 demonstrates the performance of the sensor when a set of soil samples was used for calibration. A test of the sensor four months after calibration with a set of freshly prepared soil samples demonstrated the stability of the calibration line and the ease of use of the device for low-cost soil moisture determination with minimal disturbance of the soil.

The low frequency at which sensor capacitance is measured is doubtlessly a drawback when saline soils are the focus of interest. The effect of frequency has been disclosed using a microstrip fractal sensor, referred to as Hilbert sensor [682]. Operating that device the phase velocity

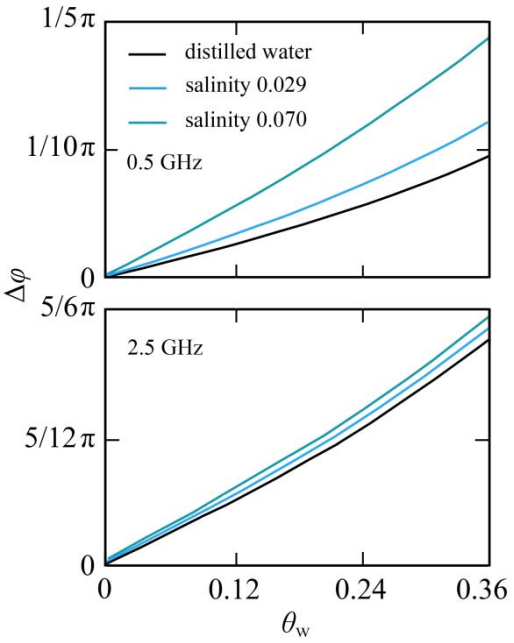

Figure 154. Phase shift $\Delta\varphi$ due to phase velocity variation when microstrip Hilbert sensor [682] is applied to soils of different volumetric water contents θ_w (Eq. 4). The upper part shows results at 500 MHz, the lower part such at 2.5 GHz. Colors distinguish different soil salinities: black, distilled water used to wet the soil; blue, salinity = 0.029; turquoise, salinity = 0.070. Adapted from Figure 7 of reference [682].

$$c = c_0/\sqrt{\varepsilon_{tot}} \tag{164}$$

of a wave propagating along the sensor when interacting with the soil is measured. The total permittivity $\varepsilon_{tot}(\nu)$ of the soil (Eq. 31) contains the conductivity contribution which is inversely proportional to the frequency. At 500 MHz the results displayed in Figure 154 show well separated phase shift –versus– water content relations for soils with different salinities. If the frequency of measurement is increased to 2.5 GHz, however, the curves obtained from the samples with different water content are close together, thereby greatly facilitating the water content determination at unknown salinity.

5.2.3 Contactless sensing

So far the focus was methods of *in-situ* soil moisture estimation, probing the soil water content at a point scale [686]. Such methods apply indeed beneficially to a variety of agricultural requirements. Due to their restriction to small observation areas, however, they are inappropriate for mapping surface soil moisture over large regions, as required as a primary parameter in climate models [687]. There are multiple demands for extended climate models, such as the need for a better understanding of correlations between meteorological events and man-made near-surface atmospheric variations [688]. Evidence has been obtained, for example, that irrigation in Nebraska has changed the amount of precipitation in Iowa and that irrigation in Texas has led to an increase in tornado activity [689]. Ground-based, airborne, as well as space-borne remote sensing techniques in the lower range of microwave frequencies have proven adequate tools, especially in meteorological and climatological research and applications [690, 691]. Some of these tools are briefly presented in the following sections.

5.2.3.1 Microwave radiometry

Since the microwave emissivity of soil is a function of water content radiometry at L-band frequencies (1 – 2 GHz) has been considered a tool for the noninvasive soil moisture determination already in the seventies of the last century [644, 686, 692-694]. Microwave radiometry is a passive method based on the sensing of thermal radiation in a small frequency band. According to Planck's radiation law [695] a black body radiates

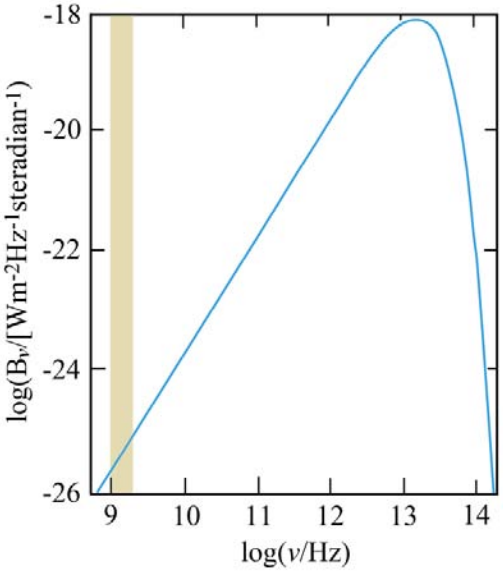

Figure 155. Spectral energy density spectrum of electromagnetic waves radiated from a black body at (T = 310 K). The light brownish area indicates the L-band frequency range.

electromagnetic waves with spectral energy density

$$B_\nu = \frac{8\pi\nu^2\Delta\nu}{c_0^2}\frac{h\nu}{e^{h\nu/k_BT}-1}, \tag{165}$$

where $h = 2\pi\hbar$ is the quantum of action, referred to as Planck's constant, and $\Delta\nu$ is the width of a frequency band around ν. The spectral energy density of a black body at ambient temperature is shown in Figure 155. At ambient temperatures microwave energy is very small compared to thermal energy ($h\nu \ll k_BT$) so that the power radiated from a black body can be represented by Rayleigh – Jeans approximation [695]

$$\Delta P = k_BT\Delta\nu. \tag{166}$$

This relation means that the temperature of a black body can be obtained as $T = \Delta P/(k_B\Delta\nu)$ from the microwave power ΔP radiated in the frequency band $\Delta\nu$.

Any real materials, including soil, radiate thermal energy at lower rates than the black body. This fact is considered by the emissivity e of the material, i.e. the ratio of the power of the thermal radiation from an actual surface to that of the radiation from an ideal black surface [696]. For convenience, the so-called brightness temperature is defined as

$$T_b = eT\,. \tag{167}$$

It can be calculated from the power radiated from a real surface using Eq. (166) analogously. Hence using microwave radiometry to measure the power which, per given frequency band, is radiated from the soil surface the emissivity e can be calculated when the natural temperature T is known. The emissivity, in turn, allows the soil permittivity and thus the water content to be estimated via adequate models.

A zero-order radiative transfer approach [696], referred to as Tau-Omega model [644], is typically employed to model microwave emission from the soil surface. Using this approach, the vegetation effects are parameterized by the vegetation opacity tau and the single-scattering albedo omega. However, for dense vegetation, such as forest or mature corn, more physically motivated models have to be applied, in order to adequately account for the vegetation canopy scattering [697]. For homogeneous soils with smooth surfaces the Fresnel equations [695] are used to relate the emissivity to the dielectric permittivity of the soil. Noticeable soil surface roughness and layering in the soil, however, calls for more sophisticated models [698, 699].

On a first glance, soil moisture monitoring at L-band frequencies appears to be inappropriate because of the comparatively small spectral density of black body radiation in that frequency range (Fig. 155). For various reasons the frequency band from 1.400 to 1.427 GHz has nevertheless been identified the optimum choice for soil moisture estimation. Firstly, this band is a protected radio astronomy band so that measurement errors due to interferences with radio frequency signals are effectively reduced. Radiometry in the L-band has also the advantage of being largely unaffected by cloud cover and solar radiation [696]. Hence L-band radiometers offer the possibility of continuous all-weather as well as day-and-night moisture monitoring. In addition, semi-transparency of vegetation canopies at those frequencies facilitates observation of the underlying soil layers [700, 701]. The measurement depth is in the cm range, naturally dependent on the water content of the soil.

Ground-based L-band radiometers are normally placed at heights ranging from a few meters to more than 20 m above the surface. Instruments fixed on an arc spanning the test area are used [702] as well as such mounted on the back of a moving truck to allow for scanning of a larger area [686]. The horizontal footprint of the radiometer, i.e. the area from which thermal radiation is collected by the radiometer antenna, is evidently dependent upon their height. As an example let us consider a set-up in which a horn antenna is fixed at a height 18 m above ground, with an ob-

servation angle of 40° relative to nadir, and characterized by a -3 db full beamwidth of 12°. The -3 db footprint will be elliptic with half axes of roughly 3.2 and 2.5 m, thus spanning an area of about 25 m^2 [644].

Reliable radiometer operation requires internal and external calibration. The former consists of the measurement of the receiver output voltage when internal reference noise sources are connected to the radiometer input. It is typically realized before each actual measurement. The latter, normally performed once a day during continuous moisture monitoring, consists of measuring the output voltage when the antenna is directed towards targets of well-known brightness temperatures, such as the sky or a microwave absorber. On favorable conditions, experimental uncertainties smaller than 0.02 or even 0.01 m^3/m^3 are reached. As mentioned before, however, soil heterogeneity and surface roughness as well as vegetation cover need to be considered by rather complex models and thus enhance the uncertainty in the soil moisture evaluation.

5.2.3.2 Radar mapping

By analogy with dielectric techniques of material characterization, application of low-amplitude electromagnetic fields (sect. 2.2.2) is often useful in the soil moisture determination of large observation areas. Ground-penetrating radar systems [686, 690, 703-705] are utilized for this purpose. Both airborne platforms, typically operated as synthetic aperture radar (SAR) instruments [706], and global navigation satellite systems (GNSS, [644, 707-714]), such as GPS, are successfully practiced.

A SAR imaging geometry for soil moisture mapping is sketched in Figure 156. The radar antenna (1) transmits series of pulses of length t_p when flying across the site of interest and the backscattered signals are evaluated to yield information about the reflectivity, i.e. the dielectric properties of the ground. The pulses are concertedly processed in order to simulate a very long antenna aperture and to thus provide a high angular resolution in the along-flight direction. The ultimate resolution of an SAR system in this (azimuth) direction is limited [703] by the antenna length L_a (Fig. 156). The ground-range resolution depends on the duration t_p of the pulses and the incident angle θ of the radar beam as [703]

$$r_g = \frac{c_0 t_p}{2\sin\theta}. \tag{168}$$

Hence, in order to reach small distances r_g at which two points can be

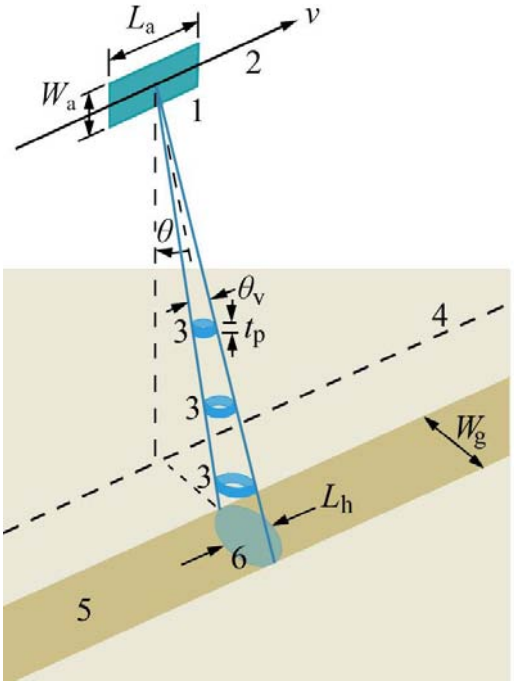

Figure 156. Radar imaging of soil moisture. 1, synthetic aperture radar antenna of length L_a and width W_a, situated, for example, on board of a shuttle; 2, trajectory of the antenna, moving with velocity v; 3, radiated electromagnetic pulses of duration t_p; 4, nadir track; 5, imaged swath; 6, footprint with axis W_g in the ground range (across swath) direction and axis L_h in the azimuth (along-flight) direction; θ, incident angle; $\theta_v = \lambda/W_a$, beam-width; λ, wavelength. Adapted from Figure 1 of reference [703].

distinguished from each other, very short pulses are commonly used and incident angles θ smaller than 15° are normally avoided.

A key feature of active radar techniques for soil moisture estimation is certainly the need for surface roughness which is indispensable for receiving reflected signals at nonvanishing incident angle θ. Hence the backscattered radar pulses received at the antenna reflect predominantly information about the surface structure. Besides, the interaction of the pulsed electromagnetic signals with the complex permittivity of the soil medium is important. The extent of interaction is not just controlled by the lateral footprint (6, Fig. 156) of the radar beam, but also by the penetration depth $\delta_p = \alpha^{-1}$. Electromagnetic theory predicts the absorption coefficient of transversal electromagnetic waves as [715]

$$\alpha = \frac{\omega\sqrt{\varepsilon'}(\nu)}{c_0}\left[(1+\tan^2\delta_{tot}(\nu))^{1/2}-1\right]^{1/2} \qquad (169)$$

where (Eq. 31)

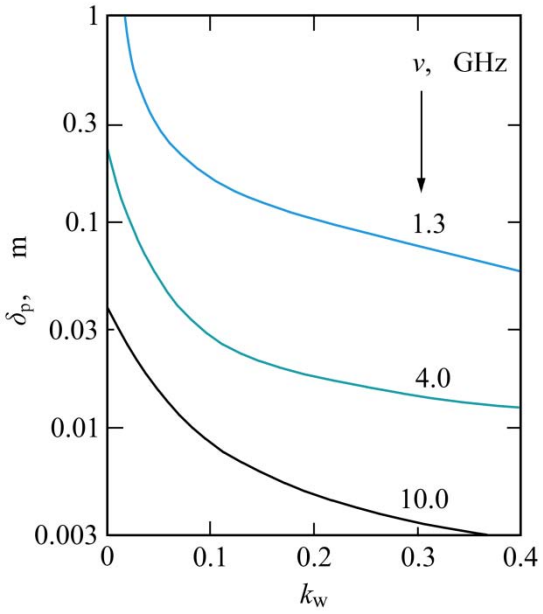

Figure 157. Penetration depth δ_p of radar signals as function of water concentration k_w for loamy soil at three microwave frequencies [703]. Blue line, L-band; turquoise line, C-band; black line, X-band.

$$\tan\delta_{tot} = [\varepsilon''(\nu) + \sigma/(\varepsilon_0\omega)]/\varepsilon'(\nu)\,. \qquad (170)$$

Hence, as illustrated by the examples shown in Figure 157, the penetration depth decreases with water content, primarily because $\sqrt{\varepsilon'}$ increases, and it decrease with frequency, mainly because of the inverse proportionality $\delta_p \propto \omega^{-1}$. Of course, the enhancement of the loss angle with frequency is also important. With pure water, for instance, $\tan\delta_{tot}$ (= $\tan\delta$) increases monotonously from 0.07 at 1.3 GHz to 0.48 at 10 GHz. Conductivity contributions to the soil complex permittivity feature, however, the opposite trend. Regardless of fine details in the soil dielectric properties, the results displayed in Figure 157 suggest a multi-frequency approach to probe different soil layers. A multi-frequency mode of operation is also beneficial for increasing the signal-to-noise ratio [703]. Multi-look images of scenes are also produced by using polarized radar waves, i.e. horizontally polarized waves (H) with their electric field pointing only along the length of the antenna (L_a, Fig. 156) and vertically polarized waves (V) whose electric field direction is along its height dimension (W_a, Fig. 156). Measuring the radar response at HH, VV, VH, HV configurations the amount of information on the ground is increased since the scattering process depends on the polarization. Here the first letter denotes the polarization of the scat-

tered wave (or receiving antenna) and the second letter characterizes the polarization of the incident wave (or transmitting antenna). Above all, multi-frequency measurements and consideration of polarization characteristics contribute to a better separation of effects from surface roughness and soil moisture.

Though active radar systems provide data with high spatial resolution at reasonable penetration depths, the method suffers from the high sensitivity of the measurement signals to the topology and roughness of the soil surface [687, 716, 717]. Various empirical scattering models [718, 719] have been developed to appropriately account for the geometric structure of the soil. These models need, however, site-specific calibrations and, unfortunately, no universal model exists that provides soil water content determination with sufficient accuracy for hydrological applications [686, 719]. In addition, active radar sensing is greatly affected by vegetation canopies [686, 703]. Figure 158 reveals the vegetation transmissivity T for signals of three frequency bands. According to our expectations the transmissivity decreases with increasing mass of biomaterial per surface area. In accord with the penetration depth (Fig. 157) it decreases also with the frequency of the radar signal. Hence again low-frequency (L-band) signals are favorable in soil moisture measurements.

In order to keep the beneficial spatial resolution of active radar systems and to extend the range of application beyond the limitations set by surface roughness and vegetation effects, ground-penetrating radar is often jointly employed with other methods, such as passive microwave radiometry discussed before [686]. Also promising are combinations of ground-penetrating radar and electromagnetic induction (EMI) techniques [704].

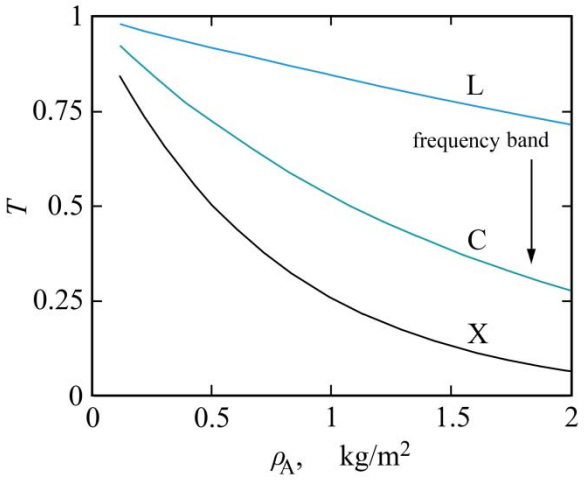

Figure 158. Vegetation canopy transmissivity T as function of biomaterial surface density (mass per area) for electromagnetic signals of different frequency bands. The data refer to the HH polarization configuration [703].

EMI yields the depth-weighted average of electrical conductivity within a given column. As an inductive method it does not need electrodes and enables measurements without any ground contact. Instruments with coil spacing of, for instance, 0.36 m and an operation frequency of 9.8 kHz are available.

Modern active soil moisture measurement techniques utilize the power variations of signals from global navigation satellite systems (GNSS). The direct signals (2a, 2b, respectively, Fig. 159) from the GNSS satellite and the signals reflected from the ground (3a, 3b) are received at the antenna (5) and add up at each satellite position to the registered signal power. Due to the different distances from the satellite to the antenna the superposition of the direct and reflected signal constitutes an interference pattern, the amplitude and phase of which depend upon the complex reflection coefficient of the ground. Since in turn the reflection coefficient depends on the soil dielectric permittivity and thus water content [710] the soil moisture can be inferred from the interference pattern.

GNSS signals comprise the L-band frequencies 1.226 and 1.574 GHz, corresponding with free-space wavelengths λ_0 = 24.45 and 19.05 cm, respectively. For soil moisture measurement dual frequency sensors which are permanently installed in geodetic networks are used as well as lower cost single-frequency devices. For a satellite pass from θ_e = 5° to 30° elevation and an antenna height h_a = 2 m the reflections shift from the distance of 70 to 2 m from the antenna [644]. The satellite needs about one hour for this passage during which a surface area of roughly 70 m × 4 m is scanned.

Soil moisture changes can indeed be directly inferred from the interference pattern, especially from the variations in the phase of the interferogram [711]. Absolute values of the water content of the soil require again local calibrations applying *in-situ* moisture sensors. Like other ground-penetrating active radar systems, the method is restricted to bare soil or only sparse vegetation cover.

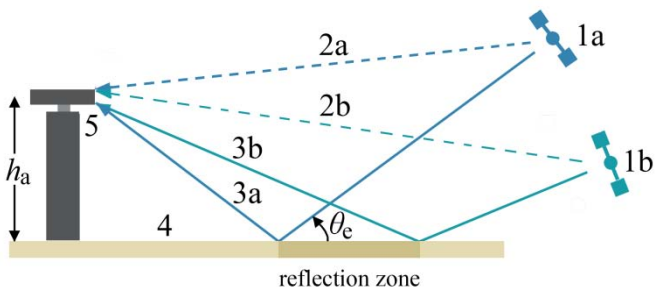

Figure 159. GNSS configuration. 1a, 1b, satellite at positions a and b, 2, direct signal paths; 3, reflected signal, 4, ground; 5, antenna with height h_a; θ_e, elevation angle [644].

5.2.3.3 Surface waves

A related cost-effective active method is based on the observation of the propagation characteristics of low-frequency electromagnetic surface waves [644, 720-723]. Using signal sources in the kHz to MHz frequency range, such an approach aims at large-scale soil moisture estimates by correlating the amplitude and phase properties of the waves with the dielectric permittivity and electric conductivity of the soil. A typical measurement configuration is sketched in Figure 160. By measuring at the receiver positions R1 and R2 the amplitude and phase of a radio-frequency surface wave, radiated from the transmitting antenna T, the average soil properties along transects d_1, Δd, as well as $d_2 = d_1 + \Delta d$ can be determined.

In principle, man-made transmitters and receivers allow for continuous measurement. Because of disturbances from other sources, however, selected periods of time are useful for soil moisture evaluation. Most disturbing are reflections of the measurement waves from the ionosphere boundary which lead to multipath propagation and adverse interferences. For that reason, an optimum measurement time is around noon when solar radiation results in strong ionospheric absorption and thus a minimum of reflection.

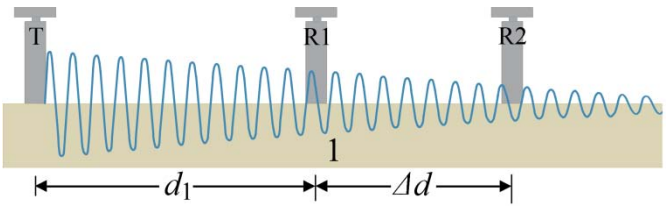

Figure 160. Surface wave propagation. 1, soil; T, transmitter; R1, R2, receivers at different distances from T [644].

The receiver distances amount from some tens of kilometers to a few hundred kilometers. Hence integral soil properties on a very large scale are provided by this technique of measurement. The propagation of surface waves depends primarily on the soil electrical conductivity. The dielectric permittivity adds only a minor effect. Calibration is currently based on empirical relationships, based on reference point sampling along selected paths [724]. In a two year field study several existent soil moisture and groundwater monitoring stations along the measurement section were utilized in order to calibrate the data [722]. In that study the DCF77 signal transmitted by the German long-wave time code and standard-frequency radio station in Mainflingen, Germany, was used. Three receiver

stations were lined up at distances of 20 km from each other to measure the phase transition of the surface waves. The GPS signal was taken as a reference in the phase transition measurement.

5.2.3.4 Free power line sensing

High-voltage power transmission lines, transporting energy as alternating current at frequencies of 50 or 60 Hz, can be utilized to monitor soil moisture variations below the lines on length scales of several km. In such application the freely suspended metallic power line acts as an antenna for additionally applied electromagnetic waves, the field of which is affected by the soil moisture and can thus be used for non-destructive sensing [671]. For this purpose, amplitude and phase of the high-frequency signal have to be determined with sufficient accuracy. A vector network analyzer combined with a *S*-parameter test set (Fig. 161) has proven to provide the required sensitivity and to allow for an adequate signal-to-noise ratio. Since synchronized comparison of the transmitted signal with the network analyzer output signal is difficult at long transmission lengths, the input reflection factor S_{11} of the line is used in the measurements instead of the power transmission factor.

Protection of the high-frequency instruments from electrical damage can be achived with the aid of the capacity post of TFH equipment. TFH, a carrier frequency technique, has been used for a long time in order to isolate low-voltage high-frequency instruments from the high voltage of power transmission lines. So far measurement signals at frequencies between 50 and 500 kHz have been used for soil moisture determination [671].

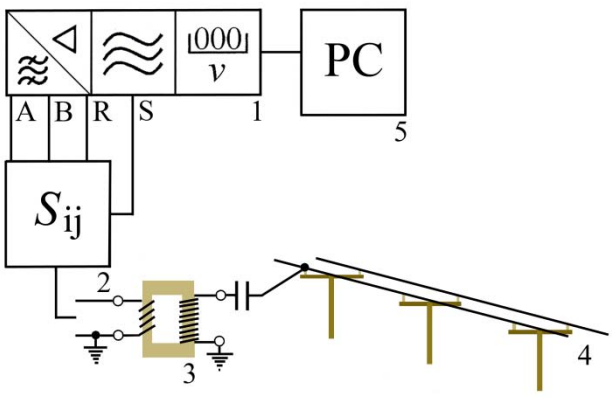

Figure 161. Set-up for soil moisture determination utilizing high-voltage power lines [671]. 1, vector network analyzer with signal output S, reference port R, input ports A and B; 2, *S*-parameter test set; 3, TFH equipment; 4, power line; 5, process control computer.

5.3 Snow cover and snow wetness

Snow is a form of precipitable water which, however, requires special attention because of the lag between the dates when it falls and when it contributes to the runoff and groundwater recharge, becoming involved in further hydrological processes. Snow cover, wetness, and density are of inestimable importance in climatology and hydrology, both on local and global scales. Illustrative examples are avalanche forecast and warning as well as glacier development and melting, with implications for flood prediction, drainage basin management, and optimization of hydro power generation. The seasonal transition from predominantly frozen to non-frozen terrestrial conditions in large areas of the earth acts a major influence on regional to global weather patterns and carbon source-sink dynamics and attracts thus considerable attention. Snow is a mixture of ice particles with inclusions of air and liquid water. It constitutes one of the simplest heterogeneous materials which is freely produced by nature. Snow is, therefore, also investigated as a model for granular media.

At frequencies above roughly 100 kHz the dielectric permittivities of the three constituents vary significantly: $\varepsilon' = 1$ for air, but 3.15 [725, 726] for ice (Fig. 130) and 87.9 [137, 145] for water at 0°C and 100 kHz ≤ ν ≤ 1 GHz. These wide differences in the dielectric properties of the constituents render electromagnetic techniques favorable tools for non-invasive or weakly invasive snow mapping and snow moisture estimation.

The requirements in snow wetness estimation often conform to the conditions of soil moisture determination. Various measurement techniques introduced in section 5.2 are therefore slightly modified to apply to snow monitoring. A common feature of both fields of application is the complementary use of small area or point measurement methods on the one hand and of methods matched to large area observations on the other hand.

5.3.1 Dielectric properties of snow

Because the dielectric relaxation of ice occurs in the lower kHz range (Fig. 130), dry snow as a mixture of ice and air is not expected to feature relaxation behavior at frequencies above 1 MHz. However, internal electric fields tend to somewhat reduce the relaxation time, i.e. to shift the relaxation of dry snow to slightly higher frequencies with respect to ice. Dielectric permittivity measurements at snow densities between 0.08 and 0.41 g·cm^{-1} and temperatures between -10 and 0 °C have yielded relaxation frequencies $(2\pi\tau)^{-1}$ in the 5- to 60-kHz range for dry snow [727, 728]. For fine and

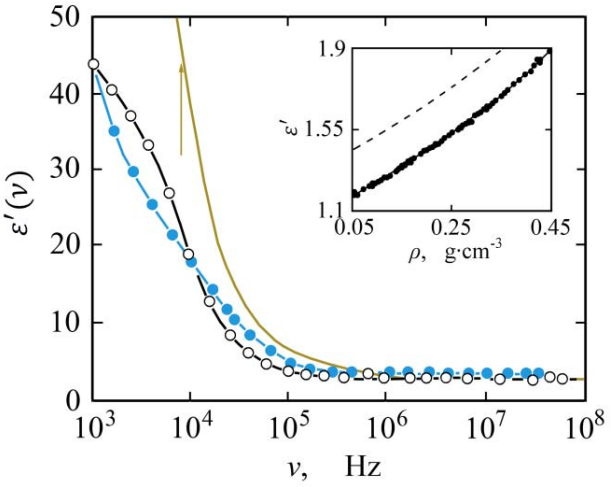

Figure 162. Real part ε' of the complex dielectric spectrum for coarse (circles, black line) and fine grained (points, blue line) wet snow [729, 730] as well as for ice at 0°C (light brown line, Fig. 130). The arrow marks the relaxation frequency of ice. The inset shows ε' data as function of snow density ρ: ●, dry snow, $0.1 \le \nu \le 30$ GHz; dashed line, 1% water added, $0.1 \le \nu \le 3$ GHz [731].

coarse grained snow samples Figure 162 shows real parts of dielectric spectra in the low-frequency region. Whereas the coarse-grained sample spectrum nearly displays Debye relaxation behavior like ice, the spectrum for fine grained snow reveals a noticeable distribution of relaxation times. This difference in the relaxation characteristics does not seem to be due to a size effect. Rather the shape of the samples is different, resulting in quite unequal depolarization factors of the ice particles [730]. Unfortunately the measurements of snow's dielectric properties have not been conducted to sufficiently low frequencies in order to allow for a clear identification of the relaxation frequencies.

At frequencies above the dispersion region the real part of the permittivity of dry snow is predominantly controlled by the snow density ρ (Fig. 162, inset). No noticeable difference in the ε' – versus – ρ relations for new fine grained snow, undisturbed snow, aged snow, and coarse old snow was found [732]. Analytically the real part $\varepsilon'_{\mathrm{d}}$ of the permittivity of dry snow has been represented by [733] the equation

$$\varepsilon'_{\mathrm{d}} = 1 + 1.7\rho_{\mathrm{d}} + 0.7\rho_{\mathrm{d}}^2\,, \tag{171}$$

where ρ_{d} is the ratio of the so-called dry density of snow to the density of water. The dry density refers to snow in which all water is replaced by air. The permittivity of wet snow has been modeled as [733]

$$\varepsilon'_{\mathrm{s}}(\nu) = \varepsilon'_{\mathrm{d}} + W\varepsilon'_{\mathrm{w}}(\nu) \tag{172}$$

and

$$\varepsilon''_{\mathrm{s}} = W\varepsilon''_{\mathrm{d}}(\nu) \tag{173}$$

with the same factor

$$W = 0.1\cdot\theta_{\mathrm{w}} + 0.8\cdot\theta_{\mathrm{w}}^2 \tag{174}$$

for both the real and imaginary part. According to these relations the frequency dependence in the permittivity of wet snow follows that of water.

5.3.2 Invasive and weakly invasive sensors

Localized measurements are again run in frequency domain [725, 734-39] or time domain [740, 741]. Combinations of both techniques are also applied [670, 742-745]. They are particularly useful when investigations aspire to the simultaneous determination of water content and snow density, utilizing, for instance, the different dielectric spectra of water and ice (Fig. 130). Often sensors that have been already tried and tested in soil moisture applications are adapted to snow wetness measurements. Examples are rod antennae [736, 738] similar to those shown in Figure 138. When applied to snow, two-rod antennae are sometimes named "snow fork" [733, 738]. Interesting, a snow fork [733] and a five-rod probe [736] have been operated as resonators. In correspondence with an open-ended coaxial line resonator [731, 735], the snow complex permittivity is calculated from the shift of the resonance frequency and the increment in the half-power bandwidth of the resonance curve (Fig. 45) when the snow probe is loaded.

Other expedient snow sensors are flat ribbon cables, as sketched in Figure 141, and long flat band cables [670, 741-745]. The latter are typically used in transient time measurements as described in section 3.2.1 and allow for snow wetness determination on a length scale up to 100 m [741]. In principle cable sensors suffer from their invasiveness. In many applications, however, they can be positioned in anticipation of snowfall so that they are successively enclosed by snow with minor disturbance of the snow pack. The vertical arrangement of the flat band cable sensor (Fig. 163) allows for convenient continuous snow depth determinations.

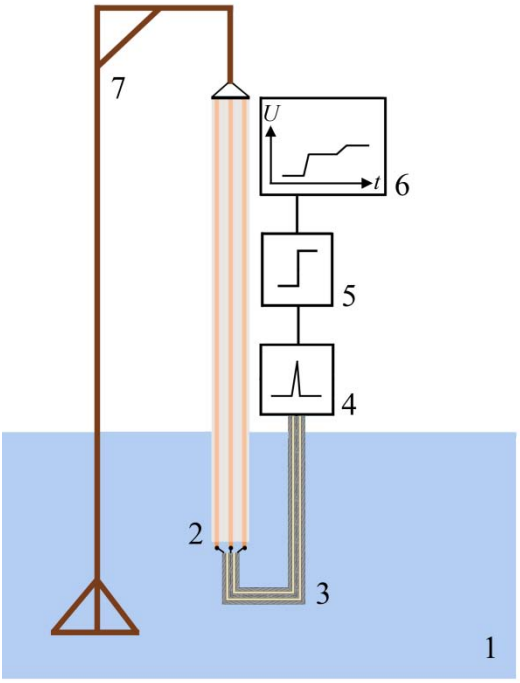

Figure 163. Installation of a flat band cable sensor for snow depth determination by transit time measurement. 1, snow; 2, cable sensor; 3, feeding coaxial cable; 4, sampling head; 5, step-voltage generator; 6, sampling scope; 7, sensor mount.

Changes in the characteristic impedance of the cable exist at the transition between the feeding coaxial cable and the sensor as well as at the snow-air and sensor-air interfaces. The time intervals in the sequence of reflected signals are thus directly utilized for the determination of the actual snow depth. Because of the relatively small difference in the permittivities of snow and air the corresponding signature in the time domain signal has to be first accentuated, e.g. by adequate amplification. Vertical snow pack structures have been also resolved using a sloping instead of an upright cable sensor [741] and appropriate reconstruction software.

5.3.3 Non-invasive measurements

Like soil moisture, snow cover and wetness in large observation areas are important parameters for climate models and for our understanding of meteorological events. Hence there are serious demands for snow sensing and freeze/thaw status monitoring over large distances. Microwave measurements benefit again from their day and night application throughout the year. Differently from soil moisture estimation, snow dielectric proper-

ties are preferably determined at higher frequencies. The reason for the different frequency ranges in soil moisture and snow applications is the higher sensitivity of L-band (1 – 2 GHz) signals to vegetation stem and soil properties, whereas vegetation canopy (Fig. 158) and snow surface features have a stronger effect at higher frequencies. Frequently K_u-band (12 – 18 GHz) signals are applied.

Satellite microwave radiometers (sect. 5.2.3.1) are exploited to investigate snow cover, preferably via determination of the brightness temperature T_b (Eq. 167). For instance, daily dual-frequency (19 and 37 GHz [746, 747]) and dual-polarization [747] T_b data evaluations have provided global maps of the freeze/thaw dynamics. The freeze/thaw variability at regional scales has been extracted with daily temporal precision and resolution of about 25 km from active radar data (sect. 5.2.3.2) as available from a spaceborne K_u-band scatterometer [12, 748]. It is again the considerable difference in the complex dielectric spectra of solid and liquid water (Fig. 130) which allows to differentiate between dry and wet snow.

Valuable information for meteorological and glaciological studies, including ice dynamic constraints and mass balance estimations, are available from snow pack and ice sheet thickness determinations [749]. Spaceborne radar altimetry has proven a suitable tool for remote sensing of the surface topography and surface height variations. Radar altimeters are active devices, normally operated at K_u-band frequency (e.g. 13.6 GHz [749]). Dual-frequency altimeters with an additional signal at C-band frequencies (e.g., 5.2 GHz) allow for adequate ionospheric corrections. The pulsed K_u-band wave radiated by the radar transmitter is partly reflected from the surface of the snow pack or ice sheet. The remaining part penetrates within the medium where it is reflected at internal layers. At given frequency the surface backscattering depends on snow roughness and snow density and the absorption coefficient on snow temperature.

Due to the penetration of the radar signal within dry and cold snowpack and ice sheet reflections come from both the surface and subsurface layers. The former are named “surface echo”, the latter “volume echo”. An example of an altimetric backscattering profile is given in Figure 164 where

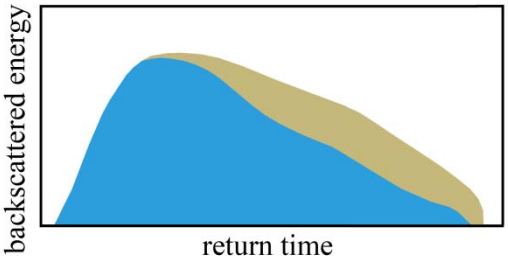

Figure 164. Altimeter backscattered energy as function of return time [749]. The total signal is a sum of the surface echo (blue) and the volume echo (light brownish).

the surface echo is indicated by blue and the volume echo by brown color. Such profiles are analyzed in order to distinguish between effects of different parameters, of which some have been mentioned before, and to deduce the snow pack/ice sheet topography and also other relevant properties such as surface roughness [749].

Albeit spaceborne-based passive and active radar techniques are most promising tools for snow cover and snow wetness applications in large observation areas, they are unsuitable for the remote sensing of the daily melt-freeze cycles in high mountains. In high mountains liquid water content of snow needs to be known with high temporal and spatial resolution because it is a major indicator for snow melt and snow stability and is thus a key parameter for avalanche and flood forecast as well as for water reservoir and hydropower management [750]. Current satellite-based remote sensing, with its daily temporal precision and its course spatial resolution of about 25 km, does not provide adequate information for application in the complex topography of high mountains. Alternatively, because of the complex topography, *in situ* water content observations at relevant snow-covered high mountain sites are difficult to perform and are even prohibited in avalanche-prone zones. For those reasons snow wetness measurements have been proposed using L-band microwave signals transmitted by satellites of a global navigation satellite systems (GNNS). In correspondence with soil moisture applications (sect. 5.2.3.2) the effect of the complex permittivity of the ground on the reflected GNSS signals is utilized in the measurements. Employing low-cost receivers and antennae matched to the global positioning system (GPS) liquid water content of snow in alpine terrain has been determined recently and the onset of melt as well as the daily freeze/thaw cycles have been clearly detected [750].

5.4 Moisture of buildings and building materials

Moisture of construction elements and air humidity are crucial parameters for both the durability and the in-door climate of buildings. Most construction materials, such as brick, lime sand brick, freestone, mortar, concrete, and rock wool insulation are porous. They are therefore able to hold variable amounts of extra water owing to capillary forces. A very large portion of the world's heritage buildings, but also most present constructions, are made from such porous materials and are thus prone to adverse effects of water in excess.

There are three main causes of wetness of construction elements: condensation of humidity, rain penetration due to defects in liquid tightness of

the building's face, and rising moistness because of leakage in the building's bottom area. All these causes involve a reduced service life time of the building and need to be eliminated. Condensation of humidity does not just entail wet walls. It is often accompanied by fungal infestation causing material-damaging effects and often also severe impairment of human health. Excess water in concrete elements may provoke corrosion of reinforcing bars and thus, in the long term, result in progressive damage of the relevant construction. Water may also dissolve and transport existing salts which tend to segregate near dry areas of the component. Because of their hygroscopic properties most crystallized salts in turn adsorb water, often leading to a significant increase in volume. This way damage will inevitably occur even after drying.

In many parts of our planet events of water penetration of buildings and building elements have increased due to environmental influences and to a growing number of natural hazards, especially of flooding catastrophes. For this reason, the demands to precisely monitor and measure the moisture content of constructions have increased. This is particularly true since the precise knowledge of the moisture distribution has proven to minimize the actual repair time and costs. Also the optimization of the construction time for new buildings calls for strict moisture inspection in order to prevent secondary damage. Occasionally moisture sensors are integrated right from the beginning in order to enable continuous moisture observation for a lifetime [21].

Electromagnetic methods have evolved into valuable tools to monitor and measure the moisture content and moisture distribution in civil engineering [751-754]. They are successfully employed by building professionals and building researchers as well, even though the former need normally only the long-term trend in the relative moisture content whereas the latter aim at the absolute moistness [755]. Sometimes building researchers therefore prefer more sophisticated methods even though they can be applied in laboratory experiments only.

5.4.1 Complex conductivity: spectral induced polarization

In addition to their moisture sensitive dielectric properties, building materials mostly reveal electrolytic conductivity which in turn measurably depends upon water content. Hence, in principle, specific electric conductivity σ (Eq. 30) can also be utilized to estimate moisture. Admittedly, the potential of conductivity measurements has been disregarded for a long time because a variety of phenomena affects the (direct current) conductivity of

the materials and renders the evaluation of σ data in terms of water contents difficult. Recent advances in accurate broadband laboratory measurements and adequate modelling of electric conductivity [756], however, are promising and give rise to expectations of future applications in near-surface moisture investigations. For that reason complex permittivity approaches, also named 'spectral induced polarization' methods [751], are briefly introduced.

In heterogeneous or microheterogeneous materials ions cannot move freely. Rather they are impeded by interfaces or electrical double layers [503]. By analogy with polarization (sect. 2.2.3) retardation in the conductivity leads to a frequency dependence and a phase shift in the ion current density (Eq. 30) with respect to the electrical field when the material is exposed to a sinusoidally varying signal. This effect implies a frequency dependent and complex specific conductivity

$$\sigma(\nu) = \sigma'(\nu) + i\sigma''(\nu)\,. \tag{175}$$

The real part $\sigma'(\nu)$ represents the current density in phase with the field. It corresponds with the normal conductivity. The imaginary part $\sigma''(\nu)$ is considering the out-of-phase current and thus reflects polarization. Measurements can be done both in the frequency domain and in the time domain by injecting a monofrequently alternating current or a current step, respectively, and measuring the responding voltage across the sample under consideration. In frequency domain applications the range between 1 mHz and 1 kHz has proven adequate: measurements at lower frequencies are inexpediently time-consuming, measurements at higher frequencies run the risk of contributions from dielectric loss in $\sigma''(\nu)$.

In order to effectively reduce electrode polarization effects, measurements are favorably performed in accordance with four-terminal systems which are provided with a pair of electrodes for feeding the current and another (inner) pair for measuring the potential difference across a given distance. The latter may be constructed as thin needles with high input impedance. Small effects of electrode polarization can be reached thereby down to comparatively low frequencies. In frequency domain observations both the amplitude and phase (relative to the alternating current) of the voltage are normally measured so that the real and imaginary parts of the complex conductivity can be calculated as function of frequency.

Recently first approaches toward three-dimensional moisture profiles of construction elements have revealed the potential of electrical impedance tomography (EIT) for applications in civil engineering [757,758]. As mentioned in chapter 3.3.2 before, so far EIT [384, 427-432, 759] has been

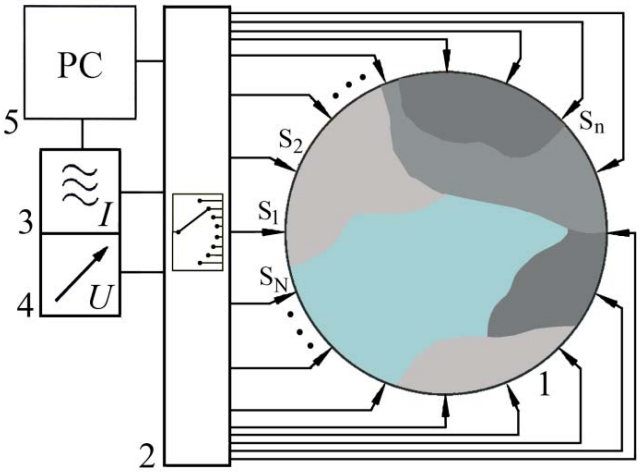

Figure 165. Scheme of an electrical impedance tomograph. 1, sample; 2, multiplexer for the feeding and transmitted signals; 3, current source; 4, voltmeter; 5, process control computer. S_n, n = 1,…N, denote the current and voltage electrodes.

predominantly used as a tool for medical diagnosis [386-391, 398-404, 760-764] but also for multiphase flow imaging [406, 407]. Geophysical applications [765], such as environmental remediation [766], have been also reported.

Similar to the microwave tomograph in Figure 74, the scheme of an EIT system is depicted in Figure 165. In this scheme current and voltage electrodes are not distinguished. Rather the process control computer is assumed to select suitable pairs of electrodes for current injection and potential difference measurement, to store the relevant data and to evaluate the resulting impedance patterns.

Depth profiles of moisture in building elements can be obtained from simple scalar conductivity (or electric resistivity) measurements using sensors with distributed electrodes. An example is depicted in Figure 166. The sensor consists of a number of electrode rings separated by isolating spacer rings. When inserted into the material under test a voltage is applied to a selected pair of neighboring electrodes and the resulting current is measured. Shifting successively the activated pair of electrodes along the axis of the device yields the moisture profile via the local electrolytic resistance of the material [767]. Sensors with electrode ring height 2.5 mm have been employed, for instance, for the long-term tracing of the water content in concrete building elements. Examples are the study of the curing process and the evaluation of the benefit from hydrophobizing concrete slabs. Also the performance of road surface waterproofing has been monitored with the aid of built-in multi-ring electrodes [767].

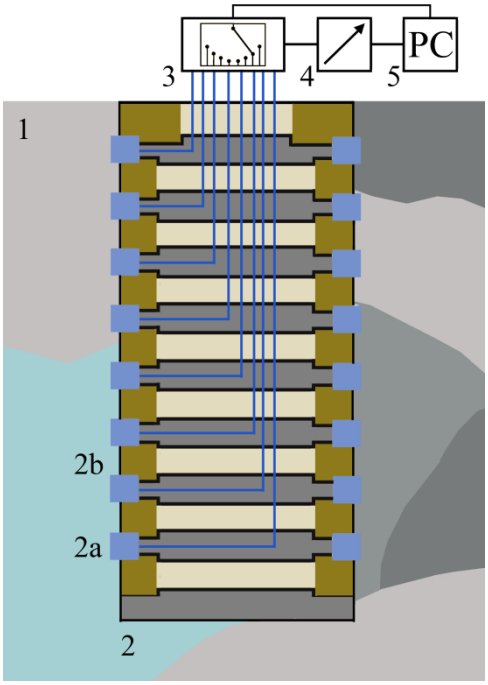

Figure 166. Multi-ring electrode measurement system for electric resistivity measurements [767]. 1, construction element; 2, sensor with 2a, stainless steel electrodes and 2b, isolating spacer rings; 3, multiplexer, 4 electronic measurement device; 5, process control computer.

5.4.2 Dielectric measurement applications

5.4.2.1 Inserted and embedded sensors

Many methods of moisture determination in civil engineering, including such in harsh environment like in bioreactor landfills [768, 769] and salt mines [665, 770, 771], use sensors that are inserted or embedded in the material under consideration. Often they rely on transit time measurements using TDR set-ups as introduced in section 3.2.1. Differences apply predominantly to the choice of the proper sensors.

Flat ribbon cables (section 5.2.1.2) are most popular for large area moisture monitoring [665, 769-772]. They are also applied as sensing element of low cost network analyzer set-ups in order to gain the embedded cable impedance in the frequency range between 1 and 200 MHz [21, 666].

An illustrative application is the integration of modified cable sensors in a concrete bridge which allow for the persistent inspection of the construction for potential moisture ingress [21]. As a byproduct the sensors revealed a continuous decrease in the mean water content of the concrete

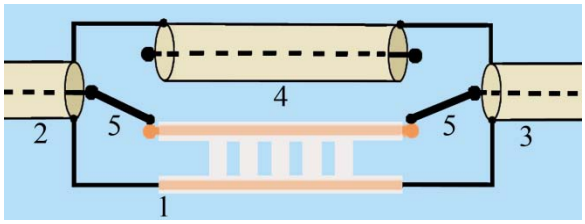

Figure 167. Element of the flat ribbon cable sensor with coaxial line bypass [21]. 1, sensor element; 2, 3, feeding and receiving coaxial line, respectively; 4, coaxial bypass; 5, switch.

over several years. In this, as in many other applications, the sensing system is to first of all indicate whenever the water content within the construction increases. In addition it should permit to approximately localize the leaky part. For that reason the flat ribbon cable is divided into segments of adequate length, of which each one can be gated separately. For this purpose each segment can be by-passed by a piece of coaxial line as sketched in Figure 167. The switches for the selection of a sensor segment may be accessed via extra control line or by applying suitable dc signals to the coaxial lines [21].

Small semi-rigid flat band cables with a width of only 5 mm have been applied in transition time measurements for the inspection of historical buildings [752, 773]. Such sensors need boreholes of minor diameter only ($\lesssim$ 7 mm) for their insertion in building elements. They can thus be used to investigate the moisture distribution in protected monuments.

Several applications use two-rod fork-like antennae [768, 774-778] as described in section 5.2.1.1 and depicted in Figure 138 B. In order to reduce the borehole diameter when the sensor is to be inserted into building elements miniprobes are used which consist of two thin wires with 0.8 mm diameter and 5 mm spacing [775, 778]. On the contrary, more expanded multi-rod transition lines containing one live conductor and three screening conductors have been also proposed as sensor in which the electromagnetic field permeates only in a more localized region of the material [779]. Such sensor resembles the four-rod antenna (Fig. 140) used for soil moisture determination [650, 656-658].

In addition to the prevailing transit time measurements, frequency domain techniques are occasionally applied. An example is the resonance frequency and quality factor (Fig. 45) observation permitted by complementing a two-rod sensor by a coil (Fig. 168). The metallic rods may be considered a capacitor in parallel with a resistor. Hence the total device operates as a LCR-circuit. At the resonance frequency of about 4.7 MHz [776] the resonance frequency is predominantly a function of the real part of the complex permittivity of the material surrounding the rod antennae.

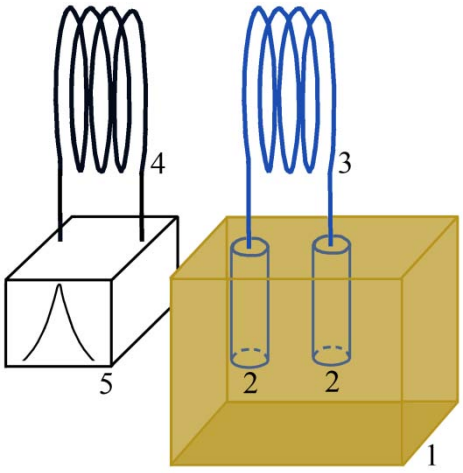

Figure 168. Resonant sensor consisting of two metallic rods (2) inserted in the material under test (1) and an inductive coil (3). The magnetic field of the measurement coil (3) couples to the receiving coil (4) that connects the sensor to the electronics (5), such as an impedance analyzer.

The quality factor depends mainly on the material's electric conductivity. After appropriate calibration of the sensor measurement of its resonance frequency and half-power bandwidth thus allows to evaluate the complex impedance of the material under test. Miniaturized resonant sensors proceed from an interdigitated electrode array (Fig. 152) serving as capacitor. Such an array is completed by an inductive spiral line system on the same single-sided printed board [780, 781]. The complete device may be likewise represented by a LCR-circuit. For moisture measurements at about 35 MHz a sensor with total length as small as 46.5 mm and broadness of only 31.5 mm has been used [781]. As with the more conventional lumped-element system shown in Figure 168, the coupling of the electronic circuit can be reached by an external antenna.

The frequency dependence in the dielectric properties of building materials may be obtained from frequency domain measurements applying network analyzers and cells based on coaxial line technology [782, 783]. If specific care is taken to guarantee a well-defined material density and to avoid air gaps between the measurement cell and the sample, coaxial transmission lines are suitable for the study of granular materials, such as bentonite and sand [783]. In order to circumvent careful drilling for precisely fitting the sample between inner and outer conductor, solid material is more favorably placed in the cylindrical section of a coaxial line - circular waveguide transition [782]. Depending on the sample permittivity and the frequency of interest a cut-off type cell with vanishing coaxial line part (b in Fig. 36) may be appropriate for a cell with metallic end face as short

[782]. Measurements are performed in a reflection mode. Again air gaps must be carefully avoided.

5.4.2.2 Fitting devices and contactless sensing

In most cases noninvasive water content determinations of buildings and building materials rely on a reflection mode of measurement. Measurement frequencies extend normally to some GHz [234, 684, 784-790], several studies use signals at the prominent frequency 2.45 GHz, corresponding to a wavelength of 12.2 cm in free space.

Transient time measurements with the aid of a suggestive two-strip line probe of 100 or 200 mm length (Fig. 169) yield the surface moisture of the building material under investigation. The time which the pulse needs to propagate along the line and be reflected back to its input is determined and evaluated in terms of the surface wetness. The relation between this time and the wetness, however, is complicated due to the complex structure of the system. The pulse does not just propagate in the material under test but also in the plastics (3, Fig. 169) supporting the strip lines and in air. For that reason specific calibrations are required for the reliable determination of the water content from the transient time data.

Transient time techniques can also be operated in a transmission mode placing the building material between a transmitting and a receiving antenna [792]. Accuracy may be increased by comparing the transient time

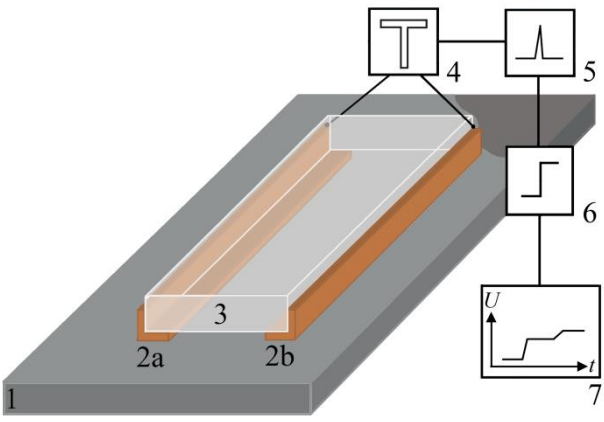

Figure 169. Surface probe for transient time measurements [791] along with TDS system. 1, element under study; 2a, 2b, two-strip line; 3, base plate made of plastics; 4, transformer connecting line 2 to a coaxial line; 5, sampling head; 6, step-voltage generator; 7, sampling scope.

to that required to pass a length of a suitable reference material, such as air. Bench-scale units have been operated both in reflection and transmission mode applying broadband Gaussian pulses with center frequency 4.7 GHz and 3.2 GHz bandwidth [787]. The transient time and also the reflected energy have been considered in view of their suitability for moisture determination.

Many techniques in use are based on classical reflection coefficient measurements applying frequency domain [234, 785, 788-790] or fast-response time domain approaches [784]. Horn antennae are convenient [788, 790] but also flanged open-ended coaxial line probes ([234], Fig. 35) and arrays of antenna with different gradation of their penetration–depth [789]. The latter enable moisture mapping in different layers.

In contrast to horn antennae, sensors which, like the two-strip line probe (Fig. 169) and the flanged open-ended coaxial line probe (Fig. 35), are directly attached to the sample require reasonably plane sample surfaces. Non-contact microstrip antennae can be applied even to temporally fluctuating surfaces, for example to monitor the water content of fresh concrete in a cement mixer [785]. A version of a suitable antenna array is depicted in Figure 170. The passive or active reflector (3, Fig. 170) may be designed to rotate the direction of polarization of linearly polarized incident waves by $\pi/2$. Primary sensitivity of the receiving antenna for waves polarized in this way suppresses effectively direct crosstalk of the incident signal. Multi-frequency operation helps to adequately consider the effects

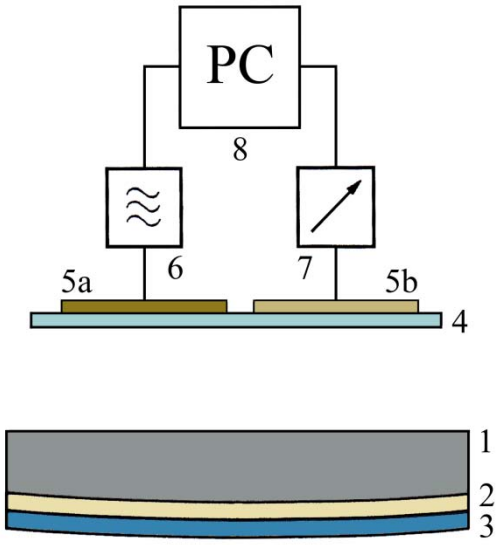

Figure 170. Principle of non-contact water content monitoring in cement mixers [785]. 1, fresh concrete; 2, extremely hard protection of 3, polarization changing reflector device; 4, protection (made, e.g. of polytetrafluorethylene) of 5a, transmitting and 5b, receiving microstrip antenna, respectively; 6, signal source; 7, receiver; 8, computer for process control and data analysis.

of the varying concrete thickness and thus changing distance between the sample surface and the transmitting and receiving antennae. The reflector (3) and the antennae (2a, 2b) need to be protected against the chemically and mechanically aggressive fresh concrete by adequate materials. A silicium nitride cap (2) and a PTFE sheet (4), for instance, have proven suitable [785].

Open-pored ceramics is also available as cover material to shield damageable sensing elements from aggressive materials. A sensor, mainly consisting of an Archimedian spiral within a short piece of circular waveguide has been protected by a commercial ceramic that provides water exchange with the sample [790]. The sensor constitutes a resonator with resonance frequency at around 2 GHz. The waveguide is operated below the cut-off frequency of its TM_{01} mode and thus prevents radiation of electromagnetic energy. Alternatively, for moisture measurements at frequencies of about 2 GHz resonant microstrip antennae, realized on a conventional substrate, have been proposed [684].

5.4.3 Mixture relations

As with soil moisture (Eq. 152) and snow wetness (Eqs. 172-174) specific mixture equations are necessary in order to relate the measured apparent permittivity ε_a of the building material or building element to the desired (volumetric, Eq. 4) water content θ_w. Various empirical equations, among them such originally derived to apply to soil moisture [645, 793, 794] have been tested. It was found that relation [755]

$$\varepsilon_a = [\theta_w \varepsilon_w^\alpha + (1-\phi)\varepsilon_{sol}^\alpha + (\phi - \theta_w)\varepsilon_{air}^\alpha)\,]^{1/\alpha} \qquad (176)$$

applies reasonably to various building materials if only the real part of the permittivity is considered. In this relation, θ_w and ε_w are the volume fraction and permittivity of water, ϕ is the porosity of the sample, ε_{sol} and ε_{air} (= 1) are the permittivities of the solid material and of air, respectively, and α ($-1 \le \alpha \le 1$, $\alpha \ne 0$) is a parameter to be discussed below.

Equation (176) is predicated on the relation

$$\varepsilon_a = \left(\sum_{l=1}^{L} \theta_l \varepsilon_l^\alpha\right)^{1/\alpha}, \qquad (177)$$

with θ_l and ε_l ($1 \le l \le L$) denoting the volume fraction and the permittivity,

respectively, of the *l*-th component of a composite dielectric. This so-called "α"-relation, first suggested by Lichtenecker [795], corresponds with the modified Looyenga formula (Eq. 140). It has indeed been considered a purely empirical equation for long but it ultimately follows from a physical model assuming a beta-function distribution of the geometrical shapes of phases of the multi-component mixture [796]. At $\alpha = 0$, the beta-function approach leads to the "geometrical mean" mixture model

$$\varepsilon_a = \prod_{l=1}^{\mathrm{L}} \varepsilon_l^{\theta_l}, \tag{178}$$

which had been also already presented by Lichtenecker.

As expected intuitively, equation (176) is not universal. Therefore, individual mixture relations are often required in order to correlate the apparent permittivity of building materials with their moisture content. An example is the empirical polynomial

$$\varepsilon_a = 6644.9 \cdot \theta_\mathrm{w}^4 - 7014.9 \cdot \theta_\mathrm{w}^3 + 2698.2 \cdot \theta_\mathrm{w}^2 - 445.26 \cdot \theta_\mathrm{w} + 29.07 \tag{179}$$

which satisfactorily represents the moisture dependent apparent permittivity of gypsum [797]. Another example is the water content of wood for which the following model has been given for the real part of the apparent permittivity [798, 799]:

$$\varepsilon_a = [(1-\theta_\mathrm{w})\varepsilon_\mathrm{sol}^\alpha + \theta_\mathrm{w}\varepsilon_\mathrm{bw}^\alpha]^{1/\alpha}, \quad \theta_\mathrm{w} \le \theta_\mathrm{c} \tag{180a}$$

$$\varepsilon_a = [(1-\theta_\mathrm{w})\varepsilon_\mathrm{sol}^\alpha + \beta\{\theta_\mathrm{c}\varepsilon_\mathrm{bw} + (\theta_\mathrm{w}-\theta_\mathrm{c})\varepsilon_\mathrm{w}'(\nu)\}^\alpha]^{1/\alpha} \tag{180b}$$

where the frequency-dependent real part of the permittivity of water has been modeled as

$$\varepsilon_\mathrm{w}'(\nu) = 3.2 + \frac{85.8 - 0.37\,\mathrm{K}^{-1}(T - 273.15\,\mathrm{K})}{1 + (\omega\tau_\mathrm{w})^2}\,. \tag{180c}$$

Here ε_bw is the permittivity of bound water and θ_c is the (critical) water content up to which all water is considered to be bound. Parameter β modifies the contribution from water in Eq. (180b). Its value has to be found by a regression analysis of pairs of carefully measured ε_a and θ_w data. The pure water relaxation times τ_w are shown in Figure 82 and are also given in numerical format in Table 10 in section 6.3.

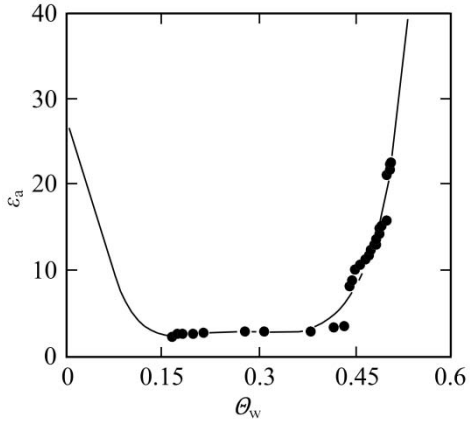

Figure 171. Apparent real part of the complex permittivity of flue gas desulpurization gypsum as measured (points) and as predicted by the empirical polynomial (Eq. 179, full line), shown as function of volumetric moisture content θ_w [797].

Obviously, the models represented by Eq. (179) as well as Eqs. (180a – c) fail to predict correctly the limiting permittivities. At $\theta = 1$, for example, at variance with the actual water value, Eq. (179) yields $\varepsilon_a = 1912$ and $\varepsilon_a = 64.6$ follows at room temperature from Eqs. (181b and c). The empirical polynomial (Eq. 179) wrongly extrapolates to vanishing water content, resulting in $\varepsilon_a = 29.1$ at $\theta = 1$ instead of the permittivity of the solid material. In a range $0.15 \lesssim \theta_w \lesssim 0.5$, however, the experimental data are well represented by the empirical function.

5.5 Moisture content of food and agricultural products

Electromagnetic fields are applied to food and agricultural products for quite different reasons. Strong high-frequency radiation is used in dielectric heating applications [800, 801]. Stored grain insects, for example, are devitalized by selective electromagnetic fields in the frequency range 10 to 100 MHz. An another example is the improvement of seed germination by dielectric heating exposures. Results of such electromagnetic power treatment are summarized in a comprehensive monograph [801] in which also dielectric data of food materials are collected. Besides high power applications small amplitude electromagnetic fields are employed for quality sensing.

One of the important quality factors of food materials and agricultural products is their moisture content. It not just determines the quantity of dry matter but is often also an essential indicator for the adequate material processing and the storability. For that reason noninvasive methods of

moisture content determination are vital needs in food industry. In this context electromagnetic techniques over the past decades have proven convenient tools for the study of diverse substances. We mention grain and seed [522, 801-807]; coffee [805], in-shell and unshelled peanuts [808, 809]; ice lettuce [810], tobacco slices [811], and tea leaves [812, 813]; seafood [653, 814-816]; rapeseed [811], oil palm fruit [817-819], and hevea rubber latex [820] and also cotton bale [821] and biofuels [822].

5.5.1. Common techniques

Many investigations into the dielectric properties of food materials and agricultural products are based on conventional methods such as time domain and frequency domain measurements using versions of open-ended coaxial probes [808, 814-816, 818, 820, 823] as well as transmission and reflection measurements in free space configurations with horn antennae as transmitting and receiving devices [802, 810-812, 821]. The principles of these methods have been discussed before in sections 3.1 and 3.2. Therefore the following will be restricted to some remarks about specially designed sensors.

A mentionable sensor is the miniaturized coaxial line probe with radii of the inner and outer conductors as small as 0.1 and 0.33 mm, respectively. The device (Fig. 172) has been designed to determine the moisture content of single rice grains by frequency domain reflection coefficient measurement in the frequency range 0.5 to 12 GHz [808]. So far such investigation needs, however, multi-parameter polynomial functions in order to adequately model the relations between the complex reflection coefficient, the measurement frequency, and the moisture content of the sample.

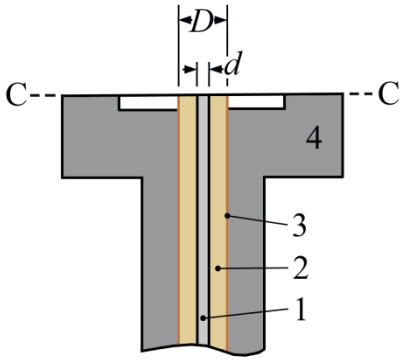

Figure 172. Cross-sectional view of a miniaturized open-ended coaxial line probe [808]. 1, inner conductor with diameter d = 0.2 mm made of silver; 2, interspace filled with polyfluorethylene; 3, coper tube serving as outer conductor with inner diameter D = 0.66 mm; 4, housing from stainless steel; C – C, calibration plane.

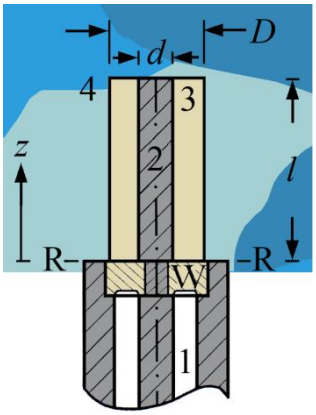

Figure 173. Design of the insulated monopole sensor [820]. 1, feeding coaxial line; 2, piece of inner conductor (diameter d = 1.3 mm, length l) serving as antenna; 3, insulating polytetrafluorethylene cover with diameter D = 4.2 mm; 4, sample; w, dielectric window; z, direction of wave propagation; R – R, reference plane.

Another rare sensor is the insulated monopole antenna sketched in Figure 173. Though the uncovered single rod monopole antenna is rather often employed, its insulated version is less popular, likely also because of its more complicated characteristics. A first comprehensive analysis of the insulated device has been provided already in 1974 [824]. To a certain extent the characteristic wave impedance

$$Z_0 = \frac{Z_3\beta}{2\pi\beta_3}\left(\ln\frac{D}{d}\right) \tag{181}$$

and wave number

$$\beta = \beta_3\left(1 + \frac{H_0^{(1)}(\beta_4 D)}{H_1^{(1)}(\beta_4 D)\ln\frac{D}{d}}\right) \tag{182}$$

of the antenna [820] can be adjusted by ratio D/d of the diameters of the insulating cover and the central conductor. In these equations, Z_3 and β_3 are the wave impedance and wave number, respectively, of the insulating material. $H_0^{(1)}$ and $H_1^{(1)}$ are the Hankel functions of first kind and zeroth as well as first order, respectively, and β_4 is the wave number of the sample. The input admittance of the monopole sensor at reference plane R – R (Fig. 173), i.e. at z = 0, is given by the relation

$$Y = (-\mathrm{i}/Z_0)\tan(\beta l), \tag{183}$$

where l denotes the length of the piece of inner conducter serving as antenna.

5.5.2 Miniaturized sensors

An alternative to the miniaturized open-ended coaxial line probe (Fig. 172) for the moisture measurement of single grain is the microstrip ring resonator sketched in Figure 174. With this device an annular metallic ring

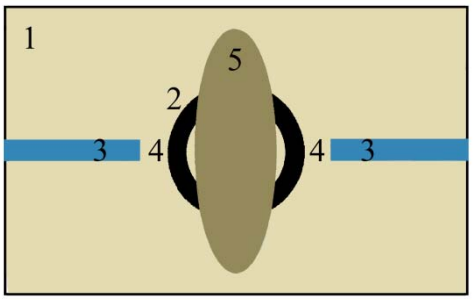

Figure 174. Top view of a microstrip ring resonator [825]. 1, substrate; 2, ring resonator; 3, feeding line with 4, coupling gap; 5, sample, e. g. wheat kernel in 90° orientation.

(2, Fig. 174) is evaporated on a suitable substrate (1). Via adequate feeding line (3) and coupling gap (4) microwaves are injected into the ring. When its circumference l agrees with an integer number of the wavelength λ a standing wave pattern is set up [826]. Hence by some analogy with cavity resonators, for which resonance occurs if their length l equals an integer number p of $\lambda/2$ (Eq. 65), the ring displays resonant characteristics if

$$\lambda = l/\mathrm{p}, \quad \mathrm{p} = 1,2,\ldots \quad . \tag{184}$$

When the ring is overlayed with material, the resonance frequency ν_r and quality factor Q_s depend on the thickness and complex permittivity of the cover. Hence again the changes in ν_r and Q_s are utilized to derive the material's moisture content. The open structure of the sensor facilitates loading and unloading of the sample. Unlike cavity resonator techniques, however, ring resonator applications require physical contact between the sample and the sensor.

Microstrip ring resonator methods designed for frequencies at around 10 GHz have proven suitable not only for the moisture determination of grain [825] but also of leaves and paper grades [827].

A variation of the ring resonator is the microstripline sensor outlined in Figure 175. When the line transmits a microwave, both the attenuation

$$A = \alpha \cdot l = F(\rho, \xi) \cdot l \tag{185}$$

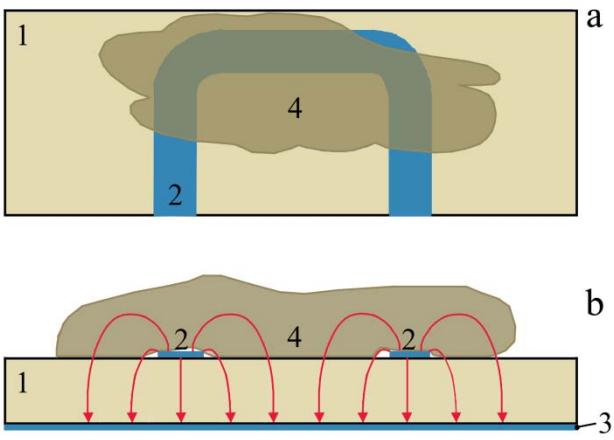

Figure 175. Top-view (a) and side view (b) of micro-stripline sensor for leaf moisture determination [813]. 1, substrate; 2, stripline; 3, metallic layer; 4, sample, e.g. a tea leaf.

and the phase difference

$$\Delta\varphi = \varphi_{out} - \varphi_{in} = G(\rho, \xi)\cdot l \tag{186}$$

depend on the density ρ and the moisture content ξ (Eq. 2) of the sample and the length l of material interacting with the stripline signal [813]. Hence the ratio

$$\frac{A}{\Delta\varphi} = \frac{F(\rho,\xi)}{G(\rho,\xi)} \tag{187}$$

can be used to estimate the water content of leaves independent of l. Here α is the atennuation coefficient (Eq. 37). The method has been primarily used as moisture sensor in tea production lines, for instance in drying units of the tea leaves [813], where it has been operated at 3 GHz.

5.5.3. Water content modelling

As already indicated before, the evaluation of the permittivity of dielectric mixtures in terms of single-component properties is a demanding problem because rigorous theoretical mixture relations are unavailable. The moisture content determination of porous and granular food materials from electromagnetic moisture measurements is the more a challenge, requiring the consideration of at least three phases, solid material, water, and air, the structure of which is insufficiently known in most cases. If, in addition,

the aqueous phase is considered to consist of at least two types of water, for example unaffected "free" water with permittivity ε_w and affected "bound" water with permittivity ε_wb ($< \varepsilon_\mathrm{w}$), even a four-component mixture relation needs to be applied. An example demonstrating the complexity is the Maxwell – De Loor equation [805] for the volumetric water content

$$\theta_\mathrm{w} = \frac{3(\varepsilon_\mathrm{s}-\varepsilon_\mathrm{a})+2\theta_\mathrm{wb}(\varepsilon_\mathrm{wb}-\varepsilon_\mathrm{w})+2\phi(\varepsilon_\mathrm{a}-\varepsilon_\mathrm{s})}{\varepsilon_\mathrm{a}\varepsilon_\mathrm{s}\left(\varepsilon_\mathrm{w}^{-1}-\varepsilon_\mathrm{a}^{-1}\right)+2(\varepsilon_\mathrm{a}-\varepsilon_\mathrm{w})}$$

$$+\frac{\varepsilon_\mathrm{a}\varepsilon_s\theta_\mathrm{wb}\left(\varepsilon_\mathrm{w}^{-1}-\varepsilon_\mathrm{a}^{-1}\right)-\varepsilon_\mathrm{a}\varepsilon_s\phi\left(\varepsilon_\mathrm{a}^{-1}-\varepsilon_\mathrm{m}^{-1}\right)}{\varepsilon_\mathrm{a}\varepsilon_\mathrm{s}\left(\varepsilon_\mathrm{w}^{-1}-\varepsilon_\mathrm{a}^{-1}\right)+2(\varepsilon_\mathrm{a}-\varepsilon_\mathrm{w})}\ . \qquad (188)$$

In this equation, θ_wb is the volume fraction of bound water, ϕ is the porosity and ε_s and ε_a are the permittivities of the solid material and air, respectively. Despite of its comparatively large number of parameters, this semi-empirical relation may fail to predict the water content of agricultural products correctly [805]. For this reason specific calibration procedures and individual product-related empirical equations are often to be preferred when deriving the moisture content from permittivity data. Nonetheless the attempt is made to find unified algorithms for product groups, such as for grain and seed [522-524, 803, 828].

The fundamental demand in the treatment of permittivity data of porous and granular materials is the consideration of the density. Approaches to gain density-independent determinations of grain moisture content are reminiscent the length-independent evaluation of tea leaf data described before (Eq. 187). For mono-frequent, linearly polarized, plane and laterally non-restricted waves interacting with low-loss (non-conducting) materials function

$$\frac{\Delta\varphi}{A} = \frac{\varepsilon'-1}{\varepsilon''}\cdot\frac{2\sqrt{\varepsilon'}}{\sqrt{\varepsilon'}+1} \qquad (189)$$

was considered a suitable density-independent calibration function for a number of dielectrics for which the second term on the right hand side of the equation has little significance [829]. On many events, however, this term could be too relevant to neglect [830].

Another function is based on the observation that, at least for hard red winter wheat, the density-normalized negative imaginary part and the real part of the permittivity at several frequencies, moisture contents, temperatures, and bulk densities are related as

$$\frac{\varepsilon''}{\rho} = s\left(\frac{\varepsilon'}{\rho} - a_0\right), \tag{190}$$

where s is a slope and a_0 an intersection point of the axis of abscissae, i.e $\varepsilon''(a_0) = 0$. This relation can be utilized to define the density-independent calibration function [829]

$$\psi = \sqrt{\frac{\tan\delta}{s\varepsilon' - \varepsilon''}} \tag{191}$$

where $\tan\delta = \varepsilon''/\varepsilon'$ (Eq. 34). Experimental data are related to the moisture content ξ on a wet basis (Eq. 2) according to

$$\psi = c_1 T + c_2 \xi + c_3, \tag{192}$$

with values of parameters c_n, n=1,...3, from a regression analysis of sets of measured data [829].

A unified moisture algorithm enables equivalent moisture predictions

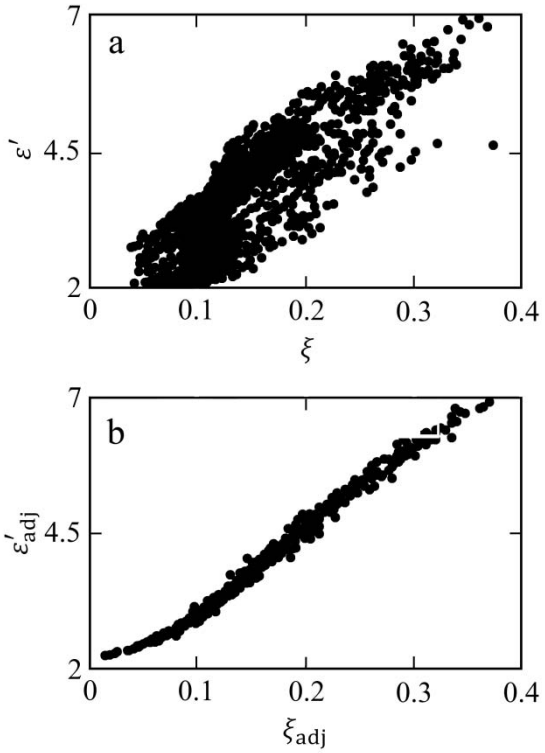

Figure 176. Plot of permittivity at 149 MHz versus reference moisture for a multitude of samples representing about fifty types of grains and nine different grain groups [828]. Part a shows the raw data, part b the same data after treatment by a unified moisture procedure.

for a large number of grain types without needing calibration special procedures [522, 828]. The effect of the algorithm is demonstrated by Figure 176, where, for nine different grain groups, the processed data are shown along with the corresponding raw data. Whereas the original data cover a considerable part of the relevant permittivity - moisture plane (part a, Fig. 176), the adjusted data condense on a narrow range around a line (part b). The algorithm effecting this data reduction requires, however, several steps: correction of the ε' values for a common density, temperature correction of the reference moisture, slope and offset adjustment separately for each grain group, as well as translation of data along a common slope line, likewise specifically for each grain group. The resulting set of adjusted moisture data $\xi - p_\mathrm{T}$ can be related by a fifth order polynomial [522]

$$\xi + p_\mathrm{T} = \sum_{\mathrm{n}=0}^{5} C_\mathrm{n} \, (\varepsilon_\mathrm{adj})^\mathrm{n} \tag{193}$$

to the adjusted permittivity ε_adj. Here p_T denotes a translation parameter. Albeit the procedure appears rather complex it includes diverse grains, such as soybeans, sorghum, sunflower, corn, oats, wheat, barley, rice, and rapeseed.

5.6 Moisture determination in manufacturing processes

The usage of electromagnetic techniques for the water content determination of soil, snow, building materials, and agricultural products is rather popular now. In addition, some electromagnetic moisture measurement applications, which have been seemingly less in the spotlight so far, will be presented in this chapter. A few examples of water content monitoring in manufacturing procedures will be briefly discussed to indicate different aspects of implementation of moisture sensors into production facilities.

5.6.1 Thin materials: paper, textile, plastic sheets, films

Adequate to materials which, due to their thinness, offer a small volume of electromagnetic field interaction only are resonator methods with virtually increased pathlength of interaction. Consequentially, the microstrip ring resonator as shown in Figure 174 has proven a suitable sensor for paper moisture estimation [831, 832]. Also slot line resonators on dielectric

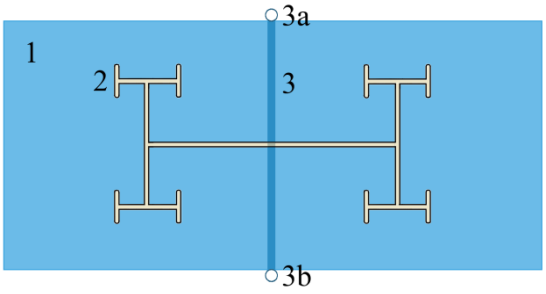

Figure 177. Top view of slot resonator sensor for paper moisture measurement [834]. 1, metallic layer covering a substrate of relatively low permittivity; 2, bended slot line sensing element; 3, microstrip line on the reverse side of the substrate, with 3a, signal generator and 3b, receiver ports.

substrates [833], coupled to a strip line, have been designed for non-invasive moisture measurement in the paper industry [832, 834]. At relatively low permittivity of the substrate ($\varepsilon' = 4.58$ [834]) the fringing electric slot mode field extending across the slot with material loading the sensor. Changes in the resonance frequency and quality factor of the device due to such near-field interaction are utilized to determine the complex permittivity of the sample and to non-invasively estimate the moisture content of paper or any thin sheets thereby. Bending of the slot lines makes the resonator more compact. The sensor shown in Figure 177 may be operated in a transition mode. Measurement of the reflection coefficient is, of course, another option.

A sensor for continuous contactless moisture measurement during fabrication is the laterally opened coaxial resonator delineated in Figure 178. It consists of a cut outer conductor (1, Fig. 178) and an inner conductor (2) that at its ends is shorted in order to cause resonance conditions. In the prototype shown in Figure 178 a rectangular inner conductor profile has

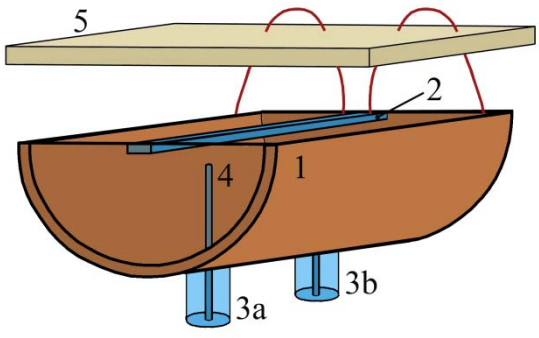

Figure 178. Sketch of a laterally opened coaxial resonator [835]. 1, cut outer conductor; 2, inner conductor; 3a, 3b, input and output feeding lines, respectively, for probes 4; 5, thin sheetlike sample; fringing field lines are indicated in red.

been chosen [835]. The length of the resonator is 114.6 mm, resulting in a resonance of the unloaded device at frequency around 2.5 GHz. Samples are maintained at some distance from the inner conductor with gaps on the order of some mm. As the fringing electromagnetic field interacts with the sample, the resonance conditions are again affected by the complex permittivity of the sample material. Hence the moisture content can be inferred in real time from the shift in the resonance frequency and reduction in the quality factor with respect to the unloaded resonator when the material passes the sensor during the production process.

Terahertz techniques are likewise most suitable for the remote determination of the moisture content of thin materials, such as paper [836]. Because of the high contrast between the permittivities in the far infrared region of water and most other relevant materials, THz techniques, on the one hand, offer a high sensitivity. On the other hand, due to the small wavelength they also provide a good spatial resolution. Using a 0.6 THz fixed-frequency system a spatial resolution in the mm range has been reached at scanning times below some minutes [836].

Various methods are available to measure the dielectric properties of thin materials at microwave frequencies, among them pseudo-Brewster-angle observations [837], free-space transmittance measurements [838], and split post dielectric resonator techniques [839, 840]. Such methods seem to be also capable of determining the moisture content of thin materials from their complex permittivity data.

The geometry of a split dielectric resonator is sketched in Figure 179. The central device is a circular cylindrical resonator (1, Fig. 179) that is split into two halves by an air gap. The gap can house the sample to be studied. As common to resonator techniques, the variation in the resonance frequency and quality factor on insertion of the sample is evaluated to gain the complex permittivity of the material. Such resonator operates with the $TE_{01\delta}$ mode which features only the azimuthal electric field component. Hence the electric field is continuous on the dielectric interfaces.

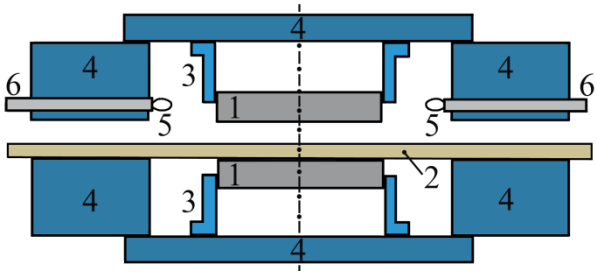

Figure 179. Sectional view of a split dielectric resonator setup [841]. 1, dielectric resonator; 2, sample; 3, support; 4, metal enclosure; 5, coupling loop of, 6, feeding line.

The resonator discs (1) are placed in a shielding metallic cavity (4) which is provided with coupling loops (5) for the connection to the electronic measuring instrumentation. Since the cavity field couples to the field of the dielectric resonator discs, the cavity dimensions have to be adjusted to the parameters of the resonator in order to facilitate proper operation [841].

5.6.2 Powders and tablets

A challenge of the measurements of powdered materials is certainly the packing closeness. Hence, as discussed for porous and granular foods in section 5.5.3, density-independent procedures of moisture determination are preferably applied. Conventional microwave approaches are predominantly employed in the dielectric measurements.

Figure 180 shows a waveguide cell for the 4.0 to 5.8 GHz frequency range [842] that corresponds to the cell sketched in part a of Figure 25. Reflection and transmission coefficients may be determined using a vector network analyzer in order to obtain the complex permittivity of the powdered sample under test. Figure 181 reveals a short-circuited oversized waveguide section used as quasi-optical resonator in the 100 GHz frequency region. The resonant cavity cell is coupled to the external electromagnetic field via a wire grid at one end face (3, Fig. 181) of the piece of waveguide. A horn antenna (5) has been applied to couple the resonator to

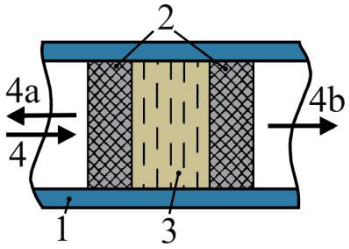

Figure 180. Rectangular waveguide cell for powder moisture measurement [842]. 1, waveguide; 2, dielectric window; 3, powdered sample; 4, measurement signal; 4a, 4b, reflected and transmitted signal, respectively.

Figure 181. Quasi-optical resonator cell for moisture measurement at around 98 GHz [843]. 1, overmoded waveguide; 2, short; 3, wire grid; 4, powdered sample; 5, horn antenna.

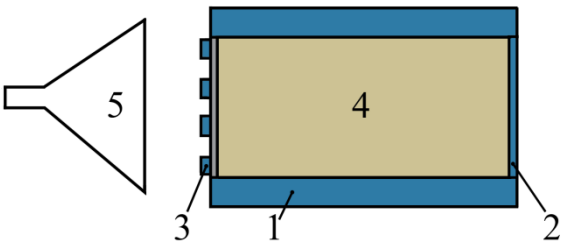

the network analyzer that records the resonance curve of the device. In applications a miniaturized microstrip array [844] may replace the bulky horn antennae. Of course the resonator can be also operated in the transition mode by replacing the short (2) by another wire grid [843]. Needless to mention, that the reflection coefficients of the grids have to be sufficiently high to produce a standing wave pattern within the cell.

The above methods are less suited for direct implementation into production lines. For *in situ* measurements during the fabrication of pharmaceutical oral solid dose forms, commercially available probes have been inserted into the granulation vessels in order to monitor the moisture content during high-shear mixing of powders and wet masses [22, 845]. A probe tested in the frequency range between 1 and 19 GHz [22] is the flanged open-ended coaxial sensor as schematically shown in part a of Figure 35.

An electromagnetic measurement technique used in the coating and drying process of pharmaceutical particles (tablets) exploits the high electric conductivity of the metallic process vessel walls [846]. The scheme

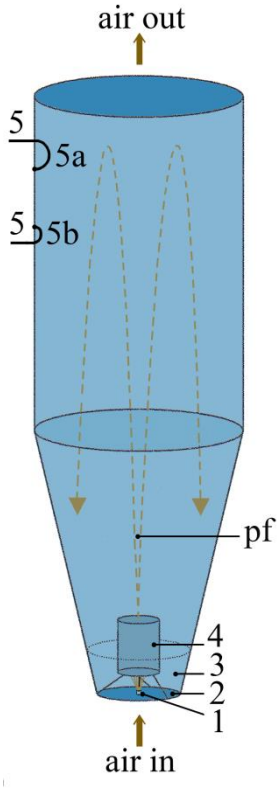

Figure 182. Schematic of metallic reaction vessel for coating and drying of particles in fluidized-bed processes [846]. 1, spray nozzle; 2, distributor plate; 3, bed of fluidized particles; 4, Wurster tube; 5, lines for the connection to the microwave set-up with 5a, 5b, feeding and receiving loop antenna; pf, particle flow.

of a fluidized-bed process vessel used for this step in the manufacturing procedure is shown in Figure 182.

The bottom plate of the vessel, also named distributor plate (2, Fig. 182) is provided with a large number of small holes so that an air flow can be applied through the plate. Such flow creates a fluidized particle bed (3). At the center of the distributor plate a pneumatic spray nozzle is deployed (1) that injects a rapidly moving mixture of air and liquid and thus accelerates the fluidized particles in an upwards motion. Above the spray nozzle stands a Wurster tube. Moving through that tube the particles form a fountain-like flow pattern (pf) and after reaching a certain height fall back into the fluidized bed outside the Wurster tube. The liquid injected through the spray nozzle is a solution containing the material to be deposited onto the surface of the particles. The solvent, commonly water, evaporates within and immediately above the Wurster tube [846].

Since the water distribution within the vessel influences the process performance and thus the quality of the end-product the water content needs to be measured. For this purpose the metallic vessel is considered an electromagnetic cavity resonator with field modes depending on its shape [846]. Two magnetic loop antennae (5a, 5b) are arranged for the coupling of the cavity to the microwave measurement system such as a network analyzer. Magnetic loops are preferred to electric antenna because they prevent the microwave apparatus from large-amplitude voltages as following, for example, from triboelectricity of the rapidly moving fluidized particles. In order to reduce direct crosstalk, the planes of the loops are rotated 90° to one another. As characteristic for resonator methods, the effective complex permittivity inside the vessel is derived from the variations in the resonance frequency and quality factor of a relevant field mode relative to the reference data for the empty vessel, i.e. the vessel without fluidized-bed process.

6 Reference Liquids for Calibrations

6.1 Concepts

The above summary of electromagnetic measurement applications clearly discloses strong demands for sensor calibrations. The need for calibrations arises primarily from the often complicated sensor structure, preventing a reasonable theoretical description of the associated electromagnetic fields. Also unwanted but unavoidable interactions of the fields with other devices, such as production facilities, may render a sole theoretical treatment of the sensor properties impossible. In many cases calibration with a suitable set of reference materials is necessary. This aspect may be illustrated by the widely used open-ended coaxial line sensors sketched in Figure 36. The proper equivalent circuit representation those devices require four capacitances of which one (εC) represents the sample volume, another one (C_0) the feeding coaxial line, and a serial connection of $\varepsilon_w C_1$ and εC_2 the flux lines passing the sealing dielectric window with permittivity ε_w as well as the sample. The (effective) capacitance of the loaded sensor is given by the relation (Eq. 58)

$$\hat{C} = C_{tot} - C_0 = \varepsilon(\nu)C + \frac{\varepsilon_w \varepsilon(\nu) C_1 C_2}{\varepsilon_w C_1 + \varepsilon(\nu) C_2}, \tag{194}$$

with $\varepsilon(\nu)$ denoting the complex permittivity of the sample. Hence, because

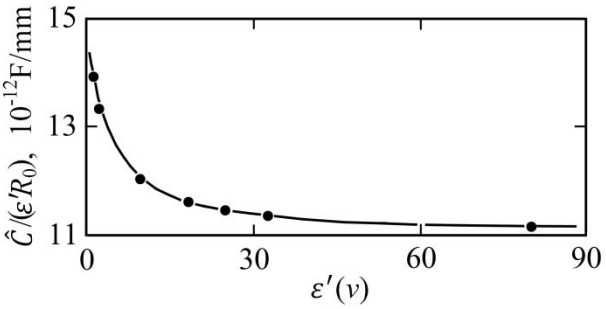

Figure 183. Apparent void capacitance $\hat{C}/\varepsilon'$ per outer radius R_0 of the cut-off type reflection cell as shown in part b of Figure 36. $\hat{C}/(\varepsilon' R_0)$, Eq. (194), is plotted versus permittivity $\varepsilon' = \varepsilon$ of the (lossless) sample filling the circular waveguide section of the cell. The line represents theoretical results from modal analysis of the electric field configuration. Figure symbols indicate experimental data measured with a R_0 = 3.5 mm cell at 25 °C [233].

of the series connection in part c of Figure 36, the capacitance $\hat{C}(\nu)/\varepsilon'(\nu)$ of the sensor is not independent of $\varepsilon(\nu)$ but depends upon the permittivity of the sample as delineated in Figure 183. If suitable reference materials are available such a relationship between C_{tot} and $\varepsilon(\nu)$ can be utilized to determine all relevant capacitances. Preferentially the permittivities of those materials should include the range in which significant changes in C_{tot} occur. A wide range of standard reference materials is also desirable in order to account for the broad variety of applications. Simulation of a sample by a reference with as close as possible dielectric properties is beneficial because spurious effects as resulting, for instance, from slightly imperfect operation of measurement devices or small impedance mismatch at cable connectors may affect the sample and reference measurements in an analogous manner and may thus compensate.

Imperfections of microwave devices and electronic instruments are typically considered by extra calibration of the set-up at a reference plane, favorably at the port to which the sensor is mounted. As briefly described in section 3.1.1.4 the frequently used network analyzer/reflection test set arrangement is normally calibrated using the open end, the short circuit, and the matched termination configurations. However, some sensors allow to combine the calibration of their properties with the network analyzer/reflection test set calibration using appropriate reference materials (e.g. Eq. 61).

Liquids are preferably used for calibration of electromagnetic sensors and cells for dielectric measurements. Liquids are commercially available in high purity grades for a range of static permittivities. Furthermore they have the advantage to completely cover the sensor electrodes, whereas solid materials often need careful fabrication and surface finishing in order to fit them to the sensor without inappropriate air gaps. The focus will thus be reference liquids here.

6.2 Static permittivity of water

In addition to air, with permittivity $\varepsilon(\nu) = \varepsilon_{\mathrm{s}} = 1.00$, water is a self-evident material for calibration of moisture sensors. In case of low-frequency moisture measurements, e.g. with LCR bridge applications (sect. 3.1.2.2), slow response time domain spectroscopy (sect. 3.2.2), and transient time measurements (sect. 3.2.1) using pulses with vanishing Fourier spectrum above 1 GHz, consideration of the static permittvity ε_{s} of water is adequate.

Static (low-frequency) permittivities of water at temperatures between 0 and 60 °C have been reported several times. In Table 4 six series of ε_{s} data are given along with their arithmetic mean $\overline{\varepsilon_{\mathrm{s}}}$. Table 5 shows the low-

Table 4: Static permittivity ε_s of water measured at low frequencies as well as $\bar{\varepsilon_s}$ values representing the arithmetic mean of the six series of data. The uncertainties $\Delta\varepsilon_s$ of these $\bar{\varepsilon_s}$ data have just been taken to include all ε_s data at the particular temperature. *, extrapolated from 0.1 °C; §, ±0.07; $, ±0.05; #, ±0.04; &, ref. 454.

T	ε_s						$\bar{\varepsilon_s} \pm \Delta\varepsilon_s$
°C	± 0.1 [452]	± 0.2 [847]	±0.005 [453]	[848]	[457]	±0.2 [849]	
0	87.735*	87.896	87.91	-	87.87§	-	87.85±0.12
5	85.764	85.897	85.89	85.752	-	-	85.83±0.09
10	83.834	83.945	83.96	83.828	83.91§	84.04	83.91±0.13
15	81.95	82.039	82.11	81.972	-	-	82.02±0.09
20	80.10	80.176	80.20	80.100	80.16$	80.29	80.17±0.12
25	78.301	78.358	78.39	78.304	78.36$	78.40&	78.35±0.05
30	76.54	76.581	-	76.541	76.57$	76.68	76.58±0.10
35	74.83	74.846	-	74.818	-	-	74.83±0.04
40	73.149	73.151	73.19	73.150	73.16#	73.31	73.18±0.13
50	69.917	69.878	-	69.893	69.90#	69.99	69.92±0.07
60	66.82	66.756	-	66.802	66.79#	-	66.79±0.09

Table 5: Three series of static permittivities $\varepsilon(0) = \lim_{\nu\to 0} \varepsilon(\nu)$ of water as extrapolated from microwave measurements. Also given are the arithmetic mean $\bar{\varepsilon}(0)$ as well as the $\bar{\varepsilon_s}$ values from Table 4. Uncertainties $\Delta\varepsilon(0)$ are again taken to just include all $\varepsilon(0)$ data. §, uncertainty = ± 0.05.

T	$\varepsilon(0)$			$\bar{\varepsilon}(0)\pm\Delta\varepsilon(0)$	$\bar{\varepsilon_s} \pm \Delta\varepsilon_s$
°C	±0.2 [137]	[145,850]	[144]		
0	87.91	87.79	-	87.85±0.06	87.85±0.12
5	85.83	-	85.84	85.84±0.01	85.83±0.09
10	83.92	83.88	83.91	83.90±0.02	83.91±0.13
15	82.05	-	82.02	82.04±0.02	82.02±0.09
20	80.21	80.15	80.16	80.17±0.04	80.17±0.12
25	78.36§	78.38	78.34	78.36±0.02	78.35±0.05
30	76.56	76.58	76.51	76.55±0.02	76.58±0.10
35	74.87	-	74.84	74.86±0.01	74.83±0.04
40	73.18	73.17	73.16	73.17±0.01	73.18±0.13
50	69.83	69.92	-	69.88±0.06	69.92±0.07
60	66.70	66.81	-	66.76±0.06	66.79±0.09

frequency permittivities $\varepsilon(0)$ extrapolated from three series of high-frequency and microwave measurements and evaluations of literature data from dielectric spectroscopy of water. Selecting the extrapolated permittivities, data from absolute measurement methods, without any need for calibrations, has been preferred. Such methods normally consider the sample properties at variable length (sect. 3.1.1). The arithmetic means $\bar{\varepsilon}(0)$ from the three series of $\varepsilon(0)$ data agree almost perfectly with the $\bar{\varepsilon}_s$ values from Table 4, indicating that appropriate relaxation spectral functions, such as the Debye function (Eq. 94), represent the dielectric spectra of water correctly at low frequencies.

Understandably there exists less data at temperatures above 60 °C. In Table 6 four series of ε_s values for liquid water up to 100 °C are displayed along with their arithmetic mean ε_S. The scatter in the static permittivities is somewhat larger than at lower temperatures (Tables 4 and 5), probably because of small temperature gradients in the specimen cells at temperatures clearly distant from room temperature.

Static permittivity values from four runs of measurements at temperatures below 0 °C are compiled in Table 7. Two sets of data were derived from static permittivities of emulsions from water and nonpolar liquids with small amounts of surfactant added as emulsifier [455, 456]. The nonpolar liquids were *n*-hexane [455] as well as *n*-heptane and carbon tetrachloride [456]. The permittivity of the water droplets formed in the emulsions has been calculated using mixture relations. Both other techniques [854, 855] relied on the fact that the degree of supercooling can be increased by reducing the size of the (macroscopic) sample. A parallel plate capacitor with plate spacing as small as 0.2 mm held the sample in one case [853], a borosilicate capillary in the other one [854]. The data from different sources shows some variation and, as already mentioned in

Table 6: Three series of static permittivities ε_s of liquid water at high temperatures. The uncertainties $\Delta\varepsilon_s$ of the arithmetic mean $\overline{\varepsilon_S}$ have again been taken to include all ε_s data at the respective temperature. A, data calculated from an interpolation formula given by the authors [851].

T	ε_s				$\overline{\varepsilon_S} \pm \Delta\varepsilon_s$
°C	±0.06 [452]	[851]	[852]	[457]	
70	63.86	64.05	63.81	63.82±0.04	63.89±0.16
80	61.02	61.22	60.95	61.02±0.05	61.06±0.16
90	58.31	58.51	58.29	58.32±0.05	58.36±0.15
100	55.73§	55.90	55.72	55.72±0.06	55.77±0.13

Table 7: Static permittivities ε_s of liquid water at temperatures $T \leqq 0$ °C.

T, °C	ε_s	ref.	T, °C	ε_s	ref.
0.00	87.85	$\bar{\varepsilon}_s$, Tab. 4	-12.10	94.62	[854]
-0.40	87.70	[456]	-15.00	95.60	[455]
-0.70	88.00	[853]	-15.10	96.42	[854]
-3.05	89.00	[853]	-16.00	95.10	[456]
-5.00	90.90	[455]	-16.25	94.80	[853]
-5.20	90.95	[854]	-20.00	98.30	[455]
-6.10	90.40	[853]	-21.40	98.00	[456]
-7.30	91.66	[854]	-22.30	98.10	[456]
-8.80	91.60	[853]	-25.00	100.80	[455]
-9.80	92.40	[456]	-28.80	101.50	[456]
-9.90	93.61	[854]	-30.00	104.20	[455]
-10.00	93.40	[455]	-35.00	107.70	[455]
-11.60	97.70	[853]	-35.00	106.30	[456]

section 4.1.1, at $T < 15$ °C they deviate from the predictions of Eq. (103) which represents the dependence of ε_s upon temperature well in the range $15\ °C \leqq T \leqq 100\ °C$ (Fig. 78). The low-temperature static permittivity data is shown in an enlarged scale in Figure 184 in which also the graph of Eq. (103) is given. It is also demonstrated by the full line that relation [463]

$$\varepsilon_s = 94.9 \cdot \exp[-0.00563(T/\mathrm{K} - 258.15)] \tag{195}$$

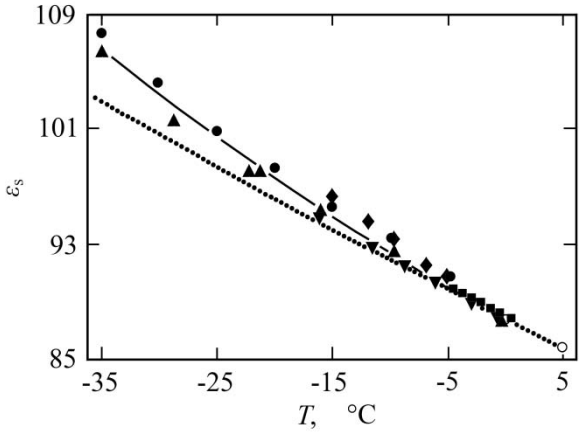

Figure 184. Static permittivity of supercooled water versus temperature. ●, [455]; ▲, [456]; ▼, [853] ;⧫, [854]; ■, [855]; ○, Table 4; dotted line, Eq. (103); full line, Eq. (195).

represents the static permittivity data of supercooled water well. Scattering of the experimental data around the predictions of Eq. (195) amounts to $\Delta\varepsilon_s = \pm 1.2$.

The properties of water at high hydrostatic pressures may be important in various applications, such as subsea petroleum production, processing, and transport. Static permittivities of water in tabular form and in terms of interpolation formulas have been presented [847, 848, 856-858] and reviewed [856, 857] for the pressure range 0.1 to 1000 MPa and for wide ranges of temperatures, including supercritical states. In Table 8 static permittivities at 25 °C are compiled in order to reveal the effect of pressure p. Data from different sources at identical or close-by temperatures suggests an uncertainty $\Delta\varepsilon_s$ smaller than ±0.2 at pressures up to 200 MPa. At even higher p larger deviations between the ε_s values from different series of measurements emerge, e.g. $\Delta\varepsilon_s \approx 2$ at 500 MPa.

Table 8: Static permittivity of liquid water at 25 °C and at hydrostatic pressure $p > 0.1$ MPa.

p, MPa	ε_s	ref.	p, MPa	ε_s	ref.
0.5	78.47	[856]	103.4	81.83	[848]
1.0	78.49	[856]	120.7	82.40	[848]
2.5	78.55	[856]	125.0	82.84	[856]
5.0	78.65	[856]	137.9	83.00	[848]
10.0	78.85	[856]	150.0	83.57	[856]
16.3	78.85	[848]	155.1	83.50	[848]
20.0	79.24	[856]	172.4	84.02	[848]
30.0	79.63	[856]	175.0	84.28	[856]
33.9	79.78	[848]	189.6	84.55	[848]
40.0	80.00	[856]	200.0	84.94	[856]
50.0	80.36	[856]	200.0	85.02	[857]
50.0	80.21	[857]	206.8	85.10	[848]
51.7	80.10	[848]	225.0	85.58	[856]
60.0	80.72	[856]	250.0	86.20	[856]
68.9	80.68	[848]	300.0	87.34	[856]
70.0	81.07	[856]	350.0	88.40	[856]
80.0	81.42	[856]	400.0	89.39	[856]
86.2	81.30	[848]	450.0	90.30	[856]
90.0	81.75	[856]	500.0	91.16	[856]
100.0	82.08	[857]	500.0	93.09	[858]
100.0	81.90	[858]	1000.0	104.60	[858]

The pressure dependence of the water static permittivity can be well represented by the empirical interpolation formula [859]

$$\varepsilon_s = \hat{\varepsilon}_s + \hat{p} \cdot \ln[(\tilde{p} + p)/(\tilde{p} + 10\ \text{MPa})]\,, \qquad (196)$$

with parameters $\hat{\varepsilon}_s$, $\hat{p}$, and $\tilde{p}$ at four temperatures compiled in Table 9. Figure 185 shows plots of static permittivity data as function of hydrostatic pressure in order to demonstrate adequacy of Eq. (196).

Table 9: Parameters at four temperatures for representing the static permittivity of water as functionof hydrostatic pressure [858].

T, K	273	298	323	348
$\hat{\varepsilon}_s$	88.28	78.85	70.27	62.59
$\hat{p}$	11.92	14.11	14.39	13.95
$\tilde{p}$, MPa	232.50	341.59	386.48	393.20

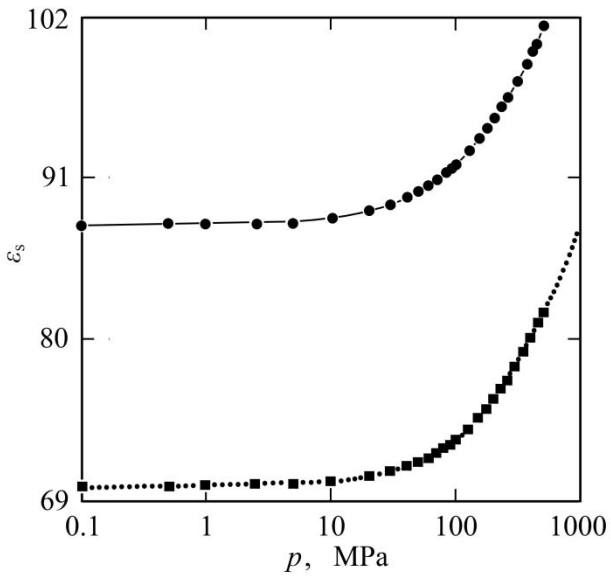

Figure 185. Predictions of Eq. (196) for the pressure dependence of the static permittivity of water at two temperatures and correspondent experimental data (symbols [856]). Points and full line: 0 °C, squares and dotted line: 50 °C.

6.3 Water dispersion and dielectric loss

Measurements including frequencies above 1 GHz need to take the dispersion and dielectric loss characteristics of the water dielectric spectrum into account. The water complex permittivity spectrum up to 25 THz has been analyzed in terms of a sum of three (Debye-type) relaxation and two

Table 10: Three series of dielectric relaxation time data for water at temperatures between 0 and 60 °C.

T, °C	τ, ps		
	[137]	[145,850]	[144]
0	17.67±0.10	17.57±0.20	-
5	14.91±0.10	-	14.30±0.30
10	12.68±0.10	12.50±0.20	12.55±0.20
15	10.83±0.10	-	10.86±0.10
20	9.36±0.05	9.40±0.10	9.38±0.05
25	8.27±0.02	8.28±0.10	8.29±0.02
30	7.28±0.05	7.35±0.10	7.35±0.06
35	6.50±0.05	-	6.59±0.07
40	5.82±0.05	5.84±0.05	5.82±0.06
50	4.75±0.05	4.80±0.05	-
60	4.01±0.05	3.85±0.05	-

Table 11: Extrapolated high-frequency permittivity data corresponding with the relaxation times in Table 10 and extrapolated low-frequency permittivities in Table 5.

T, °C	$\varepsilon(\infty)$		
	[137]	[145,850]	[144]
0	5.7±0.2	4.5±0.3	-
5	5.7±0.2	-	5.8±0.2
10	5.5±0.2	5.4±0.2	6.1±0.3
15	6.0±0.5	-	6.0±0.2
20	5.6±0.2	5.3±0.2	5.7±0.1
25	5.2±0.1	5.5±0.1	5.5±0.1
30	5.2±0.4	5.8±0.3	5.3±0.3
35	5.1±0.3	-	5.7±0.5
40	3.9±0.3	5.3±0.3	5.3±0.4
50	4.0±0.3	4.6±0.4	-
60	4.2±0.3	2.5±0.5	-

resonance terms [170]. In electromagnetic aquametry, however, microwave frequencies up to 100 GHz by far predominate applications. Therefore, and in order to keep calibrations simple and concise, the water reference data are restricted to this range.

As discussed in section 4.1 the principal dielectric relaxation of water occurs in the frequency range up to 100 GHz (Fig. 77) which can be well represented by a Debye spectral function (Eq. 78). For the three series of data for which the extrapolated low-frequency permittivity values are shown in Table 5, parameters τ and $\varepsilon(\infty)$ of this function are given in Tables 10 and 11, respectively. At a given temperature the relaxation times from different sources agree well within the limits of experimental uncertainty. Due to the difficult extrapolation of microwave $\varepsilon'(\nu)$ data to high frequencies, the uncertainty in the $\varepsilon(\infty)$ values is noticeably higher. Since the τ and $\varepsilon(\infty)$ values are correlated, no arithmetic means from the three series of data are given in Tables 10 and 11. For interpolation of $\varepsilon'(\nu, T)$ and $\varepsilon''(\nu, T)$ values within the relevant ν and T ranges it is recommended to use the τ and $\varepsilon(\infty)$ from either set of data. Mean ε' and ε'' values, if desired, may be calculated afterwards from the three individual complex permittivities obtained at each frequency and temperature.

6.4 Aqueous solutions

Additionally useful for calibrations are liquids with static permittivity between those of water ($\varepsilon_s \approx 80$) and air ($\varepsilon_s = 1$). In the middle of the last century mixtures of water with 1,4-dioxane were preferentially applied to

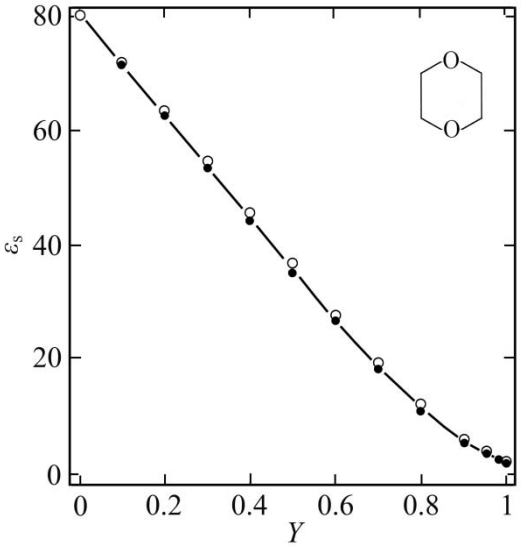

Figure 186. Static permittivities ε_s at 20 °C of mixtures of water with 1,4-dioxane, displayed as function of mass fraction Y of the heterocyclic organic compound. Two sets of data are presented: ●, ref. [498]; ○, ref. [859]. The line is drawn just to guide the eyes. Also shown ist the structure of the 1,4-dioxane molecule.

Table 12: Parameters of the Havriliak-Negami relaxation spectral function (Eqs. 113, 197) for aqueous solutions of quinoxaline at 25 °C and quinoxaline-water mixtures at 35 °C [487]. *Y* and *c* denote the mass fraction and concentration, respectively, of the organic compound.

Y *c*, mol/l	$\varepsilon(0)$ $\varepsilon(\infty)$	τ_{HN}, ps	*h* *b*
25 °C			
0.0645 0.50	73.0±0.7 2.0±2.0	9.05±0.1	0±0.01 0.17±0.07
0.1282 1.00	68.1±0.7 2.0±2.0	10.1 ±0.1	0.01±0.01 0.20±0.07
0.2499 2.00	57.8±0.6 2.5±1.0	12.4 ±0.1	0.04±0.01 0.17±0.05
0.3678 3.00	48.2±0.5 3.1±0.3	16.3 ±0.1	0.05±0.01 0.20±0.02
0.4796 4.00	39.8±0.4 4.3±0.3	21.4 ±0.4	0.08±0.02 0.09±0.06
0.5883 5.00	31.3±0.3 4.4±0.2	30.3 ±0.6	0.09±0.02 0.11±0.06
35 °C			
0.0642 0.50	69.8±0.7 0 ± 3.0	7.1±0.1	0±0.01 0.23±0.09
0.3130 2.52	50.1±0.5 3.3±1.5	10.7±0.2	0.04±0.02 0.17±0.10
0.5883 4.97	29.2±0.3 3.5±0.4	21.0 ±0.4	0.11±0.02 0.14±0.07
0.8389 7.27	11.4±0.2 3.0±0.2	44.1±1.7	0.06±0.04 0.40±0.06
0.8865 7.77	8.3±0.1 3.3±0.1	37.6±1.2	0.09±0.04 0.20±0.09
0.9286 8.12	6.2±0.1 2.9±0.1	38.1±1.8	0.03±0.05 0.41±0.08
0.9513 8.32	4.9±0.1 3.0±0.1	26.7±1.7	0.10±0.09 0.27±0.15
0.9630 8.45	4.5±0.1 2.7±0.3	36.0±5.4	0±0.05 0.60±0.20

adjust the static permittivity in wide ranges. Studies in rats, however, suggest that dioxane is not just an irritant but also a probable human carcinogen. Besides these health risks, as demonstrated by Figure 186, there is a considerable discrepancy between both popular series of static permittivity data for the 1,4-dioxane-water system. Deviations $\Delta\varepsilon_s/\varepsilon_s$ are as large as about 5% at $Y = 0.5$ and even 11% at $Y = 0.8$. For these reasons mixtures of water with another heterocyclic organic, namely quinoxaline, are proposed as a potential reference system here. Quinoxaline is made up of a benzene ring and a pyrazine ring as illustrated by the structure in Figure 89, where also the complex dielectric spectrum for a 1 mol/l solution in water is displayed. The spectra of the quinoxaline water mixtures can be analytically well represented by the Havriliak-Negami function (Eq. 113) which, for convenience, is shown here again [490]:

$$\varepsilon(\nu) = \varepsilon(\infty) + [\varepsilon(0) - \varepsilon(\infty)]/[1 + (\mathrm{i}\omega\tau_{\mathrm{HN}})^{(1-h)}]^{(1-b)} \qquad (197)$$

The parameters for these functions are compiled in Table 12 at several mixture compositions and at two temperatures. At 25 °C quinoxaline is not completely miscible with water but at 35 °C it is. The extrapolated low-frequency permittivities $\varepsilon(0)$ can be reasonably well represented by the Maxwell-Wagner mixture relation (Eq. 119). Within the limits of experimental uncertainty they also fit to the static permittivities of the dioxane – water mixtures when appropriately considered as a function of the volume fraction of the organic component (Fig. 187).

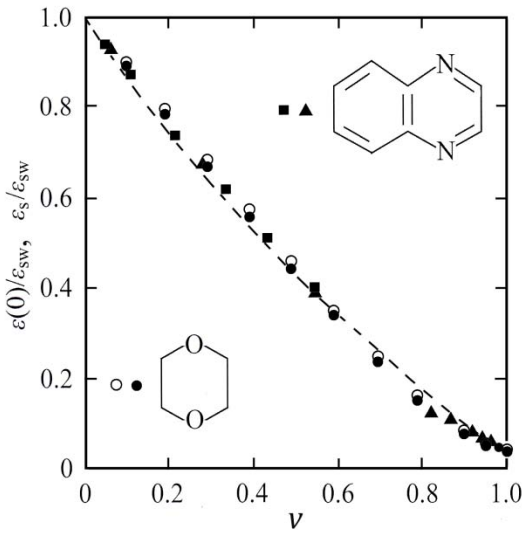

Figure 187. Ratios of extrapolated and static permittivities $\varepsilon(0)$ and ε_s, respectively, to the static permittivity ε_{sw} for mixtures of water with quinoxaline (■, 25 °C; ▲, 35 °C; [487]) and 1,4-dioxane (25 °C; ●, [498]; ○, [859]) displayed versus volume fraction ν of the organic constituent. The dashed line is the graph of the Maxwell-Wagner mixture relation (Eq. 119) with $\varepsilon_{sw} = 74.83$ (water, 35 °C) and $\varepsilon_u = 2.2$ (dioxane [332]).

Measurements of electrolyte systems require special attention because of the conductivity contribution, which typically dominates the imaginary part of their permittivity spectra at low frequencies. In order to reduce conducting spurious effects associated with noticeable ionic conductance it is beneficial to calibrate sensors for the investigation of electrically materials using electrolyte solutions. In Table 13 parameters from two independent series of measurements of aqueous solutions of sodium chloride are compiled. Such solutions are suitable reference liquids because they are easily available, because the data from independent measurements fit to one another within the limits of experimental uncertainty, and because the comparatively simple analytical representation of the spectra facilitates interpolation. The complex permittivity spectra of the NaCl solutions have been described by a sum of a Cole-Cole relaxation spectral function and a conductivity term

$$\varepsilon(\nu) = \varepsilon(\infty) + [\varepsilon(0) - \varepsilon(\infty)]/[1 + (\mathrm{i}\omega\tau_{\mathrm{cc}})^{(1-h)}] - \mathrm{i}\sigma/(\varepsilon_0\omega) \qquad (198)$$

Table 13: Parameters of the relaxation spectral function (Eq. 198) for aqueous solutions of NaCl at 20 °C. *Y* and *c* denote the mass fraction and concentration, respectively, of salt. §, data from ref. [148]; #, data from ref. [860].

Y ± 0.1%	c, mol/l ± 0.2%	$\varepsilon(0)$ ± 0.6	$\varepsilon(\infty)$ ± 1	τ, ps ± 0.2 ps	h ± 0.01	σ, S/m ± 0.07 S/m
0.0030§	0.051	80.4	4.3	9.28	0.035	0.57
0.0050#	0.085	79.4	5.6	9.48	0.020	0.83
0.0074#	0.127	78.6	5.6	9.20	0.012	1.21
0.0100§	0.172	78.7	4.1	9.00	0.047	1.60
0.0107#	0.184	78.5	5.6	9.33	0.022	1.71
0.0127#	0.219	77.4	5.6	9.18	0.017	2.01
0.0130§	0.224	77.7	3.2	9.00	0.050	2.04
0.0153#	0.268	77.0	5.4	9.27	0.029	2.43
0.0200§	0.346	74.6	4.0	8.90	0.036	3.04
0.0240§	0.416	74.9	4.5	8.90	0.041	3.59
0.0245#	0.426	75.2	5.6	9.37	0.024	3.71
0.0264#	0.463	74.4	5.6	9.01	0.026	3.97
0.0300§	0.523	73.4	4.0	8.70	0.051	4.38
0.0338#	0.592	73.2	5.6	8.90	0.036	4.98
0.0350§	0.612	72.0	5.5	8.70	0.030	5.01

with specific electric conductivity σ (Eq. 31). Since the low-frequency regime of the dielectric spectra depends sensitively upon the specific conductivity, carefully measured σ data of the actual reference solutions should be used in calibration procedures instead of just trusting in σ values from Table 13.

6.5 Non-aqueous liquids

Solutions need careful preparation, implicating the risk of weighing errors. For that reason the use of non-aqueous pure reference liquids may be preferred even though care has to be taken in preventing such (often hygroscopic) liquids from water uptake from the air.

Calibrations using nonpolar cyclohexane as reference are often useful because of its small permittivity ($\varepsilon_s \approx 2$). For cells, such as the open-ended coaxial line sensors mentioned in section 6.1, significant changes

$$\frac{\mathrm{d}(\frac{\hat{C}}{\varepsilon})}{\mathrm{d}\varepsilon} = -\frac{\varepsilon_w C_1 C_2^2}{(\varepsilon_w C_1 + \varepsilon C_2)^2} \tag{199}$$

in the total capacitance C_{tot} of the sensor occur in that range of permittivity ε of the material under test (Fig. 183). Here ε_w denotes again the permittivity of the dielectric window separating the sample volume from the feeding coaxial line (Fig. 36). Besides the above aspect cyclohexane is also a most suitable reference liquid since careful measurements over a wide

Table 14: Static permittivities ε_s {= $\varepsilon'(\nu < 1\,\mathrm{THz})$} for cyclohexane at temperatures between 10 and 75 °C. §, ref. [172], uncertainty $\Delta\varepsilon_s$ = ± 0.0056; #, uncertainty = ± 0.0015.

T, °C	ε_s [861] ± 0.002	ε_s [457] ± 0.001	T, °C	ε_s [861] ± 0.002	ε_s [457] ± 0.001
10	2.040	2.039#	40	1.992	1.992
15	2.033	-	45	1.984	-
20	2.024	2.024	50	1.975	1.976
25	2.015 2.0126§	2.016	60	- 	1.961
30	2.008	2.008	70	-	1.945
35	2.000	-	75	-	1.931

range of frequencies have revealed a frequency-independent permittivity

$$\varepsilon'(\nu, T) = \varepsilon_s(T), \quad \varepsilon''(\nu, T) = 0 \tag{200}$$

up to 1 THz [172]. Additionally that study has shown that commercially available pure cyclohexane samples have virtually the same permittivities as samples which have been carefully purified by preparative chromatography. The static permittivity of cyclohexane has been more recently measured again over a range of temperatures [861] and has been found in nice agreement with previous NBS data [457]. Both series of ε_s values are given in Table 14.

The temperature dependency of the static permittivity of cyclohexane can be represented with an error of less than ± 0.001 by the simple empirical relation [463]

$$\bar{\varepsilon}_s = 2.040 - 1.6 \cdot 10^{-3}\ \mathrm{K}^{-1}(T - 283.15\ \mathrm{K}). \tag{201}$$

Additionally desirable are reference liquids with static permittivity between 2 (cyclohexane) and 80 (water). Ethanol with $\varepsilon_s \approx 25$ at room temperature is suitable. Its dielectric properties have been investigated several times. For a range of temperatures a collection of static permittivity

Table 15: Static permittivities ε_s as well as their mean $\overline{\varepsilon_s}$ and also extrapolated low-frequency permittivities for ethanol at temperatures between 0 and 60 °C. The uncertainties $\Delta\varepsilon_s$ of these $\overline{\varepsilon_s}$ data have just been taken to include all ε_s data. #, ±0.03 [863]; §, ref. [866]; $, = 25.11 [867]; &, = 24.78 [867]; = 24.47 [868].

T	ε_s				$\overline{\varepsilon_s} \pm \Delta\varepsilon_s$	$\varepsilon(0)$
°C	±0.04 [861]	[862]	±0.03 [864]	±0.02 [865]		±0.4 [147]
0	-	28.39	-	-	28.39	28.41
10	26.79	26.68	-	26.47	26.64±0.17	26.66
15	-	-	25.92	-	25.92	-
20	25.16	25.07	25.12	25.02	25.09±0.07	25.15$
25	24.43	24.36#	24.35	24.34§	24.37±0.06	24.52&
30	23.64	23.56	23.60	-	23.60±0.04	23.89
35	-	-	22.87	-	22.87	-
40	22.16	22.14	-	-	22.15±0.01	22.43
50	20.78	20.80	-	-	20.79±0.01	21.18
60	-	-	-	-		19.80

Table 16: Parameters for the two-Debye term relaxation function (Eq. 202) for ethanol at temperatures between 0 and 60 °C [147].

T, °C	$\Delta\varepsilon_1$ ±0.1	$\Delta\varepsilon_2$ ±0.5	$\varepsilon(\infty)$ ±0.3	τ_1, ps ±2 ps	τ_2, ps ±3 ps
0	23.84	1.1	3.47	310	6
10	22.19	1.1	3.37	233	6
20	20.65	1.1	3.50	184	8
25	20.02	1.1	3.40	162	6
30	19.46	1.1	3.33	143	7
40	18.05	1.1	3.28	105	6
50	16.93	1.1	3.15	82	5
60	15.60	1.1	3.10	63	6

data is given in Table 15 where also arithmetic means $\overline{\varepsilon_s}$ and $\varepsilon(0)$ values as extrapolated from high-frequency measurements are presented. Up to 25 °C the ε_s values from different sources and also the extrapolated static permittivities fit well to one another. At higher temperatures, however, $\varepsilon(0)$ systematically exceeds the correspondent $\overline{\varepsilon_s}$, probably because of a somewhat incorrect extrapolation. It is worth to notice that at $\nu > 5$ GHz the high-frequency complex permittivities used in the extrapolation were indeed obtained using absolute microwave bridge techniques (Figs. 26,27). At $\nu \leqq 3$ GHz, however, input impedance measurements with cells of the cut-off variety (Figs. 35c, 36b) were performed which needed calibrations themselves.

Ethanol exhibits relaxation characteristics already at lower frequencies that water. At frequencies above 100 MHz the frequency dependence in the real part of the permittivity must be considered and also the non-vanishing imaginary part needs to be taken into account. For that reason relaxation parameters for the liquid are compiled in Table 16. The data refers to a two-Debye-term representation of the spectra

$$\varepsilon(\nu) = \varepsilon(\infty) + \frac{\Delta\varepsilon_1}{1+i\omega\tau_1} + \frac{\Delta\varepsilon_2}{1+i\omega\tau_2} \tag{202}$$

and represents the experimental complex permittivities well at frequencies up to 24 GHz [147]. At 25 °C the ethanol complex permittivity spectrum in the frequency range between 0.1 and 89 GHz has been described by an even more complicated relaxation model involving three Debye terms [868]. Parameters of the two- and three-Debye term models are also

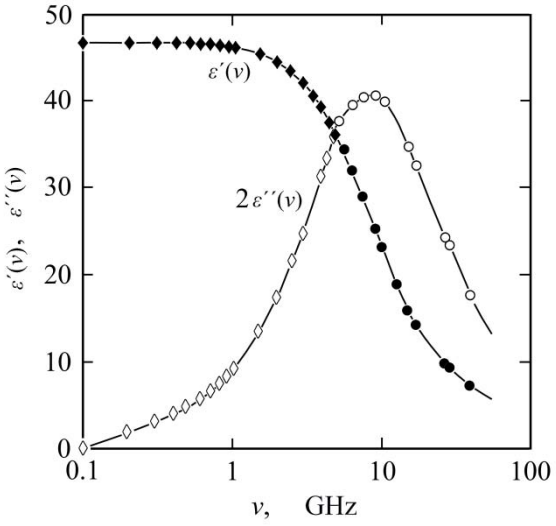

Figure 188. Real part ε' (closed symbols) and negative imaginary part ε'' (open symbols) of the complex dielectric spectrum of dimethyl sulfoxide at 25 °C: ● and ○, ref. [871]; ♦ and ◊, ref. [861]. The lines are graphs of the Cole-Davidson spectral function (Eq. 112) with parameters given in Table 17 [871].

available for mixtures of ethanol with water [147, 867, 868] and static permittivities for ethanol and ethanol-water mixtures at hydrostatic pressures up to 300 MPa have been reported as well [863].

Another suitable reference liquid is aprotic dimethyl sulfoxide (DMSO). DMSO is nonhazardous. It is utilized in pharmaceutical formulations as agent promoting transdermal drug delivery. Static permittivity data from different sources for DMSO agree excellently: $\varepsilon_s = 46.49 \pm 0.06$ [849], $\varepsilon_s = 46.48$ [869], and $\varepsilon_s = 46.50 \pm 0.1$ [870]. The latter value has been obtained by interpolation of data at temperatures between 20 and 60 °C. High-frequency complex permittivity data from two independent series of measurements also fit well to one another (Fig. 188) and also to the Cole-Davidson relaxation spectral function (Eq. 112). For two sets of microwave measurements the parameters of that function are shown in Table 17.

Table 17: Two sets of parameters of the Cole-Davidson relaxation function (Eq. 112) for dimethyl sulfoxide at 25 °C. Here $\varepsilon(0) = \varepsilon(\infty) + \Delta\varepsilon$.

$\varepsilon(0)$	$\varepsilon(\infty)$	τ_{DC}, ps	b	ref.
46.40	4.2	20.5	0.11	[869]
46.58 ± 0.2	4.3 ± 0.2	20.2 ± 0.2	0.09 ± 0.02	[871]

References

[1] F. Franks, *Water* (Roy. Soc. Chem., London, 1983).

[2] F. Franks, Introduction – Water, the unique chemical, in *Water, a Comprehensive Treatise, Vol. 1,* edited by F. Franks (Plenum, New York, 1972) pp 1-20.

[3] P. Micklin, The Aral Sea desaster, *Annu. Rev. Earth Planet Sci.* **35** (2007) 47-72.

[4] L. Gordon; M. Dunlop; B. Foran, Land cover change and water vapour flows: learning from Australia, *Phil. Trans. R. Soc. Lond. B* **358** (2003) 1973-1984.

[5] D. L. Nelson; M. M. Cox, Eds., *Lehninger, Principles of Biochemistry* (Freeman, New York, 2009).

[6] R. Lipowsky; E. Sackmann, eds., *Structure and Dynamics of Membranes: From Cells to Vesicles* (Elsevier, Amsterdam, 1995).

[7] T. Heimburg, *Thermal Physics of Membranes* (Wiley-VCH, Berlin, 2007).

[8] B. Jacobson, Hydration structure of sodium deoxyribonucleic acid and its physicaochemical properties, *Nature* **172** (1953) 666-667.

[9] Y. Levy; J. N. Onuchi, Water and proteins: a love-hate relationship, *PNAS* **101** (2004) 3325-3326.

[10] J. R. H. Tame; S. H. Sleigh; A. J. Wilkinson; J. E. Ladbury, The role of water in sequence-independent ligand binding by an oligopeptide transporter protein, *Nature Struct. Biol.* **3** (1996) 998-1001.

[11] A. J. Mujumdar, Ed., *Handbook of Industrial Drying* (CRC, Boca Raton, 2007).

[12] J. S. Kimball; K. C. McDonald; S. Frolking; S. W. Running, Radar remote sensing of the spring thaw transition across a boral landscape, *Remote Sens. Environ.* **89** (2004) 163-175.

[13] M. Rawlins; K. C. McDonald; S. Frolking; R. B. Lammers; M. Fahnestock; J. S. Kimball; C. J. Vörösmarty, Remote sensing of snow thaw at the pan-Arctic scale using the SeaWinds scatterometer, *J. Hydrol*. **312** (2005) 294-311.

[14] A. Barr, T. A. Black, H. McCaughey, Climate and phenological controls of the carbon and energy balances of three contrasting boreal forest ecosystems in Western Canada, in *Phenology of Ecosystem Processes. Applications in Global Change Research*, edited by A. Noormets (Springer, Dordrecht, 2009).

[15] C. Song; X. Xu; X. Sun; H. Tian; L. Sun; Y. Miao; X. Wang; Y. Guo, Large methane emission from natural wetlands in the northern permafrost region, *Environ. Lett.* **7** (2012) 034009.

[16] L. Wang; C. Derksen; R. Brown; T. Markus, Recent changes in pan-

Arctic melt onset from sattelite passive microwave measurements, *Geophys. Res. Let.* **40** (2013) 522-528.
[17] M. B. Kirkham, *Principles of Soil and Planet Water Relations* (Elsevier, Amsterdam, 2014).
[18] S. Blackmore; R. Godwin; S. Fountas, The analysis of spatial and temporal trends in yield map data over six years, *Biosyst. Eng.* **84** (2003) 455-466.
[19] A. Aghaei; A. J. J. van der Zanden; N. A. Hendriks, TDR technique for measuring the moisture content in brick, in *Proc. 6th Int. Conf. on Eletromagnetic Wave Interaction with Water and Moist Substances*, edited by K. Kupfer, C. Hübner, E. Trinks, H. Kupfer (MPFA, Bauhaus Universität, Weimar, 2005).
[20] F. S. Malan; K. Ahmet; A. Dunster; R. Hearing, Development of a microwave frequency sensor for the long-term localised moisture monitoring of concrete, *Mag. Concr. Res.* **56** (2004) 263-271.
[21] T. Wagenknecht; C. Hübner; F. Königer, A. Brandelik, R. Schuhmann, Large area moisture monitoring in concrete building materials, in *Aquametry 2010*, edited by K. Kupfer, N. Wagner, R. Wagner, F. Bonitz, B. Müller, and C. Hübner (MPFA, Bauhaus Universität, Weimar, 2010) pp 380-388.
[22] L. Gradinarsky; H. Brage; B. Lagerholm; I. N. Björn; S. Folestad, *In situ* monitoring and control of moisture content in Pharmaceutical powder processes using an open-ended coaxial probe, *Meas. Sci. Technol*. **17** (2006) 1847-1853.
[23] W. W. Moschler; G. R. Hanson; T. F. Gee; S. M. Killough; J. B. Wilgen, Microwave moisture measurement system for lumber drying, *Forest Prod. J.* **57** (2007) 69-74.
[24] E. Nyfors; P. Vainikainen, *Industrial Microwave Sensors* (Artech House, Norwood MA, 1989).
[25] A. Kraszewski, ed., *Microwave Aquametry* (IEEE, New York, 1996).
[26] K. Kupfer; R. Knöchel; A. Kraszewski, *RF & Microwave Sensing of Moist Materials, Food and other Dielectrics* (Wiley-VCH, Weinheim, 2000).
[27] E. Nyfors, Industrial microwave sensors – a review, *Subsurface Sens.Technol. Appl.* **1** (2000) 23-43.
[28] K. Kupfer, ed., *Electromagnetic Aquametry* (Springer, Berlin, 2005).
[29] U. Kaatze; C. Hübner, Electromagnetic techniques for moisture content determination of materials, *Meas. Sci. Technol.* **21** (2010) 082001.
[30] A. Kraszewski, Microwave aquametry: introduction to the workshop, in *Microwave Aquametry*, edited by A. Krascewski (IEEE, New York, 1996).

[31] K. Fischer, Neues Verfahren zur massanalytischen Bestimmung des Wassergehaltes von Flüssigkeiten und festen Körpern, *Angew. Chem.* **48** (1935) 394-396.
[32] E. Scholz, *Karl Fischer Titration* (Springer, Heidelberg, 1983).
[33] R. W. Bunsen, Ueber eine volumetrische Methode sehr allgemeiner Anwendbarkeit, *Liebigs Ann. Chem.* **86** (1853) 265-291.
[34] H. S. Knight; F. T. Weiss, Determination of traces of water in hydrocarbons, a calcium carbide-gas liquid chromatography method, *Anal. Chem.* **34** (1962) 749-751.
[35] K. C. Kornelsen; P. Coulibaly, Advances in soil moisture retrival from synthetic aperture radar and hydrological applications, *J. Hydrol.* **476** (2013) 460-489.
[36] N. Abraham; P. S. Hema; E. K. Sartha; S. Subramannian, Irrigation automation based on soil electrical conductivity and leaf temperature, *Agric. Water Manage.* **45** (2000) 145-157.
[37] N. A. Gewande; D. R. Reinhart; P. A. Thomas; P. T. McCreanor; T. G. Townsend, Municipal solid waste in situ moisture content measurement using an electrical resistance sensor, *Waste Mangem*. **23** (2003) 667-674.
[38] M. Nasraoui; W. Nowik; B. Lubelli, A comparative study of hygroscopic moisture content, electrical conductivity and ion chromatography for salt assessment in plasters of historical buildings, *Constr. Build. Mater.* **23** (2009) 1731-1735.
[39] J. H. Scott; R. D. Carroll; D. R. Cunningham, Dielectric constant and conductivity measurements of moist rock: A new laboratory method, *J. Geophys. Res.* **72** (2012) 5101-5115.
[40] J. P. Molin; G. D. C. Faulin, Spatial and temporal variability of soil electrical conductivity related to soil moisture, *Sci. Agric.* **70** (2013) 1-5.
[41] V. Nagy; G. Milics; N. Smuk; A. J. Kovács; I. Balla; M. Jolánkai; J. Deákvári; K. D. Szalay; L. Fenyvesi; V. Štekauerová; Z. Wilhelm; K. Rajkai; T. Németh; M. Neményi, Continuous field soil moisture content mapping by means of apparent electrical conductivity (*EC*a) measurement, *J. Hydrol. Hydromech.* **61** (2013) 305-312.
[42] H. Schwab; U. Heinemann; A. Beck; H.-P. Ebert; J. Fricke, Dependence of thermal conductivity on water content in vacuum insulation panels with fumed silica kernels, *J. Therm. Envel. Build. Sci.* **28** (2005) 319-326.
[43] T. Dias; G. B. Delkumburewatte, The influence of moisture content on the thermal conductivity of a knitted structure, *Meas. Sci. Technol.* **18** (2007) 1304-1314.
[44] Z.-T. Yu; X. Xu; L.-W. Fan; Y.-C. Hu; K.-F. Cen, Experimental

measurements of the thermal conductivity of wood species in China: effects of density, temperature, and moisture content, *Forest Prod. J.* **61** (2011) 130-135.

[45] Z. Suchorab; D. Barnat-Hunek; H. Sobczuk, Influence of moisture on heat conductivity coefficient of aerated concrete, *Ecol. Chem. Eng. S.* **18** (2011) 111-119.

[46] H. Darvishi; M. Zarein, Thermal conductivity of sunflower seed as a function of moisture content and bulk density, *World Appl. Sci. J.* **18** (2012) 1321-1325.

[47] D. Taoukil; A. El Bouardi; F. Sick; A. Mimet; H. Ezbakhe; T. Ajzoul, Moisture content influence on the thermal conductivity and diffusivity of wood-concrete composite, *Constr. Build. Mat.* **48** (2013) 104-115.

[48] C. Csieri; l. Senni; M. Romagnoli; U. Santamaria; F. De Luca, Determination of moisture fraction in wood by mobile NMR device, *J. Magn. Reson.* **171** (2004) 364-372.

[49] B. Wolter; M. Krus, Moisture measuring with nuclear magnetic resonance (NMR) in *Electromagnetic Aquametry*, edited by K. Kupfer (Springer, Berlin, 2005).

[50] G. Cartwright; B. H. McManus; T. P. Leffler; C. R. Moser, Rapid determination of moisture/solids and fat in dairy products by microwave and nuclear magnetic resonance analysis, *J. AOAC Intern.* **88** (2005) 1-14.

[51] G. Almeida; S. Gagné; R. E. Hernández, A NMR study of water distribution in hardwoods at several equilibrium moisture contents, *Wood Sci. Technol.* **41** (2007) 293-307.

[52] H. Xing; P. S. Takhar; G. Helms; B. He, NMR imaging of continuous and intermittent drying of pasta, *J. Food. Eng.* **78** (2007) 61-68.

[53] L. Senni; C. Casieri; A. Bovino; M. C. Gaetani, A portable NMR sensor for moisture monitoring of wooden works of arts, particularly paintings of woods *Wood Sci. Technol.* **43** (2009) 167-180.

[54] M. Merela; P. Oven; I. Serša; U. Mikac, A single point NMR method for an instantaneous determination of moisture content of wood, *Holzforschung* **63** (2009) 348-351.

[55] Y. Liu; J. Cao; H. Zhang; Y. He; X. Xu, Nuclear magnetic resonance rapidly testing method on the moisture content of fresh milk, *J. Chem. Pharm. Res.* **6** (2014) 254-258.

[56] B. Mazela; J. Kowalczuk; I. Ratajczak; K. Szentner, Moisture content (MC) and multinuclear magnetic resonance (MRI) study of water absorption effect on wood treated with aminofunctional silane, *Eur. J. Wood Prod.* **72** (2014) 243-248.

[57] S. R. Evett, Soil measurement by neutron thermalization, in

Encyclopedia of Water Science, edited by B. A. Stewart; T. A. Howell; S. W. Trimble (Marcel Dekker, New York, 2003).

[58] B. Kamilov, N. Ibragimov, Y. Esanbekov; S. Evett; L. Heng, Drip irrigated cotton: irrigation scheduling study by use of soil moisture neutron probe, *Int. Water Irrigation* **23** (2003) 38-41.

[59] S. Evett; N. Ibragimov; B. Kamilov; Y. Esanbekov; M. Sarmsakov; J. Shadmanov; R. Mirhashimov; R. Musaev; T. Radjabov; B. Muhammadiev, Neutron moisture meter calibration in six soils of Uzbekistan affected by carbonate accumulation, *Vadose Zone J.* **6** (2007) 406-412.

[60] P. L. Reeder; D. C. Stromswold; R. L. Brodzinski; J. H. Reeves; W. E. Wilson, Moisture measurement for radioactive wastes using neutron activation of copper, *Appl. Radiat. Isot.* **48** (1997) 247-256.

[61] A. K. Chaubey; A. Taddesse; D. Assefa; A. Y. Hibstie, Elemental analysis of alluvial soil samples using neutron activation techniques in Blue Nile basin, East Gojjam, Ethiopia, *E-Intern. Sci. Res. J.* **3** (2011) 232-242.

[62] R. A. Livingston,; M. Al-Sheikhly; C. Grissom; E. Aloiz; R. Paul, Feasibility study of prompt gamma neutron activation for NDT measurement of moisture in stone and brick, *AIP Conf. Proc.* **1581** (2014) 828-835.

[63] M. C. da Rocha; L..M. da Silva; C. R. Appoloni; O. Portezan Filho; F. Lopes; F. L. Melquíades; E. A. dos Santos; A. O. dos Santos; A. C. Moreira; W. E. Pötker; E. de Almeida; C. Q. Tannous; R. Kuramoto; F. H. de M Cavalcante; P. F. Barbieri; A. F. Caleffi; B. T. Carbonari; G. Carbonari, Moisture profile measurements of concrete samples in vertical water flow by gamma ray transmission method, *Radiat. Phys. Chem.* **61** (2001) 567-569.

[64] J. M. de Oliveira Jr.; A. C. G. Martins; J. A. De Milito, Analysis of concrete material through gamma ray computerized tomography, *Braz. J. Phys.* **34** (2004) 1020-1023.

[65] Y. Yu; J. Wang, Effect of gamma-ray irradiation on modeling equilibrium moisture content of wheat, *J. Food Sci.* **72** (2007) 405-411.

[66] M. M. Nagadi; A. A. Naqvi, Gamma-ray yield dependence on bulk density and moisture content of a sample of a PGNAA setup: a Monte Carlo study, *J. Radioanal. Nucl. Chem.* **271** (2007) 691-695.

[67] D. Bucurescu; I. Bucurescu, Non-destructive measurement of moisture in building materials by Compton scattering of gamma rays, *Rom. Rep. Phys.* **63** (2011) 61-75.

[68] E. L. Peck, *Boreas Hyd-6 Aircraft Gamma Ray Moisture Data* (Bibliogov, Columbus, 2013).

[69] C. Udagani, Gamma ray attenuation study with varying moisture content of clay brick, *Int. J. Eng. Sci. Invent.* **2** (2013) 35-38.
[70] A. Ahl; K. Motschka; P. Slapansky, Precipitation correction of airborne gamma-ray spectroscopy data using monitoring profiles: methodology and case study, *Expl. Geophys.* **45** (2014) 8-15.
[71] X. P. Maldague, *Theory and Practice of Infrared Technology for Nondestructive Testing* (Wiley, New York, 2001).
[72] N. P. Avdelidis; A. Moropoulou; P. Theoulakis, Detection of water deposits and movement in porous materials by infrared imaging, *Infrared Phys. Technol.* **44** (2004) 183-190.
[73] N. Ludwig; V. Rosina; F. Rosina, Moisture detection in wood and plaster by IR thermography, *Infrared Phys. Technol.* **46** (2004) 161-166.
[74] N. P. Avdelidis; A. Moropoulou, Applications of infrared thermography for the investigation of historic structures, *J. Cult. Herit.* **5** (2004) 119-127.
[75] E. Barreira; V. P. de Freitas, Evaluation of building materials using infrared thermography, *Constr. Build. Mat.* **21** (2007) 218-224.
[76] L. Bitjoka; J.-B. Tchatchueng; D. G. Libouga, Measurement of the moisture content of granulated sugar by infrared transphotometry, *Afr. J. Biotechnol.* **2** (2007) 120-122.
[77] A. Kandemir-Yucel; A. Tavukcuoglu; E. N. Caner-Saltik, *In situ* assessment of structural timber elements of a historic building by infrared thermography and ultrasonic velocity, *Infrared Phys. Technol.* **49** (2007) 243-248.
[78] R. Vasel; G. Kemper; R. Schuhmann; F. Köninger, New airborne thermal infrared photogrammetric applications and sensors for moisture detection, *Int. Arch. Photogramm., Remote Sens. Spat. Inf. Sci.* **37**, part B8 (2008) 17-22.
[79] E. Grinzato; G. Cadelano; P. Bison, Moisture map by IR thermography, *J. Mod. Opt.* **57** (2010) 1770-1778.
[80] M. B. Ormerod, *The Architecture and Properties of Matter* (Edward Arnold, London, 1970).
[81] A. G. Császár; G. Czakó; T. Furtenbacher; J. Tennyson; V. Szalay; S. V. Shirin; N. F. Zobov; O. L. Polansky, On equilibrium structures of the water molecule, *J. Chem. Phys.* **122** (2005) 214305.
[82] D. Eisenberg; W. Kauzmann, *The Structure and Properties of Water* (Oxford University Press, Oxford, 1969).
[83] J. B. Hasted, *Aqueous Dielectrics* (Chapman and Hall, London, 1973).
[84] O. J. Samoilow, *Die Struktur wässriger Elektrolytlösungen und die Hydratation von Ionen* (Teubner, Leipzig, 1961).
[85] E. V. Tsiper, Polarization forces in water deduced from single

molecule data, *Phys. Rev. Lett.* **94** (2005) 013204.
[86] O. Markovitch; N. Agmon, The distribution of acceptor and donor hydrogen-bonds in bulk liquid water, *Mol. Phys.* **106** (2008) 485-495.
[87] N. Agmon, Liquid water: from symmetry distortions to diffusive motion, *Acc. Chem. Res.* **45** (2012) 63-73.
[88] P. Maksyutenko; T. O. Rizzo; O. V. Boyarkin, A direct measurement of the dissociation energy of water, *J. Chem. Phys.* **125** (2006) 181101.
[89] S. J. Suresh; V. M. Naik, Hydrogen bond thermodynamic properties of water from dielectric constant data, *J. Chem. Phys.* **113** (2000) 9727-9732.
[90] P. L. Silvestrelly; M. Parrinello, Structural, electronic, and bonding properties of liquid water from first principles, *J. Chem. Phys*. **111** (1999) 3572-3580.
[91] S. S. Xantheas, Cooperativity and hydrogen bonding network in water clusters, *Chem. Phys.* **258** (2000) 225-231.
[92] W. O. George; B. F. Jones; R. Lewis, Water and its homologues: a comparison of hydrogen-bonding phenomena*, Phil. Trans. R. Soc. Lond. A* **359** (2001) 1611-1629.
[93] K. Stokely; M. G. Mazza; H. E. Stanley; G. Franzese, Effect of hydrogen bond cooperativity on the behavior of water, *Proc. Natl. Acad. Sci. USA* **107** (2010) 1301-1306.
[94] L. Pauling, *The Chemical Bond* (Cornell University Press, Ithaca, 1967).
[95] J. D. Bernal; R. H. Fowler, A theory of water and ionic solution, with particular reference to hydrogen and hydroxyl ions, *J. Chem. Phys.* **1** (1933) 515-548.
[96] J. L. Finney, Bernal and the structure of water, *J. Phys.: Conf. Ser.* **57** (2007) 40-52.
[97] G. S. Kell, Thermodynamic and transport properties of fluid Water, in *Water, a Comprehensive Treatise, Vol. 1,* edited by F. Franks (Plenum, New York, 1972) pp 363-412.
[98] G. S. Kell, Density, thermal expansivity, and compressibility of liquid water from 0 °C tp 150 °C: correlations and tables for atmospheric pressure and saturation reviewed and expressed on 1968 temperature scale, *J. Chem. Eng. Data* **20** (1975) 97-105.
[99] H. Watanabe, Thermal dilatation of water between 0 °C and 44 °C, *Metrologia* **28** (1991) 33-43.
[100] J. B. Patterson; E. C. Morris, Measurement of absolute water density, 1 °C to 40 °C, *Metrologia* **31** (1994) 277-288.
[101] M. Tanaka; G. Girard; R. Davis; A. Peuto; N. Bignell, Recommended

table for the density of water between 0 °C and 40 °C based on recent experimental reports, *Metrologia* **38** (2001) 301-309.
[102] W. C. Röntgen, Über die Constitution des flüssigen Wassers, *Ann. Phys. Chem.* (*Leipzig*) **49** (1892) 91-97.
[103] H. Le Chatelier; O. Boudouard, Limits of flammability of gaseous mixtures, *Bull. Soc. Chim. France* (*Paris*) **19** (1898) 483–488.
[104] P. Atkins; J. de Paula, *Atkins' Physical Chemistry* (Oxford University Press, Oxford, 2010).
[105] W. M. Latimer; W. H. Rodebush, Polarity and ionization from the standpoint of the Lewis theory and valence, *J. Am. Chem. Soc.* **42** (1920) 1419-1433.
[106] J. A. Pople, Molecular association in liquids. I. A theory of the structure of water, *Proc. Roy. Soc. Lond. A* **205** (1951) 163-178.
[107] H. S. Frank, Structural models, in *Water, a Comprehensive Treatise, Vol. 1,* edited by F. Franks (Plenum, New York, 1972) pp 515-543.
[108] H. S. Frank; A. S. Quist, Pauling's model and the thermodynamic properties of water, *J. Chem. Phys. 34* (1961) 604-611.
[109] M. D. Danford; H. A. Levy, The structure of water at room temperature, *J. Am. Chem. Soc.* **84** (1962) 3965-3966.
[110] O. Y. Samoilow, *Structure of Aqueous Electrolyte Solutions and the Hydration of Ions*, translated by D. J. G. Ives (Consultants Bureau, New York, 1965).
[111] R. H. Henchman; S. J. Irudayam, Topological hydrogen-bond definition to characterize the structure and dynamics of liquid water, *J. Phys. Chem. B* **114**, (2010) 16792.
[112] M. C. R. Symons, Water structure: unique but not anomalous, *Phil. Trans. R. Soc. Lond. A* **359** (2001) 1631-1646.
[113] J. L. Finney, Water? What's so special about it? *Phil. Trans. R. Soc. Lond. B* **359** (2004) 1145-1165.
[114] A. Ben-Naim, *Molecular Theory of Water and Aqueous Solutions: Part I: Understanding Water* (World Scientific, Singapore, 2010).
[115] A. Nilsson; L. G. M. Pettersson, Perspective on the structure of liquid water, *Chem. Phys.* **389** (2011) 1-34.
[116] F. Sciortino; A. Geiger; H. E. Stanley, Network defects and the mobility in liquid water, *J. Chem. Phys.* **96**, (1992) 3857-3865.
[117] C. Knight; G. A. Voth, The curious case of the hydrated proton, *Acc. Chem. Res.* **45** (2012) 101-109.
[118] O. Markovitch; H. Chen; S. Izvekov; F. Paesani; G. A. Voth; N. Agmon, Special pair dance and partner selection: elementary steps in proton transport in liquid water, *J. Phys. Chem. B* **112** (2008) 9456-9466.
[119] B. Kirchner, Eigen or Zundel ion: news from calculated and

experimental photoelectron spectroscopy, *Chem. Phys. Chem.* **8** (2007) 41-43.

[120] M. Holz; S. R. Heil; A. Sacco, Temperature-dependent self-diffusion coefficients of water and six selected molecular liquids for calibration in accurate ^{1}H NMR PFG measurements, *Phys. Chem. Chem. Phys.* **2** (2000) 4740-4742.

[121] A. Chernyshev; R. Pomès; S. Cuikerman, Kinetic isotope effects of proton transfer in aqueous and methanol containing solutions, and in gramicidine A channels, *Biophys. Chem.* **103** (2003) 179-190.

[122] S. Cuikerman, Et tu, Grotthuss! And other unfinished stories, *Biochim. Biophys. Acta* **1757** (2006) 876-885.

[123] C. J. T. Grotthuss, Sur la décomposition de l'eau et des corps q'elle tient en dissolution à l'aide de l'électricité galvanique, *Ann. Chim. (Paris)* **58** (1806) 54-74.

[124] N. Agmon, The Grotthuss mechanism, *Chem. Phys. Lett.* **244** (1995) 456-462.

[125] E. Wicke; M. Eigen; T. Ackermann, Über den Zustand des Protons (Hydroniumions) in wäßriger Lösung, *Z. Phys. Chem. NF* **1** (1954) 340-346.

[126] M. Eigen, Proton transfer, acid-base catalysis, and enzymatic hydrolysis. Part I. Elementary processes, *Angew. Chem. Int. Ed. Engl.* **3** (1964) 1-19.

[127] G. Zundel; H. Metzger, Energiebänder der tunnelnden Überschuß-Protonen in flüssigen Säuren. Eine IR-spectroskopische Untersuchung der Natur der Gruppierungen $H_5O_2^+$, *Z. Phys. Chem. NF* **58** (1968) 225-245.

[128] G. Zundel, Easily polarizable hydrogen bonds – their interactions with the environment – IR continuum and anomalous large conductivity, in *The Hydrogen Bond – Recent Developments in Theory and Experiments*, *Vol. 2*, edited by P. Schuster; G. Zundel; C. Sandorfy (North-Holland, Amsterdam, 1976) pp 683-766.

[129] S. H. Lee; J. C. Rasaiah, Local dynamics and structure of the solvated hydroxide ion in water, *Mol. Simul.* **36** (2010) 69-73.

[130] B. Winter, F. Faubel, I. V. Hertel, C. Pettenkofer, S. E. Bradforth, B. Jagoda-Cwiklik, L. Cwiklik, P. Jungwirth, Electron binding energie of hydrated H_3O^+ and OH^-: photoelectron spectroscopy of aqueous acid and base solutions combined with electronic structure calculations, *J. Am. Chem. Soc.* **128** (2006) 3864-3865.

[131] A. Chandra; M. E. Tuckerman; D. Marx, Connecting solvation shell structure to proton transport kinetics in hydrogen-bonded networks via population correlation functions, *Phys. Rev. Lett.* **99**

(2007) 145901.
[132] T. C. Berkelbach; H.-S. Lee; M. E. Tuckerman, Concerted hydrogen-bond dynamics in the transport mechanism of the hydrated proton: a first principles molecular dynamics study, *Phys. Rev. Lett.* **103** (2009) 238302.
[133] H. Lapid; N. Agmon, M. K. Petersen; G. A. Voth, A bond-order analysis of the mechanism for the hydrated proton mobility in liquid water, *J. Chem. Phys.* **122** (2005) 014506.
[134] H. Chen; G. A. Voth; N. Agmon, Kinetics of proton migration in liquid water, *J. Phys. Chem. B* **114** (2010) 333-339.
[135] D. A. Lown; H. R. Thirsk, Proton transfer conductance in aqueous solution. Part 1. Conductance of concentrated aqueous alkali metal hydroxide solutions at elevated temperatures and pressures, *Trans. Faraday Soc.* **67** (1971) 132-148.
[136] P. L. Silvestrelli; M. Parrinello, Water molecule dipole in the gas and in the liquid phase, *Phys. Rev. Lett.* **82** (1999) 3308-3311.
[137] U. Kaatze, Complex permittivity of water as a function of frequency and temperature, *J. Chem. Eng. Data* **34** (1989) 371-374.
[138] R. Pottel, Dielektrische Relaxation und molekulare Relaxationszeit, in *Sommerschule Physik des flüssigen Zustands, Vol. 3*, edited by F. Kohler; P. Weinzierl (MPI Kohleforschung, Mühlheim, 1977) pp 183-201.
[139] D. Kivelson; P. Madden, Theory of dielectric relaxation, *Mol. Phys.* **30** (1975) 1749-1780.
[140] J. G. Kirkwood, The dielectric polarization of polar liquids, *J. Chem. Phys.* **7** (1939) 911-919.
[141] A. Volmari; H. Weingärtner, Cross terms and Kirkwood factors in dielectric relaxation of pure liquids, *J. Mol. Liq.* **98-99** (2002) 293-301.
[142] U. Kaatze; R. Behrends; R. Pottel, Hydrogen network fluctuations and dielectric spectrometry of liquids, *J. Non-Cryst. Solids* **305** (2001) 19-28.
[143] M. N. Afsar; J. B. Hasted, Measurement of the optical constant of liquid H_2O and D_2O between 6 and 450 cm^{-1}, *J. Opt. Soc. Am.* **67** (1977) 902-904.
[144] M. G. M. Richards, *The Development of Techniques to Measure the Complex Permittivity of Liquids and Biological Tissues at 90 GHz*, Thesis (King's College London, London, 1993).
[145] W. J. Ellison; K. Lamkaouchi; J. M. Moreau, Water, a dielectric reference, *J. Mol. Liq.* **68** (1996) 171-279.
[146] C. Rønne; L. Thrane; P.-O. Åstrand; A. Wallqvist, K. V. Mikkelsen;

S. Keiding, Investigation of the temperature dependence of dielectric relaxation in liquid water by THz reflection spectroscopy and molecular dynamics simulation, *J. Chem. Phys.***107** (1997) 5319-5331.

[147] P. Petong; R. Pottel; U. Kaatze, Dielectric relaxation of H-bonded liquids. Mixtures of ethanol and *n*-hexanol at different compositions and temperatures, *J. Phys. Chem. A* **103** (1999) 6114-6121.

[148] K. Nörtemann; J. Hilland; U. Kaatze, Dielectric properties of aqueous NaCl solutions at microwave frequencies, *J. Phys. Chem A* **101** (1997) 6864-6869.

[149] U. Kaatze, Techniques for measuring the microwave dielectric properties of materials, *Metrologia* **47** (2010) S91-S113.

[150] U. Kaatze, Measuring the dielectric properties of materials. Ninty-year development from low-frequency techniques to broadband spectroscopy and high-frequency imaging, *Meas. Sci. Technol.* **24** (2013) 012005.

[151] S. Mashimao; R. Nozaki; S. Yagihara; S. Takeishi, Dielectric relaxation of poly(vinyl acetate), *J. Chem. Phys.* **77** (1982) 6259-6262.

[152] R. Nozaki; S. Mashimo, Dielectric relaxation measurements of poly(vinyl acaetate) in glassy state in the frequency range 10^{-6} – 10^{6} Hz, *J. Chem. Phys.* **87** (1987) 2271-2277.

[153] R. Brand; P. Lunkenheimer; A. Loidl, Relaxation dynamics in plastic crystals, *J. Chem. Phys.* **116** (2002) 10386-10401.

[154] F. Kremer, Dielectric spectroscopy – yesterday, today and tomorrow, *J. Non-Cryst. Solids* **305** (2002) 1-9.

[155] H. G. Roskos, Overview on time-domain terahertz spectroscopy and its applications in atomic and semiconductor physics, *Physica Scripta* **T86** (2000) 51-54.

[156] M. C. Beard; G. M. Turner; C. A. Schmuttenmaer, Terahertz spectroscopy, *J. Phys. Chem. B* **106** (2002) 7146-7159.

[157] C. Rønne; S. R. Keiding, Low frequency spectroscopy of liquid water using THz-time domain spectroscopy, *J. Mol. Liq.* **101** (2002) 199-218.

[158] M. L. T. Asaki; A. Redondo; T. A. Zawodzinski; A. J. Taylor, Dielectric relaxation of electrolyte solutions using terahertz transmission spectroscopy, *J. Chem. Phys.* **116** (2002) 8469-8482.

[159] C. A. Schmuttenmaer, Exploring dynamics in the far-infrared with terahertz spectroscopy, *Chem. Rev.* **104** (2004) 1759-1779.

[160] S. Watanabe; R. Shimano , Compact terahertz time domain

spectroscopy system with diffraction-limited spatial resolution, *Rev. Sci. Instrum.* **78** (2007) 103906.
[161] S. L. Dexheimer S L (ed) *Terahertz Spectroscopy: Principles and Applications* (CRC Press, Boca Raton, 2008).
[162] K.-E. Peiponen; A. Zeitler; M. Kuwata-Gonokami (eds) *Terahertz Spectroscopy and Imaging* (Springer, Berlin, 2012).
[163] S. Grimmes; Ø. G. Martinson, *Bioimpedance and Bioelectricity* (Academic, New York, 2000).
[164] R. Buchner; J. Barthel, Dielectric relaxation in solutions, *Ann. Rep. Prog. Chem. C* **97** (2001) 349-382.
[165] Y. Feldman; T. Skodvin; J. Sjöblom, Dielectric spectroscopy on emulsions and related colloidal systems – a review, in *Encyclopedic Handbook of Emulsion Technology*, edited by J. Sjöblom (Dekker, New York, 2001) pp 109-168.
[166] G. G. Raju, *Dielectrics in Electric Fields* (Marcel Dekker, New York, 2003).
[167] F. Kremer; A. Schönhals, *Broadband Dielectric Spectroscopy* (Springer, Berlin, 2003).
[168] Y. Feldman; A. Puzenko; Y. Ryabov, Dielectric relaxation phenomena in complex materials, in *Fractals, Diffusion and Relaxation in Disordered Complex Systems*, edited by Y. Kalmykov; W. T. Coffey; S. A. Rice (Wiley, New York, 2006) pp 1-125.
[169] H. P. Schwan; R. J. Sheppard; E. H. Grant, Complex permittivity of water at 25 °C, *J. Chem. Phys.* **64** (1976) 2257-2258.
[170] W. J. Ellison, Permittivity of pure water, at standard atmospheric pressure, over the frequency range 0-25 THz and temperature range 0-100 °C, *J. Phys. Chem. Ref. Data* **36** (2007) 1-18.
[171] S. Sharma; A. Kumar; D. Kaur, Cavity perturbation measurement of complex permittivity of dielectric material at microwave frequencies, *Int. J. Emerg. Technol. Comput. Appl. Sci.* **13-119** (2013) 116-120.
[172] N. M. Afsar; A. Bellemans; J. R. Birch; G. W. Chantry; R. N. Clarke; R. J. Cook; R. Finsey; O. Göttmann; J. Goulon; R. G. Jones; U. Kaatze; E. Kestemont; H. Kilp; M. Mandel; R. Pottel; J.-L. Rivail; C. B. Rosenberg; R. van Loon, A comparison of dielectric measurement methods for liquids in the frequency range 1 GHz to 4 THz, *IEEE Trans. Instrum. Meas.* **29** (1980) 283-288.
[173] M. Stråål; I. Chmutin; A. Boldizar, Dielectric properties of polyethylene foams at medium and high frequencies, *Ann. Trans. Nordic Rheol. Soc*. 1**8** (2010) 107-116.
[174] E. Meyer; R. Pottel, *Physikalische Grundlagen der*

Hochfrequenztechnik (Vieweg, Braunschweig, 1969).
[175] A. H. Price; G. H. Wegdam, Dielectric spectroscopy at microwave frequencies, *J. Phys. E : Sci. Instrum.* **10** (1977) 178-181.
[176] O. Göttmann; A. Dittrich, A broad-band measuring equipment for determining the complex permittivity of liquid dielectric materials within the frequency range of 1 MHz to 1 GHz, *J. Phys. E: Sci. Instrum.* **17** (1984) 772-772.
[177] M. A. Tsankov, Permittivity measurement of a thin slab centrally located in a rectangular waveguide, *J. Phys. E: Sci. Instrum.* **8** (1975) 963-966.
[178] G. Nimtz ; R. Dornhaus ; M. Schifferdecker; I. Shih; E. Tyssen, Dielectric properties of multilayers of solids and liquids at microwave frequencies, *J. Phys. E: Sci. Instrum.* **11** (1978) 1109-1112.
[179] S. Swarnowski, A transmission line cell for measuring the permittivity of liquids over the frequency range 90 MHz to 2 GHz, *J. Phys. E: Sci. Instrum.* **15** (1982) 1068-1072.
[180] H. A. Buckmaster; C. H. Hansen; T. H. T. van Kalleveen, Design optimization of a high precision microwave complex permittivity instrumentation system for use with high loss liquids, *IEEE Trans. Instrum. Meas.* **39** (1990) 964-968.
[181] U. Kaatze U; R. Pottel; A. Wallusch, A new automated waveguide system for the precise measurement of complex permittivity of low-to-high-loss liquids at microwave frequencies, *Meas. Sci. Technol.* **6** (1995) 1201-1207.
[182] S. Roberts; A. von Hippel, A new method for measuring dielectric constant and loss in the range of centimeter waves, *J. Appl. Phys.* **17** (1946) 610-616.
[183] M. Rodríguez-Vidal; E. Martín; M. Sancho, Microwave permittivity measurement using a multipoint technique, *IEEE Trans. Microw. Theory Techn.* **22** (1974) 542-544.
[184] E. Fatuzzo; P. R. Mason, Precision measurement of the microwave dielectric constant of liquids, *J. Appl. Phys.* **36** (1965) 427-435.
[185] A. Göllei; A. Vass; E. Pallei; M. Gerzson; L. Ludányi; J. Mink, Apparatus and method to measure dielectric properties (ε' and ε'') of ionic liquids, *Rev. Sci. Instrum.* **80** (2009) 044703.
[186] I. J. Bahl; H. M. Gupta, Microwave measurement of dielectric constant of liquids and solids using partially loaded slotted waveguide, *IEEE Trans. Microw. Theory Techn.* **22** (1974) 52-54.
[187] T. S. Natarajan; U. M. S. Murthy U M S; J. Sobhanadri, Microprocessor-based microwave dielectric measurement of

liquids by waveguide plunger technique, *IEEE Trans. Instrum. Meas.* **34** (1985) 643-646.

[188] J. M. Alison; R. J. Sheppard, A precision waveguide system for the measurement of complex permittivity of lossy liquids and solid tissues in the frequency range 29 GHz to 90 GHz – I. The liquid system for 29 to 45 GHz; an investigation into water, *Meas. Sci. Technol.* **1** (1990) 1093-1098.

[189] M. G. M. Richards; R. J. Sheppard, A precision waveguide system for the measurement of complex permittivity of lossy liquids and solid tissues in the frequency range 29 GHz to 90 GHz – II. The liquid system for 90 GHz; high-frequency cell design, *Meas. Sci. Technol.* **2** (1991) 663-667.

[190] T. J. Buchanan, Balance methods for the measurement of permittivity in the microwave region, *Proc. IEE, Part III*, **99** (1952) 61-66.

[191] R. Pottel, Die komplexe Dielektrizitätskonstante wäßriger Lösungen einiger 2:2-wertiger Elektrolyte im Frequenzbereich 0.1 bis 38 GHz, *Ber. Bunsenges. Phys. Chem.* **69** (1965) 363-378.

[192] U. Kaatze; K. Giese, Dielectric spectroscopy on some aqueous solutions of 3:2 valent electrolytes. A combined frequency and time domain study, *J. Mol. Liq.* **36** (1987) 15-35.

[193] H. A. Buckmaster; C. H. Hansen; T. H. T. van Kalleveen, Design optimization of a high precision microwave complex permittivity instrumentation system for use with high loss liquids, *IEEE Trans. Instrum. Meas.* **39** (1990) 964-968.

[194] U. Kaatze; Y. Feldman, Broadband dielectric spectroscopy of liquids and biosystems, *Meas. Sci. Technol.* **17** (2006) R17-R35.

[195] N. Marcuvitz, *Waveguide Handbook* (McGraw-Hill, New York, 1951).

[196] A. M. Bottreau; Y. Dutuit; C. Marzat; J. Moreau, Réalisation d'un réflecto-interféromètre dans la bande des 70 GHz destiné à la mesure de la permittivité complexe de liquides à fortes pertes. Application a l'étude de l'eau, de l'éthylène-glycol et du formamide en function de la température*, Rev. Phys. Appl.* **11** (1976) 163-166.

[197] R. Van Loon; R. Finsy, Measurement of complex permittivity of liquid at frequencies from 60 t0 150 GHz, *Rev. Sci. Instrum.* **45** (1974) 523-525.

[198] W. M. Heston Jr.; A. D. Franklin; E. J. Hennelly; C. P. Smyth, Microwave adsorption and molecular structure in liquids. V. Measurement of the dielectric constant and loss of low-loss solutions, *J. Am. Chem. Soc.* **72** (1950) 3442-3447.

[199] T. J. Buchanan; E. H. Grant, Phase and amplitude balance methods for permittivity measurements between 4 and 50 cm, *Br. J. Appl. Phys.* **6** (1955) 64-66.

[200] G. Williams, The measurement of dielectric constant and loss factor of liquids and solutions between 250 and 920 Mc/s by means of a coaxial transmission line, *J. Phys. Chem.* **63** (1959) 534-537.

[201] E. H.Grant, Method for measuring the complex dielectric constant of a high-loss liquid at 8 mm wavelength, *Br. J. Appl. Phys.* **10** (1959) 87-89.

[202] E. H. Grant; S. E. Keefe, Standing wave methods for measuring permittivities at meter and decimeter wavelength, *Rev. Sci. Instrum.* **12** (1968) 1800-1803.

[203] R. J. Sheppard, An automated coaxial line system for determining the permittivity of a liquid, *J. Phys. D: Appl. Phys.* **5** (1972) 1576-1587.

[204] E. A. S. Cavell; P. M. Horton, The automated acquisition of dielectric dispersion data, *J. Phys. E: Sci. Instrum*. **6** (1973) 516-516.

[205] H. A. Kołodziej; M. Pajdowska; L. Sobczyk, Lumped-capacitance method applied to measurements of complex dielectric permittivity in polar liquids from 100 MHz to 3 GHz, *J. Phys. E: Sci. Instrum.* **11** (1978) 752-754.

[206] O. S. Josyulu; J. Gowri Krishna; J. Sobhanadri, A method for the evaluation of dielectric parameters of solids at microwave frequencies, *J. Phys. E: Sci. Instrum.* **15** (1982) 318-321.

[207] J. Hilland, Simple sensor system for measuring the dielectric properties of saline solutions, *Meas. Sci. Technol.* **8** (1997) 901-910.

[208] B. L. McLaughlin; P. A. Robertson, Miniature open-ended coaxial probes for dielectric spectroscopy applications, *J. Phys. D: Appl. Phys.* **40** (2007) 45-53.

[209] E. C. Burnette; F. L. Cain; J. Seals, *In vivo* probe measurement technique for determining dielectric properties at VHF through microwave frequencies, *IEEE Trans. Microw. Theory Tech.* **28** (1980) 414-427.

[210] M. A. Stuchly; T. W. Athey; S. S. Stuchly; G. M. Samaras; G. Taylor, Dielectric properties of animal tissues *in vivo* at frequencies 10 MHz – 1 GHz, *Bioelectromagn*. **2** (1981) 93-103.

[211] C. Gabriel; E. H. Grant; I. R. Young, Use of time domain spectroscopy for measuring dielectric properties with a coaxial probe, *J. Phys. E: Sci. Instrum.* **19** (1986) 843-846.

[212] J. P. Grant; R. N. Clarke; G. T. Symm; N. M. Spyrou, A critical study of the open-ended coaxial line sensor technique for RF and

microwave complex permittivity measurements, *J. Phys. E: Sci. Instrum.* **22** (1989) 757-770.

[213] D. Misra; M. Chabbra; B. R. Epstein; M. Microtznik: K. R. Foster, Noninvasive electrical characterization of materials at microwave frequencies using an open-ended coaxial line: test of improved calibration technique, *IEEE Trans. Microw. Theory Tech.* **38** (1990) 8-14.

[214] S. Jenkins; T. E. Hodgetts; R. N. Clarke; A. W. Preece, Dielectric measurements on reference liquids using automated network analysers and calculable geometries, *Meas. Sci. Technol.* **1** (1990) 691-702.

[215] S. Jenkins; A. G. P. Warham; R. N. Clarke, Use of open-ended coaxial line sensor with a laminar or liquid dielectric backed by a conducting plane, *IEE Proc.* H **139** (1992) 179-182.

[216] P. De Langhe; K. Blome; L. Martens; D. De Zutter, Measurement of low-permittivity materials based on a spectral-domain analysis for the open-ended coaxial probe, *IEEE Trans. Instrum. Meas.* **42** (1993) 879-886.

[217] J. M. Moreau; R. Aziz, Dielectric study of granular media according to the type of measurement device: coaxial cell or open-ended probe, *Meas. Sci. Technol.* **4** (1993) 124-129.

[218] J. Baker-Jarvis; M. D. Janezic; P. D. Domich; R. G. Geyer, Analysis of an open-ended coaxial probe with lift-off for non-destructive testing, *IEEE Trans. Instrum. Meas.* **43** (1994) 711-718.

[219] C. Gabriel; T. Y. A. Chan; E. H. Grant, Admittance models for open ended coaxial probes and their place in dielectric spectroscopy, *Phys. Med. Biol.* **39** (1994) 2183-2200.

[220] V. Raicu, A simple theoretical and practical approach to measuring dielectric properties with an open-ended coaxial probe, *Meas. Sci. Technol.* **6** (1995) 410-414.

[221] D. V. Blackham; R. D. Pollard, An improved technique for permittivity measurement using coaxial probes, *IEEE Trans. Instrum. Meas.* **46** (1997) 1093-1099.

[222] C. L. Pounaropoulos; D. K. Misra, The co-axial aperture electromagnetic sensor and its application in material characterization, *Meas. Sci. Technol.* **8** (1997) 1191-1202.

[223] J. Hilland; T. Friisø, Evaluation of modelling routines for on-line implementation of the open-ended coaxial probe, *Meas. Sci. Technol.* **9** (1998) 790-796.

[224] M. Wu; X. Yao; L. Zhang, An improved coaxial probe technique for measuring microwave permittivity of thin dielectric materials,

Meas. Sci. Technol. **11** (2000) 1617-1622.
[225] R. Olmi; M. Bini; A. Igneti; C. Riminesi, Non-destructive permittivity measurement of solid materials, *Meas. Sci. Technol.* **11** (2000) 1623-1629.
[226] D. Propovic; L. McCartney; C. Beasley; M. Lazebnik; M. Oboniewski; S. C. Hagness; J. Booske, Precision open-ended coaxial probes for *in vivo* and *ex vivo* dielectric spectroscopy of biological tissues at microwave frequencies, *IEEE Trans. Microw. Theory Tech.* **53** (2005) 1713-1722.
[227] B. García-Baños; J. M. Calatá-Civera; A. J. Canós; F. Peñaranda-Foix, Design rules for the optimizatioin of the sensitivity of open-ended coaxial microwave sensors for monitoring changes in dielectric materials, *Meas. Sci. Technol.* **16** (2005) 1186-1192.
[228] I. K. Ivanov; A. O. Silin; A. M. Stadnik, Determination of dielectric permittivity of materials by an isolated coaxial probe, *Radioelectron. Commun. Syst.* **50** (2007) 367-374.
[229] A. P. Gregory; R. N. Clarke, Dielectric metrology with coaxial sensors, *Meas. Sci. Technol.* **18** (2007) 1372-1386.
[230] H. Cachet; J.-C. Lestrade; J. Epelboïn, Measure de la permittivité diélectrique de liquides en ondes décimétriques, *J. Chim. Phys.* **62** (1965) 802-810.
[231] R. H. Cole; J. G. Berberian; S. Mashimo; G. Chryssikos; A. Burns; E. Tombari, Time domain reflection methods for dielectric measurements to 10 GHz, *J. Appl. Phys.* **66** (1989) 793-802.
[232] K. Folgerø; T. Frisø; J. Hilland; T. Tjomsland, A broadband and high-sensitive dielectric spectroscopy measurement system for quality determination of low-permittivity fluids, *Meas. Sci. Technol.* **6** (1995) 995-1008.
[233] O. Göttmann; U. Kaatze; P. Petong, Coaxial to circular waveguide transition as high-precision easy-to-handle measuring cell for broadband dielectric spectroscopy of liquids, *Meas. Sci. Technol.* **7** (1996) 525-534.
[234] S. van Damme; A. Franchois; D. de Zutter; L. Taerwe, Nondestructive determination of the steel fiber content in concrete slabs with open-ended coaxial probe *IEEE Trans. Geosci. Remote Sens.* **42** (2004) 2511-2521.
[235] J. S. Avestas, Radiation of coaxial line into half-space, *IEEE Trans. Antennas Propag.* **54** (2006) 1624-1631.
[236] K. Folgerø; T. Tjomsland, Permittivity measurement of thin layers using open-ended coaxial line probes, *Meas. Sci. Technol.* **7** (1996) 1164-1173.

[237] S. Evans; S. C. Michelson, Intercomparison of dielectric reference materials available for calibration of an open-ended probe at different temperatures, *Meas. Sci. Technol.* **6** (1995) 1721-1732.
[238] K. Folgerø, Bilinear calibration of coaxial transmission/reflection cells for permittivity measurements of low-loss liquids, *Meas. Sci. Technol.* **7** (1996) 1260-1269.
[239] T. Jakobsen; K. Folgerø, Dielectric measurements of gas hydrate formation in water-in-oil emulsions using open-ended coaxial probes, *Meas. Sci. Technol.* **8** (1997) 1006-1015.
[240] S. B. Lee; R. L. Smith, Jr.; H. Inomata; K. Arai, Coaxial probe and apparatus for measuring the dielectric spectra of high pressure liquids and supercritical fluid mixtures, *Rev. Sci. Instrum.* **71** (2000) 4226-4230.
[241] G. A. Dimitrakis; M. George; M. Poliakoff; I. Harrison; J. Robinson; S. Klingman; E. Lester; A. P. Gregory; K. Lees, A system for traceable measurement of the microwave complex permittivity of liquids at high pressures and temperatures, *Meas. Sci. Technol.* **20** (2009) 045901.
[242] R. Pottel; E. Asselborn, Measurements for determining the dielectric relaxation rate of water and of an aqueous solution at high pressures, *Ber. Bunsenges. Phys. Chem.* **93** (1979) 29-34.
[243] R. Pottel ; E. Asselborn; R. Eck ; V. Tresp, Dielectric relaxation rate and static dielectric permittivity of water and aqueous solutions at high pressures, *Ber. Bunsenges. Phys. Chem.* **83** (1989) 676-681.
[244] K. Okada ; Y. Imashuku ; M. Yao, Microwave spectroscopy of supercritical water, *J. Chem Phys.* **107** (1997) 9302-9311.
[245] R. H. Dicke, A computational method applicable to microwave networks, *J. Appl. Phys.* **18** (1947) 873-878.
[246] R. Mavaddat, *Network Scattering Parameter* (World Scientific, Singapore, 1996).
[247] D. M. Pozar, *Microwave Engineering* (Wiley, Hoboken, 2012).
[248] S. S. Stuchly; M. Matuszewski, A combined total reflection-transmission method in application to dielectric spectroscopy, *IEEE Trans. Instrum. Meas.* **27** (1978) 285-288.
[249] J. Baker-Jarvis; E. J. Vanzura; W. A. Kissick, Improved technique for determining complex permittivity with the transmission/reflection method, *IEEE Trans. Microw. Theory Tech.* **30** (1990) 1096-1103.
[250] D. Vincent; L. Jorat; J. Monin; G. Noyel, Improvement of the transmission/reflection method for dielectric and magnetic measurements on liquids between 0.1 and 20 GHz, *Meas. Sci. Technol.* **5** (1994) 990-995.

[251] K.-H. Baek; H.-Y. Sung; W. S. Park, A 3-position transmission/ reflection method for measuring the permittivity of low loss materials, *IEEE Microw. Guided Wave Lett.* **5** (1995) 3-5.
[252] A. Kozhevnikov, Wideband radio-frequency device for measurements of dielectric properties of small volumes of liquids, *Meas. Sci. Technol.* **21** (2010) 043001.
[253] M. Opalinski, S. Manus, M. George, A. Brüggemann, N. Fertig, F. C. Simmel, Detection of lipid bilayer and peptide pore formation at gigahertz frequencies, *Appl. Phys. Lett.* **88** (2006) 013902.
[254] C. Song, P. Wang, A radio frequency device for measurement of minute dielectric property changes in microfluidic channels, *Appl. Phys. Lett.* **94** (2009) 023901.
[255] K. Grenier, D. Dubuc, P.-E. Poleni, M. Komemura, H. Toshiyoshi, T. Fujii, H. Fujita, Integrated broadband and microfluidic sensor dedicated to bioengineering, *IEEE Trans. Microw. Theory Tech.* **57** (2009) 3246-3253.
[256] J. C. Booth, N. D. Orloff, J. Mateu, M. Janezic, M. Rinehart, J. A. Beall, Quantitative permittivity measurements of nanoliter liquid volumes in microfluidic channels to 40 GHz, *IEEE Trans. Instrum. Meas.* **59** (2010) 3279-3288.
[257] M. Giraud-Carrier, K. Moon, E. Teng, A. R. Hawkins, K. F. Warnick, B. A. Mazzeo, Broadband RF impedance spectroscopy in micromachined microfluidic channels, in *Proc. 33rd Ann. Intern. Conf. IEEE EMBS* (IEEE, Boston, MA, 2011).
[258] J. Shao, Dual-Band Microwave Components and Their Applications, Master Thesis (University of NorthTexas, Denton, TX, 2011).
[259] T. Chen, D. Dubuc, M. Poupot, J.-J. Fournié, K. Grenier, Accurate nanoliter liquid characterization up to 40 GHz for biomedical applications: Toward noninvasive living cells monitoring, *IEEE Trans. Microw. Theory Tech.* **60** (2012) 4171-4177.
[260] T. Chretiennot, D. Dubuc, K. Grenier, A microwave and microfluidic planar resonator for efficient and accurate complex permittivity characterization of aqueous solutions, *IEEE Trans. Microw. Theory Tech.* **61** (2013) 972-978.
[261] S. S. Stuchly, C. E. Bassey, Microwave coplanar sensors for dielectric measurements, *Meas. Sci, Technol.* **9** (1998) 1324-1329.
[262] K. Greiner, D. Dubuc, T. Chen, F. Artis, T. Chretiennot, M. Poupot, J.-J. Fournié, Recent advances in microwave-based dielectric spectroscopy at the cellutar level, *IEEE Trans. Microw.Theory Tech.* **61** (2013) 2023-2030.
[263] B. S. Blankenagel, S. Khadka, A. R. Hawkins, K. F. Warnick,

B. A. Mazzeo, Radio-frequency microfluidic interferometer in printed circuit board process, *Microw. Opt. Technol. Lett*. **55** (2013) 1616-1618.

[264] C. D. Gupta, Microwave measurement of a complex dielectric constant over a wide range of values by means of a waveguide-resonator method, *IEEE Trans. Microw. Teory Tech.* **22** (1974) 365-372.

[265] K. Hallenga, New method for very sensitive dielectric difference measurements on high-loss liquids at microwave frequencies, *Rev. Sci. Instrum.* **46** (1975) 1691-1696.

[266] G. Birnbaum; J. Franeau, Measurement of the dielectric constant and loss of solids and liquids by a cavity perturbation method, *J. Appl. Phys.***20** (1949) 817-818.

[267] H. B. G. Casimir, On the theory of electromagnetic waves in resonant cavities, *Philips Res. Rep.* **6** (1951) 162-182.

[268] A. Bonicontro; C. Cametti, On the applicability of the cavity perturbation method to high-loss dielectrics, *J. Phys. E: Sci. Instrum.* **10** (1977) 1232-1233.

[269] A. W. Kraszewski; S. O. Nelson, Contactless mass determination of arbitrarily shaped dielectric objects, *Meas. Sci. Technol.* 6 (1995) 1598-1604.

[270] L. Chen; C. K. Ong; B. T. G. Tan, A resonant cavity for high-accuracy measurement of microwave dielectric properties, *Meas. Sci. Technol.* **7** (1996) 1255-1259.

[271] D. A. Stone; M. P. Robinson, Total body water measurements using resonant cavity perturbation techniques, *Phys. Med. Biol.* **49** (2004) 1773-1788.

[272] A. Nesbitt; P. Navabpour; B. Degamber; C. Nightingale; T. Mann; G. Fernamdo; R. J. Day, Developent of a microwave calorimeter for simultaneous thermal analysis, infrared spectroscopy and dielectric measurements, *Meas. Sci. Technol.* **15** (2004) 2313-2324.

[273] M. P. Robinson; I. D. Flintoft; L. Dawson; J. Clegg; J. G. Truscott; X. Zhu, Application of resonant cavity perturbation to *in vivo* segmental hydration measurement, *Meas. Sci. Technol.* **21** (2010) 015804.

[274] F. Horner; T. A. Taylor; R. Duinsmuir; J. Lamb; W. Jackson, Resonance methods of dielectric measurement at centimeter wavelength, *J. IEEE* **93** (1946) 53-68.

[275] G. Roussy; M. Felden, A sensitive method for measuring complex permittivity with a microwave resonator, *IEEE Microw. Theory Tech.***14** (1966) 171-175.

[276] A. Parkash; J. K. Vaid; A. Mansingh, Modified relations for evaluation of dielectric parameters in cylindrical cavities operating in E_{010} mode, *J. Phys. E: Sci. Instrum*. **12** (1979) 308-310.
[277] C. G. Montgomery; R. H. Dicke; E. M. Purcell, *Principles of Microwave Circuits* (McGraw-Hill, New York, 1948).
[278] D. J. Rowe; A. Porch; D. A. Barrow; C. J. Allender, Integrated microwave resonant device for dielectric analysis of microfluidic systems, *J. Phys.: Conf. Ser.* **310** (2011) 012004.
[279] D. J. Rowe; A. Porch; D. A. Barrow; C. J. Allender, Microfluidic device for compositional analysis of solvent systems at microwave frequencies, *Sens. Actuators B: Chem.* **169** (2012) 213-221.
[280] D. J. Rowe; A. Porch; D. A. Barrow; C. J. Allender, Microfluidic microwave sensor for simultaneous dielectric and magnetic characterization, *IEEE Microw. Theory Tech.* **61** (2013) 234-243.
[281] E. M. Ganapolskii; A. V. Golik, A sapphire sphere resonator for the measurement of low dielectric losses in the milimetre-wave range in liquids, *Meas. Sci. Technol.* **8** (1997) 1016-1022.
[282] A. Annino; D. Bertolini; M. Cassettari; M. Fittipaldi; I. Longo; M. Martinelli; Dielectric properties of materials using whispering gallery dielectric resonators: Experiments and perspectives of ultra-wideband characterization, *J. Chem. Phys.* **112** (2000) 2308-2314.
[283] Z. E. Eremenko; E. M. Ganapolskii; V. V. Vasilchenko, Exact-calculated resonator method for permittivity measurement of high loss liquids at millimeter wavelength, *Meas. Sci. Technol.* **16** (2005) 1619-1627.
[284] A. I. Gubin; A. A. Barannik; N. T. Cherpak; S. Vitusevich; A. Offenhaeusser; N. Klein, Whispering-gallary mode resonator technique for characterization of small volumes of biochemical liquids in microfluidic channel, in *41st Europ. Microw. Conf. 2011, Manchester* (IEEE, New York, 2012) pp 615-618.
[285] M. Nehat; H. Chen; S. Gigoyan; D. Saeedkia; S. Safavi-Naeini, Whispering-gallary-mode resonance sensor for dielectric sensing of drug tablets, *Meas. Sci. Technol.* **21** (2010) 015202.
[286] F. Eggers, Analysis of phase slope or group delay time in ultrasonic resonators and its application for liquid absorption and velocity measurements, *Acustica* **80** (1994) 397-405.
[287] S. K. Garg; H. Kilp; C. P. Smyth, Microwave absorption and molecular structure in liquids. LXV. A precise Michelson interferometer for millimeter wavelengths and the dielectric constants and loss of some low-loss liquids at 2.1 mm, *J. Chem.*

Phys. **43** (1965) 2341-2346.
[288] A. L. Cullen; P. K. Yu, The accurate measurement of permittivity by means of an open resonator, *Proc. Roy. Soc. Lond. A* **325** (1971) 493-509.
[289] K. Chitoku; K. Higasi, Dielectric relaxation and molecular structure. VI. Dielectric measurements at the frequency of 100 GHz, *Bull. Chem. Soc. Japan* **44** (1971) 992-997.
[290] R. G. Jones, Precise dielectric measurements at 35 GHz using an open microwave resonator, *Proc. IEE* **123** (1976) 285-290.
[291] H. Kilp, Precise measurement of the complex permittivity of low-to-medium loss standard liquids at 285 GHz, *J. Phys. E: Sci. Instrum*. **10** (277) 985-989.
[292] N. Beverini; S. Marchetti; F. Strumia F, Analysis of near-confocal spherical mirror resonators in the microwave region, *J. Phys. E: Sci. Instrum.* **10** (1977) 1072-1075.
[293] P. K. Yu; A. L. Cullen, Measurement of permittivity by means of an open resonator, *Proc. Roy. Soc. Lond. A* **380** (1982) 49-71.
[294] R. N. Clarke; C. B. Rosenberg, Fabry-Perot and open resonators at microwave and millimetre wave frequencies, 2-300 GHz, *J. Phys. E: Sci. Instrum.* **15** (1982) 9-24.
[295] A. C. Lynch, Measurement of permittivity using an open resonator, *IEE Proc.* A **130** (1983) 365-368.
[296] W. F. P. Chan; B. Chambers B, Measurement of nonplanar dielectric samples using an open resonator *IEEE Trans. Microw. Theory Techn.* **35** (1987) 1429-1434
[297] A. C. Lynch; R. N. Clarke, Open resonators: improvement of confidence in measurement of loss *IEE Proc.* A **139** (1992) 221-225.
[298] M. Wübbenhorst; J. van Turnhout, Analysis of complex dielectric spectra. I. One-dimensional derivative techniques and three-dimensional modelling, *J. Non-Cryst. Solids* **305** (2002) 40-49.
[299] U. Kaatze, Logarithmic derivative complex permittivity spectrometry, *Meas. Sci. Technol.* **14** (2003) N55-N58.
[300] P. Debye, *Polar Molecules* (Chemical Catalog, New York, 1929).
[301] R. Richert, Insulated electrodes for eliminating conductivity in dielectric relaxation experiments, *Eur. Phys. J. B* **68** (2009) 197-200.
[302] D. Rosen; R. Bignall; J. D. M. Wisse; A. C. M. van der Drift, Radio frequency measurement of the dielectric constant of conducting liquids with tanδ up to 500, *J. Sci. Instrum.* **2** (1969) 22-28.
[303] C. G. Essex; G. P. South; R. J. Sheppard; E. H. Grant, A bridge

technique for measuring the permittivity of a biological solution between 1 and 100 MHz, *J. Phys. E.: Sci. Instrum.* **8** (1975) 385-389.
[304] F. van der Touw; J. de Goede; W. M. van Beek; M. Mandel, A measuring device for the determination of the electric permittivity of conducting liquids in the frequency range 2-500 kHz. Part I: The bridge, *J. Phys. E: Sci. Instrum*. **8** (1975) 840-844.
[305] C. Wheatstone, The Bakerian lecture: An account of several new instruments and processes for determining the constants of a voltaic circuit, *Philos. Trans. Roy. Soc.* **133** pt II (1843) 303-327.
[306] S. Ekelöf, The genesis of the Wheatstone bridge, *Eng. Sci. Educ. J.* **10** (2001) 37-40.
[307] M. Wien, Messung der Indutionsconstanten mit dem "optischen Telephon", *Wied. Ann. Phys. Chem.* **280** (1891) 689-712.
[308] S. C. Bera; D. N. Kole, Study of modified ac bridge technique for loss angle measurement of dielectric material, *Sensor Transd. J.* **96** (2008) 104-111.
[309] D. J. Scheiber, An ultra low frequency bridge for dielectric measurements, *J. Res. Natl. Bur. Stand. C*, **65** (1961) 23-42.
[310] G. Schaumburg, New broadband dielectric spectrometers, *Dielectrics Newslett.,* **July 1994**, 8-12.
[311] K. Lautscham; F. Wente; W. Schrader; U. Kaatze, High resolution and small volume automatic ultrasonic velocimeter for liquids, *Meas. Sci. Technol.* **11** (2000) 1432-1439.
[312] M. Grazia Giri; M. Carlà; C. M. C. Gambi; D. Senatra; A. Chittofrati; A. Sanguineti, Dielectric permittivity measurements on highly conductive perfluoropolyether microemulsions at frequencies up to 100 MHz, *Meas. Sci. Technol*. **4** (1993) 627-631.
[313] F. Wolter; F. Thom, A parallel-plate capacitor used to determine the complex permittivity of supercooled aqueous solutions in the 1 MHz range, *Meas. Sci. Technol.* **7** (1996) 969-975.
[314] G. Schaumburg, On the accuracy of dielectric measurements, *Dielectrics Newslett*., **November 1997**, 5-10.
[315] I. C. Halalay, Versatile cell for complex permittivity measurements on liquids, *Rev. Sci. Instrum.* **70** (1999) 3432-3434.
[316] D. Mizuno; T. Nishino; Y. Kimura; R. Hayakawa, Dielectric response in dilute lyotropic lamellar and sponge phases of nonionic surfactant, *Phys. Rev. E* **67** (2003) 061505.
[317] M. Becchi; L. Callegaro; F. Durbiano; V. D'Elia; A. Strigazzi, Novel impedance cell for low conductive liquids: Determination of bulk and interface contributions, *Rev. Sci. Instrum.* **78** (2007) 113902.

[318] E. W. Greenfield, Application of guard electrodes in dielectric measurements, *Rev. Sci. Instrum.* **13** (1942) 489-492.
[319] B. J. Jones; D. Tidy; G. Williams, Cells for the measurement of dielectric permittivity and thermally stimulated discharge current, *J. Phys. E: Sci. Instrum*. **9** (1976) 693-694.
[320] E. M. Breitung; W. E. Vaughan; R. J. McMahon, Measurement of solute dipole moments in dilute solution: A simple three-terminal cell, *Rev. Sci. Instrum.* **71** (2000) 224-227.
[321] C. Grosse; M. C. Tirado, Low-frequency dielectric spectroscopy of colloidal suspensions, *J. Non-Cryst. Solids* **305** (2002) 386-392.
[322] S. E. Young; E. H. Young, Measurement of permittivity of some biological solutions at frequencies below 1 MHz, *J. Phys. E: Sci. Instrum.* **1** (1968) 429-432.
[323] S. B. Sachs; A. Katchalsky; K. S. Spiegler, Dielectric cell for radiofrequency measurement of conductive media, *Electrochim. Acta* **15** (1970) 693-701.
[324] F. van der Touw, G. Selier; M. Mandel, A measuring device for the determination of the electric permittivity of conducting liquids in the frequency range 2-500 kHz. Part II: The cell, *J. Phys. E: Sci. Instrum*. **8** (1975) 844-846.
[325] N. C. Lockhart; J. W. Snaith, Apparatus for dielectric measurements on fluids and dispersions, *J. Phys. E: Sci. Instrum.* **11** (1978) 1011-1014.
[326] J. Blom, Measurement of dielectric relaxation of conducting solutions at low frequencies, *J. Phys. E: Sci. Instrum.* **12** (1979) 889-893.
[327] D. G. W. Goad; H. J. Wintle, Capacitance corrections for guard gaps, *Meas. Sci. Technol.* **1** (1990) 965-969.
[328] S. Ďad'o, Capacitive sensors with pre-calculable capacitance, *Trans. Elec. Eng*. **2** (2013) 34-39.
[329] V. Uhlendorf, Fatty acid contamination and dielectric relaxation in phospholipid vesicle suspensions, *Biophys. Chem.* **20** (1984) 261-273.
[330] F. Bordi; C. Cametti; T. Gili, Reduction of the contribution of electrode polarization effects in the radiowave dielectric measurements of highly conductive biological cell suspensions, *Bioelectrochem.* **54** (2001) 53-61.
[331] Y. Feldman, E. Polygalov, I. Ermolina; Y. Polevaya; B. Tsentsiper, Electrode polarization correction in time domain dielectric spectroscopy, *Meas. Sci. Technol.* **12** (2001) 1355-1364.
[332] H. Sanabria; J. H. Miller, Jr., Relaxation process due to the electrode-

electrolyte interface in ionic solutions, *Phys. Rev. E* **74** (2006) 051505.
[333] C. Prodan; C. Bot, Correcting the polarization effect in very low frequency dielectric spectroscopy, *J. Phys. D: Appl. Phys.* **42** (2009) 175505.
[334] B. A. Mazzeo; S. Chandra; B. L. Mellor; J. Arellano, Temperature-stable parallel-plate dielectric cell for broadband liquid impedance measurements, *Rev. Sci. Instrum.* **81** (2010) 125103.
[335] H. P. Schwan; C. D. Ferris, Four-electrode null techniques for impedance measurement with high resolution, *Rev. Sci. Instrum.* **39** (1968) 481-485.
[336] R. Hayakawa; H. Kanda; M. Sakamoto; Y. Wada, New apparatus for measuring the complex dielectric constant of highly conductive material, *Jap. J. Appl. Phys.* **14** (1975) 2039-2052.
[337] B. A. Mazzeo; A. J. Flewitt, Two- and four-electrode, wide-bandwidth, dielectric spectrometer for conductive liquids: Theory, limitations, and experiment, *J. Appl. Phys.* **102** (2007) 104106.
[338] B. A. Mazzeo, Parasitic capacitance influence of potential-sensing electrodes on four-electrode liquid impedance measurements, *J. Appl. Phys.* **105** (2009) 094106.
[339] H. Asfour; W. Soller; N. G. Posnack; A. E. Pollard; M. W. Kay, Low frequency impedance spectroscopy of cell monolayers using the four-electrode method, *J. Phys.: Conf. Ser.* **224** (2010) 012085.
[340] I. Yu, Electrodeless measurement of RF dielectric constant and loss, *Meas. Sci. Technol.* **4** (1993) 344-348.
[341] K. S. Cole; R. H. Cole, Dispersion and absorption in dielectrics. I. Alternating current characteristics, *J. Chem. Phys.* **9** (1941) 341-351.
[342] M. C. Beard; G. M. Turner; C. A. Schmuttenmaer, Terahertz spectroscopy, *J. Phys. Chem. B* **106** (2002) 7146-7159.
[343] K. Kogermann; J. A. Zeitler; J. Rantanen; T. Rades; P. F. Taday; M. Pepper, J. Heinämäki; C. J. Strachan, Investigating dehydration from compacts using terahertz pulsed, Raman, and near-infrared spectroscopy, *Appl. Spectrosc.* 61 (2007) 1265-1274.
[344] M. N. Afsar; J. B. Hasted, Submillimetre wave measurements of optical constants of water at various temperatures, *Infrared Phys.* **18** (1978) 835-841.
[345] M. N. Afsar, J. R. Birch; R. N. Birch; G. W. Chantry, The measurement of the properties of materials, *Proc. IEEE* **74** (1986) 183-199.
[346] J. R. Birch; G. P. O'Neill; J. Yarwood; M. Bennouna, A variable-thickness variable-temperature liquid cell for dispersive Fourier

transform spectrometry, *J. Phys. E: Sci. Instrum.* **15** (1982) 684-688.
[347] H. R. Zelsmann, Temperature dependence of the optical constants for liquid H_2O and D_2O in the far IR region, *J. Mol. Struct.* **350** (1995) 5-114.
[348] J. A. Reedijk; H. C. F. Martens; B. J. G. Smits; H. B. Brom, Measurement of the complex dielectric constant down to helium temperatures. II. Quasioptical technique from 0.03 to 1 THz, *Rev. Sci. Instrum.* **71** (2000) 478-481.
[349] J. R. Peacock, Millimetre wave permittivity of water near 25 °C, *J. Phys. D: Appl. Phys.* **42** (2009) 205501.
[350] N. Q. Vinh; S. J. Allen; K. W. Plaxco, Dielectric spectroscopy of proteins as a quantitative experimental test of computational models of their low-frequency harmonic motions, *J. Am. Chem. Soc.* **133** (2011) 8942-8947.
[351] Y. Husimi; A. Wada, Time-domain measurement of dielectric dispersion as a response to pseudorandom noise, *Rev. Sci. Instrum.* **47** (1976) 213-217.
[352] J. M. Ramsey; W. B. Whitten, Fourier transform microwave spectrometer using an electric-field cross-correlation technique, *Rev. Sci. Instrum.* **57** (1986) 1329-1337.
[353] O. Kirchner; R. Böhmer; G. Hinze, Pseudo-stochastic multiple-pulse excitation in dielectric spectroscopy: application to a relaxor ferroelectric, J. *Phys. D: Condens. Matter* **15** (2003) S1069-S1075.
[354] H. B. Callen; T. A. Welton, Irreversibility and generalized noise, *Phys. Rev.* **83** (1951) 34-40.
[355] R. Kubo, The fluctuation-dissipation theorem, *Rep. Prog. Phys.* **29** (1966) 255-284.
[356] R. de L. Kronig, On the theory of the dispersion of X-rays, *J. Opt. Soc. Am.* **12** (1926) 547–557.
[357] H. A. Kramers, La diffusion de la lumière par les atomes, *Atti Cong. Intern. Fisici, Como* **2** (1927) 545–557.
[358] S. Takeishi; S. Mashimo, Dielectric relaxation measurements in the ultralow frequency region, *Rev. Sci. Instrum.* **53** (1982) 1155-1159.
[359] W. E. Vaughan, Experminetal methods, in *Dielectric Properties and Molecular Behaviour*, edited by N. Hill; W. E. Vaughan; A. H. Price; M. Davies (Van Nostrand Reinhold, London, 1969) pp 108-190.
[360] P. J. Hyde, Wide-frequency-range dielectric spectrometer, *Proc. IEE* **117** (1970) 1891-1901.
[361] A. Suggett, Time domain methods, in *Dielectric and Related Molecular Processes*, Vol. 1, edited by M. Davies (The Chemical Society, London, 1972).

[362] F. I. Mopsik, Precision time-domain dielectric spectrometer, *Rev. Sci. Instrum.* **55** (1984) 79-87.
[363] R. Böhmer; B. Schiener; J. Hemberger; R. V. Chamberlin, Pulsed dielectric spectroscopy of supercooled liquids, *Z. Phys. B* **99** (1995) 91-99.
[364] S. Sudo; M. Shimomura; T. Saito; T. Kashiwagi; N. Shinyashiki; S. Yagihara, Dielectric study on α- and β-processes in supercooled diethyleneglycol-pentaethyleneglycol-water mixtures, *J. Non-Cryst. Solids* **305** (2002) 197-203.
[365] K. Giese; R. Tiemann, Determination of the complex permittivity from thin-sample time domain reflectometry. Improved analysis of the step response waveform, *Adv. Mol. Relax. Process.* **7** (1975) 45-59.
[366] J. G. Berberian; E. King, An overview of time domain spectroscopy, *J. Non-Cryst. Solids* **305** (2002) 10-18.
[367] R. Nozaki; T. K. Bose, Broadband complex permittivity measurement by time-domain spectroscopy, *IEEE Trans. Instrum. Meas.* **39** (1990) 945-951.
[368] D. Bertolini; M. Cassettari; G. Salvetti; E. Tombari; S. Veronesi, Time domain reflectometry to study the dielectric properties of liquids: Some problems and solutions, *Rev. Sci. Instrum.* **62** (1991) 450-456.
[369] Y. Feldman; A. Adrianov; E. Polygalov; I. Ermolina; G. Romanychev ; Y. Zuev ; B. Milgotin, Time domain dielectric spectroscopy: An advanced measuring system, *Rev. Sci. Instrum.* **67** (1996) 3208-3216.
[370] R. Buchner; J. Barthel, A time domain reflectometer for dielectric relaxation spectroscopy of electrolyte solutions, *Ber. Bunsenges. Phys. Chem.* **101** (1997) 1509-1516.
[371] Y. Feldman; I. Ermolina; Y. Hayashi, Time domain spectroscopy study of biological systems, *IEEE Trans. Diel. Elect. Insul.* **10** (2003) 728-753.
[372] Y. Feldman; A. Puzenko; Y. Ryabov, Dielectric relaxation phenomena in complex materials, in *Advances in Chemical Physics, Part A, Vol 133: Fractals, Diffusion, and Relaxation in Disordered Complex Systems*, edited by W. T. Coffey; Y. P. Kalnykov (Wiley, New York, 2006) pp 1-125.
[373] R. H. Cole; S. Mashimo; P. Winsor IV, Evaluation of dielectric behavior by time domain spectroscopy, *J. Phys. Chem.* **84** (1980) 786-793.
[374] Y. Feldman; V. D. Fedotov, Investigation of rotational diffusion of

globular proteins by time domain spectroscopy, *Russ. J. Phys. Chem.* **61** (1987) 1045-1051.

[375] Y. Feldman; Y. F. Zuev; I. V. Ermolina; V. A. Goncharov, Difference method of analyzing dielectric data in the time domain, *Russ. J. Phys. Chem.* **62** (1988) 269-271.

[376] K. Giese, TDS-studies of aqueous ionic solutions, in *Proc. 2nd Int. Time Domain Spectroscopy Meeting Vol 2* edited by A. M.Bottreau; Y. Dutuit; C. Marzat (University of Bordeaux, Bordeaux, 1975) pp 10-19.

[377] T. Sato; A. Chiba; R. Nozaki, Dielectric relaxation mechanism and dynamical structures of the alcohol / water mixtures, *J. Mol. Liq.* **101** (2002) 99-111.

[378] C. Rønne; P.-O. Åstrand; S. R. Keiding, THz spectroscopy of liquid H_2O and D_2O, *Phys. Rev. Lett.* **82** (1999) 2888-2891.

[379] P. Y. Han; X.-C. Zhang, Free-space coherent broadband terahertz time-domain spectroscopy, *Meas. Sci. Technol.* **12** (2001) 1747-1756.

[380] M. Naftaly; R. E. Miles, Terahertz time-domain spectroscopy for material characterization, *Proc. IEEE* **95** (2007) 1658-1665.

[381] M. Krumbholz; T. Hochrein; N, Vieweg; T. Hasek; K. Kretchmer; M. Bastian; M. Miculics; M. Koch, Monitoring polymeric compounding processes in line with THz time-domain spectroscopy, *Polym. Test.* **28** (2009) 30-35.

[382] W. Quiao; K. Yang ; A. Thoma; T. Dekorsy, Dielectric relaxation of HCl and NaCl solutions investigated by terahertz time-domain spectroscopy, *J. Infrared Millim. Terahertz Waves* **33** (2012) 1029-1038.

[383] R. Gente; N. Born; N. Voss; W. Sannemann; J. Leon; M. Koch; E. Castro-Camus, Determination of leaf water content from terahertz time-domain spectroscopic data, *J. Infrared Millim. Terahertz Waves* **34** (2013) 316-323.

[384] D. S. Holder (ed.) *Electrical Impedance Tomography Methods, History and Applications* (Institute of Physics, Bristol, 2005).

[385] N. K. Nikolova, Microwave biomedical imaging, in *Wiley Encyclopedia of Electrical and Electronics Engineering Vol. 24*, edited by J. G. Webster (Wiley, New York, 2014) pp 1-22.

[386] J. A. Victorino; J. B. Borges; V. N. Okamoto; G. F. Matos; M. R. Tucci; M. P. Caramez; H. Tanaka; F. S. Sipmann; D. C. Santos; C. S. Barbas; C. R. Carvalho; M. B. Amato, Imbalances in regional lung ventilation: a validation study on electrical impedance tomography, *Am. Resp. Crit. Care Med*. **169** (2004) 791-800.

[387] I. Frerichs; S. Pulletz; G. Elke; F. Reifferscheid; D. Schadler; J. Scholz; N. Weiler, Assessment of changes in distribution of lung perfusion by electrical impedance tomography, *Respiration* **77** (2009) 282-291.

[388] A. Fagerberg; O. Stenqvist; A. Aneman, Monitoring pulmatory perfusion by electrical impedance tomography: an evaluation in a pig model, *Anaesthesiol. Scand.* **53** (2009) 152-158.

[389] C. A. Grant; T. Pham; J. Hough; T. Riedel; C. Stocker; A. Schibler, Measurement of ventilation and cardiac relatad impedance changes with electrical impedance tomography, *Critical Care* **15** (2001) R37-R45.

[390] D. T. Nguyen; C, Jin; A. Thiagalingam; A. L. McEwan, A review on electrical impedance tomography for pulmatory perfusion imaging, *Physiol. Meas.* **33** (2012) 695-706.

[391] S. Leonhardt; B. Lachmann, Electrical impedance tomography: the holy grail of ventilation and perfusion monitoring?, *Intensive Care Med.* **38** (2012) 1917-1929.

[392] G. Bindu; A. Lonappan; V. Thomas; C. K. Aanandan; K. T. Mathew, Active microwave imaging for breast cancer detection, *Progr. Electromagn. Res.* **58** (2006) 149-169.

[393] J. Suri; R. M. Rangayyan; S. Laxminarayan (eds.), *Emerging Technology in Breast Immaging and Mammography* (Am. Sci. Publ., Valencia, CA, 2007).

[394] J. Yu; M. Yuan; Q. H. Liu, A wideband half oval patch antenna for breast imaging, *Progr. Electromagn. Res.* **98** (2009) 1-13.

[395] T. F. Zanoon; M. Z. Abdullah, Early stage breast cancer detection by means of time-domain ultra-wide band sensing, *Meas. Sci. Technol.* **22** (2011) 114016.

[396] N. K. Nikolova, Microwave near-field imaging of human tissue and its applications to breast cancer detection, *IEEE Microw. Mag.* **12** (2011) 78-94.

[397] P. M. Meaney; P. A. Kaufman; L. S. Muffly; M. Click; S. P. Poplack; W. A. Wells; G. N. Schwartz; R. M. di Florio-Alexander; T. D. Tosteson; Z. Li; S. D. Geimer; M. W. Fanning; T. Zhou; N. R. Epstein; K. D. Paulsen, Microwave imaging for neoadjuvant chemotherapy monitoring: initial clinical experience, *Breast Cancer Res.* **15** (2013) R35-R50.

[398] K. M. Putnam; D. A. Pizzagally; D. C. Gooding; N. H. Kalin; R. J. Davidson, Neural activity and diurnal variation of cortisol: evidence from brain electrical tomography analysis and relevance to anhedonia, *Psychophysiol.* **45** (2008) 886-895.

[399] O. Gilad; D. S. Holder, Impedance changes recorded with scalp electrodes during visual evoked responses: implications for electric impedance tomography of fast neural activity, *Neuroimage* **47** (2009) 412-522.
[400] S. P. Kumar; N. Sriraam; P. G. Benakop; B. C. Jinaga, Reconstruction of brain electrical impedance tomography images using particle swarm optimization, *Proc. 5th Intern. Conf. Indust. Inform. Syst.* **ICIIS** (2010) 339-342.
[401] K. Y. Aristovich; G. Sato dos Santos; B. C. Packham; D. S. Holder, A method for reconstructing tomographic images of evoked neural activity with electrical impedance tomography using intracranial planar arrays, *Physiol. Meas.* **35** (2014) 1095-1109.
[402] S. K. Pahuja; S. Anand; A. Sengupta, Electrical impedance tomography based image reconstruction and feto-maternal monitoring in pregnancy, *Health* **3** (2011) 482-486.
[403] V. A. Cherepenin; Y. V. Gulyaev; A. V. Korjenevsky; S. A. Sapetsky; T. S. Tuykin, An electrical impedance tomography system for gynecological application GIT with a tiny electrode array, *Physiol. Meas.* **33** (2012) 849-862.
[404] O. V. Trokhanova; Y. A. Chijova; M. B. Okhapkin; A. V. Korjenevsky; T. S. Tuykin, Possibilities of electrical impedance tomography in gynecology, *J. Phys. : Conf. Ser.* **434** (2013) 012038.
[405] J. C. Gamio; C. Ortiz-Alemán; R. Martin, Electrical capacitance tomography two-phase oil-gas flow imaging by linear back-projection algorithm, *Geofís. Intern.* **44** (2005) 265-273.
[406] L. M. Heikkinen; J. Kourunen; T. Savolainen; P. J. Vauhkonen; J. P. Kaipio ; M. Vauhkonen, Real time three-dimensional electrical impedance tomography applied in multiphase flow imaging, *Meas. Sci. Technol.* **17** (2006) 2083-2087.
[407] Z. Wu; H. McCann; L. E. Davis; J. Hu; A. Fontes; C. G. Xie, Microwave-tomographic system for oil- and gas-multiphase flow imaging, *Meas. Sci. Technol.* **20** (2009) 104026.
[408] L. F. M. Moura; E. Cenedese; A. C. Azevedo Filho, Experimental study of a capacitive tomography system for multiphase flow, *Engenharia Térmica* **8** (2009) 56-66.
[409] B. S. Kim; A. K. Khambampati; Y. J. Hong; S. Kim; K. Y. Kim, Multi phase flow imaging using an adaptive multi-threshold technique in electrical resistance tomography, *Flow Meas. Instrum.* **31** (2013) 25-34.
[410] C. Eckhardt; W. Brezna; O. Bethge; E. Bertagnolli; J. Smoliner, The geometry effects in scanning capacitance microscopy on GaAs

Schottky and metal-oxide-semiconductor-type junctions, *J. Appl. Phys.* **105** (2009) 113709.

[411] I. Humer; O. Bethge; M. Bodnarchuk; M. Kovalenko; M. Yarem ; W. Heiss; H. P. Hube ; M. Hochleitner; P. Hinterdorfer; F. Kienberger; J. Smoliner, Scanning microwave microscopy and scanning capacitance microscopy on colloidal nanocrystals, *J. Appl. Phys.* **109** (2011) 064313.

[412] M. Koch; S. Hunsche; P. Schumacher; M. C. Nuss; J. Feldmann; J. Fromm, THz-imaging: a new method for density mapping of wood, *Wood Sci. Technol.* **32** (1998) 421-427.

[413] V. Bucur, *Nondestructive Characterization and Imaging of Wood* (Springer, Berlin, 2003).

[414] M. G. Pelletier; J. A. Viera; J. Wanjura; G. Holt, Accurate permittivity measurements for microwave imaging via ultra-wideband removal of spurious reflectors, *Sensors* **10** (2010) 8491-8503.

[415] J. Kim; M. S. Kim; K. Lee; J. Lee; D. Cha; B. Friedman, Development of a near-field scanning microwave microscope using a tunable resonance cavity for high resolution, *Meas. Sci. Technol.* **14** (2003) 7-12.

[416] C. Gao; B. Hu; I. Takeuchi; K.-S. Chang; X.-D. Xiang; G. Wang, Quantitative scanning evanescent microwave microscopy and its applications in characterization of functional materials libraries, *Meas. Sci. Technol.* **16** (2005) 248-260.

[417] V. V. Talanov; A. Scherz; R. L. Moreland; A. R. Schwartz, A near-field scanned microwave probe for spatially localized electrical metrology, *Appl. Phys. Lett.* **88** (2006) 134106.

[418] K. Lai; M. B. Ji M; N. Leindecker; M. A. Kelly; Z. X. Shen, Atomic-force-microscope-compatible near-field scanning microwave microscope with separated excitation and sensing probes, *Rev. Sci. Instrum.* **78** (2007) 063702.

[419] V. V. Talanov; A. R. Schwartz, Near-field scanning microscope for interline capacitance characterization of nanoelectronics interconnect, *IEEE Trans Microw. Theory Tech.* **57** (2009) 1224-1229.

[420] X.-Y. Zhuang; X.-C. Wang; F. Xu; Y.-G. Ma; C. K. Ong, High frequency dielectric properties distribution of $BiFeO_3$ thin film using near-field microwave microscopy, *Rev. Sci. Instrum.* **80** (2009) 114701.

[421] K. Lai; W. Kundiikanjana; H. Peng; Y. Cui; M. A. Kelly; Z. X. Shen, Tapping mode microwave impedance microscopy, *Rev. Sci. Instrum.* **80** (2009) 043707.

[422] H. P. Huber; M. Moertelmaier; T. M. Wallis; C. J. Chiang;

M. Hochleitner; A. Imtiaz; Y. J. Oh; K. Schilcher; M. Dieudonne; J. Smoliner; P. Hinterdorfer; S. J. Rosner; H. Tanbakuchi; P. Kabos; F. Kienberger, Calibrated nanoscale capacitance measurements using scanning microwave microscope, *Rev. Sci. Instrum.* **81** (2010) 113701.

[423] K. Ohara; Y. Cho, Non-contact scanning nonlinear dielectric microscopy, *Nanotechnol.* **16** (2005) S54-S58.

[424] K. Tanaka; Y. Kurihashi; T. Uda; Y. Daimon; N. Odagawa; R. Hirose; Y. Hiranaga; Y. Cho, Scanning nonlinear dielectric microscopy nano-science and technology for next generation high density ferroelectric data storage *Japan. J. Appl. Phys.* **5** (2008) 3311-3325.

[425] Y. Hiranaga; Y. Cho, Intermittent contact scanning nonlinear dielectric microscopy *Rev. Sci. Instrum.* **81** (2010) 023705.

[426] Y. Cho, Scanning nonlinear dielectric microscopy, *J. Mater. Res.* **26** (2011) 2007-2016.

[427] L. Borcea, Electrical impedance tomography, *Inverse Problems* **18** (2002) R99-R136.

[428] R. H. Bayford, Bioimpedance Tomography, *Annu. Rev. Biomed. Eng.* **8** (2006) 63-91.

[429] O.-P. Tossavainen; M. Vauhkonen; L. M. Heikkinen; T. Savolainen, Estimating shapes and free surfaces with electrical impedance tomography, *Meas. Sci. Technol.* **15** (2004) 1402-1411.

[430] J. Kourunen; T. Savolainen; A. Lehikoinen; M. Vauhkonen, Suitability of a PXI platform for an electrical impedance tomography system, *Meas. Sci. Technol.* **20** (2009) 015503.

[431] A. Voutilainen; A. Lehikoinen; M. Vauhkonen; P. Kaipio, Three-dimensional nonstationary electrical impedance tomography with a single electrode layer, *Meas. Sci. Technol.* **21** (2010) 035107.

[432] A. Voutilainen; A. Lehikoinen; M. Vauhkonen; J. Kaipio, A reduced-order filtering approach for 3D dynamical electrical impedance tomography *Meas. Sci. Technol.* **22** (2011) 025504.

[433] A. J. Jaworski; G. T. Bolton, The design of an electrical capacitance tomography sensor for use with media of high dielectric permittivity, *Meas. Sci. Technol.* **11** (2000) 743-757.

[434] S. Lui; W- Q. Yang; H. Wang; F. Jiang; Y. Su, Investigation of square fluidized beds using capacitance tomography: preliminary results, *Meas. Sci. Technol.* **12** (2001) 1120-1125.

[435] M. A. Nurge, Electrical capacitance volume tomography with high contrast dielectrics using a cuboid sensor geometry, *Meas. Sci. Technol.* **18** (2007) 1511-1120.

[436] W. Yang, Design of electrical capacitance tomography sensors,

Meas. Sci. Technol. **21** (2010) 042001.
[437] A. S. Pandya; A. Arimoto; A. Agarwal; Y. Kinouchi, A novel approach for measuring electrical impedance tomography for local tissue with artificial intelligent algorithm, *Intern. J. Biometrics Bioinform.* **3** (2009) 66-81.
[438] T. Sun; S. Tsuda; K.-P. Zauner, H. Morgan, On-chip electrical impedance tomography for imaging biological cells, *Biosensors Bioelectron.* **25** (2010) 1109-1115.
[439] J. K. Seo; O. Kwon; E. J. Woo, Magnetic resonance electrical impedance tomography (MREIT): conductivity and current density imaging, *J. Phys.: Conf. Ser.* **12** (2005) 140-155.
[440] A. Kak; M. Slaney, *Principles of Computerized Tomographic Imaging* (SIAM, Philadelphia, 2007).
[441] Z. Cao; L. Xu, Direct image reconstruction for electrical capacitance tomography by using the enclosure method, *Meas. Sci. Technol.* **22** (2011) 104001.
[442] B. T. Hjertaker; R. Maad; G. A. Johansen, Dual-mode capacitance and gamma-ray tomography using the Landweber reconstruction mechamism, *Meas. Sci. Technol.* **22** (2011) 104002.
[443] M. Neumayer; D. Watzenig; H. Zangl, H_∞ approach for robost estimation of material parameters in electrical capacitance tomography *Meas. Sci. Technol.* **22** (2011) 104004.
[444] Y. Ru; C. Pradeep; S. Mylvaganam, Neural networks in electrical capacitance tomography (ECT)-based interface detection *Meas. Sci. Technol.* **22** (2011) 104006.
[445] X. Chen; H. Hu; F. Liu; X. X. Gao, Image reconstruction for an electrical capacitance tomography system based on a least-squares support vector machine and self-adaptive particle swarm optimization algorithm, *Meas. Sci. Technol.* **22** (2011) 104008.
[446] B. S. Kim; A. K. Khambampati; S. Kim, K. Y. Kim, Image reconstruction with adaptive threshold technique in electrical resistance tomography, *Meas. Sci. Technol.* **22** (2011) 104009.
[447] Q. Wang; H. Wang; S. Xin, Suitability of an MRMCE (multi-resolution minimum cross entropy) algorithm for online monitoring of a two-phase flow, *Meas. Sci. Technol.* **22** 104010.
[448] B. B. Hu; M. C. Nuss, Imaging with terahertz waves, *Opt. Lett.* **20** (1995) 1717-1718.
[449] Y. Watanabe; K. Kawase; T. Ikari; H. Ito; Y. Ishikawa; H. Minamide, Component analysis of chemical mixtures using terahertz spectroscopic imaging, *Opt. Commun.* **234** (2004) 125-129.
[450] E. J. Woo, Impedance spectroscopy and multi-frequency electrical

impedance tomography, *Intern J. Bioelectromagn.* **9** (2007) 101-102.
[451] D. Banerjee; W. von Spiegel; M. D. Thomson; S. Schnabel; H. G. Roskos; Diagnosing water content in paper by terahertz radiation, *Opt. Express* **16** (2008) 9060-9066.
[452] C. G. Malmberg; A. A. Maryott, Dielectric constant of water from 0 °C to 100 °C, *J. Res. Natl. Bur. Stand.* **56** (1956) 1-7.
[453] G. A. Vidulich; D. F. Evans; R. L. Kay, The dielectric constant of water and heavy water between 0 and 40°, *J. Phys. Chem.* **71** (1967) 656-662.
[454] R. L. Kay; G. A. Vidulich; K. S. Pribadi, Reinvestigation of the dielectric constant of water and its temperature coefficient, *J. Phys. Chem.* **73** (1969) 445-447.
[455] J. B. Hasted; M. Shahidi, The low frequency dielectric constant of supercooled water, *Nature* **262** (1976) 777-778.
[456] I. M. Hodge; C. A. Angell, The relative permittivity of supercooled water, *J. Chem. Phys.* **68** (1978) 1363-1368.
[457] K. N. Marsh, ed., Recommended reference materials for realization of physicochemical properties: permittivity, *Pure Appl. Chem.* **53** (1981) 1847-1862.
[458] W. F. Brown, Jr., Dielectrics, in *Encyclopedia of Physics, Vol 17*, edited by S. Flügge (Springer, Berlin 1956) pp 1-154.
[459] G. Oster; J. G. Kirkwood, The influence of hindered molecular rotation on the dielectric constants of water, alcohols, and other polar liquids, *J. Chem. Phys.* **11** (1943) 175-178.
[460] H. Fröhlich, *Theory of Dielectrics* (Clarendon, London, 1958).
[461] N. E. Hill, Theoretical Treatment of Permittivity and Loss, in *Dielectric Properties and Molecular Behaviour*, edited by N. E. Hill; W. E. Vaughan; A. H. Price; M. Davies (Van Nostrand Reinhold, London, 1969).
[462] C. J. F. Böttcher, O. C. Van Belle; P. Bordewijk; A. Rip, Theory of Electric Polarization, Vol. 1: Dielectrics in Static Fields (Elsevier, Amsterdam, 1973).
[463] U. Kaatze, Reference liquids for the calibration of dielectric sensors and measurement instruments, *Meas. Sci. Technol.* **18** (2007) 967-976.
[464] N. E. Hill, The temperature dependence of the dielectric properties of water, *J. Phys. D: Solid State Phys.* **3** (1970) 238-239.
[465] H. Eyring, The activated complex in chemical reactions, *J. Chem. Phys.* **3** (1935) 107-115.
[466] S. Glasstone; K. J. Laidler; H. Eyring, *The Theory of Rate Processes*

(McGraw-Hill, New York, 1941).
[467] H. Vogel, Das Temperaturabhängigkeitsgesetz der Viskosität von Flüssigkeiten, *Phys. Z.* **22** (1921) 645-646.
[468] G. S. Fulcher, Analysis of recent measurements of viscosity of glases, *J. Am. Ceram. Soc.* **8** (1225) 339-355.
[469] G. Tammann; W. Hesse, Die Abhängigkeit der Viscosität von der Temperatur bei Flüssigkeiten, *Z. Anorg. Allg. Chem.* **156** (1926) 245-257.
[470] M. W. Sagal, Dielectric relaxation in liquid alcohols and diols, *J. Chem. Phys.* **36** (1962) 2437-2442.
[471] A. Geiger; P. Mausbach; J. Schnitker, Computer simulation study of the hydrogen-bond network in metastable water, in *Water and Aqueous Solutions*, edited by G. W. Neilson; J. E. Enderby (Adam Hilger, Bristol, 1986) pp 15-30.
[472] H. Tanaka; I. Ohmine, Large local fluctuations in water, *J. Chem. Phys.* **87** (1987) 6128-6139.
[473] I. Ohmine; H. Tanaka; P. G. Wolynes, Large local energy fluctuations in water. II. Cooperative motions and fluctuations, *J. Chem. Phys.* **89** (1988) 5852- 5860.
[474] F. Sciortino; S. L. Fornili, Hydrogen bond cooperativity in simulated water: Time dependence analysis of pair interactions, *J. Chem. Phys.* **90** (1989) 2786-2792.
[475] F. Sciortino; A. Geiger; H. E. Stanley, Isochoric differential scattering functions in liquid water: The fifth neighbor as a network defect, *Phys. Rev. Lett.* **65** (1990) 3452-3455.
[476] F. Sciortino; A. Geiger; H. E. Stanley, Effect of defects on molecular mobility in liquid water, *Nature* **354** (1991) 218-221.
[477] I. Ohmine; H. Tanaka, Fluctuations, relaxations, and hydration in liquid water. Hydrogen-bond rearrangement dynamics, *Chem. Rev.* **93** (1993) 2545-2566.
[478] B. Gestblom; J. Sjöblom, Dielectric relaxation studies of aqueous long-chain alcohol solutions, *Acta Chem. Scand. A* **38** (1984) 47-56.
[479] B. Gestblom; J. Sjöblom, Dielectric relaxation study of aqueous methanol-butanol solutions. A comparison with higher homologues, *Acta Chem. Scand. A* **38** (1984) 575-578.
[480] J. Barthel; R. Buchner, High frequency permittivity and its use in the investigation of solution properties, *Pure Appl. Chem.* **63** (1991) 1473-1483.
[481] J. Barthel; R. Buchner, Dielectric permittivity and relaxation of electrolyte solutions and their solvents, *Chem. Soc. Rev.* **21** (1992) 263-270.

[482] S. Schwerdtfeger; F. Köhler, R. Pottel; U. Kaatze, Dielectric relaxation of hydrogen bonded liquids: Mixtures of monohydric alcohols with *n*-alkanes, *J. Chem. Phys.* **115** (2001) 4186-4194.
[483] U. Kaatze; R. Behrends; K. von Roden, Structural aspects in the dielectric properties of pentyl alcohols, *J. Chem. Phys.* **133** (2010) 094508.
[484] M. Mandal; D. G. Frood; M. A. Saleh; B. K. Morgan; S. Walker, Dielectric and viscosity studies of the principal relaxation process of liquid 1-alkanols and their solutions, *Chem. Phys.* **134** (1989) 441-451.
[485] U. Kaatze, Dielectric relaxation of H_2O/D_2O mixtures, *Chem. Phys. Lett.* **203** (1993) 1-4.
[486] J. B. Hasted, Liquid water: Dielectric properties, in *Water, a Comprehensive Treatise, Vol. 1,* edited by F. Franks (Plenum, New York, 1972) pp 255-309.
[487] U. Kaatze; R. Pottel; P. Schmidt, Dielectric properties of aqueous quinoxaline solutins in the complete composition range, *J. Phys. Chem.* **92** (1988) 3669-3674.
[488] K. S. Cole; R. H. Cole, Dispersion and absorption in dielectrics. II. Direct current characteristics, *J. Chem. Phys.* **10** (1942) 98-105.
[489] D. W. Davidson; R. H. Cole, Dielectric relaxation in glycerine, *J. Chem. Phys.* **18** (1950) 1417.
[490] S. Havriliak; S. Negami, A complex plane analysis of α-dispersion in some polymer systems, *J. Polym. Sci.* **C14** (1966) 99-117.
[491] R. M. Hill, Evaluation of susceptibility functions, *Phys. Status Solidi B* **103** (1981) 319-328.
[492] K. Menzel; A. Rupprecht; U. Kaatze, Hill-type ultrasonic relaxation spectra of liquids, *J. Acoust. Soc. Am.* **104** (1998) 2741-2749.
[493] R. M. Hill, Characterization of dielectric loss in solids and liquids, *Nature* **275** (1978) 96-99.
[494] R. M. Hill, Characterization of dielectric materials, *J. Mater. Sci.* **16** (1981) 118-124.
[495] U. Kaatze; W.-Y. Wen, Molecular motion and structure of solutions of triethylenediamine in H_2O and D_2O as studied by dielectric relaxation measurements, *J. Phys. Chem.* **82** (1978) 109-111.
[496] U. Kaatze; R. Pottel, On a hydration model utilized in the discussion of dielectric spectra of aqueous solutions, *J. Mol. Liq.* **30** (1985) 115-131.
[497] U. Kaatze; P. Schmidt; R. Pottel, Dielectric spectroscopy on aqueous solutions of purine and 6-methylpurine, *Ber. Bunsenges. Phys. Chem.* **92** (1988) 609-615.

[498] G. Akerlöf; A. O. Short, The dielectric constant of dioxane – water mixtures between 0 and 80 °C, *J. Am. Chem. Soc.* **58** (1936) 1241-1243.
[499] R. Pottel; U. Kaatze, Permittivity and dielectric relaxation of aqueous solutions of hydrocarbons, *Ber. Bunsenges. Phys. Chem.* **73** (1969) 437-446.
[500] D. Polder; J. H. van Santen, The effective permeability of mixtures of solids, *Physica* **12** (1946) 257-271.
[501] G. P. de Loor, Dielectric properties of heterogenous mixtures with polar constituent, *Appl. Sci. Res. B* **11** (1964) 310-320.
[502] L. K. H. van Beek, Dielectric behavior of heterogeneous systems, in *Progress in Dielectrics*, edited by J. B. Birks (Heywood, London, 1967) pp 69-114.
[503] S. S. Dukhin; V. N. Shilov, *Dielectric Phenomena and the Double Layer in Disperse Systems and Polyelectrolytes* (Halsted Press, New York, 1974).
[504] C. J. F. Böttcher; P. Bordewijk, *Theory of Electric Polarization, Vol. 2: Dielectrics in Time-Dependent Fields* (Elsevier, Amsterdam, 1978).
[505] A. Shivola, Dielectric mixture theories in permittivity prediction: effect of water on macroscopic parameters in *Microwave Aquametry*, edited by A. Kraszewski (IEEE, New York, 1996) pp 111-122.
[506] A. Shivola, *Electromagnetic Mixing Formulas and Applications, Electromagnetic Wave Series 47* (IEE Publishing, London, 1999).
[507] J. C. Maxwell, *Electricity and Magnetism* (Clarendon, Oxford, 1892).
[508] J. C. Maxwell-Garnett, Colours in metal glases and metal fims, *Philos.Trans. Roy. Soc., London, Sect. A*, **3** (1904) 385-420.
[509] K. W. Wagner, Erklärung der dielektrischen Nachwirkungsvorgänge auf Grund Maxwellscher Vorstellungen, *Arch. Elektrotechn.* **2** (1914) 371-387.
[510] D. A. G. Bruggeman, Berechnung verschiedener physikalischer Konstanten von heterogenen Substanzen. I. Dielektrizitätskonstanten und Leitfähigkeiten der Mischkörper aus isotropen Substanzen, *Ann. Phys. Lpz.* **5** (1935) 636-679.
[511] H. Looyenga, Dielectric constants of heterogeneous mixtures, *Physica* **31** (1965) 401-406.
[512] L. Landau; E. Lifshitz, *Electrodynamics of Continuous Media*, *2nd Ed.* (Pergamon, New York, 1982).
[513] U. Kaatze; K.-D. Göpel; R. Pottel, Zwitterion motions in differently aggregated phospholipids in aqueous and methanolic solutions. A dielectric relaxation study, *J. Phys. Chem.* **89** (1985) 2565-2571.

[514] W. Schrader; S. Halstenberg; R. Behrends; U. Kaatze; Critical slowing in lipid bilayers, *J. Phys. Chem. B* **107** (2003) 14457-14463.

[515] I. M. Woodhead; J. H. Christie; I. Platt; M. Hagedorn, Density compensation for moisture measurements in wood, in *Proc. 8th Int. Conf. on Electromagnagnetic Wave Interaction with Water and Moist Substances*, edited by P. Vainikainen; T. Laitinen (Helsinki University of Technology, Espoo, 2009) pp 281-288.

[516] M. C. Dobson; F. T. Ulaby; M. T. Hallikainen; M. A. El-Rayes, Microwave dielectric behavior of wet soil – Part II: Dielectric mixing models, *IEEE Trans. Geosci. Remote Sens.* **23** (1985) 35-46.

[517] S. O. Nelson, Correlating dielectric properties of solids and particulate samples through mixture relationships, *Trans. Am. Soc. Agric. Eng.* **35** (1992) 625-629.

[518] G. C. Topp; M. Watt; H. N. Hayhoe, Point specific measurement and monitoring of soil water content with an emphasis on TDR, *Can. J. Soil Sci.* **76** (1996) 307-316.

[519] E. Tuncer; Y. V. Serdyuk; S. M. Gubanski, Dielectric mixtures – electrical properties and modelling, *IEEE Trans. Diel. Elect. Insul.* **9** (2002) 809-828.

[520] S. P. Friedman, Electrical properties of soils, in *Encyclopedia of Agrophysics*, edited by J. Gliński; J. Horabik; J. Lipiec (Springer, Dordrecht, 2011).

[521] G. C. Topp; J. L. Davis; A. P. Annan, Electromagnetic determination of soil water content: measurements in coaxial transmission lines, *Water Resources Res.* **16** (1980) 574-582.

[522] D. B. Funk; Z. Gillay; P. Mészáros, Unified moisture algorithm for improved RF dielectric grain moisture measurement, *Meas. Sci. Technol.* **18** (2007) 1004-1015.

[523] W. Meyer; W. M. Schilz, Feasibility study of density-independent moisture measurement with microwaves, *IEEE Trans. Microw. Theory Techn.* **29** (1981)732-739.

[524] S. Trabelsi; S. O. Nelson, Density-independent functions for on-line microwave moisture meters: a general discussion, *Meas. Sci. Technol.* **9** (1998) 570-578.

[525] B. L. Shrestha; H. C. Wood; S. Sokhansanj, Prediction of moisture content of alfalfa using density-independent functions of microwave dielectric properties, *Meas. Sci. Technol.* **16** (2005) 1179-1185.

[526] K. Kupfer, Methods of density-independent moisture measurement, in *Electromagnetic Aquametry*, edited by K. Kupfer (Springer,

Berlin, 2005) pp 135-168.
[527] U. Kaatze, Dielectric properties of aqueous solutions of pyrazine and some of its derivatives, *Z. Phys. Chem. NF* **153** (1987) 141-150.
[528] U. Kaatze; C. Neumann; R. Pottel, Dielectric spectroscopy on aqueous solutions of pyridine and its derivatives, *J. Solut. Chem.* **16** (1987) 191-204.
[529] U. Kaatze; H. Gerke; R. Pottel, Dielectric relaxation in aqueous solutions of urea and some of its derivatives, *J. Phys. Chem.* **90** (1986) 5464-5469.
[530] U. Kaatze, Dielectric relaxation in aqueous solutions of polyvinylpyrrolidone, *Adv. Mol. Relax. Processes* **7** (1975) 71-85.
[531] U. Kaatze, Hydration properties of oxygen containing linear heterohydrocarbons as studied by dielectric relaxation measurements, *Ber. Bunsenges. Phys. Chem.* **83** (1978) 690-696.
[532] U. Kaatze; O. Göttmann; R. Podbielski; R. Pottel, Dielectric spectroscopy an aqueous solutions of some nitrogen-containing linear hydrocarbon polymers, *J. Mol. Liq.* **37** (1988) 127-141.
[533] U. Kaatze, Dielectric spectrum of a 0.5 M aqueous NaCl solution, *J. Chem. Phys.* **91** (1987) 3111-3113.
[534] U. Kaatze, Dielektrizitätszahl und dielektrische Relaxation spezieller wäßriger Elektrolytlösungen, *Ber. Bunsenges. Phys. Chem.* **77** (1973) 447-455.
[535] R. Pottel, The complex dielectric constant of some aqueous electrolyte solutions in a wide frequency range, in *Chemical Physics of Ionic Solutions*, edited by B. E. Conway; R. G. Barradas (Wiley, New York, 1966) pp 581-596.
[536] H. Falkenhagen, *Theorie der Elektrolyte* (Hirzel, Leipzig, 1971).
[537] J. M. G. Barthel; H. Krienke; W. Kunz, *Physical Chemistry of Electrolyte Solutions* (Steinkopff, Darmstadt, 1998).
[538] R. Pottel; J. Haller; U. Kaatze, Multistep association of cations and anions. The Eigen-Tamm mechanism some decades later, in *Oscillations, Waves and Interactions*, edited by T. Kurz; U. Parlitz; U. Kaatze (Universitätsverlag Göttingen, Göttingen 2007) pp 333-366.
[539] J. E. Anderson, The Debye-Falkenhagen effect: experimental fact or fiction?, *J. Non-Cryst. Solids* **172-174** (1994) 1190-1194.
[540] A. Chandra; B. Bagchi, Beyond the classical transport laws of electrochemistry: New microscopic approach to ionic conductance and viscosity, *J. Phys. Chem. B* **104** (2000) 9067-9080.
[541] A. Eiberweiser; R. Buchner, Ion-pair or ion-cloud relaxation. On the origin of small-amplitude low-frequency relaxation of weakly

associating aqueous electrolytes, *J. Mol. Liq.* **176** (2012) 52-59.
[542] K. Giese; U. Kaatze; R. Pottel, Permittivity and dielectric and proton magnetic relaxation of aqueous solutions of alkali halides, *J. Phys. Chem.* **74** (1970) 3718-3725.
[543] U. Kaatze, Dielectric effects in aqueous solutions of 1:1, 2:1, and 3:1 valent electrolytes: Kinetic depolarization, saturation, and solvent relaxation, *Z. Phys. Chem. N.F.* **135** (1983) 51-75.
[544] W.-Y. Wen; U. Kaatze, Aqueous solutions of azoniaspiroalkane halides. 3. Dielectric relaxation, *J. Phys. Chem.* **81** (1977) 177-181.
[545] L. Onsager, private communication (1973).
[546] B. J. Alder; T. E. Wainwright, Decay of the velocity autocorrelation function, *Phys. Rev. A* **1** (1970) 18-21.
[547] B. J. Alder; W. E. Alley, Generalized hydrodynamics, *Phys. Today* **37** (1984) 56-63.
[548] J. B. Hubbard; L. Onsager; W. M. van Beek; M. Mandel, Kinetic polarization deficiency in electrolyte solutions, *Proc. Natl. Acad. Sci. USA* **74** (1977) 401-404.
[549] J. B. Hubbard; L. Onsager, Dielectric dispersion and dielectric friction in electrolyte solutions. I., *J. Chem. Phys.* **67** (1977) 4850-4857.
[550] R. Pottel, Dielectric properties, in *Water, a Comprehensive Treatise, Vol. 3 : Aqueous Solutions of Simple Electrolytes*, edited by F. Franks (Plenum, New York, 1973) pp 401- 431.
[551] U. Kaatze; R. Pottel, On the static electric permittivity of aqueous and non-aqueous electrolyte solutions, *Z. Phys. Chem. N.F.* **141** (1984) 1-13.
[552] J. B. Hubbard; P. Colonomos; P. G. Wolynes, Molecular theory of solvated ion dynamics. III. The kinetic dielectric decrement, *J. Chem. Phys.* **71** (1979) 2652-2661.
[553] P. G. Kusalik; G. N. Patey, Theoretical results for dielectric and structural properties of aqueous electrolytes: The influence of ion size and charge, *J. Chem. Phys.* **79** (1983) 4468-4474.
[554] P. G. Wolynes, Dynamics of electrolyte solutions, *Ann. Rev. Phys. Chem.* **31** (1980) 345-376.
[555] J. B. Hubbard; R. F. Kayser, Dielectric friction and dielectric dispersion in electrolyte with spin, *J. Chem. Phys.* **74** (1981) 3535-3545.
[556] J. E. Enderby; G. W. Neilson, Structural properties of ionic liquids, *Adv. Phys.* **29** (1980) 323-365.
[557] R. Buchner, What can be learnt from dielectric relaxation spectroscopy about ion solvation and association?, *Pure Appl.*

Chem. **80** (2008) 1239-1252.
[558] R. Buchner ; G. Hefter, Interactions and dynamics in electrolyte solutions by dielectric spectroscopy, *Phys. Chem. Chem. Phys.* **11** (2009) 8984-8999.
[559] T. G. Chang; D. E. Irish, Ion-pair formation in aqueous solutions of silver nitrate: A Raman and infrared spectral study, *J. Solut. Chem.* **3** (1974) 175-189.
[560] L. Endom; H. G. Hertz; B. Thül; M. D. Zeidler, A microdynamic model of electrolyte solutions as derived from nuclear magnetic relaxation and self-diffusion data, *Ber. Bunsenges. Phys. Chem.* **71** (1967) 1008-1031.
[561] G. Engel; H. G. Hertz, On the negative hydration. A nuclear magnetic relaxation study, *Ber. Bunsenges. Phys. Chem.* **72** (1968) 808-834.
[562] B. E. Conway, *Ionic Hydration in Chemistry* (Elsevier, Amsterdam, 1981).
[563] K. Giese, Dielectric relaxation in alkali halide solutions due to hydration water exchange, *Ber. Bunsenges. Phys. Chem.* **76** (1972) 495-500.
[564] H. G. Hertz; M. D. Zeidler, Elementarvorgänge in der Hydrathülle von Ionen aus Protonen- und Deuteronenrelaxationsmessungen, *Ber. Bunsenges. Phys. Chem.* **67** (1963) 774-786.
[565] H. G. Hertz, Nuclear magnetic relaxation spectroscopy, in *Water, a Comprehensive Treatise, Vol. 3 : Aqueous Solutions of Simple Electrolytes*, edited by F. Franks (Plenum, New York, 1973) pp 301- 499.
[566] U. Kaatze; C. H. Limberg; R. Pottel, Dielectric relaxation of water in aqueous solutions of *n*-alkylamine hydrochlorides. Part 1: Solute concentrations smaller than the critical micelle concentrations, *Ber. Bunsenges. Phys. Chem.* **78** (1974) 555-560.
[567] U. Kaatze; C. H. Limberg; R. Pottel, Dielectric relaxation of water in aqueous solutions of *n*-alkylamine hydrochlorides. Part 2: Solute concentrations larger than the critical micelle concentrations, *Ber. Bunsenges. Phys. Chem.* **78** (1974) 561-568.
[568] A. Rupprecht; U. Kaatze, Solution properties of urea and its derivatives in water: Evidence from ultrasonic relaxation spectra, *J. Phys. Chem. A* **106** (2002) 8850-8858.
[569] A. Rupprecht; U. Kaatze, Model of noncritical concentration fluctuations in binary liquids. Verification by ultrasonic spectrometry of aqueous systems and evidence of hydrophobic effects, *J. Phys. Chem. A* **103** (1999) 6485-6491.
[570] P. Sears; C.-H- Wong, Toward automated synthesis of

oligosaccharides and glycoproteins, *Science* **291** (2001) 2344-2350.
[571] C. R. Bertozzi; L. L. Kiessling, Chemical glycobiology, *Science* **291** (2001) 2357-2364.
[572] T. Maeder, Sweet medicines, *Sci. Am.* (*Int. Ed.)* **287** (2002) 24-31.
[573] H. Kogelberg; D. Solis; J. Jiménez-Barbero; H. Rüdiger, New structural insights into carbohydrate – protein interactions from NMR spectroscopy, *Curr. Opin. Struct. Biol.* **13** (2003) 646-653.
[574] H.-J. Gabius; H.-C. Siebert; S. André; J. Jiménez-Barbero; H. Rüdiger, Chemical biology of the sugar code, *ChemBioChem* **5** (2004) 740-764.
[575] K. Fuchs; U. Kaatze, Molecular dynamics of carbohydrate aqueous solutions. Dielectric relaxation as a function of glucose and fructose concentration, *J. Phys. Chem. B* **105** (2001) 2036-2042.
[576] U. Kaatze; M. Schäfer; R. Pottel, The complex dielectric spectrum of aqueous methanol and isopropanol solutions, *Z. Phys. Chem. (Munich)* **165** (1989) 103-117.
[577] P. Petong; R. Pottel; U. Kaatze, Water-ethanol mixtures at different compositions and temperatures. A dielectric relaxation study. *J. Phys. Chem. A* **104** (2000) 7420-7428.
[578] U. Kaatze; A. Schumacher; R. Pottel, The dielectric properties of *tert.*-butanol / water mixtures as a function of composition. *Ber. Bunsenges. Phys. Chem.* **95** (1991) 585-592.
[579] K. Tamm; G. Kurtze, Absorption of sound in aqueous solutions of electrolytes, *Nature* **168** (1951) 346.
[580] M. Eigen, Immeasurably fast reactions, Nobel lecture, December 11, 1967, in *Nobel Lectures, Chemistry 1963-1970* (Elsevier, Amsterdam, 1972).
[581] G. Kurtze; K. Tamm, Measurements of sound absorption in water and aqueous solutions of electrolytes, *Acustica* **3** (1953) 33-48.
[582] L. G. Jackopin; E. Yeager, Ultrasonic relaxation in manganese sulfate solutions, *J. Chem. Phys.* **74** (1970) 3766-3772.
[583] S. Petrucci, Kinetic approach to the study of ionic association and complexation: relaxation kinetics, in *Ionic Interactions, from Dilute Solutions to Fused Salts, Vol. 2*, edited by S. Petrucci (Academic, New York, 1971).
[584] R. Buchner; T. Chen; G. Hefter, Complexity in „simple“ electrolyte solutions: Ion pairing in $MgSO_4$ (aq), *J. Phys. Chem. B* **108** (2004) 2365-2375.
[585] T. Chen; G. Hefter; R. Buchner, Ion association and hydration in aqueous solutions of nickel(II) and cobalt(II) sulfate, *J. Solut.*

Chem. **34** (2005) 1045-1066.
[586] C. Akilan; N. Rohman; G. Hefter; R. Buchner, Temperature effects on ion association and hydration in $MgSO_4$ by dielectric spectroscopy, *ChemPhysChem* **7** (2006) 2319-2330.
[587] R. Buchner; G. Hefter, Interactions and dynamics in electrolyte solutions by dielectric spectroscopy, *Phys. Chem. Chem. Phys.* **11** (2009) 8984-8999.
[588] R. Buchner; S. G. Capewell; G. Hefter; P. M. May, Ion-pair and solvent relaxation processes in aqueous Na_2SO_4 solutions, *J. Phys. Chem. B* **103** (1999) 1185-1192.
[589] R. Buchner; F. Samani; P. M. May; P. Sturm; G. Hefter, Hydration and ion pairing in aqueous sodium oxalate solutions, *ChemPhysChem* **4** (2003) 373-378.
[590] U. Kaatze; V. Lönnecke; R. Pottel, Dielectric spectroscopy on aqueous solutions of zinc(II)chloride. Evidence of ion complexes, *J. Phys. Chem.* **91** (2987) 2206-2211.
[591] R. Buchner; C. Hölzl; J. Stauber; J. Barthel, Dielectric spectroscopy of ion-pairing and hydration in aqueous tetra-*n*-alkylammonium halide solutions, *Phys. Chem. Chem. Phys.* **4** (2002) 2169-2179.
[592] A. Bonsen; W. Knoche; W. Berger; K. Giese; S. Petrucci, Ultrasonic relaxation studies in aqueous solutions of aluminium sulphate and scandium sulfate, *Ber. Bunsenges. Phys. Chem.* **82** (1978) 678-683.
[593] G. S. Darbari; M. R. Richelson; S. Petrucci, Ultrasonic study of aqueous solutions of $ZnCl_2$: From dilute solutions to hydrated melts, *J. Chem. Phys.* **53** (1970) 859-866.
[594] H. Weingärtner; K. J. Müller; H. G. Hertz; A. V. J. Edge; R. Mills, Unusual behavior of transport coefficients in aqueous solutions of zinc chloride, *J. Phys. Chem.* **88** (1984) 2173-2178.
[595] Y. Yongyai; S. Kokpol; B. S. Rode, Microstructure and species distribution of aqueous zinc chloride solutions. Results from Monte Carlo simulations*, J. Chem. Soc. Faraday Trans.* **88** (1992) 1537-1540.
[596] U. Kaatze; B. Wehrmann, Broadband ultrasonic spectroscopy on aqueous solutions of zinc(II)chloride. I. Kinetics of complexation, *Z. Phys. Chem. (Munich)* **17789** (1992) 9-26.
[597] F. Oosawa, *Polyelectrolytes* (Marcel Dekker, New York, 1971).
[598] G. Schwarz, Dielectric relaxation phenomena in biomolecular systems in *Dielectric and Related Molecular Processes Vol. 1*, edited by M. Davis (The Chemical Society, London, 1972) pp 163-191.
[599] E. H. Grant; R. J. Sheppard; G. P. South, *Dielectric Behaviour of Biological Molecules in Solution* (Clarendon, Oxford, 1978).

[600] S. Takashima, *Electrical Properties of Biopolymers and Membranes* (Adam Hilger, Bristol, 1989).
[601] W. B. Russel; D. A. Saville; W. R. Schowalter, *Colloidal Dispersions* (Cambridge University Press, Cambridge, 1991).
[602] S. Grimmes; Ø. G. Martinsen, *Bioimpedance Bioelectricity Basics* (Academic, San Diego, 2000).
[603] U. Kaatze, unpublished results.
[604] V. Uhlendorf, *Messungen der dielektrischen Relaxation wäßriger Polyelektrolyt-Lösungen zwischen 5 MHz und 40 GHz*, Diploma-Thesis (Georg-August-Universität Göttingen, Göttingen, 1978).
[605] C. Grosse; M. Tirado; W. Pieper; R. Pottel, Broad frequency range study of the dielectric properties of suspensions of colloidal polystyrene particles in aqueous electrolyte solutions, *J. Colloid Interface Sci.* **205** (1998) 26-41.
[606] M. L. Jiménez; F. J. Arroyo; F. Carrique; U. Kaatze, Broadband dielectric spectra of spheroidal hematite particles, *J. Phys. Chem. B* **107** (2003) 12192-12200.
[607] J. J. López-García; J. Horno; C. Grosse, Influence of the finite size and effective permittivity of ions on the equilibrium double layer around colloidal particles in aqueous electrolyte solution, *J. Colloid Interface Sci.* **428** (2014) 308-315.
[608] U. Kaatze, Bound water: Evidence from and implications for the dielectric properties of aqueous solutions, *J. Mol. Liq.* **162** (2011) 105-112.
[609] A. Cataldo; M. Vallone; L. Tarricone; G. Cannazza; M. Cipressa, TDR moisture estimation for granular material: An application in agro-food industrial monitoring, *IEEE Trans. Instrum. Meas.* **58** (2009) 2597-2605.
[610] X. Yu; V. P. Drnevich; R. L. Nowack, Improvements of Soil Dielectric Mixing Model for Inversion Analysis of Time Domain Reflectometry Measurements, in *Proc. TDR 2006* (Purdue University, West Lafyette, IN, 2006); https://engineering.purdue.edu/TDR/Papers
[611] E. Piuzzi; A. Cataldo; G. Cannazza; E. De Benedetto, An improved reflectometric method for soil moisture measurement exploiting an innovative triple-short calibration, *IEEE Trans. Instrum. Meas.* **59** (2010) 2747-2754.
[612] H. Fricke, The Maxwell-Wagner dispersion in a suspension of ellipsoids, *J. Phys. Chem.* **57** (1953) 934-937.
[613] F. Franks, The properties of ice, in *Water, a Comprehensive Treatise, Vol. 1,* edited by F. Franks (Plenum, New York, 1972) pp 115-149.
[614] Ref. [94] p 228.

[615] L.-M. Wang; R. Richert, Dynamics of glass-forming liquids. IX. Structural versus dielectric relaxation in monohydroxy alcohols, *J. Chem. Phys.* **121** (2004) 11170.
[616] M. Shinohara; T. Goto; M. Oyama; S. Suzuki; N. Shinyashiki; S. Yagihara; T. Inoue; S. Oyaizu; S. Yamamoto, Glass transition in fructose-water mixture studied by broadband dielectric spectroscopy, *AIP Conference Proc.* **832** (2006) 145-148.
[617] S. E. Pagnotta; S. Cerveny; A. Alegría; J. Colmenero; Dielectric relaxations in ribose and deoxyribose supercooled water solutions, *J. Chem. Phys.* **131** (2009) 085102.
[618] N. Shinyashiki; S. Sudo; S. Yagihara; A. Spanoudaki; A. Kyritsis; P. Pissis, Relaxation processes of water in the liquid to glassy states of water mixtures studied by broadband dielectric spectroscopy**,** *J. Phys.: Condens. Matter* **19** (2007) 205113.
[619] J. Sjöström; J. Mattsson; R. Bergman; E. Johansson; K. Josefsson; D. Svantesson; J. Swenson, Dielectric secondary relaxation of water in aqueous binary glass-formers, *Phys. Chem. Chem. Phys*. **12** (2010) 10452.
[620] L. P. Singh; S. Cerveny; A. Alegría; J. Colmenero; Dynamics of water in supercooled aqueous solutions of poly(propylene glycol) as studied by broadband dielectric spectroscopy and low-temperature FTIR-ATR spectroscopy, *J. Phys. Chem. B* **115** (2011) 13817-13827.
[621] S. Sudo, M. Shimomura, N. Shinyashiki, S, Yagihara, Broadband dielectric study of α-β separation for supercooled glycerol-water mixtures, *J. Non-Cryst. Solids* **307-310** (2002) 356-363.
[622] A. Puzenko; Y. Hayashi; Y. E. Ryabov; I. Balin; Y. Feldman; U. Kaatze; R. Behrends, Relaxation dynamics in glycerol-water mixtures: I. Glycerol-rich mixtures, *J. Phys. Chem. B* **109** (2005) 6031-6035.
[623] K. L. Ngai; S. Capaccioli; N. Shinyashiki; The protein "glass" transition and the role of the solvent, *J. Phys. Chem. B* **112** [2008] 3826-3832.
[624] N. Shinyashiki; W. Yamamoto; A. Yokoyama; T. Yoshinari; S. Yagihara; R. Kita; K. L. Ngai; S. Capaccioli, Glass transitions in aqueous solutions of protein (bovine serum albumin), *J. Phys. Chem. B* **113** (2009) 14448-14456.
[625] K. L. Ngai; S. Capaccioli; S. Ancherbak; N. Shinyashiki, Resolving the ambiguity of the dynamics of water and clarifying its role in hydrated proteins, *Philos. Mag.* **13-15** (2011) 1809-1835.
[626] U. Schneider; R. Brand; P. Lunkenheimer; A. Loidl, Excess wing in the dielectric loss of glass formers: A Johary-Goldstein *β* relaxation?

Phys. Rev. Lett. **84** (2000) 5560-5563.
[627] K. L. Ngai; M. Palluch, Classification of secondary relaxation in glass formers based on dynamic properties, *J. Chem. Phys.* **120** (2004) 857-873.
[628] U. Kaatze; K. Menzel; R. Pottel, Broad-band dielectric spectroscopy on carboxylic acid/water mixtures. Dependence upon composition, *J. Phys. Chem.* **95** (1991) 324-331.
[629] F. Franks; J. R. Grigera, Solution properties of low molecular weight polyhydroxy compounds, in *Water, Science Reviews,Vol. 1,* edited by F. Franks (Cambridge University Press, Cambridge, 1990) pp 187-289.
[630] S. Mashimo; N. Miura; T. Umehara, The structure of water determined by microwave dielectric study on water mixture with glucose, polysaccarides, and L-ascorbic acid, *J. Chem. Phys.* **97** (1992) 6759-6765.
[631] K. Fuchs; U. Kaatze, Dielectric spectra of mono- and disaccharide aqueous solutions, *J. Chem Phys.* **116** (2002) 7137-7144.
[632] U. Kaatze; H. Bieler; R. Pottel, Dielectric spectroscopy on aqueous solutions of some zwitterionic amino acids, *J. Mol. Liq.* **30** (1985) 101-113.
[633] J. Sachs; P. Peyerl; S. Wöckel; M. Kmec; R. Herrmann; R. Zetik, Liquid and moisture sensing by ultra-wideband pseudo-noise sequence signals, *Meas. Sci. Technol.* **18** (2007) 1074-1087.
[634] O. Schimmer; A. Gülck; F. Daschner; J. K. Piotrowski; R. Knöchel, Noncontacting determination of moisture content in bulk materials using sub-nanosecond UWB pulses, *IEEE Trans. Microw. Theory Techn*. **53** (2005) 2107-2113.
[635] D. A. Robinson; C. S. Campbell; J. W. Hopmans; B. K. Hornbuckle; S. B. Jones; R. Knight; F. Odgen; J. Selker; O. Wendroth, Soil moisture measurement for ecological and hydrological water-shed-scale observations: A review, *Vadose Zone J.* **7** (2008) 358-389.
[636] H. Vereecken; J. A. Huisman; Y. Pachepsky; C. Montzka; J. van der Kruk; H. Bogena; l. Weihermüller; M. Herbst; G. Martinez; J. Vanderborgth, On the spatio-temporal dynamics of soil moisture at field scale, *J. Hydrol.* **516** (2014) 76-96.
[637] H. Vereecken; J. A. Huisman; H. Bogena; J. Vanderborgth: J. A. Vrugt; J. W. Hopmans, On the value of soil moisture measurements in vadose zone hydrology: A review, *Water Resources Res.* **44** (2008) W00D06.
[638] S. I. Seneviratne; T. Corti; E. L. Davin; M. Hirschi; E. B. Jaeger; I. Lehner; B. Orlowsky; A. J. Teuling, Investigating soil moisture –

climate interactions in changing climate: A review, *Earth-Sci. Rev.* **99** (1010) 125-161.

[639] Q. Zhu; K. Liao; Y. Xu; G. Yang; S. Wu; S. Zhou, Monitoring and prediction of soil moisture spatial-temporal variations from a hydropedological perspective: A review, *Soil Res.* **50** (2013) 625-637.

[640] G. C. Topp; J. Les Davis; A. P. Annan, The early development of TDR for soil measurements, *Vadose Zone J.* **2** (2003) 292-499.

[641] G. C. Topp, State of the art of measuring soil water content, *Hydrol. Process.* **17** (2003) 2993-2996.

[642] D. A. Robinson; A. Binley; N. Crook; F. D. Day-Lewis; T. P. A. Ferré; V. J. S. Grauch; R. Knight; M. Knoll; V. Lakshmi; R. Miller; J. Nyquist; L. Pellerin; K. Singha; L. Slater, Advancing process-based watershed hydrological research using near-surface geophysics: a vision for, and review of, electrical and magnetic geophysical methods, *Hydrol. Process.* **22** (2008) 3604-3635.

[643] S. Rudolph; J. van der Kruk; C. von Hebel; M. Ali; C. Montzka; S. Pätzold; D. A. Robinson; H. Vereecken; L. Weihermüller, Linking satellite derived LAI patterns with subsoil heterogeneity using large-scale ground-based electromagnetic induction measurements, *Geoderma* **241-242** (2014) 262-271.

[644] H. R. Bogena; J. A. Huisman; A. Güntner; C. Hübner; J. Kusche; F. Jonard; S. Vey; H. Vereecken, Emerging methods for non-invasive sensing of soil moisture dynamics from field to catchment scale: A review, WIREs Water 2015; DOI: 10.1002/wat2.1097.

[645] G. C. Topp; J. L. Davis; W. G. Bailey; W. D. Zebchuk, The measurement of soil water content using a portable TDR hand probe, *Can. J. Soil Sci.* **64** (1984) 313-321.

[646] J. E. Campbell, Dielectric properties and influence of conductivity in soils at one to fifty megahertz, *Soil Sci. Soc. Am. J.* **54** (1990) 332-341.

[647] T. J. Heimovaara, Frequency analysis of time domain reflectometry waveforms: 1. Measurement of the complex dielectric permittivity of soils, *Water Resources Res.* **30** (1994) 189-199.

[648] I. White; S. J. Zegelin, Electric and dielectric methods for monitoring soil-water content, in *Handbook of Vadose Zone Characterization and Monitoring*, edited by L. G. Wilson; L. G. Everett; S. J. Cullen (Lewis, Ann Arbor, 1995) pp 343-385.

[649] S. B. Jones; J. M. Wraith; D. Or, Time domain reflectometry measurement principles and applications, *Hydrol. Process.* **16** (2002) 141-153.

[650] S. Arsoy; M. Özgür; E. Keskin; C. Yilmaz, Accuracy of soil Moisture Content with ADR probes in saline soils, in *Proc. 8th Int. Conf. on Electromagnetic Wave Interaction with Water and Moist Substances*, edited by P. Vainikainen; T. Laitinen (Helsinki University of Technology, Espoo, 2009) pp 124-130.
[651] B. Will; M. Gerding, Spatially resolved measurements of arbitrarily shaped dielectric profiles using displaceable scatterers, in *Proc. 8th Int. Conf. on Electromagnetic Wave Interaction with Water and Moist Substances*, edited by P. Vainikainen; T. Laitinen (Helsinki University of Technology, Espoo, 2009) pp 358-364.
[652] E. Piuzzi; A. Cataldo; G. Cannazza; E. De Benedetto, An improved reflectometric method for soil moisture measurement exploiting an innovative triple-short calibration, *IEEE Trans. Instrum. Meas.* **58** (2010) 2747-2754.
[653] O. Schimmer; B. Oberheitmann; F. Baumann; R. Knöchel, Instantaneous distinction between double and single frozen fish using a new handheld time domain reflectometer, in *Proc. 7th Int. Conf. on Electromagnetic Wave Interaction with Water and Moist Substances*, edited by S. Okamura; N. Sobue; S. Yagihara; Y. Zhang (Shizuoka University, Hamamatsu, 2007) pp 167-174.
[654] D. Trebbels; A. Kern; F. Fellhauer; C. Hübner; R. Zengerle, Miniaturized FPGA-based high-resolution time-domain reflectometer, *IEEE Trans. Instrum Meas.* **62** (2013) 2101-2113.
[655] B. Will; M. Gerding, A novel sensor design for the determination of dielectric profiles using time domain reflectometry, in *Proc. 39th Europ. Microwave Conf.* (Rome, 2009) pp 791-794.
[656] M. S. Syfried; M. D. Murdock, Measurement of soil water content with a 50 MHz soil dielectric sensor, *Soil Sci. Soc. Am. J.* **68** (2004) 394-403.
[657] www.dynamax.com
[658] www.delta-t.co.uk
[659] E. J. A. Spaans; J. M. Baker; Simple baluns in parallel probes for time domain reflectometry, *Soil Sci. Soc. Am. J.* **57** (1993) 668-673.
[660] S. J. Zegelin; I. White; D. R. Jenkins, Improved field probes for soil water content and electrical conductivity measurements using time domain reflectometry, *Water Resources Res.* **25** (1989) 2367-2376.
[661] A. Scheuermann, C. Hübner; H. Wienbroer; D. Rebstock; G. Huber, Fast time domain reflectometry (TDR) measurement approach for investigating the liquefaction of soils, *Meas. Sci. Technol.* **21** (2010) 025104.
[662] H. Vereecken; R. Kasteel; J. Vanderborght; T. Harter, Upscaling

hydraulic properties and soil water flow processes in heterogeneous soils: A review, *Vadose Zone J.* **6** (2007) 1-28.

[663] C. Hübner; A. Brandelik, Distinguished problems in soil and snow aquametry, *Sensors Update Vol. 7*, edited by H. Baltes; W. Goepel; J. Hess (Wiley-VCH, New York, 2000) pp 317-340.

[664] A. Scheuermann; N. Wagner; A. Bieberstein; K. Kupfer; S. Schlaeger; R. Becker; C. Hübner, Monitoring system for river dykes based on spatial-TDR, in *Proc. 8th Int. Conf. on Electromagnetic Wave Interaction with Water and Moist Substances*, edited by P. Vainikainen; T. Laitinen (Helsinki University of Technology, Espoo, 2009) pp 131-138.

[665] K. Kupfer; E. Trinks; N. Wagner; M. Kuhne; C. Hübner, TDR-measurement system and its application in a salt mine, in *Proc. 7th Int. Conf. on Electromagnetic Wave Interaction with Water and Moist Substances*, edited by S. Okamura; N. Sobue; S. Yagihara; Y. Zhang (Shizuoka University, Hamamatsu, 2007) pp 139-149.

[666] T. Wagenknecht; C. Hübner; F. Königer; A. Brandelik; R. Schuhmann, Large area moisture monitoring in buildings and building materials in *Proc. 8th Int. Conf. on Electromagnetic Wave Interaction with Water and Moist Substances,* edited by P. Vainikainen; T. Laitinen (Espoo: Helsinki University of Technology, 2009) pp 84-91.

[667] S. Schlaeger, A fast TDR-inversion technique for the reconstruction of spatial soil moisture content, *Hydrol. Earth Syst. Sci.* **9** (2005) 481-492.

[668] C. Hübner; S. Schlaeger; R. Becker; A. Scheuermann; A. Brandelik; W. Schaedel; R. Schuhmann, Advanced measurement methods in time domain reflectometry for soil moisture determination, in *Electromagnetic Aquametry*, edited by K. Kupfer (Springer, Berlin, 2005) pp 317-347.

[669] C. Hübner; K. Kupfer, Modelling of electromagnetic wave propagation along transmission lines in inhomogeneous media, *Meas. Sci. Technol.* **18** (2007) 1147-1154.

[670] A. Scheuermann; A. Bieberstein; S. Schlaeger; R. Becker, Optimiertes Sensordesign zur Bestimmung von Feuchteprofilen in verlustbehafteten Böden, *Techn. Messen* **74** (2007) 308-315.

[671] M. Stacheder; F. Koeniger; R. Schuhmann, New dielectric sensors and sensing techniques for soil and snow moisture measurements, *Sensors* **9** (2009) 2951-2967.

[672] C. Hübner; R. Cardell-Oliver; R. Becker; Klaus Spohrer; K. Jotter; T. Wagenknecht, Wireless soil moisture sensor networks for

environmental monitoring and vineyard irrigation, in *Proc. 8th Int. Conf. on Electromagnetic Wave Interaction with Water and Moist Substances*, edited by P. Vainikainen; T. Laitinen (Helsinki University of Technology, Espoo, 2009) pp 408-415.

[673] S. Schlaeger; C. Hübner; R. Becker, Simple soil-moisture probe for low-cost measurement applications, in *Proc. 6th Int. Conf. on Electromagnetic Wave Interaction with Water and Moist Substances*, edited by K. Kupfer; C. Hübner; E. Trinks: H. Kupfer (Bauhaus University, Weimar, 2005) pp 258-265.

[674] C. Hübner; K. Spohrer; D. Hambsch; M. Lenz; T. Wagenknecht; K. Jotter; J. Müller, Wetting front detection with a profile soil moisture sensor, in *Proc. 9th Int. Conf. on Electromagnetic Wave Interaction with Water and Moist Substances*, edited by D. B. Funk; S. Trabelsi; R. O. Pierce (United States Department of Agriculture, Kansas City, 2011) pp 139-145.

[675] C. Hübner; K. Spohrer; D. Hambsch; T. Wagenknecht; K. Jotter; J. Müller, Soil moisture profile sensor for irrigation, in *Proc. 6. CMM-Tagung Innovative Feuchtemessung in Forschung und Praxis – Materialeigenschaften und Prozesse*, edited by R. Schuhmann; A. Ehbrecht; K. Emmerich; F. Königer (Kompetenzzentrum für Materialfeuchte am KIT, Karlsruhe, 2011) pp 177-185.

[676] M. K. Mandal; B. C. Sakar, Ring oscillators: Characteristics and applications, *Ind. J. Pure Appl. Phys.* **48** (2010) 136-145.

[677] J. M. Blomquist, Jr.; S. B. Jones; D. A. Robinson, Precise irrigation scheduling for turfgrass using a subsurface electromagnetic soil sensor, *Agricult. Water Managem.* **84** (2006) 153-165.

[678] B. Will; M. Garding; C. Schulz; C. Baer; T. Musch; I. Rolfes, A time domain transmission measurement system for dielectric characterizations, *Int. J. Microw. Wireless Technol.* **4** (2012) 349-355.

[679] B. Will; I. Rolfes, Comparative study of moisture measurements by time domain transmissometry, in *Proc. IEEE Sensors* (*Baltimore, 2013*) pp 1-4; DOI: 10.1109/ICSENS.2013.6688529.

[680] B. Will; V. Crnojević-Bengin; G. Kitić, Microwave soil moisture sensors, in *Proc. 43rd Europ. Microw. Conf.* (*Nuremberg, 2013*) pp 862-865.

[681] B. Will; C. Schulz; C. Baer; M. Gerding; T. Musch; I. Rolfes, A measurement system for soil moisture characterizations based on time domain transmission, in *Proc. 10th Int. Conf. on Electromagnetic Wave Interaction with Water and Moist Substances*, edited by K. Kupfer; N. Wagner; R. Wagner; B. Müller; F. Bonitz;

C. Hübner; M. Noack (Bauhaus University, Weimar, 2013) pp 275-282.
[682] B. Will; I. Rolfes, A miniaturized soil moisture sensor based on time domain transmissiometry, *Proc. Sensor Applic. Symp*. (Qneenstown, 2014) pp 233-236; DOI: 10.1109/SAS.2014.6798952.
[683] M. S. S. Karaj; K. Spohrer; C. Hübner; J. Müller, Dual soil moisture sensor for simultaneous water content and water potential measurements: Functional principle and first results, *VDI-Bericht Landtechnik 2173* (2013) pp 475-481.
[684] A. Cataldo; G. Monti; E. De Benedetto; G. Cannazza; L. Tarricone, A noninvasive resonance-based method for moisture content evaluation through microstrip antennas, *IEEE Trans. Instrum. Meas.* **58** (2009) 1420-1426.
[685] R. N. Dean; A. K. Rane; M. E. Baginski; J. Richard; Z. Hartzog; D. J. Elton, A capacitive fringing field sensor design for moisture measurement based on printed circuit board technology, *IEEE Trans. Instrum. Meas.* **61** (2012) 1105-1112.
[686] F. Jonard; L. Weihermüller; K. Z. Jadoon; M. Schwank; H. Vereecken; S. Lambot, Mapping field-scale soil moisture with L-band radiometer and ground-penetrating radar over bare soil, *IEEE Trans. Geosci. Remote Sens.* **49** (2011) 2863-2875.
[687] N. N. Das; D. Entekhabi; E. G. Njoku, An algorithm for merging SMAP radiometer and radar data for high-resolution soil-moisture retrival, *IEEE Trans. Geosci. Remote Sens.* **49** (2011) 1504-1512.
[688] C. P. Weaver; R. Avissar, Atmospheric disturbances caused by human modification of landscape, *Bull. Am. Meteorol. Soc.* **82** (2001) 269-281.
[689] A. Monerris; T. Schmugge, Soil moisture estimation using L-band radiometry, in *Advances in Geoscience and Remote Sensing*, edited by G. Jedlovec (InTech, Rijeka, 2009).
[690] J. A. Huisman; S. S. Hubbard; J. D. Redman; A. P. Annan, Measuring soil moisture content with ground penetrating radar: A review, *Vadose Zone J.* **3** (2003) 476-491.
[691] W. Wagner; G. Blöschl; P. Pampaloni; J. C. Calvet; B. Bizzarri; J. P. Wigneron; Y. Kerr, Operational readiness of microwave remote sensing of soil moisture for hydrologic applications, *Nordic Hydrol.* **38** (2007)1-20.
[692] T. Schmugge; P. Gloersen; T. T. Wilheit; F. Geiger, Remote sensing of soil moisture with microwave radiometers, *J. Geophys. Res.* **79** (1974) 317-323.
[693] J. R. Eagleman; W. C. Lin, Remote sensing of soil moisture by a

21 cm passive radiometer, *J. Geophys. Res.* **81** (1976) 3660-3666.
[694] T. J. Jackson; T. J. Schmugge; J. R. Wang, Passive microwave sensing of soil moisture under vegetation canopies, *Water Resources Res.* **18** (1982) 1137-1142.
[695] E. Hecht, *Optics* (Addison Wesley Longman, Boston, 2002).
[696] E. G. Njoku; D. Entekhabi, Passive microwave remote sensing of soil moisture, *J. Hydrol.* **184** (1996) 101-129.
[697] J. P. Wigneron; Y. Kerr; P. Waldteufel; K. Saleh; M. J. Escorihuela; P. Richaume; P. Ferrazzoli; P. de Rosnay; R. Gurney; J. C. Calvet; T. Pellarin; R. Gurney; C. Mätzler, L-band microwave emission of the biosphere (L-MEB) model: Description and calibration against experimental sets over crop fields, *Remote Sens. Environm.* **107** (2007) 639-655.
[698] K. Schneeberger; M. Schwank; C. Stamm; P. de Rosnay; C. Mätzler; H. Flühler, Topsoil structure influencing soil water retrival by microwave radiometry, *Vadose Zone J.* **3** (2004) 1169-1179.
[699] M. Kurum; R. H. Lang; P. E. O'Neill; A. T. Joseph; T. J. Jackson; M. H. Cosh, A first-order radiative transfer model for microwave radiometry of forest canopies at L-band, *IEEE J. Geosc. Remote Sens. Lett.* **49** (2011) 3167-3179.
[700] M. Guglielmetti; M. Schwank; C. Mätzler; C. Oberdorster; J. Vanderborght; H. Fluhler, Fosmex: Forest soil moisture experiments with microwave radiometry, *IEEE Trans. Geosci. Remote Sens.* **46** (2008) 727-735.
[701] J. P. Grant; A. A. Van de Griend; M. Schwank; J. P. Wigneron, Observations and modeling of a pine forest floor at L-band, *IEEE Trans. Geosci. Remote Sens.* **47** (2009) 2024-2034.
[702] F. Jonard; L. Weihermüller; M. Schwank; K. Z. Jadoon; H. Vereecken; S. Lambot, Estimation of hydraulic properties of a sandy soil using ground-based active and passive microwave remote sensing, *IEEE Trans. Geosci. Remote Sens.* **53** (2015) 3095-3109.
[703] F. T. Ulaby; P. C. Dubois; J. van Zyl, Radar mapping of surface soil moisture, *J. Hydrol.* **184** (1996) 57-84.
[704] D. J. Inman; R. S. Freeland; J. T. Ammons; R. E. Yoder, Soil investigations using electromagnetic induction and ground-penetrating radar in southwest Tennessee, *Soil Sci. Soc. Am. J.* **66** (2002) 206-211.
[705] A. P. Annan, GPR methods for hydrogeological studies, in *Hydrogeophysics*, edited by Y. Rubin; S. Hubbard (Springer, New York, 2005) pp 185-213.
[706] N. Pierdicca; P. Castracane; L. Pulvirenti, Inversion of electro-

magnetic models for bare soil parameter estimation from multifrequency polarimetric SAR data, *Sensors* **8** (2008) 8181-8200.

[707] S. J. Katzberg; O. Torres; M. S. Grant; D. Masters, Utilizing calibrated GPS reflected signals to estimate soil reflectivity and dielectric constant: results from SMEX02, *Remote Sens. Environ.* **100** (2005) 17-28.

[708] K. M. Larson; E. E. Small; E. D. Gutmann; A. L. Billich; J. J. Braun; V. U. Zavorotny, Use of GPS receivers as a soil moisture network for water cycle studies, *Geophys. Res. Lett.* **35** (2008) L24405.

[709] K. M. Larson; E. E. Small; E. D. Gutmann; A. L. Billich; P. Axelrad; J. J. Braun, Using GPS multipath to measure soil moisture fluctuations: initial results, *GPS Solut.* **12** (2008) 173-177.

[710] K. M. Larson; J. J. Braun; E. E. Small; V. U. Zavorotny; E. D. Gutmann; A. L. Billich, GPS multipath and its relation to near-surface soil moisture content, *IEEE J. Sel. Topics Appl. Earth Observ. Remote Sens.* **3** (2010) 91-99.

[711] C. C. Chew; E. E. Small; K. M. Larson; V. U. Zavorotny, Effects of near-surface soil-moisture on GPS SNR data: development of a retrieval algorithm for soil moisture, *IEEE Trans Geosci. Remote Sens.* **52** (2014) 537-543.

[712] N. Rodriguez-Alvarez; X. Bosch-Lluis; A. Camps; M. Vall-Ilossera; E. Valencia; J. F. Marchan-Hernandez; I. Ramos-Perez, Soil moisture retrival using GNSS-R techniques: experimental results over a bare soil field, *IEEE J. Geosci. Remote Sens. Lett.* **47** (2009) 3616-3624.

[713] N. Rodriguez-Alvarez; X. Bosch-Lluis; A. Camps; A. Aguasca; M. Vall-Ilossera; E. Valencia; I. Ramos-Perez; H. Park, Review of crop growth and soil moisture monitoring from a ground-based instrument implementing the interference pattern GNSS-R technique, *Radio Sci.* **46** (2011) RS0C03.

[714] K. M. Larson; E. E. Small, Using GPS to study the terrestrial water cycle, *Eos Trans. Am. Geophys. Union* **94** (3013) 505-506.

[715] A. R. von Hippel, *Dielectrics and Waves* (Wiley, New York, 1954).

[716] N. E. C. Verhoest, H. Lievens; W. Wagner; J. Alvares-Mozos; M. S. Moran; F. Mattia, On the soil roughness parameterization problem in soil moisture retrieval of bare surfaces from synthetic aperture radar, *Sensors* **8** (2008) 4213-4248.

[717] P. C. Dubois; J. Vanzyl; T. Engman, Measuring soil-moisture with imaging radars, *IEEE Trans. Geosci. Remote Sens.* **33** (1995) 915-926.

[718] J. P. Deroin; A. Company; A. Simonin, An empirical model for

interpreting the relationship between backscattering and aric land surface roughness as seen with SAR, *IEEE Trans. Geosci. Remote Sens.* **35** (1997) 86-92.
[719] G. D'Urso; M. Minacapilli, A semi-empirical approach for surface soil water content estimation from radar data without a-priori information on surface roughness, *J. Hydrol.* **321** (2006) 297-310.
[720] C. Hübner; C. Kottmeier; A. Brandelik, A new approach towards large scale soil moisture mapping by radio waves, *Sens. Imaging* **12** (2011) 1-13.
[721] V. Cooray; K. L. Cummins, Propagation effects caused by stratified ground on electromagnetic fields of return strokes, in *20th Int. Lightening Detection Conf.* (Tuscon, 2008).
[722] O. Kiseleva; C. Hübner; A. Brandelik; N. Kalthoff; M. Kohler; F. Königer; C. Kottmeier, A new approach to investigate soil moisture dynamics by radio waves, in *TERENO Int. Conf. (Tuscon, 2014)* pp 3-35.
[723] F. Yi; I. Astin, Remote sensing of soil moisture using the propagation of Loran-C navigation signals, *IEEE J. Geosci. Remote Sens. Lett.* **12** (2015) 195-198.
[724] A. Overeem; H. Leijnse; R. Uijlenhoet, Measuring urban rainfall using microwave links from commercial cellular communication networks, *Water Resources Res.* **47** (2011) W12505.
[725] W. A. Cumming, The dielectric properties of ice and snow at 3.2 cm, *J. Appl. Phys.* **23** (1952) 768-773.
[726] R. P. Auty; R. H. Cole, Dielectric properties of ice and solid D_2O, *J. Chem. Phys.* **20** (1952) 1309-1314.
[727] S. Evans, Dielectric properties of ice and snow – a review, *J. Glaciol*. **5** (1965) 773-792.
[728] J. G. Paren; J. W. Glen, Electrical behavior of finely divided ice, *J. Glaciol.* **21** (1978) 173-192.
[729] W. Ambach; A. Denoth, The dielectric behavior of snow: A study versus liquid water content, in *Proc. NASA Workshop on the Microwave Remote Sensing of Snowpack Properties*, edited by A. Rango (NASA Goddard Space Flight Center, Greenbelt, 1980; NASA CP-2153).
[730] W. H. Stiles; F. T. Ulaby, Dielectric Properties of Snow, *Remote Sensing Laboratory Technical Report 527-1* (University of Kansas Center for Research, Inc., Lawrence, 1981) pp 91-103.
[731] C. Mätzler, Microwave permittivity of dry snow, *IEEE Trans. Geosci. Remote Sens.* **34** (1996) 573-581.
[732] M. E. Tiuri; A. H. Sihvola; E. G. Nyfors; M. T. Hallikaiken, The

complex dielectric constant of snow at microwave frequencies, *IEEE J. Ocean. Engin.* **9** (1984) 377-382.

[733] A. Sihvola; M. Tiuri, Snow fork for field determination of the density and wetness profiles of snow pack, *IEEE Trans. Geosci. Remote Sens.* **24** (1986) 717-721.

[734] A. Denoth, Snow dielectric measurements, *Adv. Space Res.* **9** (1989) 233-243.

[735] H. Aebischer; C. Maetzler, A microwave sensor for the Measurement of the liquid water content on the surface of the snow cover, *Proc. 13th Europ. Microw. Conf.*, edited by D. H. Groll (Microwave Exhibitions, Tunbridge-Wells, 1983) pp 483-487.

[736] J. R. Kendra; F. T. Ulaby; K. Sarabandi, Snow probe for *in situ* determination of wetness and density, *IEEE Trans Geosci. Remote Sens.* **32** (1994) 1152-1158.

[737] S. K. Goel, S. K. Mittal; N. Gupta, Development of a sensor for *in-situ* determination of snow moisture and density, in *Proc. 6th Conf. on Electromagnetic Wave Interaction with Water and Moist Substances*, edited by K. Kupfer, C. Hübner, E. Trinks, H. Kupfer (MPFA, Bauhaus Universität, Weimar, 2005) pp 405-412.

[738] S. K. Mittal, M. Singh; R. K. Garg, Development of an instrument to measure density and moisture content of snow, *J. Sci. Industr. Res.* **68** (2009) 188-191.

[739] A. Carta; A. Ghaghazanian; R. Stefanelli; D. Trichero, Radiofrequency sensors for snow conditions monitoring and real time avalanche alerts, *Proc. IEEE Topical Conf. Wireless Sensors and Sensor Networks* (Austin, 2013) pp 49-51.

[740] J. Stein; G. Laberge; D. Lévesque; Monitoring the dry density and the liquid water content of snow using time domain reflecometry (TDR), *Cold Reg. Sci. Technol.* **25** (1997) 123-136.

[741] P. Waldner; C. Hübner; M. Schneebeli; A. Brandelik; F. Rau, Continuous measurements of liquid water content and density in snow using TDR, *Proc. 2nd Intern. Symp. Workshop Time Domain Reflectometry Innov. Geotechn. Appl.*, edited by C. H. Dowding (Infrastruture and Technology Institute, Northwestern University, Evanston) pp 446-456.

[742] M. Niang; M. Bernier; Y. Gauthier; G. Fortin; E. van Bochove; M. Stacheder; A. Brandelik, On the validation of snow densities derived from Snowpower probes in a temperate snow cover in eastern Canada: first results, in *Proc. 60th East. Snow Conf.* (Sherbrooke, 2003) pp 175-187.

[743] M. Stacheder; C. Hübner; S. Schlaeger; A. Brandelik, Combined TDR

and low-frequency permittivity measurements for continuous snow wetness and snow density determination, in *Electromagnetic Aquametry*, edited by K. Kupfer (Springer, Berlin, 2005) pp 367-382.

[744] M. Stähli; D. Gustafsson; M. Stacheder; M. Bernier; M. Niang; K. Chokmani; S. Savary; E. van Bochove; W. Sommer; I. Völksch, Test of a new *in-situ* snow sensor for validation of remote sensing images, *Proc. EARSeL*, Berne, 2005.

[745] M. Niang; M. Bernier; M. Stacheder; A. Brandelik; E. van Bochove, Influence of snow temperature interpolation algorithm and dielectric mixing-model coefficient on density and liquid water content determination in a cold seasonal snow pack, *Sens. Imag. Intern. J.* **7** (2006) 1-22.

[746] A. Langlois; A. Royer; E. Fillol; A. Frigon; R. Laprise, Evaluation of the snow cover variation in the Canadian regional climate model over eastern Canada using passive microwave satellite data, *Hydrol. Process.* **18** (2004) 1127-1138.

[747] Y. Kim; J. S. Kimball; K. C. McDonald; J. Glassy, Developing a global data record of daily landscape freeze/thaw status using satellite passive microwave remote sensing, *IEEE Trans. Geosci. Remote Sens.* **49** (2011) 949-960.

[748] M. A. Rawlins; K. C. McDonald; S. Frolking; R. B. Lammers; M. Fahnestock; J. S. Kimball, C. J. Vörösmarty, Remote sensing of snow thaw at the pan-Arctic scale using the SeaWinds scatterometer, *J. Hydrol.* **312** (2005) 294-311.

[749] F. Rémy; S. Parouty, Antarctic ice sheet and radar altimetry: a review, *Remote Sens.* **1** (2009) 1212-1239.

[750] F. Koch; M. Prasch; L. Schmid; J. Schweizer; W. Mauser, Measuring snow liquid water content with low-cost GPS receivers, *Sensors* **14** (2014) 20975-20999.

[751] S. Kruschwitz; E. Niederleithinger; C. Trela; J. Wöstmann, Complex resistivity and radar investigation of building material: first results of field scale measurements, *Acta Geophys.* **58** (2009) 96-113.

[752] H. Garrecht; S. Reeb; E. Alexandrakis, Feuchtemessung im Bauwesen mittels TDR, in *Baustoff und Konstruktion*, edited by R. Nothnagel; H. Twelmeier (Springer, Berlin, 2013) pp 299-307.

[753] S. Kruschwitz, Feuchtemessung im Bauwesen – ein Überblick, in *Fachtagung Bauwerksdiagnose Berlin 2014* (DGZfP eV, Berlin, 2014) .

[754] C. Ferrara, P. M. Barone, Detecting moisture damage in archaeology and cultural heritage sites using the GPR technique: a brief

introduction, *J. Archaeol.* **3** (2015) 57-61.
[755] M. C. Phillipson; P. H. Baker; M. Davies; Z. Ye; G. H. Galbraith; R. C. McLean, Suitability of time domain reflectometry for monitoring moisture in building materials, *Building Serv. Eng. Res. Technol.* **29** (2008) 261-272.
[756] A. Kemma; A. Binley; G. Cassiani; E. Niederleithinger; A. Revil; L. Slater; K. H. Williams; A. F. Orozco; F.-H- Haegel; A. Hördt; S. Kruschwitz; V. Leroux; K. Titov; E. Zimmermann, An overview of the spectral induced polarization method for near-surface applications, *Near Surface Geophys.* **10** (2012) 453-468.
[757] O. Sass; H. A. Viles, Wetting and drying of masonry walls: 2D-resistivity monitoring of driving rain experiments on historic stonework in Oxford, UK, *J. Appl. Geosci.* **70** (2010) 72-83.
[758] S. Kruschwitz; E. Niederleithinger; C. Trela; J. Wöstmann, Use of complex resistivity tomography for moisture monitoring in a flooded masonry specimen, *J. Infrastruct. Syst.* **18** (2012) 2-11.
[759] B. H. Brown, Electrical impedance tomography (EIT) – A review, *J. Med. Eng. Technol.* **27** (2003) 97-108.
[760] I. Frerichs, Electrical impedance tomography (EIT) in applications related to lung and ventilation: a review of experimental and clinical activities, *Physiol. Meas.* **21** (2000) R1-R21.
[761] M. Bodenstein; M. David; K. Markstaller, Principles of electrical impedance tomography and ist clinical application, *Crit. Care Med.* **37** (2009) 713-724.
[762] P. O. Gaggero; A. Adler; J. Brunner; P. Seitz, Electrical impedance tomography system based on active electrodes, *Physiol. Meas.* **33** (2012) 831-847.
[763] R. Harikumar; R. Prabu; S. Raghavan, Electrical impedance tomography (EIT) and its medical applications: a review, *Intern. J. Soft Comput. Engin.* **3** (2013) 193-198.
[764] K. Y. Aristovich; B. C. Packham; H. Koo; G. Satos dos Santos, Imaging fast electrical activity in the brain with electrical impedance tomography, *NeuroImage* **124** (2016) 204-213.
[765] M. Pessel; D. Gibert, Multiscale electrical impedance tomography, *J. Geophys. Res.* **108** (2003) doi: 10.1029/2001JB000233.
[766] W. Daily; A. Ramirez, Electrical imaging of engineered hydraulic barriers, *Geophys.* **65** (2000) 83-94.
[767] C. Sodeikat, Feuchtesensoren in der Bauwerksüberwachung, in *Proc. Fachtagung Bauwerksdiagnose Berlin 2010* (Deutsche Gesellschaft für zerstörungsfreie Prüfung e.V., Berlin, 2010) lecture 9: www.ndt.net/article/dgzfp-bau2010/papers/V07.pdf.

[768] R. S. Li; C. Zeiss, In situ moisture content measurement in MSW landfills with TDR, *Environm. Engin. Sci.* **18** (2001) 53-66.

[769] F. Königer, R. Nüesch, W. Rabl-Lasar; J. Roth; P. Ruppert, R. Schuhmann, Alternative surface covering of landfill using the TAUPE sealing control system, in *Proc. 6th Int. Conf. on Electromagnetic Wave Interaction with Water and Moist Substances*, edited by K. Kupfer; C. Hübner; E. Trinks; H. Kupfer (Bauhaus University, Weimar, 2005) pp 422-428.

[770] K. Kupfer; E. Trinks; N. Wagner; M. Kuhne; B. Müller, TDR-Measurements in underground MgO-concrete barriers for hazardous waste in salt mines, in *Proc. 8th Int.Conf. on Electromagnetic Wave Interaction with Water and Moist Substances*, edited by P. Vainikainen; T. Laitinen (Helsinki University of Technology, Espoo, 2009) pp 337-343.

[771] F. Königer; K. Emmerich; G. Kemper; M. Gruner; W. Gaßner; M. Stacheder; R. Schuhmann, Monitoring of moisture spreading in a multi-layer hydraulic sealing system during saturation with a rock salt brine by TDR sensors, in *Proc. 8th Int.Conf. on Electromagnetic Wave Interaction with Water and Moist Substances*, edited by P. Vainikainen; T. Laitinen (Helsinki University of Technology, Espoo, 2009) pp 365-371.

[772] C. Hübner; A. Brandelik; A. Gerdes; K. Kupfer; P. Ruppert, Moisture measurement system for monitoring large area building constructions, in *Proc. 7th Int. Conf. on Electromagnetic Wave Interaction with Water and Moist Substances*, edited by S. Okamura; N. Sobue; S. Yagihara; Y. Zhang (Shizuoka University, Hamamatsu, 2007) pp 139-149.

[773] A. Cataldo; E. De Benedetto; G. Cannazza, Hydration monitoring and moisture control of cement-based samples through embedded wire-like sensing elements, *IEEE Sensors J.* **15** (2015) 1208-1214.

[774] R. Plagge; J. Grunewald, Measurement of continuous drying out of subterranean concrete walls, in *Proc. 6th Int. Conf. on Electromagnetic Wave Interaction with Water and Moist Substances*, edited by K. Kupfer; C. Hübner; E. Trinks: H. Kupfer (Bauhaus University, Weimar, 2005) pp 294-301.

[775] R. Černý; M. Pavlíková; Z. Pavlík; Z. Suchorab, Effect of sensor installation method on the applicability of TDR moisture measurement technique, in *Proc. 8th Int. Conf. on Electromagnetic Wave Interaction with Water and Moist Substances*, edited by P. Vainikainen; T. Laitinen (Helsinki University of Technology, Espoo, 2009) pp 113-117.

[776] J. H. Zhao; E. Rivera; A. Mufti; D. Stephenson; D. J. Thomson, Evaluation of dielectric based and other methods for moisture content measurement in building stones, *J. Civil Struct. Health Monit.* **2** (2012) 137-148.

[777] R. Plagge, TDR measurement of continuous drying out of concrete walls, in *Proc. 10th Int. Conf. on Electromagnetic Wave Interaction with Water and Moist Substances*, edited by K. Kupfer; N. Wagner; R. Wagner; B. Müller; F. Bonitz; C. Hübner; M. Noack (Bauhaus University, Weimar, 2013) pp 373-379.

[778] Z. Suchorab; M. K. Widomski; G. Łagód; D. Barnat-Hunek; P. Smarzewski, Methodology of moisture measurement in porous materials using time domain reflectometry, *Chem. Didact. Ecol. Metrol.* **19** (2014) 97-107.

[779] F. S. Malan; K. Ahmat; A. Dunster; R. Hearing, Development of a microwave frequency sensor for the long-term localised moisture monitoring of concrete, *Mag. Concrete Res.* **56** (2004) 263-271.

[780] J. B. Ong; Z. You; J. Mills-Beale; E. Lim Tan; B. D. Pereles; K. Ghee Ong, A wireless, passive embedded sensor for real-time monitoring of water content in civil engineering materials, *IEEE Sensors J.* **8** (2008)2053-2058.

[781] G. Stojanović; M. Radovanović; M. Malešev; V. Radonjanin, Monitoring of water content in building materials using a wireless passive sensor, *Sensors* **10** (2010) 4270-4280.

[782] M. Adous; P. Quéffélec; L. Laguerre, Coaxial/cylindrical transition line for broadband permittivity measurement of civil engineering materials, *Meas. Sci. Technol.* **17** (2006) 2241-2246.

[783] K. Kupfer; E. Trinks; N. Wagner; C. Hübner, TDR measurements and simulations in high lossy bentonite materials, *Meas. Sci. Technol.* **18** (2007) 1118-1136.

[784] N. E. Hager III; R. C. Domszy, Monitoring of cement hydration by broadband time-domain-reflectometry dielectric spectroscopy, *J. Appl. Phys.* **96** (2004) 5117-5128.

[785] F. Volgyi, Non-contact moisture sensor for fresh concrete, in *Proc. 6th Int. Conf. on Electromagnetic Wave Interaction with Water and Moist Substances*, edited by K. Kupfer; C. Hübner; E. Trinks; H. Kupfer (Bauhaus University, Weimar, 2005) pp 267-277.

[786] W. M. Healy, *In-situ* measurement of moisture content of building materials using ultra-wideband radio waves, in *Research in Buildin Physics and Building Engineeriung*, edited by P. Fazio; H. Ge; J. Rao; G. Desmarais (Taylor & Francis, London, 2006).

[787] K. Haddadi; M. M. Wang; D. Glay; T. Lasri, Free-space microwave

moisture content evaluation by means of low-cost four-port based reflectometer, in *Proc. 8th Int. Conf. on Electromagnetic Wave Interaction with Water and Moist Substances*, edited by P. Vainikainen; T. Laitinen (Helsinki University of Technology, Espoo, 2009) pp 63-70.

[788] A. Göller, MOIST SCAN – Multi layer moisture scans on large areas in practice, in *Aquametry 2010*, edited by K. Kupfer, N. Wagner, R. Wagner, F. Bonitz, B. Müller, and C. Hübner (MPFA, Bauhaus Universität, Weimar, 2010) pp 389-397.

[789] K. Haddadi; T. Lasri, CW radar for monitoring water-to cellular concrete, in *Proc. 44th Europ. Microw. Conf. Rome 2014*, pp 1832-1835, doi: 978-2-87487-035-4

[790] T. Sokoll; A. F. Jacob, Self-oscillating measurement system for *in-situ*-monitoring moisture in buildings, *IEEE Trans. Instrum. Meas.* **63** (2014) 2911-2918.

[791] Z. Suchorab; H. Sobczuk; R. Černý; Z. Pavlik; R. Plagge, Noninvasive moisture measurement of building materials using TDR method, in *Proc. 8th Int. Conf. on Electromagnetic Wave Interaction with Water and Moist Substances*, edited by P. Vainikainen; T. Laitinen (Helsinki University of Technology, Espoo, 2009) pp 147-155.

[792] J. Pavlik; P. Tesárek; R. Černý, Application of microwave impuls method for measuring moisture profiles in building materials, in *Proc. 6th Int. Conf. on Electromagnetic Wave Interaction with Water and Moist Substances*, edited by K. Kupfer; C. Hübner; E. Trinks; H. Kupfer (Bauhaus University, Weimar, 2005) pp 278-285.

[793] J. Lidieu; P. De Ridder; P. De Clerck; S. Dautrebande, A method of measuring soil moisture by time-domain reflectometry, *J. Hydrol.* **88** (1986) 319-328.

[794] M. A. Malecki; R. Plagge; C. H. Roth, Improving the calibration of dielectric TDR soil moisture determination taking into account the solid soil, *Eur. J. Soil Sci.* **47** (1996) 357-366.

[795] K. Lichtenecker, Die Dielektrizitätskonstante natürlicher und künstlicher Mischkörper, *Phys. Z.* **27** (1926) 115-158.

[796] T. Zakri; J.-P. Laurent; M. Vauclin, Theoretical evidence for „Lichtenecker's mixture formulae" based on effective medium theory, *J. Phys. D: Appl. Phys.* **31** (1998) 1589-1594.

[797] Z. Pavlík; L. Fiala; R. Černý, Determination of moisture content of hygroscopic building materials using time domain reflectometry, *J. Appl. Sci.* **8** (2008) 1732-1737.

[798] I. M. Woodhead; G. D. Buchan; J. H. Christie; K. A. Irie, A general dielectric model for time domain reflectometry, *Biosyst. Engin.* **86**

(2003) 207-216.
[799] I. M. Woodhead; J. H. Christie; I. Platt; M. Hagedorn, Density compensation for moisture measurements in wood, in *Proc. 8th Int. Conf. on Electromagnetic Wave Interaction with Water and Moist Substances*, edited by P. Vainikainen; T. Laitinen (Helsinki University of Technology, Espoo, 2009) pp 281-288.
[800] G. Szabó; R. Rajkó; C. Hodúr, Combined energy transfer by microwave-convective drying of agriculture materials, *Hung. Agricult. Engin.* **11** (1998) 23-25.
[801] S. O. Nelson, *Dielectric properties of agricultural materials and their applications* (Elsevier, Amsterdam, 2015).
[802] S. Trabelsi; S. O. Nelson, Temperature-dependent behavior of dielectric properties of bound water in grain at microwave frequencies, *Meas. Sci. Technol.* **17** (2006) 2289-2293.
[803] S. Trabelsi; S. O. Nelson, Unified microwave moisture sensing technique for grain and seed, *Meas. Sci. Technol.* **18** (2007) 997-1003.
[804] V. M. Serdyuk, Dielectric study of bound water in grain at radio and microwave frequencies, *Progr. Electromag. Research* **84** (2008) 379-406.
[805] A. Cataldo; M. Vallone; L. Tarricone; G. Cannazza; M. Cipressa, TDR moisture estimation for granular materials: an application in agro-food industrial monitoring, *IEEE Trans. Instrum. Meas.* **58** (2009) 2597-2605.
[806] Z. M. Tong; L. H. Rong; C. J. Huang, Grain moisture content measurement system based on time-domain transmission technology, *Appl. Mech. Materials* **241-244**, (2012) 214-217.
[807] K. Y. You; H. K. Mun; L. L. You; J. Salleh; Z. Abbas, A small and slim coaxial probe for single rice grain moisture sensing, *Sensors* **13** (2013) 3652-3663.
[808] C. V. K. Kandala; S. O. Nelson, RF impedance method for nondestructive moisture content determination for in-shell peanuts, *Meas. Sci. Technol.* **10** (2007) 991-996.
[809] S. Trabelsi; M. Lewis; S. O. Nelson, Rapid sensing of peanut kernel moisture content from microwave permittivity measurements on unshelled pods, in *Proc. 8th Int. Conf. on Electromagnetic Wave Interaction with Water and Moist Substances*, edited by P. Vainikainen; T. Laitinen (Helsinki University of Technology, Espoo, 2009) pp 405-407.
[810] E. Vozáry; G. Jónás; G. Hitka; G. Koncz; G. Hanula-Kövér; R. P. Benkő, Effect of air humidifying on impedance parameters of ice lettuce, in

Proc. 8th Int. Conf. on Electromagnetic Wave Interaction with Water and Moist Substances, edited by P. Vainikainen; T. Laitinen (Helsinki University of Technology, Espoo, 2009) pp 398-404.

[811] T. Hinz; F. Menke; R. Eggers; R. Knöchel, Development of a microwave moisture sensor for application in the food industry, *Lebensm.-Wiss. Technol.* **29** (1996) 316-325.

[812] S. Okamura, Microwave technology for moisture measurement, *Subsurf. Sens. Technol. Appl.* **1** (2000) 205-227.

[813] S. Okamura; Y. Zhang; N. Tsukamoto, A new microstripline-type moisture sensor for heavily wet tea leaves, *Meas. Sci. Technol.* **18** (2007) 1022-1028.

[814] O. Schimmer; F. Daschner; M. Kent; R. Knöchel, Determination of quality and storage-time of dielectric mixtures using time domain spectroscopy, *Adv. Radio Sci.* **2** (2004) 1-5.

[815] O. Schimmer; R. Osen; K. Schönfeld; B. Hemmy, Detection of added water in seafood using a dielectric time domain reflectometer, in *Proc. 8th Int. Conf. on Electromagnetic Wave Interaction with Water and Moist Substances*, edited by P. Vainikainen; T. Laitinen (Helsinki University of Technology, Espoo, 2009) pp 350-357.

[816] M. Kent; R. Knöchel; F. Daschner; O. Schimmer; J. Oehlenschläger; S. Mierke-Klemeyer; M. Kroeger; U.-K. Barr; P. Floberg; M. Tejada; A. Huidobro; L. Nunes; A. Martins; I. Batista; C. Cardoso, Intangible but not intractable: the prediction of fish „quality" variables using dielectric spectroscopy, *Meas. Sci. Technol.* **18** (2007) 1029-1037.

[817] K. bin Khalid; T. Lay Hua, Development of conductor-backed coplanar waveguide moisture sensor for oil palm fruit, *Meas. Sci. Technol.* **9** (1998) 1191-1195.

[818] Y. K. Yeow; Z. Abbas; K. Khalid, Application of microwave moisture sensors for determination of oil palm fruits ripeness, *Meas. Sci. Rev.* **10** (2010) 7-14.

[819] N. Misrom; N. H. Harun; Y. K. Lee; R. M. Sidek; I. Aris; H. Wakiwaka; K. Tashiro, Improvement in sensitivity of an inductive oil palm fruit sensor, *Sensors* **14** (2014) 2431-2448.

[820] F. Ansarudin; Z. Abbas; J. Hassan; N. Z. Yahaga; M. A. Ismail, A simple insulated monopole sensor technique for determination of moisture content in hevea rubber latex, *Meas. Sci. Rev.* **12** (2012) 249-253.

[821] M. Pelletier, Multi-path interference mitigation for cotton bale microwave moisture sensing, *J. Cotton Sci.* **9** (2005) 135-144.

[822] S. Trabelsi; S. O. Nelson, Sensing moisture content and bulk density of pelleted biofuels by microwave permittivity measurements, in

Proc. 8th Int. Conf. on Electromagnetic Wave Interaction with Water and Moist Substances, edited by P. Vainikainen; T. Laitinen (Helsinki University of Technology, Espoo, 2009) pp 256-262.

[823] N. I. Sheen; I. M. Woodhead, An open-ended coaxial probe for broad-band permittivity measurement of agricultural products, *J. Agric. Engin. Res.* **74** (1999) 193-202.

[824] R. W. P. King; K.-M. Lee; S. R. Mishra; G. S. Smith, Insulated linear antenna: theory and experiment, *J. Appl. Phys.* **45** (1974) 1688-1697.

[825] M. P. Abegaonkar; R. N. Karekar; R. C. Aiyer, A microwave microstripring resonator as a moisture sensor for biomaterials: application to wheat grains, *Meas. Sci. Technol.* **10** (1999) 195-200.

[826] P. Throughton, Measurement techniques in microstrip, *Electron. Lett.* 5 (1969) 25-26.

[827] R. A. Yogi; S. A. Gangal; R. C. Aiyer; R. N. Karekar, Microwave ring resonator as a novel bio-material moisture sensor, *Sensors Actuators B* **50** (1998) 38-44.

[828] P. Mészáros; D. B. Funk, Unifying calibration parameters for dielectric moisture meter, *Progr. Agricult. Eng. Sci.* **2** (2006) 73-94.

[829] S. O. Nelson, Agricultural applications of dielectric measurements, *IEEE Trans. Diel. Electr. Insul.* **10** (2006) 688-702.

[830] E. Kress-Rogers; M. Kent, Microwave measurement of powder moisture and density, *J. Food. Eng.* **6** (1987) 345-376.

[831] R. A. Yogi; R. S. Parolia; R. N. Karekar; R. C. Aiyer, Microwave microstrip ring resonator as a paper moisture sensor: study with different grammage, *Meas. Sci. Technol.* **13** (2002) 1558-1562.

[832] G. Biffi Gentili; C. Riminesi, Full-wave modeling of microwave planar reflection sensors for material moisture testing, *Subsurf. Sens. Technol. Appl.* **2** (2001) 453-470.

[833] S. B. Cohn, Slot line on dielectric substrate, *IEEE Trans. Microw. Theory Techn.* **17** (1969) 768-778.

[834] G. Biffi Gentili; C. Riminesi; V. Tesi, Low cost microwave sensor for moisture content measurement in paper milling industry, *Sens. Imag.: Int. J.* **7** (2006) 155-173.

[835] R. Bhunjun; R. W. Vogt, Sensor system for contactless and online moisture measurements, *IEEE Trans. Instrum. Meas.* **59** (2010) 3034-3040.

[836] D. Banerjee; W. von Spiegel; M. D. Thomson; S. Schnabel; H. G. Roskos, Diagnosing water content in paper by terahertz radiation, *Optics Express* **16** (2008) 9060-9066.

[837] R. Afzalzadeh, Dielectric constant measurements of finite-size sheet

at microwave frequencies by pseudo-Brewster's angle method, *IEEE Trans. Microw. Theory Techn.* **46** (1998) 1307-1309.

[838] S. W. Harmer; N. Rezgui; N. Bowring; Z. Luklinska; G. Ren, Determination of the complex permittivity of textiles and leather in the 14 – 40 GHz, mm wave band using a free-wave transmittance only method, *IET Microw. Antenn. Propag.* **2** (2008) 606-614.

[839] J. Krupka; R. N. Clarke; O. C. Rochard; A. P. Gregory, Split post dielectric resonator technique for precise measurements of laminar dielectric specimens – measurement uncertainties, *Proc. XIII Conf. MIKON 2000*, Wrocław (2000) 305-308.

[840] C. D. Easton; M. V. Jacob; J. Krupka, Non-destructive complex permittivity measurement of low permittivity thin film materials, *Meas. Sci. Technol.* **18** (2007) 2869-2877.

[841] F. Chen; S. Mao; X. Wang; E. Semouchkina; M. Lanagan, Effect of cavity dimensions on $TE_{01\delta}$ mode resonance in split-post dielectric resonator techniques, *J. Electromag. Analysis Appl.* **4** (2012) 358-361.

[842] H. Ebara; T. Inoue; O. Hashimoto, Measurement method of complex permittivity and permeability for a powdered material using a waveguide in microwave band, *Sci. Technol. Adv. Materi.* **7** (2006) 77-83.

[843] B. Kapilevich; B. Litvak; V. Wainstein; D. Moshe, Density-independent moisture measurements of polymer powders using a mm-wave quasi-optical resonator, *Meas. Sci. Technol.* **18** (2007) 1069-1073.

[844] Y. Zhang, T. Okuda; N. Xu; T. Miyashita, Microstrip array antenna for moisture measurement using free space technique, in *Proc. 8th Int. Conf. on Electromagnetic Wave Interaction with Water and Moist Substances*, edited by P. Vainikainen; T. Laitinen (Helsinki University of Technology, Espoo, 2009) pp 92-95.

[845] L. Gradinarsky; F. Knutsson; S. Folestad, Modeling of the complex dielectric constant of wet pharmaceutical powders using dielectric probe measurements, in *Proc. 7th Int. Conf. on Electromagnetic Wave Interaction with Water and Moist Substances*, edited by S. Okamura; N. Sobue; S. Yagihara; Y. Zhang (Shizuoka University, Hamamatsu, 2007) pp 19-24.

[846] J. Nohlert; L. Cerullo; J. Winges; T. Rylander; T. McKelvey; A. Holmgren; L. Gradinarsky; S. Folestad; M. Viberg; A. Rasmuson, Global monitoring of fluidized-bed process by means of microwave cavity resonances, *Meas.* **55** (2014) 520-535.

[847] B. B. Owen; R. C. Miller; C. F. Milner; H. L. Cogan, The dielectric

constant of water as a function of temperature and pressure, *J. Phys. Chem.* **65** (1961) 2065-2071.
[848] L. A. Dunn; R. H. Stokes, Pressure and temperature dependence of the electrical permittivities of formamide and water, *Trans. Faraday Soc.* **65** (1969) 2906-2912.
[849] A. P. Gregory; R. N. Clarke, Traceable measurements of the static permittivity of dielectric reference liquids over the temperature range 5-50 °C, *Meas. Sci. Technol.* **16** (2005) 1506-1516.
[850] K. Lamkaouchi, L'eau: étalon dielectrique. Etude de lois diélectriques appliquées à l'eau et à des émulsions de pétrole mesurées en micro-ondes, Thesis (Universite Bordeaux I, Bordeaux, 1992).
[851] J. Wyman; E. N. Ingalls, The dielectric constant of deuterium oxide, *J. Am. Chem. Soc.* **60** (1938) 1182-1186.
[852] D. P. Fernández; Y. Mulev; A. R. H. Goodwin; J. M. H. Levelt Sengers, A database for the dielectric constant of water and steam, *J. Phys. Chem. Ref. Data* **24** (1995) 33-69.
[853] D. Bertolini; M. Cassettari; G. Salvetti, The dielectric relaxation time of supercooled water, *J. Chem. Phys.* **76** (1982) 3285-3290.
[854] P. O. Risman; B. Wäppling-Raaholt, Accurate dielectric properties of liquid water from -15 to +40 °C as determined by retromodelling of a dual resonator applicator, in *Proc. 6th Int. Conf. on Electromagnetic Wave Interaction with Water and Moist Substances*, edited by K. Kupfer; C. Hübner; E. Trinks; H. Kupfer (Bauhaus University, Weimar, 2005) pp 32-40.
[855] E. W. Rusche; W. B. Good, Search for discontinuities in the temperature dependence of the dielectric constant of pure water from -5 to +25 °C, *J. Chem. Phys.* **45** (1966) 4467-4469.
[856] M. Uematsu; E. U. Franck, Static dielectric constant of water and steam, *J. Phys. Chem. Ref. Data* **9** (1980) 1291-1305.
[857] D. P. Fernández; A. R. H. Goodwin; E. W. Lemmon; J. M. H. Levelt Sengers; R. C. Williams, A formulation for the static permittivity of water and steam at temperatures from 238 K to 873 K at pressures up to 1200 MPa, including derivatives and Debye-Hückel coefficients, *J. Phys. Chem. Ref. Data* **26** (1997) 1125-1166.
[858] W. B. Floriano; M. A. C. Nascimento, Dielectric constant and density of water as a function of pressure at constant temperature, *Braz. J. Phys.* **34** (2004) 38-41.
[859] F. D. Critchfield; J. A. Gibson, Jr.; J. L. Hall, Dielectric constant for the dioxane-water system from 20 to 35°, *J. Am. Chem. Soc.* **75** (1953) 1991-1992.

[860] R. Buchner; G. T. Hefter; P. M. May, Dielectric relaxation in aqueous NaCl solutions, *J. Phys. Chem. A* **103** (1999) 1-9.
[861] A. P. Gregory; R. N. Clarke, *Tables of the Complex Permittivity of Dielectric Reference Liquids at Frequencies up to 5 GHz* (National Physical Laboratory, Tedington, 2009) *NPL Report Mar 23*.
[862] F. Buckley; A. A. Maryott, *Tables of Dielectric Dispersion Data for Pure Liquids and Dilute Solutions* (National Bureau of Standards, Washington, 1958) *NBS Circular 589*.
[863] T. Moriyoshi; T. Ishii; Y. Tamai; M. Tado, Static dielectric constants of water + ethanol and water + 2-methyl-2-propanol mixtures from 0.1 to 300 MPa at 298.15 K, *J. Chem. Eng. Data* **35** (1990) 17-20.
[864] A. Chmielewska; M. Żurada; K. Klimaszewski; A. Bald, Dielectric properties of methanol mixtures with ethanol, isomers of propanol, and butanol, *J. Chem. Eng. Data* **54** (2009) 801-806.
[865] M. Mohsen-Nia; H. Amiri; B. Jazi, Dielectric constants of water, methanol, ethanol, butanol and acetone: measurement and computational study, *J. Sol. Chem.* **39** (2010) 701-708.
[866] F. X. Hassion; R. H. Cole, Dielectric properties of liquid ethanol and 2-propanol, *J. Chem. Phys.* **23** (1955) 1756-1761.
[867] T. Sato; A. Chiba; R. Nozaki, Dynamical aspects of mixing schemes in ethanol-water mixtures in terms of the excesss partial molar activation free energy, enthalpy, and entropy of the dielectric relaxation process, *J. Chem. Phys.* **110** (1999) 2508-2521.
[868] T. Sato; R. Buchner, Dielectric relaxation processes in ethanol / water mixtures, *J. Phys. Chem. A* **108** (2004) 5007-5015.
[869] J. Barthel; K. Bachhuber; R. Buchner; M. Kleebauer, Dielectric spectra of some common solvents in the microwave region. Dipolar aprotic solvents and amides, *Chem. Phys. Lett.* **167** (1990) 62-66.
[870] D. Bourgoin; E. Volf; M. Joly, Mesure de la permittivité complexe relative en ondes centrimétriques à l'eau et au diméthylsulfoxyde, *J. Phys. D: Appl. Phys.* **5** (1972) 589-599.
[871] U. Kaatze; R. Pottel; M. Schäfer, Dielectric spectrum of dimethyl sulfoxide / water mixtures as a function of composition, *J. Phys. Chem.* **93** (1989) 5623-5627.

Electromagnetic moisture measurement technologies have proven to be valuable tools in diverse applications. This monograph covers basic aspects of nondestructive electromagnetic methods of water content determination and relates to the associated highly multidisciplinary field of research and development. It also presents a comprehensive selection of relevant field-tested methods and instruments.

The fundamentals of electromagnetic field interactions with dipolar materials are briefly discussed, with special attention towards the dielectric properties of water and aqueous solutions. A tutorial and overview of electromagnetic measurement methods is presented, including dielectric spectroscopy in broad frequency and time domains, as well as dielectric imaging techniques. This review is complemented by a demonstration of successful real-world implementations for the moisture determination of soils, snow, buildings and building materials, food and agricultural goods, as well as various industrial products. The text is completed by a guide concerning the use of reference liquids for the calibration of sensors and instrumentation and by a bibliography of more than 850 references.

The monograph is useful as a reference book for researchers and engineers and as a textbook for upper-level students interested in the water content determination of materials.

GEORG-AUGUST-UNIVERSITÄT
GÖTTINGEN

ISBN: 978-3-86395-260-0

Universitätsverlag Göttingen